

# Real-time in-situ Monitoring of Photocatalytic Reactions by ATR Infrared Spectroscopy

Applications of Titanium Dioxide for Water Purification

**Author: Jessica Briony Mabin**

Supervisor: Dr. Stephen Lynch

Thesis submitted in fulfillment of the requirements for the degree of  
Philosophy in the Condensed Matter Physics Group  
Cardiff School of Physics and Astronomy



School of Physics and Astronomy  
Cardiff University  
Wales  
20-02-2020

---

## Acknowledgments

This PhD was one of the hardest experiences I have had to face, however I feel that I have grown in my knowledge of optical measurements techniques using FTIR and am proud of the work that has gone into this thesis. I wouldn't have been able to write this thesis if it wasn't for the tremendous amount of support that I received. I would firstly like to acknowledge my wonderful family who were constantly praying and supporting me as I worked long hours in the lab/ had writers block on how to best present my research. Mum, Dad, Beth and Beccy you have been my rock during this project and I can't thank you enough for all that you've done for me.

Next, I would like to thank my friends who stood by my side throughout and supported me in my times of need, namely Ross, Callum, Corinne, Amber and Susannah. Without the support of my amazing friends this thesis wouldn't have been possible. About a year into this project I met Adam who didn't quite know what to expect when dating someone doing a PhD, but he has loved and supported me through the whole project. You have made me laugh when I wanted to cry and stopped me from overthinking what to write in this thesis, you have been amazing so thank you.

Last and by no means least I would like to thank all of the people who have supported me from Cardiff. Rosie and George, you welcomed me into your home and let me stay on multiple occasions when I had to periodically frequent the lab overnight which I am very thankful for. Chris, you sat with me in the lab, helped me with measurements, reviewed chapters and generally steering me through this PhD and for that I am very grateful. Steve, as my supervisor you helped me when you could, and ultimately guided my understanding of the analysis tools and their capabilities that were used in this thesis.

I hope the research presented in this thesis will be furthered, and the data published can be used in taking future steps towards solving the global water crisis.



---

## Abstract

The work described in this PhD thesis describes efforts to develop a real-time in-situ infrared spectroscopy technique with the aim of better understanding the chemistry behind the photocatalytic decomposition of methylene blue dye in water. Methylene blue is a commonly used proxy for several types kinds of toxic organic chemicals that can make their way into water systems. In the presence of the semiconductor photocatalyst titanium dioxide, and under ultraviolet illumination, methylene blue breaks down into simpler chemical components, including water and carbon dioxide. However, the reaction pathway is not well understood. Infrared spectroscopy provides a diagnostic tool to study the chemical bonding of molecules, but implementing this in liquid systems is challenging because of their high infrared opacity. Attenuated total internal reflection (ATR) offers a way to shrink the effective path length to allow the infrared light to traverse the liquid, and provide enough signal to make a spectroscopic measurement. An additional challenge is to find an infrared material for ATR crystals that is chemically stable in an aqueous environment. During my PhD, several potential ATR materials were studied and the best compromise solution was found to be single-crystal zinc sulphide. An ATR flow-cell based on zinc sulphide was constructed in a multi-bounce geometry. This ATR flowcell was used to study the photocatalytic decomposition of methylene blue under ultraviolet light in the presence of titanium dioxide. A bespoke peak fitting algorithm was designed to de-convolve the peaks in the infrared spectrum during the reaction, and the changes were tracked over time. The results are compared with a simultaneous measurement of the visible absorption of methylene blue.

---

## Publications

J. Mabin, C. Hodges, S. J. Freakley, and S. A. Lynch,  
*Monitoring the Photocatalytic Degradation of Water-based Organic Pollutants by FT-IR Spectroscopy in Real-time*, Conference Proceedings of the 41st International Conference on Infrared, Millimeter, and Terahertz Waves (IRMMW-THz 2016),  
DOI: 10.1109/IRMMW-THz.2016.7758467.

## Presentations

J. Mabin, E. Alghamdi, C. Hodges, S. Freakley, S. A. Lynch,  
*“Visible and Infrared Spectroscopy of Photocatalytic Reactions for Water Treatment”*, PHOTON16 International Conference, Leeds, UK, 5-8 SEP 2016.

J. Mabin, E. Alghamdi, C. Hodges, S. Freakley, S. A. Lynch,  
*“Monitoring the Photocatalytic Degradation of Water-based Organic Pollutants by FT-IR Spectroscopy in Real-time”*, 41st International Conference on Infrared, Millimeter, and Terahertz Waves (IRMMW-THz 2016), Copenhagen 2016.

# Contents

|          |   |           |
|----------|---|-----------|
| <b>1</b> | <b>Introduction</b>                                       | <b>1</b>  |
| 1.1      | Motivation . . . . .                                      | 1         |
| 1.1.1    | Humanitarian motivation . . . . .                         | 1         |
| 1.1.2    | Scientific motivation . . . . .                           | 2         |
| 1.2      | Current Research . . . . .                                | 3         |
| 1.2.1    | Water Treatment Techniques . . . . .                      | 3         |
| 1.3      | Photocatalysis in water treatment . . . . .               | 6         |
| 1.4      | Thesis aims . . . . .                                     | 7         |
| 1.5      | Summary . . . . .   | 9         |
| <b>2</b> | <b>Background Theory</b>                                  | <b>11</b> |
| 2.1      | Catalysts . . . . .                                       | 11        |
| 2.1.1    | Homogeneous catalyst . . . . .                            | 13        |
| 2.1.2    | Heterogeneous catalyst . . . . .                          | 14        |
| 2.2      | Photocatalysis and Photocatalytic Reactions . . . . .     | 14        |
| 2.2.1    | Homogeneous photocatalyst . . . . .                       | 14        |
| 2.2.2    | Heterogeneous photocatalyst . . . . .                     | 15        |
| 2.3      | Semiconductors . . . . .                                  | 18        |
| 2.3.1    | Band structure . . . . .                                  | 20        |
| 2.3.2    | Molecular bonding . . . . .                               | 23        |
| 2.3.3    | Bandgap engineering and Doping . . . . .                  | 30        |
| 2.4      | Titanium Dioxide . . . . .                                | 32        |
| 2.4.1    | Polymorphs of $\text{TiO}_2$ . . . . .                    | 35        |
| 2.4.2    | Nano-structuring . . . . .                                | 35        |
| 2.4.3    | Limitations of $\text{TiO}_2$ bandgap . . . . .           | 37        |
| 2.5      | Simulating Pollutants . . . . .                           | 38        |
| 2.6      | Experimental Determination of Reaction Lifetime . . . . . | 42        |
| 2.6.1    | The Beer-Lambert Law . . . . .                            | 43        |
| 2.7      | Summary . . . . .   | 51        |
| <b>3</b> | <b>Vibrational Spectroscopy</b>                           | <b>53</b> |
| 3.1      | Background to Vibrational Spectroscopy . . . . .          | 53        |
| 3.1.1    | Vibrational modes . . . . .                               | 53        |
| 3.1.2    | Group Theory . . . . .                                    | 56        |
| 3.1.3    | Infrared Radiation . . . . .                              | 56        |
| 3.2      | Infrared Spectroscopy Techniques . . . . .                | 57        |
| 3.2.1    | Dispersion Spectroscopy . . . . .                         | 58        |
| 3.2.2    | FTIR Spectroscopy . . . . .                               | 59        |
| 3.3      | Attenuated total internal reflection (ATR) . . . . .      | 67        |
| 3.3.1    | Fresnel Equations . . . . .                               | 67        |

---

|          |  |            |
|----------|--|------------|
| 3.3.2    | Evanescent field . . . . .   | 70         |
| 3.3.3    | Choice of ATR material for IR measurements . . . . .                         | 72         |
| 3.3.4    | Depth of penetration . . . . .   | 73         |
| 3.3.5    | Multi-reflection vs single reflection . . . . .                              | 74         |
| 3.4      | Summary . . . . .  | 75         |
| <b>4</b> | <b>Initial optical results and design</b>                                    | <b>77</b>  |
| 4.1      | Visible spectroscopy . . . . .   | 77         |
| 4.2      | 1 mm pathlength flowcell results . . . . .                                   | 81         |
| 4.3      | Water absorptivity . . . . .   | 84         |
| 4.4      | Attenuated Total Internal Reflection (ATR) . . . . .                         | 85         |
| 4.4.1    | ATR calculations . . . . .   | 86         |
| 4.4.2    | Single reflection ATR . . . . .  | 88         |
| 4.5      | Multi-reflection ATR sensitivity . . . . .                                   | 92         |
| 4.6      | Summary . . . . .  | 97         |
| <b>5</b> | <b>Vibrational modes using ATR materials</b>                                 | <b>99</b>  |
| 5.1      | Vibrational Modes Background . . . . .                                       | 99         |
| 5.2      | Experimental Setup . . . . .   | 101        |
| 5.3      | MIR Optical Properties of ATR Materials . . . . .                            | 102        |
| 5.3.1    | ATR Materials . . . . .  | 102        |
| 5.3.2    | Bond Catalogue . . . . .   | 106        |
| 5.4      | Chemical Stability of ATR Materials in Water . . . . .                       | 119        |
| 5.5      | Summary . . . . .  | 125        |
| <b>6</b> | <b>Real-time MIR Spectroscopy of Methylene Blue Photocatalytic Reactions</b> | <b>127</b> |
| 6.1      | Current Knowledge of TiO <sub>2</sub> Photocatalytic Chemistry . . . . .     | 127        |
| 6.2      | Refining the Experimental Setup . . . . .                                    | 132        |
| 6.3      | Steady-state Spectroscopic Measurements . . . . .                            | 133        |
| 6.4      | Challenges of In-situ Real-time Measurements . . . . .                       | 134        |
| 6.4.1    | Mixing Issues . . . . .  | 135        |
| 6.4.2    | Detector hold time . . . . .   | 137        |
| 6.5      | Rationale for Using a Peak Fitting Algorithm . . . . .                       | 139        |
| 6.6      | Results and Discussion . . . . .   | 144        |
| 6.6.1    | Visible absorbance result . . . . .  | 144        |
| 6.6.2    | Peak fitting result . . . . .  | 145        |
| 6.6.3    | Understanding the MIR absorbance data . . . . .                              | 152        |
| 6.6.4    | Calculating a decay time for each bond . . . . .                             | 157        |
| 6.7      | Summary . . . . .  | 158        |
| <b>7</b> | <b>Conclusions and Future work</b>   | <b>160</b> |
| 7.1      | Summary and Perspective on Main Research Outcomes . . . . .                  | 160        |
| 7.2      | Future Work . . . . .  | 162        |
| 7.2.1    | Speeding up the Reaction . . . . .   | 162        |
| 7.2.2    | Increasing the Sensitivity . . . . .   | 163        |
| 7.2.3    | Experimental Variables . . . . .   | 163        |
| 7.2.4    | Chemical Stability of ATR Crystal . . . . .                                  | 163        |

---

---

|       |  |     |
|-------|--|-----|
| 7.2.5 | Improving the Peak Fitting Algorithm . . . . . | 164 |
| 7.2.6 | Surface Analysis Techniques . . . . .          | 165 |

# List of Figures

|      |  |    |
|------|--|----|
| 1.1  | Schematic diagram of UV sterilization unit . . . . .   | 4  |
| 1.2  | Flowchart to show RO purification process . . . . .  | 5  |
| 2.1  | Graph to show activation energy with and without a catalyst. . . . .   | 12 |
| 2.2  | Diagram of a photocatalytic reaction using aTiO <sub>2</sub> nanoparticle . . . . .  | 16 |
| 2.3  | Diagram of the band structure of an insulator, conductor and semiconductor . .   | 19 |
| 2.4  | The Bohr model of a hydrogen atom . . . . .  | 21 |
| 2.5  | Diagram to represent allowed states for an electron in the hydrogen atom . . . .   | 22 |
| 2.6  | Diagram to represent the linear combination of two s-orbitals . . . . .  | 24 |
| 2.7  | Diagram of bonding/antibonding molecular orbitals when two hydrogen atoms<br>are within the internuclear distance corresponding to H <sub>2</sub> . . . . .              | 25 |
| 2.8  | Theoretical energy bands for a material plotted against lattice constant . . . . .   | 26 |
| 2.9  | Hypothetical allowed energy states calculated by solving Schrödinger's wave equa-<br>tion . . . . .  | 27 |
| 2.10 | Energy vs wave-vector result from the 1D Kronig-Penney model . . . . .   | 28 |
| 2.11 | Diagram to represent energy vs quasi-momentum for both indirect and direct<br>bandgap . . . . .  | 29 |
| 2.12 | Energy bandgap (E <sub>g</sub> ) plotted against lattice structure . . . . .   | 31 |
| 2.13 | Diagram to represent p-type and n-type semiconductors . . . . .  | 32 |
| 2.14 | Schematic diagram of an electro-chemical process using n-type TiO <sub>2</sub> . . . . .   | 33 |
| 2.15 | Results from two separate publications showing the crystalline structure and<br>refractive indices of anatase and rutile as well as amorphous TiO <sub>2</sub> . . . . . | 36 |
| 2.16 | Solar irradiance spectrum plotted against emitted wavelength . . . . .   | 37 |
| 2.17 | Chemical structures of benzene and 2,3,7,8-tetrachlorodibenzo-para-dioxin (2,3,7,8-<br>TCDD) (dioxin). . . . .   | 38 |
| 2.18 | The chemical structures of Formetante and Diuron . . . . .   | 40 |
| 2.19 | Chemical structures of methylene blue and methyl orange . . . . .  | 41 |
| 2.20 | Absorption spectrum of methylene blue hydrate . . . . .  | 42 |
| 2.21 | Diagram used to derive the Beer-Lambert law from first principles . . . . .  | 44 |
| 2.22 | Schematic diagram of experimental setup used in Nickels, Patrick <i>et al</i> paper . .  | 47 |
| 2.23 | The experimental setup using a Raspberry Pi and function board to power and<br>record a methylene blue degradation reaction. . . . .                                     | 48 |
| 2.24 | Absorbance against time of a methylene blue degradation reaction . . . . .   | 49 |
| 3.1  | The vibrational modes of diatomic molecules present within the MIR region . . .  | 55 |
| 3.2  | Diagram of the Czerny Turner monochromator . . . . .   | 58 |
| 3.3  | Diagram representing constructive and destructive wave interference. . . . .   | 60 |
| 3.4  | Schematics of the michelson interferometer found in an FTIR spectrometer . . .   | 61 |
| 3.5  | Interferograms of both broadband and monochromatic light . . . . .   | 62 |
| 3.6  | Decomposition of a broadband light source interferogram . . . . .  | 63 |

---

|      |   |     |
|------|---|-----|
| 3.7  | Propagation vectors for the incident, reflected and transmitted waves. . . . .  | 68  |
| 3.8  | Plot of zinc sulphide, silicon, germanium and their respective penetration depth plotted against wavenumber . . . . .   | 74  |
| 4.1  | Published visible spectra of a methylene blue photocatalytic degradation using mixed phase TiO <sub>2</sub> nano-tubes and irradiated using UV LEDs . . . . .   | 78  |
| 4.2  | Measured methylene blue degradation over a 22 hour period using a millimolar input concentration . . . . .  | 79  |
| 4.3  | Plots of the spectral feature peak amplitude at 661 nm and 612 nm against time. The fits for 661 nm gave an initial decay time of $5.88 \pm 0.1$ hours, and secondary decay time (after the first 4 hours of the experiment) of $11.1 \pm 0.1$ hours. The fits for 612 nm gave an initial decay time of $6.9 \pm 0.1$ hours and a secondary decay time (after the first 4 hours of the experiment) of $11.1 \pm 0.1$ hours. . . . . | 80  |
| 4.4  | Not to scale diagram of a 1 mm path length flowcell . . . . .   | 81  |
| 4.5  | Schematic diagram and photograph of the BRUKER Vertex 80V FTIR spectrometer. . . . .  | 83  |
| 4.6  | A graph to show the absorption of water measured over the IR spectrum . . . . .   | 84  |
| 4.7  | Schematic diagram to show the trigonometric calculations for the desired polishing angle to achieve total internal reflection for windows of specific optical materials . . . . .   | 87  |
| 4.8  | Two 3D models of a calcium fluoride CaF <sub>2</sub> window before and after polishing respectively. . . . .  | 87  |
| 4.9  | A 3D model of the first CaF <sub>2</sub> single reflection ATR unit . . . . .   | 89  |
| 4.10 | Deionised water absorbance spectrum using CaF <sub>2</sub> . . . . .  | 90  |
| 4.11 | Refractive index over the MIR region for CaF <sub>2</sub> , Ge, ZnS, H <sub>2</sub> O and Si. . . . .   | 91  |
| 4.12 | Image of CaF <sub>2</sub> and Ge single reflection units . . . . .  | 92  |
| 4.13 | Diagram to represent the desired internal reflections (L) and the method with which each reflection was achieved (R). . . . .   | 93  |
| 4.14 | Material transmission spectra of both germanium and zinc sulphide as published by Crystran . . . . .  | 94  |
| 4.15 | Graph to show the difference in transmission from single to multi-reflections . . . . .   | 95  |
| 4.16 | Single to multi-reflection data which displaying a linear trend on all peak amplitudes. . . . .   | 96  |
| 5.1  | Full FTIR setup with ATR flowcell in the sample compartment. The ATR crystal is held in place using the designs seen in the previous chapter. . . . .   | 102 |
| 5.2  | Infra-red material spectra of a) CaF <sub>2</sub> , b) Ge, c) Si and d) ZnS . . . . .   | 103 |
| 5.3  | Refractive index range over the MIR region for CaF <sub>2</sub> , Ge, ZnS, H <sub>2</sub> O and Si. . . . .   | 104 |
| 5.4  | Effective penetration depth for Ge, ZnS and Si. . . . .   | 105 |
| 5.5  | Published spectrum using 1 $\mu$ m thick sample of 'normal' liquid water (filled line) and heavy water (dotted line) at three different temperatures . . . . .  | 108 |
| 5.6  | Published transmission spectrum of a thin capillary film containing isopropyl-alcohol (IPA) . . . . .   | 108 |
| 5.7  | Published transmission spectrum of toluene with bond assignment . . . . .   | 109 |
| 5.8  | Published transmission spectrum of benzaldehyde measured between two KBr plates . . . . .   | 109 |

---

---

|      |  |     |
|------|--|-----|
| 5.9  | Deionised water spectrum using Ge multi-reflection ATR crystal, both ‘corrected’ and ‘raw data’ . . . . .  | 110 |
| 5.10 | Isopropyl alcohol spectrum using the Ge multi-reflection ATR crystal. . . . .  | 112 |
| 5.11 | Toluene spectrum using a multi-reflection Ge ATR crystal. . . . .  | 113 |
| 5.12 | Benzaldehyde spectrum using a multi-reflection Ge ATR crystal. . . . .   | 114 |
| 5.13 | Deionised water spectrum using a multi-reflection Si ATR crystal. . . . .  | 115 |
| 5.14 | IPA spectrum using multi-reflection Si ATR crystal . . . . .   | 116 |
| 5.15 | Toluene spectrum using a multi-reflection Si ATR crystal . . . . .   | 117 |
| 5.16 | Benzaldehyde spectrum using a multi-reflection Si ATR crystal . . . . .  | 118 |
| 5.17 | Absorbance spectrum of a multi-reflection Ge crystal measuring its chemical stability in water over a 24 hour time period . . . . .  | 120 |
| 5.18 | Images of the multi-reflection Ge ATR crystal before and after the chemical stability in water measurement. . . . .  | 121 |
| 5.19 | Absorbance spectra of a multi-reflection ATR Si crystal measuring its material response to water over a 12 hour time period. . . . .   | 122 |
| 5.20 | Images of the Si ATR crystal before chemical stability in water measurements . .   | 123 |
| 5.21 | Absorbance spectra using a multi-reflection ZnS crystal measuring its material response to water over a 12 hour time period . . . . .  | 124 |
| 5.22 | Images of the ZnS multi-reflection ATR crystals after the full methylene blue degradation reaction. . . . .  | 124 |
| 6.1  | Structural representation of possible methylene blue groupings in solution . . . .   | 128 |
| 6.2  | Figure from Ovchinnikov’s paper <sup>98</sup> showing the calculated and experimental results showing IR spectra of varying concentrations and states of Methylene Blue  | 130 |
| 6.3  | Figure from the Houas paper <sup>58</sup> which shows the proposed theoretical break down of methylene blue degradation . . . . .  | 132 |
| 6.4  | Schematic diagram of the experimental setup . . . . .  | 134 |
| 6.5  | Graph showing the direct comparison between a measured spectrum of a millimolar solution of methylene blue and the published results of the same concentration.  | 135 |
| 6.6  | Graph showing the mixing process that happens when 10 ml of millimolar methylene blue is added to 150 ml of deionised water . . . . .  | 136 |
| 6.7  | Graph showing the chemical stability of ZnS using a millimolar solution of methylene blue . . . . .  | 137 |
| 6.8  | Figures to show the peak amplitude and peak width for a vibrational frequency of $1391\text{ cm}^{-1}$ . . . . .   | 138 |
| 6.9  | Infrared ATR absorbance spectrum plotted in time steps of approximately 47 minutes over the time range 18.4-41.1 hours . . . . .   | 139 |
| 6.10 | ATR spectra recorded at two different times showing how the baseline changes .   | 141 |
| 6.11 | Initial attempts at the piecewise fitting windows showing the three groups of peaks labelled from right to left (low to high wavenumber), U-P, O-M, L-G. . . .   | 142 |
| 6.12 | Fitted data showing the three groups of peaks labelled from left to right (low to high wavenumber) . . . . .   | 143 |
| 6.13 | Visible absorbance data on a logarithmic scale over the full degradation reaction. The initial 6 hours were the mixing period of the methylene blue with deionised water. The start and end text indicates the points at which the data was linearly fitted. . . . . | 144 |

---



---

|      |  |     |
|------|--|-----|
| 6.14 | Fitted data from the visible absorbance plot seen in figure 6.13. The linear fit gave a gradient of -0.113 which translates to a reaction time of $8.85 \pm 0.04$ hrs. . | 145 |
| 6.15 | Fitting peak amplitude for peaks G-N. . . . .  | 146 |
| 6.16 | Fitting peak amplitude for peaks O-U. . . . .  | 147 |
| 6.17 | Fitting peak centres for peaks G-N. . . . .  | 148 |
| 6.18 | Fitting peak centres for peaks O-U. . . . .  | 149 |
| 6.19 | Fitting peak widths for peaks G-N. . . . .   | 150 |
| 6.20 | Fitting peak widths for peaks O-U. . . . .   | 151 |
| 6.21 | Time evolution of background subtracted integrated absorbance in the range $1100\text{-}1600\text{ cm}^{-1}$ over the course of the methylene blue reaction . . . . .    | 153 |
| 6.22 | Signal response $R$ to step function changes in the concentration of adsorbed molecules on a surface . . . . .   | 155 |
| 6.23 | Signal response $R$ to changes in the concentration of adsorbed molecules on a surface under the same detector parameters used in figure 6.22 . . . . .                  | 156 |

## List of Tables

|     |  |     |
|-----|--|-----|
| 3.1 | Advantages of FTIR over Dispersive spectroscopy . . . . .                      | 65  |
| 3.2 | Material Properties for ATR application . . . . .                              | 73  |
| 4.1 | Optical properties of $\text{CaF}_2$ . . . . .                                 | 89  |
| 5.1 | Bond Catalogue . . . . .   | 107 |
| 6.1 | Table of bond assignments to measured peaks with calculated decay time . . . . | 157 |

# 1 Introduction

*Environmental pollution is an incurable disease. It can only be prevented.*

---

Thomas Vinciguerra<sup>125</sup>

This PhD project looked at the process of developing an optical technique for the measurement of a chemical reaction. The chemical reaction that was measured was a dye degradation in the presence of a semiconductor photocatalyst, which has possible applications in water treatment. The drive behind my PhD research comes from two different motivations. The first being from a humanitarian standpoint as this project had possible real-world applications. This thesis topic interested me personally as I could see the potential real-world application and the progressive research steps that would lead there. In addition to this, I was interested in the field of optical detection and sensing, specifically infrared spectroscopy. One of the main drivers behind this particular research topic was the quest to better understand the molecular chemistry behind photocatalytic reactions.

## 1.1 Motivation

### 1.1.1 Humanitarian motivation

From a humanitarian standpoint there is a demand for clean water in developing countries. 2.5% of the Earth's water supplies are 'clean' (safe for consumption), and a mere 1% accessible for drinking. Water is essential for life, from photosynthesis in plants to the maintenance of bodily functions in human beings. However, mass populations throughout the western world are denied access to a safe source of water for consumption<sup>25</sup>. In 2015 the World Health

---

Organization (WHO) stated that poor water sanitation was the number one global crisis<sup>26</sup> which is also reflected in a recent report from the WHO:

“2.1 billion people lack access to safe, readily available water at home. Of the 2.1 billion people who do not have safely managed water, 844 million do not have even a basic drinking water service. This includes 263 million people who have to spend over 30 minutes per trip collecting water from sources outside the home, and 159 million who still drink untreated water from surface water sources, such as streams or lakes”<sup>138</sup>

Waterborne diseases are one of the primary causes of infant mortality in developing countries. A report from the WHO for Kenya stated that over half of the hospital visits documented (during 2011) were related to water supply, sanitation and hygiene (WASH) related diseases<sup>137</sup>. These statistics highlight the poor living conditions in developing countries and the demand for a long-term solution. Despite the aid given by established charities, many of the solutions that are implemented are short-term solutions<sup>135</sup>. As a consequence of this, research into long-term solutions must be investigated. Current water treatment techniques include chlorine sterilization tablets and water filters among others. Current techniques in the field of water treatment are efficient at removing biological material polluting water sources, however they are not necessarily a reliable/affordable technique to remove dissolved chemical pollutants. Chemical pollutants (which can also be toxic) are introduced into water systems through agricultural and industrial waste. Consequently, a new technique to remove chemical pollutants from waste-water sources is required. This lead to the scientific motivation of this project, to identify the breakdown of chemical pollutants in a water treatment reaction.

### **1.1.2 Scientific motivation**

This PhD project was aimed at optically measuring the degradation of chemical pollutants. Chemical pollutants are highly toxic and consequently were simulated for the purpose of the experiment by using organic dyes with similar chemical structures (methylene blue). The degradation reaction of methylene blue has been theorised in publications but not proved. In order

---

to measure the reaction pathways of a methylene blue degradation reaction, infrared (IR) light is used. However, using aqueous solutions in the IR region proves difficult as a result of the high absorption through water. This work explores these difficulties and aimed to overcome them using different optical technique. To be able to remove chemical pollutants, the technique of using heterogeneous photocatalysis was used in this thesis. To understand if photocatalytic methods can be used in water treatment, they must first be understood. If a photocatalytic reaction could be identified spectrally to understand the reaction chemistry, this technique could be applied to any aqueous chemical reactions and would therefore be a powerful detection technique. The degradation reaction of methylene blue using photocatalysis is currently a field of interest as its reaction pathways are yet to be identified. Due to this factor and my interest in spectroscopy, this was an important motivation behind this thesis topic.

## **1.2 Current Research**

### **1.2.1 Water Treatment Techniques**

The research field of water treatment has progressed since the 1700s when the first water filter was used for domestic application. It is an important field, as it will always have real-world applications. Since the 1700s there have been new techniques for treating contaminated water sources, these include: gravity filtration, deep UV purifiers and reverse osmosis purifiers. Each of these technologies displays a different technique for removing suspended particles from water sources. The first water treatment design was a simple water filter which consisted of four layers, leading from large rocks and refining down to coarse sand. This water filter design could remove larger suspended particles in the water, however it failed to remove smaller particles and bacteria. Current water filters have progressed from this initial four layer design with the incorporation of nanoscale grating width separations, effectively blocking all particles in suspension down to a nanoscale<sup>124</sup>. One particular water filter design that has exceeded other is the LIFESAVER bottle<sup>77</sup>. This design incorporates activated carbon among other nanoscale filter layers which has been proven to remove the smallest known waterborne virus, Parovirus (18 nm); and the smallest discovered waterborne microbe, Nanoarchaeum equitans (400 nm)

---

from polluted water sources<sup>77</sup>.

The second technology to discuss is UV purifiers. Commercial UV water purifiers use short-wavelength UV photons (254 nm)<sup>101</sup> to effectively kill microorganisms found in polluted water samples<sup>108,101</sup>. UV purification units have been used in a variety of different applications, from quality control in the food industry to safe drinking water for hospitals<sup>22,131</sup>. Although these UV purifiers can be designed for a variety of different applications, the basic design remains the same (see figure 1.1). As can be seen in figure 1.1 there is a simple design for this technique, where the output light is high energy (high photon flux) acting as the purifier. Further fields that facilitate sterilisation of polluted water sources use chemical tablets to treat the water, namely chlorination<sup>140</sup>.

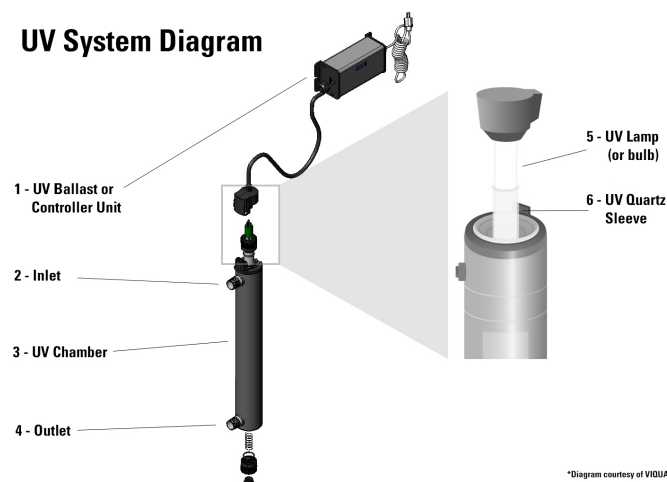


Figure 1.1: Schematic diagram taken from VIQUA website of their ultraviolet germicidal irradiation unit<sup>22</sup>. The UV lamp and sleeve are in the centre of the chamber with the polluted sample surrounding the UV light for treatment.

The final technology to review is reverse osmosis (RO). Reverse osmosis purifiers combine the technologies of filtration and the chemical process of osmosis. The purification process begins with a contaminated water source<sup>117</sup>, this source is then pre-filtered to remove large suspended sedimentary objects. The water is then passed through a carbon filter to remove contaminants and impurities through the process of chemical adsorption. The main component of the RO unit is a semipermeable membrane<sup>101</sup>, the water sample is passed through the semipermeable membrane using the pressure from the water source itself. Once the water has been passed

---

through the membrane, it is stored in a pressurized water tank. From the storage tank, the water is passed through a final post-filter, to ensure any remaining odours are removed before consumption. This process has been summarised in figure 1.2.

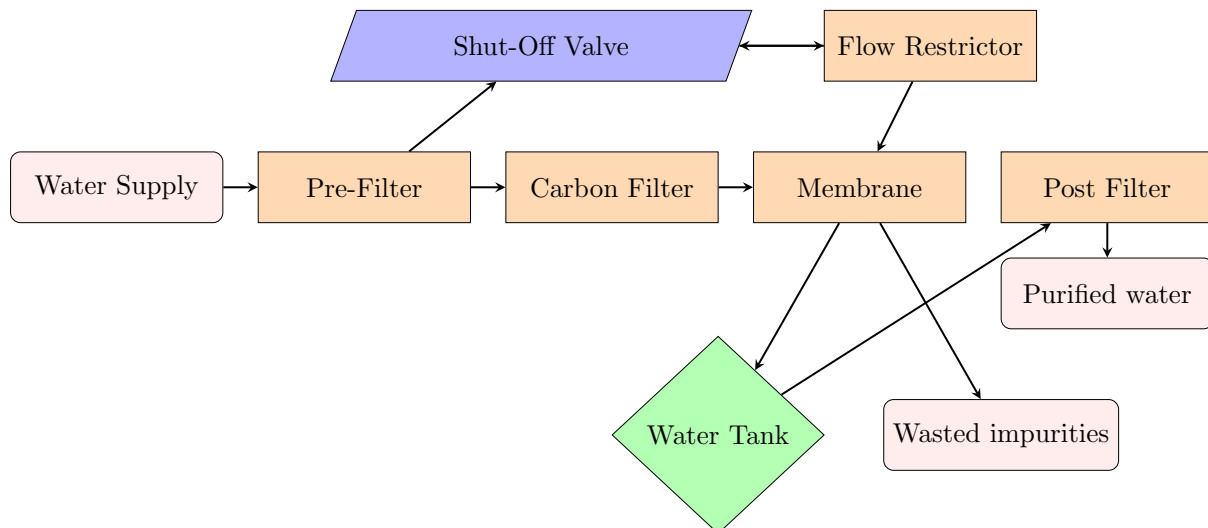


Figure 1.2: A flowchart to represent the RO purifier process<sup>101</sup>. Water flows into the RO purifier through a water supply, where it is then pre-filtered. Once filtered, the flow of the water supply forces it through a membrane that filters impurities from the water and stored the purified water in a water tank. The water is then taken from the tank and passed through a final filtration stage ready for consumption.

### 1.2.1.1 Limitations

The three main techniques used in water treatment as highlighted above all share a common limitation. With respect to a water treatment solution for the developing world, there are certain criteria that must be met, these specify that the solution needs to be: sustainable, inexpensive and simple. Sustainability is important, as for countries with low capital there isn't enough money to support maintenance costs. Further to this, developing countries can't afford to build large-scale treatment units, so a water treatment technique that is both sustainable and inexpensive is crucial. The final criterion for this technology is simplicity. Simplicity is important as the people who would potentially be using this technique have very little or no prior scientific knowledge and in the majority of cases, no education. The current technologies outlined above all fall short of one or more of these criterion. Filters are as sustainable as their

---

filter lifetimes, making them unsustainable (for long-term use) and expensive to maintain. UV purifiers require high energy light and are expensive to manufacture<sup>52</sup>. With both high running and manufacturing costs this technique cannot be used in the developing world<sup>140</sup>. The final technique discussed above is RO purifiers. These systems require infrastructure for implementation and are expensive to build/maintain thus removing it as a possible water treatment solution for developing countries<sup>117</sup>. All of these techniques have been proven to efficiently kill/remove all living material in waste-water. However, they don't necessarily remove the dissolved organic chemical pollutants that can be found in surface water sources. The limitations discussed above are the motivation for investigating an alternative water treatment technique.

This PhD project focused on a water treatment solution that used photocatalysis in a chemical water treatment reaction. One of the benefits of using a photocatalyst is due to its properties, allowing it to be used in a reaction without consuming any part of itself<sup>41</sup> thus, making it a sustainable solution. The photocatalyst material used in this PhD project was titanium dioxide which is inexpensive, non-toxic and has an activation energy equal to that of the ultraviolet region in the solar spectrum. This means, using titanium dioxide to catalyse a water treatment reaction is both sustainable and inexpensive. This PhD project explored the optical measurement/optimisation of such a technique.

### 1.3 Photocatalysis in water treatment

A full description of photocatalysts and their applications can be found in chapter 2, however for the purpose of this chapter I will make the assumption that photocatalysts are commonly made of metal oxides. One specific metal oxide that has been seen to facilitate a reaction that has potential applications in water treatment is that of titanium dioxide ( $\text{TiO}_2$ ).

In 1972, titanium dioxide ( $\text{TiO}_2$ ) was used in a water splitting reaction that promoted its application in other water 'cleaning' reactions, namely a dye degradation<sup>40</sup>. 5 years later in 1977, N. Frank and J. Bard published a letter that highlighted the power of using  $\text{TiO}_2$  in a water treatment reaction<sup>39</sup>. The letter was entitled 'Heterogeneous Photocatalytic Oxidation of Cyanide Ion in Aqueous Solutions at  $\text{TiO}_2$  Powder'. In this letter they summarised their



---

findings using two polymorphic phases of  $\text{TiO}_2$ , anatase and rutile to oxidise cyanide ions which occur as a frequent industrial pollutant. They found that by changing the input concentration and varying photon flux, the reactions all took place within a measurable time frame. They also noted, that under different variable environments (in the presence of unactivated  $\text{TiO}_2$ , with a UV source and no  $\text{TiO}_2$ ), there was very little or no oxidising of the cyanide ions. From this result, in 1990 Peral *et al* published a paper looking at other variables that may be contributing to the reactions, particularly pH, temperature and the mass of photocatalyst used for reaction<sup>100</sup>. They concluded that as the pH increased, the number of oxidised cyanide ions decreased, however at higher temperatures there was a greater oxidation rate. Following this paper, in 1993 Butler *et al* published a paper on using  $\text{TiO}_2$  to remove dissolved metals from water sources<sup>21</sup>. From this paper, the conclusion stated that only specific metals with correlating reduction potentials greater than that of 0.3 V could be removed using  $\text{TiO}_2$  photocatalysis. As a result of this publication, a shift of focus to the oxidation and reduction reactions that both take place at the  $\text{TiO}_2$  particle surface was observed. The research into using  $\text{TiO}_2$  for both oxidation and reduction reactions spanned the years between 1998 to 2010 where the same photocatalytic reaction using  $\text{TiO}_2$  was tested with different environmental variables<sup>86,92,2</sup>. Present day, there is the same focus of research into  $\text{TiO}_2$  photocatalysis which has progressed into measuring polluted water treatment reactions<sup>2</sup>. Real-world chemical pollutants are highly toxic, so for the purpose of experimentation a proxy pollutant can be used an example of this is methylene blue. Research in  $\text{TiO}_2$  and its photocatalytic efficiency in methylene blue degradation has been successful over the past century, however one area of this research field that is still yet to be concluded is the reaction pathways. Due to scientific curiosity this became the primary aim of this PhD project.

## 1.4 Thesis aims

The aims of this PhD project were a direct consequence of the motivation behind the research topic; to better understand the molecular chemistry behind photocatalytic reactions. These aims can be summarised as:

- 
- Develop a visible diagnostic tool to monitor the methylene blue degradation reaction to explore the parameter space.
  - Develop an infrared flowcell with the aim of understanding how chemical bonding changes during a photocatalytic reaction.

A visible absorbance experiment was used to identify specific parameters of the reaction, for example the amount of photocatalyst used, the input concentration of the pollutant and the reaction lifetime. However, to understand the internal chemistry of the reaction, it had to be measured using infrared frequencies. Taking infrared measurements brings its own unique challenges. While the atmosphere is effectively transparent at visible wavelengths, many atmospheric trace gases such as water vapour and carbon dioxide have strong absorption bands which can crowd out other spectral information. Consequently, many infrared measurements need to be taken under vacuum to remove the influence of these gases on the measurement result. This therefore complicates the design of any experimental apparatus for this purpose. A further complication is that most liquids are highly opaque at infrared frequencies, making any form of transmission spectroscopy very difficult. Liquid cells can of course be designed to have very short path lengths, but if the cell is to allow a continuous flow of liquid, then this would produce a severe constriction in any flow system. An alternative method for this is using ATR to reduce the effective path length. However again nature finds a way of making things difficult for the spectroscopist. Constructing an ATR crystal that is simultaneously transparent to infrared light and chemically stable in aqueous solutions lead to the following project goals:

- Finding an infrared transparent material which is safe (non-toxic) to cut and polish to make ATR crystals with.
- Narrowing down the list of ATR materials to identify one which has chemical stability in water.
- Optimising the geometry of ATR crystals to increase sensitivity for IR monitoring.

With a refined experimental setup, both the visible absorbance data and the reaction chemistry could be measured simultaneously. Finally, an automated algorithm for looking through

---

all of the data files and extracting information such as the peak absorbances and concentrations of specific bonds was developed and used to give resultant data.

## 1.5 Summary

The motivations for this PhD project stem from an interest in optical detection and a humanitarian outlook for real-world scientific application. My research aims were to monitor the chemical reaction of an aqueous solution to identify its reaction pathways. The specific reaction chosen was a dye degradation which has potential applications in water treatment. There has been research into water treatment techniques since the first filter was designed in the 1700s. The development of three main industrial techniques have been adopted worldwide, these include filtration, sterilisation and reverse osmosis. These techniques are well suited to the developed world, however for countries with reduced capital these techniques can't be used. From a humanitarian standpoint, this result motivated me to research a technique that had real-world applications specifically designed for the developing world. The three criteria that this technique needed to satisfy were: sustainability, simplicity and inexpensive to manufacture/maintain. From these criteria, a new technique using photocatalysis to degrade water pollutants was investigated. The specific photocatalyst chosen was titanium dioxide ( $\text{TiO}_2$ ) which has been widely researched since 1972 when a paper was published identifying that it facilitated a water splitting reaction<sup>41</sup>. Since this publication, research into  $\text{TiO}_2$  has lead to doping the material and analysing its polymorphic structures. Whilst these variables are important to consider, I was particularly interested in its potential application in a water treatment reaction. The most recent research using  $\text{TiO}_2$  in a water treatment reaction uses organic dyes as proxy pollutants (due to the high toxicity of the water borne pollutants)<sup>129,71</sup>. Methylene blue degradation is a reaction that has been well-published and multiple research groups have concluded that  $\text{TiO}_2$  has effectively degraded the organic dye<sup>71,112</sup>. However, there is minimal information on the reaction pathways of this degradation. Consequently, due to both scientific curiosity and a humanitarian outlook this became the research topic for this PhD project.

The thesis is structured in a way that follows the research stages taken before achieving the

primary aim of identifying reaction pathways of a degradation reaction using  $\text{TiO}_2$ . The first two chapters review the background theory and experimental techniques that were used throughout the project. Following these chapters is the first results chapter which displays the initial visible spectroscopy results along with optical design units that include a reduced path length flowcell and attenuated total internal reflection (ATR) cells. The next chapter highlights the materials used in each ATR cell and their advantages/limitations for infrared measurement. The final results chapter used the material that was seen to be the best fit for infrared measurements with both chemical stability in water and transparency in the full infrared region. These results show the reaction pathways of a methylene blue degradation reaction and a discussion on these results follows. All of these results are summarised and future work for this research project are discussed in the the final conclusions chapter.

## 2 Background Theory

To begin this thesis, the theory of catalysts and photocatalysts is explained. This is important to understand as the reaction that is optically measured throughout the thesis is based on a photocatalytic reaction. From simple catalytic convertors found in cars to heterogeneous photocatalytic reactions that have potential applications in water treatment, the basic understanding of catalysis is explained in this theory chapter. Progressing from photocatalysts, semiconductor materials are explained, from their band structure to potential applications. The reason to include semiconductors in this theory chapter is due to a material used in this thesis that acts as both a semiconductor and photocatalyst, titanium dioxide ( $\text{TiO}_2$ ). This material has been seen to facilitate a water splitting reaction when exposed to ultraviolet (UV) light. This reaction has then been applied to water treatment, using proxy pollutants and measuring the photocatalytic reaction of their degradation. The final section of this chapter quantifies a reaction lifetime for this water treatment reaction among other parameter variables.

### 2.1 Catalysts

In order to better understand this thesis and its aims, catalysts and their applications will be discussed. Catalysts are chemicals that are used to effectively speed up a reaction. Catalysts can be found in biological material<sup>14</sup>, in nature (e.g oxygenic photosynthesis seen in plants) and can also be manufactured. The most common types of catalysts are: acid-based catalysts, enzymes and heterogeneous catalysts. A catalyst is a substance that increases the rate of a reaction without being consumed in the process<sup>18</sup>. Catalysts work by either lowering the energy of the transition state and decreasing the effective activation energy (see figure 2.1), or changing the

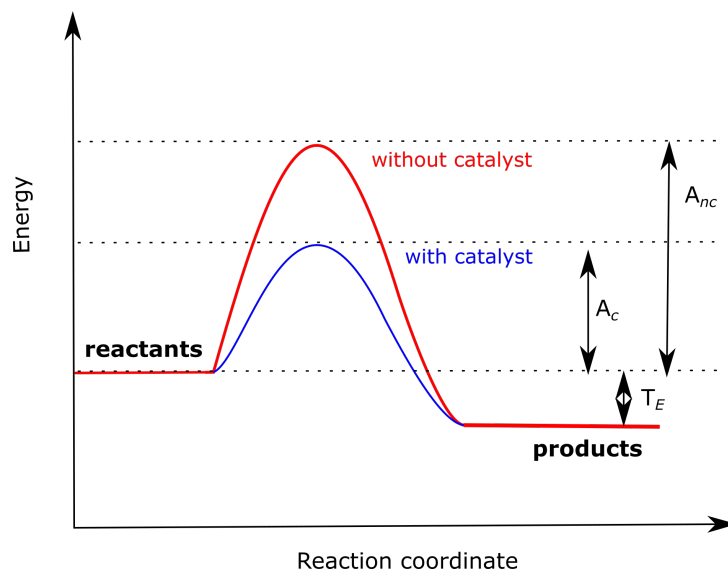


Figure 2.1: Graph showing the activation energy difference for a reaction, both in the presence of a catalyst and without. Here  $A_c$  is the activation energy with the catalyst,  $A_{nc}$  is the activation energy without the catalyst and  $T_E$  is the overall energy released during reaction. The reactants must overcome an initial potential energy barrier to form reaction products. In the presence of a catalyst, a transition state with a reduced potential energy is present which speeds up the process of reaction<sup>63</sup>.

mechanism of the reaction (changing the transition state).

In order for a chemical reaction to take place, some or all of the chemical bonds in the reactants must be broken. Once these bonds have been broken, new bonds are formed which make the products. To get to a state where the bonds are able to break, the reactants must be deformed into an unstable state called the transition state. This transition state is high energy meaning that a specific amount of energy (activation energy) must be added for the reaction to take place. The transition state is unstable and consequently the reactants don't remain there for long periods of time, but instead progress to the next step of the chemical reaction. Looking to figure 2.1, the trend of the curves shows an initial incline to a peak and then a decline, the peak represents the transition state and the chemical reaction takes place from left to right<sup>18</sup>.

There are two curves seen in figure 2.1, the red curve shows the reaction pathways without a catalyst and the blue graph shows the reaction pathway in the presence of a catalyst. The catalyst works through the reactants bonding to the active sites of the catalyst. From this initial bonding, the activation energy for the reactants to get to the transition state is lowered.

However, the overall energy released for the reaction is unchanged, with the catalyst working as an intermediate step<sup>63</sup>. Enzyme catalysts and acid-based catalysts are in the same phase as that of the reactants, because of this, they are called homogeneous catalysts. However, heterogeneous catalysts are in a different phase to that of the reactants, a good example of this can be seen in a catalytic converter of a car<sup>55,67,70</sup>. Catalytic converters commonly contain transition metal catalysts embedded onto a solid support. The catalyst comes into contact with the gases produced from the car's exhaust system, converting reactants such as carbon monoxide and unburnt fuel into a form of less toxic product at an increased rate. The catalyst is seeded onto a core support that is usually made from a ceramic monolith (thin layer structures that are the core of catalytic converters). The core is structured in a honeycomb pattern to optimise the surface area in contact with the reactants. The catalyst used is usually a mix of precious metals, the most commonly used are palladium and rhodium<sup>139</sup>.

In comparison to enzyme catalysts and some acid-based catalysts, a catalytic converter has to be powered, this meaning it requires an energy source to drive the catalyst. In the context of the catalytic converter, the energy source is heat. At a specified temperature which is greater than that required to activate the catalyst, the catalyst will increase the rate of reaction, however below this energy the catalyst will remain idle. The most common source of activation energy in catalysts is thermal. The thermal energy speeds up the motion of the reactants and consequently increases the frequency of the collisions, thus increasing the overall probability of chemical bonds breaking<sup>66,67</sup>. Catalysis can be divided into two categories, homogeneous and heterogeneous.

### 2.1.1 Homogeneous catalyst

Homogeneous catalysts are in the same state of matter as the reactants, this is typically liquid or gas phase. A typical example of a homogeneous catalyst is an acid or enzyme catalysts. Generally, the advantage of homogeneous catalysts over heterogeneous catalysts is the uniformity in composition when mixed with a sample, as both the sample and the catalyst are in the same state of matter, they create a homogeneous mixture<sup>67</sup>.

### 2.1.2 Heterogeneous catalyst

Unlike homogeneous catalysts, heterogeneous catalysts are in a different state of matter to that of the reactant, and are more commonly made from transition metal oxides and semiconductor materials<sup>60,66,67</sup>. Typically heterogeneous catalysts are solids and are mixed with reactants in the liquid/gas phase. A classic example of a heterogeneous catalyst is the catalytic converter in gas/diesel-fuelled cars. In addition to thermal excitation, catalysts can be activated using light. When they are photo-activated (from light) they are called photocatalysts<sup>67</sup>.

## 2.2 Photocatalysis and Photocatalytic Reactions

The term ‘photocatalyst’ can be broken into *photo* and *catalyst*. Here, catalyst can be defined as a substance that is used to increase the rate of a reaction, and photo means that activation source is light. Just as catalysts, photocatalysts can also be found as homogeneous and heterogeneous.

### 2.2.1 Homogeneous photocatalyst

One of the first homogeneous catalysis reactions published was called the photo-Fenton reaction. This reaction is based on the Fenton reaction which was discovered by H.J.H Fenton in 1894<sup>62</sup>. Fenton discovered that several metal oxide metals had oxygen transfer properties, in addition to this he discovered that some metals had strong catalytic power that lead to the production of free radicals. As the name suggests the common Fenton reaction uses iron ( $\text{Fe}^{2+}$ ) which is found to be effective, owing to its high oxidation potential in aqueous solutions. This catalytic process can also be activated with photon energy (visible spectrum) in the photo-Fenton reaction<sup>85</sup>. The photo-Fenton reaction uses energies similar to that found in the visible region of the solar spectrum, making it sustainable. In addition to the photo-Fenton reaction, ozone is another common homogeneous photocatalyst. The advantage of these homogeneous photocatalysts is their ability to harness visible wavelengths (up to 450 nm), thus removing the need for expensive UV lamps and electrical energy. The disadvantage of these photocatalysts however is the requirement of low pH values, as specifically in the photo-Fenton process, iron



has to be removed after reaction, and iron precipitates at higher pH values. The other form of photocatalyst that is commonly used is called heterogeneous photocatalysts<sup>62</sup>.

### 2.2.2 Heterogeneous photocatalyst

Heterogeneous photocatalysts are not in the same phase as the reactants and just as homogeneous photocatalysts can also be activated with visible wavelengths<sup>55, 55,60</sup>. The process of photocatalysis relies on the materials ability to simultaneously adsorb reactants and absorb photons of sufficient energy<sup>1,55</sup> this give heterogeneous photocatalysis a wide range of uses. The industrial applications of heterogeneous photocatalysts range from self-cleaning paints<sup>80</sup>, to more recent research into drug delivery<sup>132</sup>. Consequently, heterogeneous photocatalysis is a popular field of research from analytical chemistry to nanoscale material science<sup>55, 62</sup>. The most common materials used in heterogeneous photocatalysts are transition metal oxides and semiconductors, which gives them unique characteristics. Semiconductors are used as heterogeneous photocatalysts due to their band structure. The process of activating electrons acts in the same way that a catalyst provides a transition state for reaction, the electrons and holes produced in a semiconductor then facilitate the creation of radicals which in turn breakdown molecular bonds<sup>122</sup>.

When a semiconducting metal oxide is activated, an electron is promoted from the valence to the conduction band on a femtosecond timescale. This photonic excitation generates an electron hole pair, this process is otherwise known as pair production<sup>122</sup>. After photo-excitation, the electron and hole can follow different paths based on their spatial position within the particle and their energy wave-function. Figure 2.2 shows the possible paths the electron and hole can take once excited. Option 'a' shows the electron and hole being in the same spatial location and recombining on the particle surface. Option 'b' shows the same recombination away from the surface of the particle. Option 'c' demonstrates what would happen if the hole was found at the surface of the particle. Here, a reduction reaction takes place, where a de-localized electron combined with the hole and the external atom becomes neutral in charge, and creates free radicals. Finally, option 'd' shows an oxidation reaction, where an electron at the particle surface is used to produce a negative unstable oxygen, which in-turn also produces free radicals<sup>1,88</sup>.

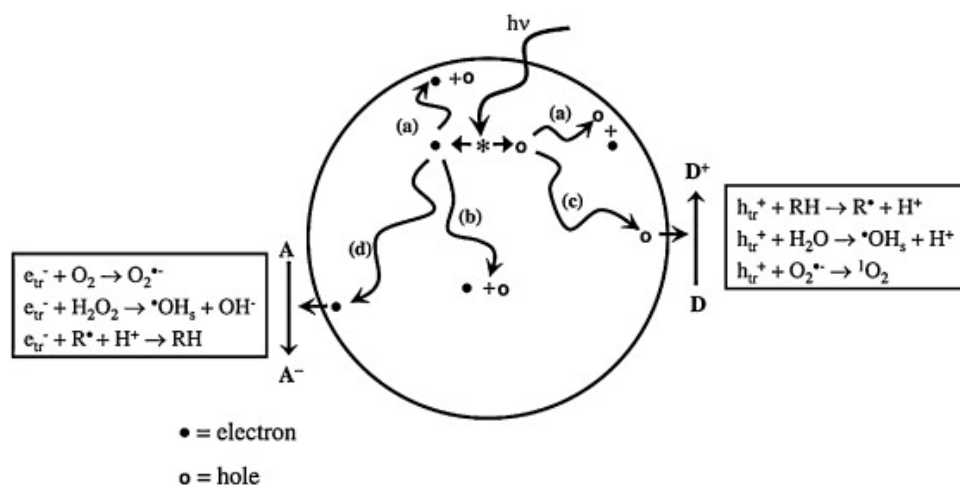


Figure 2.2: Diagram of a photocatalytic reaction using a  $\text{TiO}_2$  nanoparticle. Activation energy ( $h\nu$ ) creates an electron hole pair, from that creation there are multiple different paths it can take. (a) shows the process of surface recombination where both hole and electron are spatially next to one another but the electron releases energy when it recombines. (b) shows the same recombination in the valence band. (c) shows what happens if the hole is at the surface of the particle, it can then participate in a reduction reaction by combining with an electron from the reactant. Finally, (d) shows the electron at the surface of the particle facilitating an oxidation reaction<sup>91</sup>.

A fundamental issue with heterogeneous photocatalysis is the rate of recombination<sup>31,78</sup>. This has led to experimental doping of the photocatalysts, to offer alternative routes for recombination that increase the separation energy of the photo generated electron and hole. The reaction process from photo excitation (using  $\text{TiO}_2$ ), to reactant degradation have been proposed in the following equations (2.1 - 2.7)<sup>58</sup>.

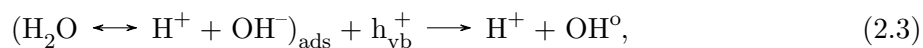


Where vb - valence band, cb - conductance band and  $h\nu$  is the energy of the exciting source photon. This reaction shows the photo-excitation of an electron-hole pair.



Where ads - adsorbed, and the '-' sign indicates an overall negative charge on the molecule.

The electron in the conduction band then goes on to react with an adsorbed oxygen molecule (oxidation reaction), creating a free radical.



Where ‘ $^\circ$ ’ indicates an overall neutral charge. The hole in the valence band is then free for a reduction reaction with adsorbed water molecules; as water can be split into hydrogen and  $\text{OH}^-$ . This results in a hydrogen atom and an unstable OH molecule.



The hydrogen atom then reacts with the free radical oxygen to give an unstable  $\text{HO}_2$  molecule.



The  $\text{HO}_2$  molecule can pair with itself to form a negative molecule that can be split into  $\text{H}_2\text{O}_2$  and an oxygen  $\text{O}_2$ .



A secondary oxygen reduction reaction then takes place between the  $\text{H}_2\text{O}_2$  and another electron in the conduction band, to give a further free radical  $\text{OH}^\circ$  and an unstable  $\text{OH}^-$ .



Where R is the reactant and R' are the by-products of the reaction.

This final equation is a view of how the free radicals produced would breakdown an organic reactant, leaving water and unidentified by-products. A good photocatalyst must be able to create a transition state for the reactants to complete the reaction. Another important requirement for a catalyst is its ability to create free radicals from a reaction. As mentioned previously, semiconductors act in a similar way to photocatalysts. Semiconductors have bandgaps that al-

low them to create electron hole pairs when activated and consequently facilitate free radical production. This makes semiconductors (transition metals) good materials for photo catalysis.

## 2.3 Semiconductors

Many photo-catalytic materials are semiconductors because of the ways semiconductors harness the energy from the light. Semiconductors can be defined as solid substances that has a conductivity between that of an insulator and that of most metals due to their bandgap structure. Materials are commonly split into one of three categories, conductors, insulators and semiconductors based on their electronic band structure. The band structure of a material determines its electrical and photo response as can be seen in figure 2.3. The typical band structure for a semi-conductor material consists of large bands called the conductance and valence bands. with a bandgap energy (difference in energy between the valence and conductance band) . The conductance and valence bands contain multiple quantised energy levels, however the overall image of a semiconductors band structure will show the low level energy states in the valence band and the high level energy states within the conductance band<sup>11,53</sup>.

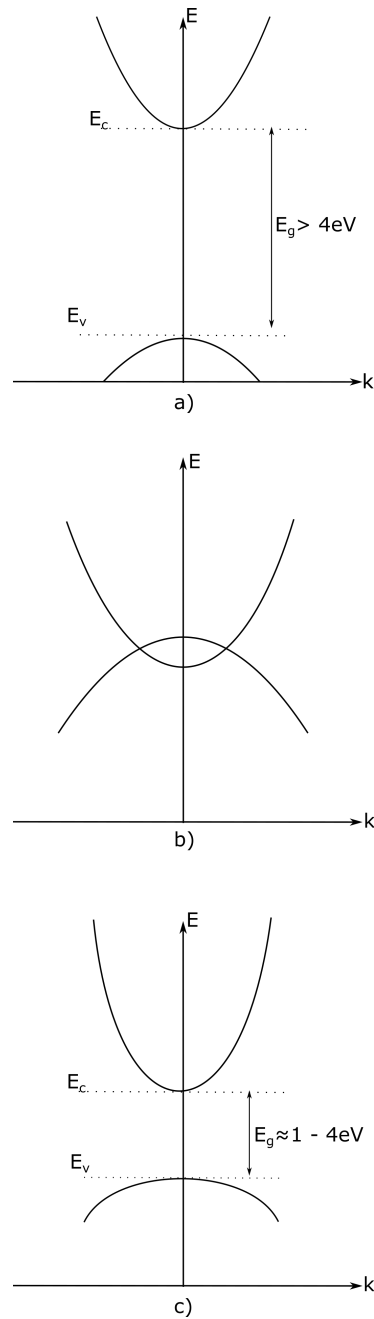


Figure 2.3: Diagram of the band structure of an a) insulator, b) conductor and c) semiconductor, where  $E_v$  is the top of the valence band,  $E_c$  is the bottom of the conductance band and  $E_g$  is the energy difference between the two (bandgap). For an insulator, the energy bandgap is wide, requiring substantial energy to produce de-localized electrons. For a conductor, the conductance and valence bands are overlapping, this meaning that there are already de-localized electrons to conduct electricity. Finally, the semiconductor shows a similar structure to an insulator but with a reduced bandgap<sup>11</sup>.

As demonstrated in figure 2.3, conductors have an overlap of their conductance and valence bands meaning electrons within a metal require zero input energy to enter the conductance band energy levels, making these materials good *conductors* of electricity. The second group of materials with large bandgaps are insulators. For an insulator to conduct electricity, a large amount of energy has to be given to the electrons in the valence band for them to be able to move to the conductance band<sup>11</sup>. The final group of materials has a bandgap which falls between that of a conductor and that of an insulator, these materials are called semiconductors<sup>120,11</sup>.

### 2.3.1 Band structure

Figure 2.3 represents the band structures of conductors, insulators and semiconductors. All of these groups of materials have different band structures, which makes their material properties different. Semiconductors can have either a narrow or wide bandgap, and the reasoning as to why these bands are visualised the way they are, can be understood by looking at an atomic picture of molecular bonding.

#### 2.3.1.1 Atomic/Molecular orbital theory

The atomic picture of a simple hydrogen atom comes from the Bohr model which can be seen in figure 2.4. This theoretical model identified a nucleus in the centre of the atom, within which the protons and neutrons could be found, and orbiting the nucleus are the electrons. Although this image was accurate in its depiction of the protons and neutrons, it gave very little information about the electrons. To understand the nature of the electrons in an atom, the quantised energy levels they can be found in needed to be analysed<sup>11</sup>.

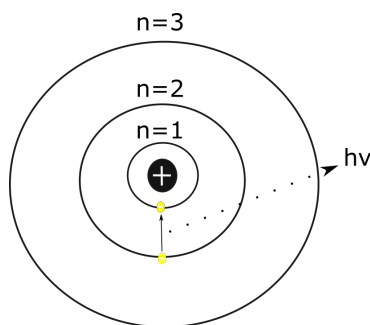


Figure 2.4: The Bohr model of a Hydrogen atom, with  $n$  representing the orbital number and  $h\nu$  representing the energy released when an electron transfers from one orbital of higher energy to that of lower energy<sup>11</sup>.

Electrons are found in orbitals of quantized energy, these orbitals can be seen as circular standing waves which can contain multiple wavelengths in relation to their orbital distance from the atoms nucleus. Standing waves must contain an integer number of half wavelengths as the wave must return to 0 at both boundaries to create a standing wave. Consequently, each orbital has a quantized energy level that the electron can be found in. The Bohr model of a hydrogen atom gives a description of what an atom with a single electron could be, however many other atoms can be theorised using this same model. From single atoms to molecules, the energy orbitals of the electrons can be explained by looking at bonding/anti-bonding orbitals<sup>11</sup>.

Continuing with the model of a basic hydrogen atom, each allowed energy shell/orbit is governed by four quantum numbers:  $n$  - the principal quantum number which defines the total energy  $n = 1, 2, 3, \dots$   $l$  - the angular momentum quantum number, also a positive integer relates to the magnitude of angular momentum  $l = 0, 1, 2, \dots, n-1$  which identifies sub-levels within the electron energy levels.  $m$  - the magnetic orbital number is a real integer that distinguishes the orbitals available within a sub shell, and can be used to calculate the angular momentum quantum number  $m = \pm l$ . And finally,  $s$  - the electrons spin which can only be one of two directions<sup>11</sup>. These four numbers describe the unique quantum state of an electron, see figure 2.5.

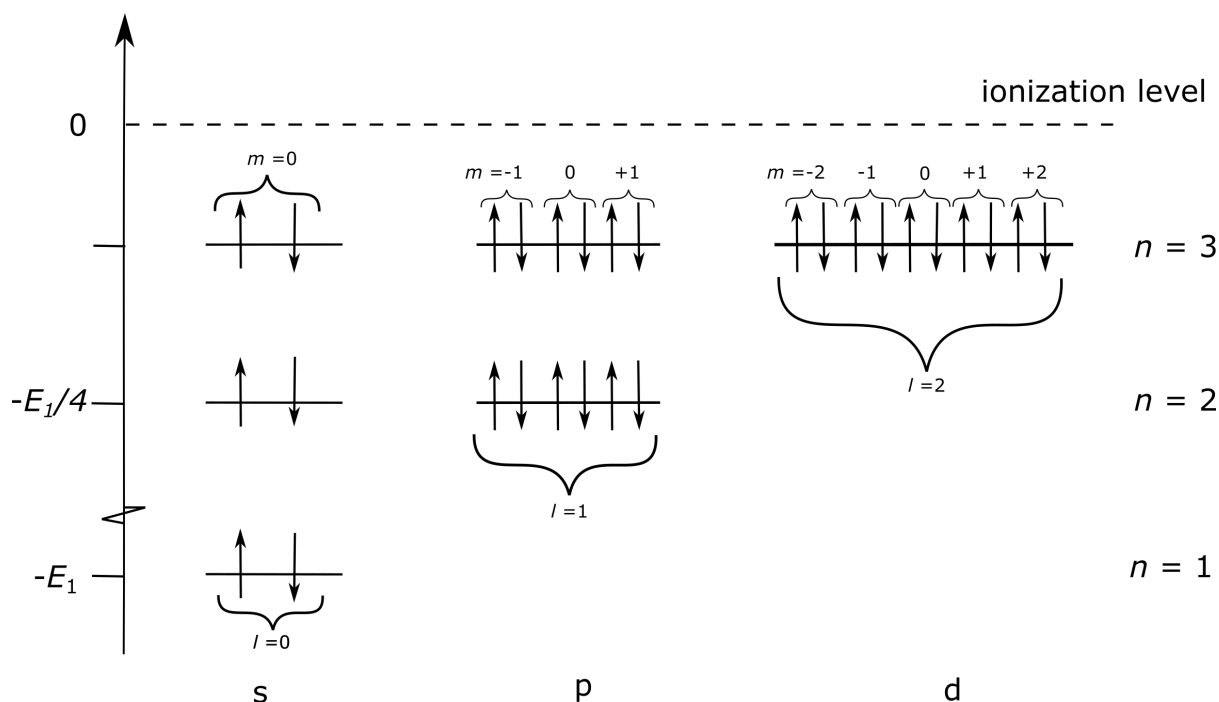


Figure 2.5: A diagram to represent the allowed states for an electron in the hydrogen atom. Here all four quantum numbers are displayed:  $n$  defines the total energy,  $l$  characterizes the angular momentum, and describes the sub-shells within each orbital ( $l=0$  is the s state,  $l=1$  is the p state..),  $m$  is a value that is between  $\pm 1$  that identifies the orbitals available within the sub-shells and  $s$  is depicted simply as the electron's spin, which as simplified in this diagram is either up or down.<sup>11</sup>

Figure 2.5 shows the ionization energy for a free electron has been taken as 0, giving the lowest energy of a bound electron as  $-E_1$  which corresponds to the  $n=1$  orbital. This energy ( $-E_1$ ) is the energy required to ionize the hydrogen atom. The values of  $n$  represent the shells of allowed states dependent upon the other quantum numbers. The quantum number, which is an integer value that is smaller than  $n$ , characterises subgroups of states within each shell which have specific names. For  $l = 0$ , it is called an s state, for  $l = 1$  it is a p state, for  $l = 2$  it is a d state and for  $l=3$  it is an f state<sup>11</sup>. The energy of an electron cannot be between these allowed states, and any energy produced as a result of electron relaxation (to a lower energy level) must be in quantised energy 'packets' equal to the energy difference between the energy levels. For the simple case of the hydrogen atom, there is a single electron and the possible energy states available to that electron can be simulated using figure 2.5. However, for a multi-electron system this diagram is wrong. The Pauli exclusion principle states that no two electrons in the



same system can have the same four quantum numbers, meaning two electrons can be within the 1s state as their spins ( $s$  values) are different, however two electrons with the same spin cannot exist in the same state. In an equilibrium state, every electron within the multi-electron system will occupy the lowest energy that is available according to Aufbau principle<sup>11</sup>.

### 2.3.2 Molecular bonding

The previous section outlines what the atomic structure was believed to be, however this is a simplified model. Commonly, substances aren't made up of single atoms, but instead bound atoms otherwise known as molecules. The molecular bonding between atoms on a basic level can be likened to the band structures seen in semiconductors with a bonding and anti-bonding molecular orbital. For example, when two hydrogen atoms bond to become  $H_2$ , there will be a bonding and anti-bonding orbital produced (see figure 2.7). Figure 2.7 shows a molecular bonding diagram, to give this diagram context, molecular orbital theory must be discussed.

#### 2.3.2.1 Molecular Orbitals

Molecular Orbital Theory (MO) states that any linear combination of atomic orbitals (AO) gives corresponding molecular orbitals. When speaking about linear combinations of atomic orbitals, this correlates to the spacial movement of atomic orbitals towards one another linearly (in one axis dimension) until they overlap. The overlap of the orbitals can be seen as a spacial overlap, but when dealing with electrons, their wave-functions have to also be considered. An example of the wave-function for a hydrogen isotope atom can be seen in figure 2.6 where two hydrogen isotopes that have wave-functions in phase with one another overlap and through constructive interference, a bonding molecular orbital is formed. In the case of two hydrogen isotopes overlapping with wave-functions out of phase, through destructive interference an anti-bonding molecular orbital is formed. Looking to figure 2.7 the anti-bonding and bonding orbital can be seen with the anti-bonding orbital being higher energy than that of the bonding orbital. This is a direct consequence of the nodal plane seen in figure 2.6 which is a node where electrons can never be found (electron density of 0 within this region). Due to this nodal plane, nuclear repulsion is promoted therefore increasing the energy of the anti-bonding MO to higher than

that of the bonding orbital. On the other hand, bonding orbitals increase electron density between the two atomic orbitals and therefore minimise the effect of nuclear repulsion, lowering the energy of the bonding MO.

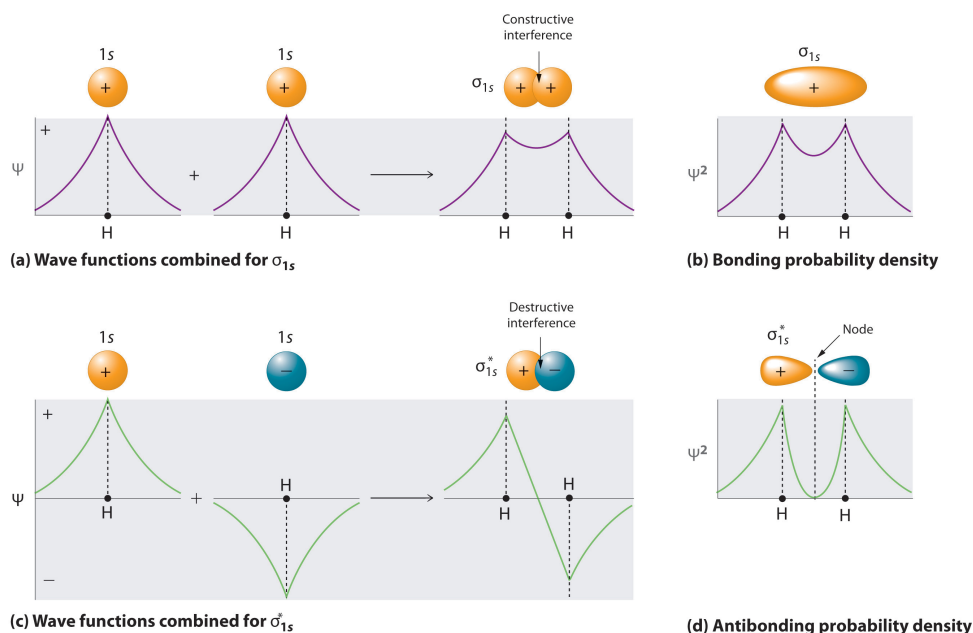


Figure 2.6: Diagram to represent the linear combination of two s orbitals with wave-functions that combine constructively and destructively. The concluding molecular orbitals show both a  $\sigma$  bonding orbital and a  $\sigma^*$  anti-bonding molecular orbital<sup>106</sup>.

In addition to molecular orbital theory, the bonding/anti-bonding orbitals can be represented using a molecular orbital diagram (see figure 2.7). Figure 2.7 shows a single valence electron in its 1s state for each hydrogen atom. When the atoms are within a threshold internuclear distance corresponding to the molecule of interest, there is an anti-bonding and bonding orbital available for populating. Due to Aufbaus principle, that states electrons will always populate the lowest energy state before occupying higher levels, both electrons will populate the bonding orbital. The number of molecular orbitals has to equal the number of atomic orbitals, therefore in the case of  $H_2$  there are two states for bonding/anti-bonding. As populating the bonding orbital is favourable (lower energy than the atomic orbitals), an exothermic reaction takes place and the molecule is created.

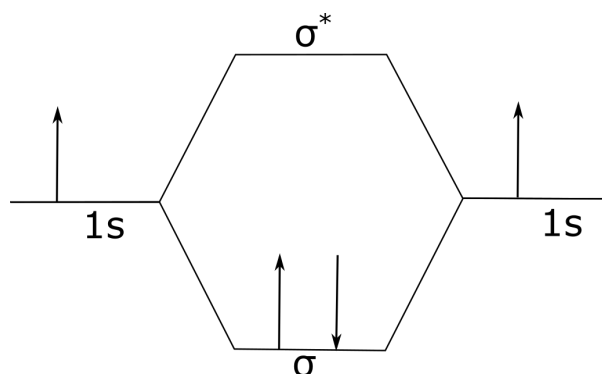


Figure 2.7: Diagram of bonding/antibonding molecular orbitals when two hydrogen atoms are within the internuclear distance corresponding to  $H_2$ . Here the  $\sigma$  represents the bonding molecular orbital (lower energy than either of the hydrogen 1s atomic orbitals) and  $\sigma^*$  represents the anti bonding molecular orbital. On the left from the base to the top of the diagram is an energy scale.<sup>11</sup>

### 2.3.2.2 Hybridization

Hybridization is the term for a process in which atomic orbitals fuse together to form newly hybridized orbitals. An example of this can be seen in methane ( $CH_4$ ). Methane contains a carbon atom and four hydrogen atoms, the electronic configuration of carbon is:  $1s^2 2s^2 2p^2$ . From the electronic configuration it can be seen that the valence electrons are in the  $2s^2$  and  $2p^2$  states. Theoretically, this means that carbon can only form 2 bonds as it only has two valence electrons. However, in practice and as can be seen in methane, carbon can form 4 bonds. This is a direct consequence of hybridization of the 2s and the 2p state to make an  $sp^3$  molecular orbital/state<sup>84</sup>. When two atomic orbitals overlap (one of which is hybridized) a sigma bond is formed), for atomic orbitals with valence electrons in a p-orbital, this forms pi bonds. Sigma bonds represent single bonds between atoms, for double and triple bonds to form, un-hybridized p orbitals must overlap with one another<sup>11</sup>.

With reference to figure 2.7, these bonding and anti-bonding orbitals are formed when two atoms are in close proximity. Figure 2.8 shows a hypothetical model of what would happen when multiple atoms with valence electrons in the 2s and 2p state meet. As the distance between them decreases, the molecular orbitals split into multiple orbitals/states that fall within what can be described as 'bands'. Between these bands there lies a forbidden energy, with the top

energy of the lower band called the valence band, (seen as  $E_v$  in figure 2.8) and the lowest energy of the upper energy band called the conductance band (seen as  $E_c$  in figure 2.8)<sup>11</sup>. This directly relates to the band structure of a semiconductor, however this model only qualitatively describes why the band structures within semiconductors exists. To quantify the band structure of semiconductors, the Schrödinger equation can be used<sup>68</sup>.

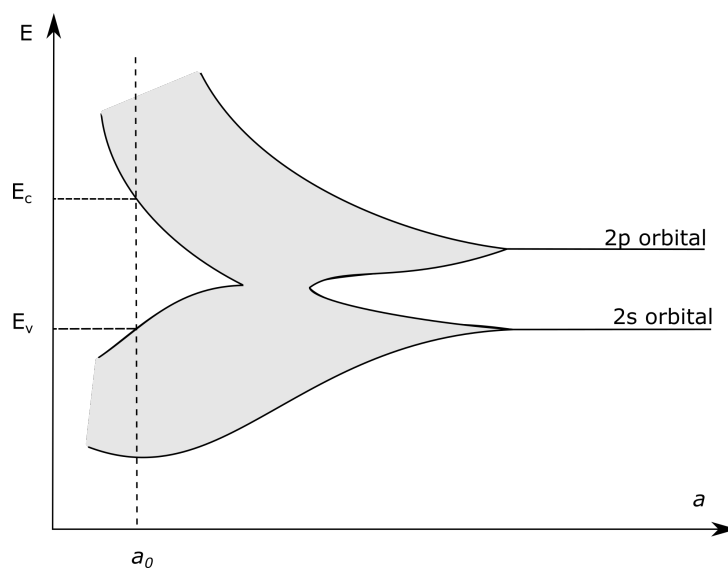


Figure 2.8: Theoretical energy band structure model for a material plotted against lattice constant. This model simulates the case of multiple atoms in a material lattice structure coming together. As the atoms move closer in proximity to one another, the 2s and 2p orbitals split into multiple different orbitals with a forbidden energy between them. For a multi-electron system the electrons in each of these orbitals will split into closely packed states that resemble bands, this is one way of observing the valence and conductance bands seen in semiconductor materials<sup>11</sup>.

### 2.3.2.3 Using the Schrödinger equation

Molecular orbital theory doesn't provide any quantitative information about the quantised energy states within molecules. To calculate the probability that an electron can be found in a specific orbital, the Schrödinger equation with an atoms potential energy field  $V(x)$  (Coulomb potential) is used. Substituting an atoms potential energy field into the Schrödinger equation gives a solution that dictates a discrete energy state (see figure 2.9a). This model works for a single atom, however a semiconductor material consists of multiple atoms arranged in a lattice formation. To further simplify the lattice composition of a semiconductor a basic model of a

single periodic atomic structure is used<sup>68</sup>. In a system of atoms arranged periodically as in a crystal lattice, the outer electrons of each atom are affected by the neighbouring atoms external electrons. The crystal as a whole then becomes a single system where the Pauli exclusion principle states that no two electrons in the same system can have the same quantum state. The discrete energy levels seen in the single atom split to form discrete potential energy levels of allowed states in the periodic lattice model (see figure 2.9b) which form the conductance and valence bands seen in simplified semiconductor band diagrams.

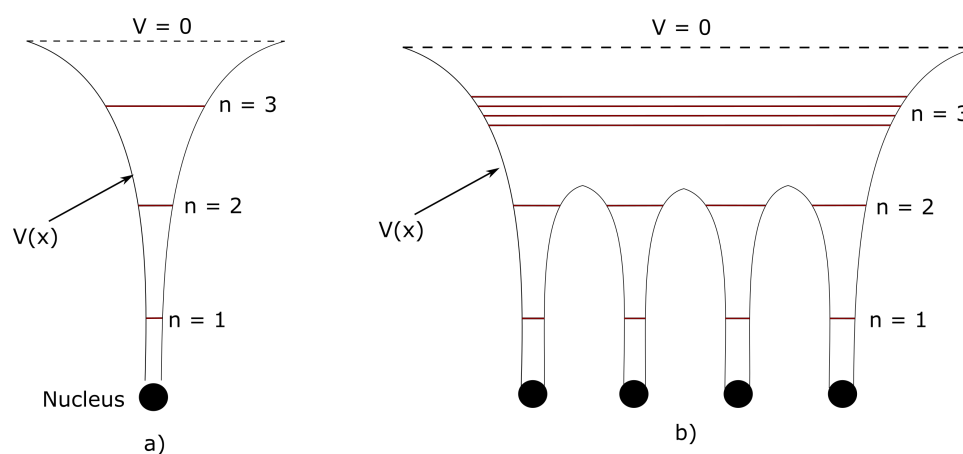


Figure 2.9: Hypothetical allowed energy states calculated by solving Schrödinger's wave equation a) for a potential field  $V(x)$  of a single atom and b) for a potential field  $V(x)$  of a periodic crystal of four atoms<sup>11</sup>.

Figure 2.9a shows the three lowest states in a single atom, obtained from the results of the Schrödinger equation. Figure 2.9b however, demonstrates a potential wave-function that contains the wave functions of each atom. The result of this is then substituted into the Schrödinger wave equation. Here, the first two energy states at  $n = 1, 2$  remain the same as the single atom model (as the orbitals are close to the nucleus and consequently unaffected by neighbouring atoms). The  $n = 3$  orbital however, is further away from the nucleus and  $V(x)$  is then strongly influenced by the potential fields of the neighbouring atoms. This state now belongs to the crystal lattice as a whole and due to the Pauli exclusion principle, contains sub-levels for each electron within the system to ensure they will have different quantum numbers. For a crystal with multiple atoms, the third level will be split into a virtually continuous band of allowed sub-levels where the electrons belong to the whole crystal and not each atom<sup>142</sup>. As

a consequence of this, a periodic potential substituted into the Schrödinger equation leads to the band structure of a material. This can be seen in the Kronig and Penney model.

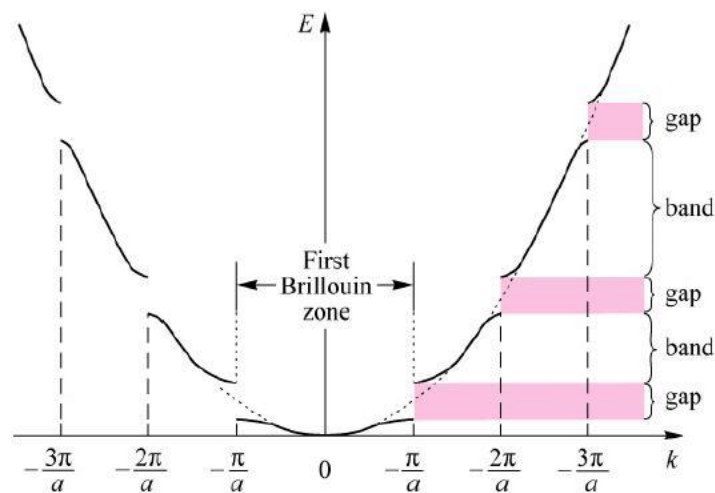


Figure 2.10: Energy vs wave-vector result from the 1D Kronig-Penney model. This result clearly shows the ‘breaks’ in electron dispersion which quantitatively identifies bands of allowed energies within materials which have periodic lattice structures.<sup>109</sup>

Kronig and Penney were the first people to develop a mathematical model for atoms within a periodic lattice in 1D<sup>79</sup>. They assumed a unit cell length for the periodicity of the lattice and calculated the energy of the electron as an eigenvalue from the solution of the wave equation. To simplify their model, they used a 1D crystal that they assumed had a circular ring form or crystals of identical structure either side of it. The results from using this model led to an  $E$ - $k$  diagram of allowed energies (from the Schrödinger equation). This was found to be a quantifiable method for calculating the allowed energy bands seen in semiconductors<sup>142,11</sup>.

Figure 2.10 shows the results from solving the Schrödinger equation for a 1D periodic lattice<sup>109</sup>. The main result to be seen here is the bands (which are labelled as dispersion curves), and the gaps between each curve which are labelled as energy gaps between bands. The results from this model confirm the band structure seen in semiconductors and allow a way to calculate the bandgap energies. Looking back to figure 2.3 this bandgap is what defined materials as conductors, insulators and semiconductors. Conductors have overlapping band structures, meaning there is no gap between bands and the electrons can be excited into the conductance

band with low input energy. Insulators have a large gap between bands, meaning electrons have to be excited by a large amount of energy to go into the conductance band. Semiconductors have a bandgap in-between insulators and conductors, and the energy required for electrons to be excited into the conductance band is called the bandgap energy. In semiconductors, the bandgap between the valence and conductance bands can be described as direct or indirect (see figure 2.11). When an external electric field is applied to a semiconductor, electrons can be excited into a higher energy level. However, after a period of time the electron releases the energy and returns to a lower energy level. The principles of physics state that energy and momentum must be conserved. So, when an electron returns to a lower energy level it has to release energy equal to that of the difference between the energy states, this is commonly either light energy or thermal energy.

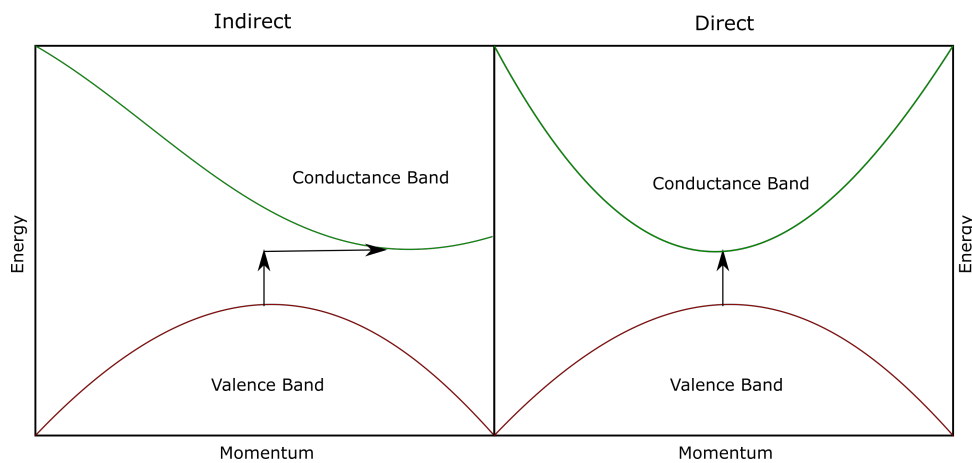


Figure 2.11: Diagram to represent energy vs quasi-momentum for both indirect and direct bandgap semiconductors<sup>11</sup>.

In a direct bandgap semiconductor, commonly the energy from an electron returning to a lower energy level is released as a photon, and both energy and momentum are conserved. However, in an indirect bandgap semiconductor, the electron cannot return directly to a lower energy level as the momentum is not conserved. In an indirect bandgap semiconductor, a two-particle absorption/emission process is introduced which allows the electron to return to a lower energy level. Commonly, in an indirect bandgap, as the electron returns to a lower energy level it releases thermal energy<sup>34</sup>. The indirect/direct nature of bandgaps is relevant

to how efficiently a material can harness light. For indirect bandgap materials, an excited electron in the conductance band has a different momentum to that of the hole in the valence band. To recombine, the momentum of both electron and hole have to be the same due to the momentum conservation law spoken about previously. A direct bandgap allows an excited electron to recombine with a hole in the valence band directly by emitting a photon with the same energy as the bandgap. This means that direct bandgaps are more efficient as LEDs and have a higher recombination rate than indirect bandgaps.

### 2.3.3 Bandgap engineering and Doping

#### 2.3.3.1 Semiconductor materials

Semiconductor materials are made from atoms connected in a lattice formation. The atomic separation in crystal structures characterize the materials energy bandgap. Figure 2.12 displays this relationship, and shows that the smaller the atomic separation in a lattice the larger the energy bandgap, this is a product of the orbital splits seen in figure 2.8. The bandgap of a semiconductor can be used to categorise the material, these semiconductor categories are: conventional, narrow band and wide band<sup>75</sup>. Conventional semiconductors can have a bandgap energy range between 1.0 - 1.5 eV, a common example is silicon which can be found in group IV in the periodic table. Narrow-gap semiconductors have bandgaps less than that of conventional semiconductors and therefore require a lower input energy for excitation. An example of a narrow-bandgap semiconductor is mercury cadmium telluride (HgCdTe) which is commonly used as an IR detector for spectroscopy and has a band gap (at 300K) of between 0 - 1.5 eV<sup>75</sup>.

Finally, there are wide-gap semiconductors, these aren't as common due to their large bandgaps (ranging between 2 - 4 eV). The wide bandgap that these semiconductors have put them in-between insulators and semiconductors in band structure. This means that wide-gap semiconductors can sustain high voltages, frequencies and temperatures, giving wide gap semiconductors an advantage over conventional and narrow-band semiconductors<sup>119</sup>. Typically wide band semiconductors are used in light emitting diodes (LEDs), as their wide bandgap facilitates an electron relaxation transition in the frequency region of ultraviolet to visible light. Looking



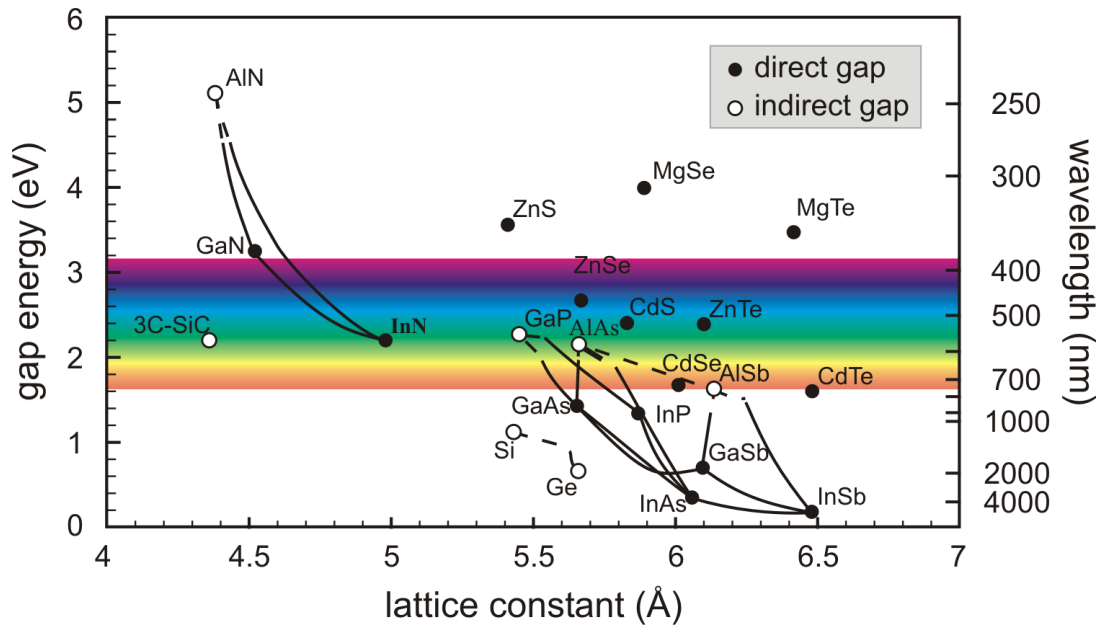


Figure 2.12: Energy bandgap ( $E_g$ ) plotted against lattice structure. This plot shows that the closer the atomic spacing in a lattice, the higher the energy bandgap<sup>38</sup>.

to the periodic table, wide bandgap semiconductors can be found in groups III -V and II - VI. Common examples of wide-band semiconductor materials are aluminium nitride (AlN) and titanium dioxide ( $\text{TiO}_2$ )<sup>75</sup>.

Figure 2.12 shows that a smaller lattice constant (the atomic separation) in a material, the higher the bandgap will be and vice versa. This figure makes sense when linking back to the Kronig-Penney model, where it can be seen that for a periodic lattice of the same atom, the electrons of an atom are directly affected by their neighbouring atoms. Therefore, if two atoms were in close proximity to one another, the electrons within their energy shells will interfere and increase the energy difference between the valence and conductance bands of a material. In addition to lattice formation, there is another way to manipulate the activation energy of a semiconductor and that is through doping.

### 2.3.3.2 Doping to control the bandgap

Doping a material involves introducing an impurity into the semiconductor by replacing some of the semiconductor materials atoms with those from other materials, however this can only

effectively change the activation energy of a material if high doses of the dopant is used. There are two common types of doping p-doping and n-doping. P-doping is when an impurity with fewer electrons than that of the atoms in the material are added, and these atoms act as acceptors. As a consequence of this, a localised energy level is created above the valence band of the material, effectively ‘shrinking’ the bandgap. N-doping is when impurities that have a greater number of electrons than those in the materials are injected into the material, and these atoms act as donors. When a high volume of these impurities are injected into a material, a localised energy level is created below that of the conductance band which can also be seen as effectively ‘shrinking’ the bandgap of the material. An example of n-doping could be adding phosphorus or arsenic impurities to silicon, phosphorus and arsenic both have a larger number of electrons than silicon atoms, and so the extra electrons can be found in impurity levels just below that of the conductance band (see figure 2.13). The electrons within these impurity levels require a reduced amount of energy to be promoted, and thus increase the conductivity of the semiconductor<sup>34</sup>. An example of p-doping would be if boron or aluminium was added to a silicon semiconductor, there would be an excess of holes. The electrons would require a reduced amount of energy to migrate to the impurity level/state (separated by approximately a tenth of an eV) above the valence band<sup>34</sup>.

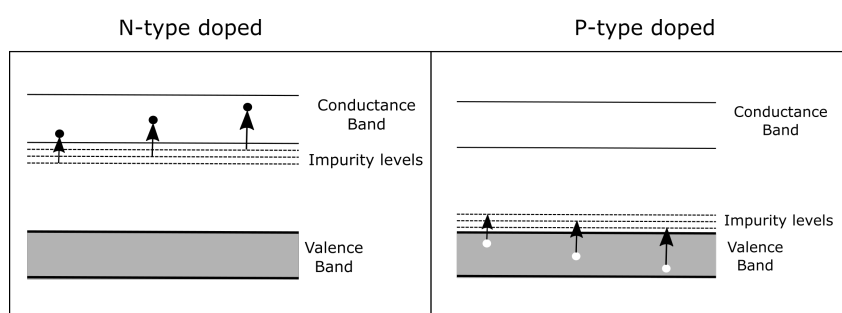


Figure 2.13: Diagram to represent p-type and n-type semiconductors, highlighting the impurity levels that exist due to defects in the crystal lattice or as a product of doping<sup>34</sup>.

## 2.4 Titanium Dioxide

A material that acts as both a photocatalyst and a semiconductor is Titanium Dioxide ( $\text{TiO}_2$ ).  $\text{TiO}_2$  is an inexpensive, non-toxic, versatile chemical<sup>28</sup> with a characteristic bandgap that lies

between 3.2 eV to 3.4 eV (this is within the range of the UV LED that is used in the experimental setup (see section 2.6.1.2)). This means that its bandgap is within the UV region of the electromagnetic spectrum<sup>78</sup>.  $\text{TiO}_2$  can be found as a key ingredient within many industrial companies, such as sun protective creams, whitening toothpastes, cosmetic products and the pigment within white paints<sup>64,141</sup>. Research into  $\text{TiO}_2$  as a photocatalyst began almost two and a half decades ago when its photocatalytic abilities lead to a water splitting reaction<sup>145,121</sup>.

In 1969, Akira Fujishima and Kenichi Honda published a letter on the application of titanium dioxide ( $\text{TiO}_2$ ) as a photocatalyst in a water splitting experiment<sup>40</sup>. Their results showed that by exposing  $\text{TiO}_2$  to an ultra-violet light source a reaction takes place (Honda-Fujishima effect). This is called a water splitting reaction which as the name suggests, splits a water molecule into  $\text{H}_2$  and  $\frac{1}{2}\text{O}_2$ . This research was furthered by Fujishima and since the 1970's  $\text{TiO}_2$  as a material has been widely investigated for its unique properties. The two main properties of  $\text{TiO}_2$  that make it unique are its ability to convert photoelectrochemical solar energy, and its photoinduced hydrophilicity<sup>145</sup>. The mechanisms behind these two reactions are completely different, however both can occur on the same surface at the same time, this is what makes  $\text{TiO}_2$  an interesting material. In 2000, Fujishima and Honda published a review on the progress of  $\text{TiO}_2$  as a material in a photoelectrochemical reaction<sup>41</sup>.

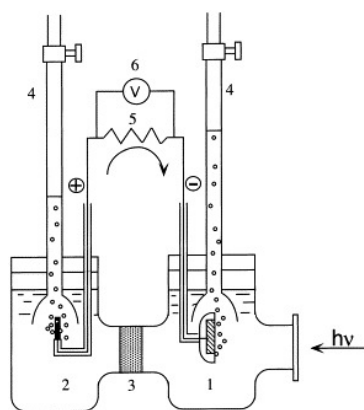


Figure 2.14: Schematic diagram of an electro-chemical process using n-type  $\text{TiO}_2$ [1] and a platinum black counter electrode [2]<sup>41</sup>. This figure represents the experimental equipment used to identify the Honda-Fujishima effect of water splitting by exposing  $\text{TiO}_2$  to UV light and recording the potential difference between a cathode and anode.

The technique Fujishima and Honda used to identify the photocatalytic behaviour of  $\text{TiO}_2$  was using a solar photovoltaic cell to measure the electrical work generated between an n-type  $\text{TiO}_2$  electrode and a counter electrode. The voltage generated was directly related to the chemical reduction reactions that took place at the surface of the semiconductor electrode, which in turn was a product of electron-hole pairs. In Fujishimas' experiment (see figure 2.14), the semiconductor is n-type  $\text{TiO}_2$ , and the electric field across the electrode drives the photo-generated holes towards the surface of the electrode and the electrons towards the external circuit<sup>41</sup>. In 2007, Fujishima stated that  $\text{TiO}_2$  was an ideal photocatalyst based on its material properties, namely its high chemical stability. To this day, this statement stands true as  $\text{TiO}_2$  is one of the most common photocatalysts used.

#### 2.4.0.1 $\text{TiO}_2$ in water treatment

The applications of  $\text{TiO}_2$  in research show it to be a versatile and effective material, from an air purifier to water splitting, this material has tremendous potential. Currently, detoxification of polluted water is one of the most successful photo chemical applications of  $\text{TiO}_2$ <sup>58</sup>. The first published results that focused on the photocatalytic potential of  $\text{TiO}_2$  for water purification was by N. Frank and J. Bard in 1977<sup>39</sup>. They wrote a letter entitled 'Heterogeneous Photocatalytic Oxidation of Cyanide Ion in Aqueous Solutions at  $\text{TiO}_2$  Powder'. In this letter they discuss their experimental parameters using both anatase and rutile forms of  $\text{TiO}_2$  to oxidise cyanide ions; which occur as a frequent industrial pollutant. Their findings demonstrated that by varying concentrations and illuminations, the reaction completed (over numerous tests) within a measurable time-frame by oxidising the cyanide ions. They also noted that in the presence of unactivated  $\text{TiO}_2$ , and without  $\text{TiO}_2$ , there was very little or no oxidising of the cyanide ions. From their results, the conclusion that  $\text{TiO}_2$  was an effective photocatalyst for oxidation reactions was published.

As a result of Frank and Bards findings,  $\text{TiO}_2$  has been a material of interest for its applications in water treatment. To optimise the optical properties of  $\text{TiO}_2$  (specifically its photocatalytic efficiency), it can be doped (to effectively shrink the bandgap), and different crystalline forms of  $\text{TiO}_2$  can be tested to identify their differing optical properties<sup>128</sup>.

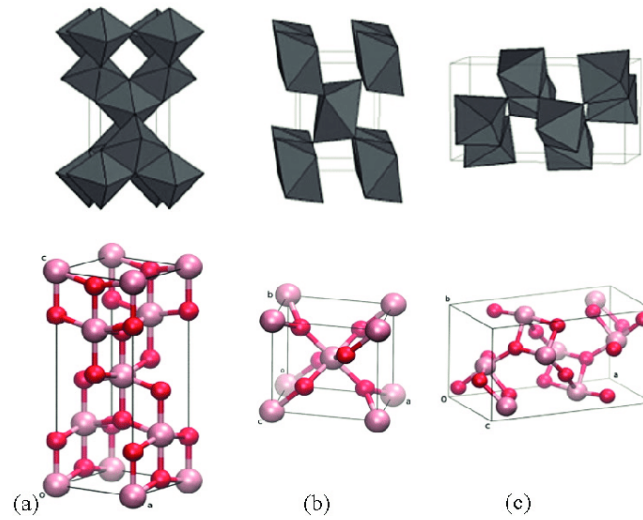
### 2.4.1 Polymorphs of $\text{TiO}_2$

Titanium dioxide is a polymorph that can exist in three crystalline forms: brookite, rutile and anatase<sup>47</sup>. Each crystalline structure has advantageous properties, for example, rutile is thermally stable (due to its crystalline structure) whereas anatase and brookite are meta-stable (can be heated to produce rutile). Both anatase and rutile are more common, and consequently the volume of research into these forms is greater than that for brookite<sup>28,88,128</sup>. Rutile is the most common crystalline form of  $\text{TiO}_2$  and is often used as a material for interference optics due to its high refractive index (see figure 2.15). 80% of all  $\text{TiO}_2$  usage is in pigments, and the powdered form of rutile is used as a white pigment for products such as paper, paint, plastics and foods<sup>103</sup>. Figure 2.15 displays the main optical variable differences between the three crystalline structures of  $\text{TiO}_2$ .

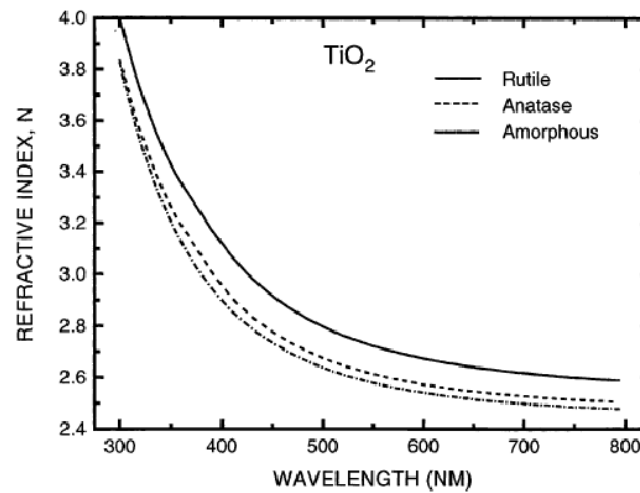
Figure 2.15a shows the crystalline structures of the three polymorphs of  $\text{TiO}_2$ , each form of  $\text{TiO}_2$  has its own unique structure which affects its optical properties. The refractive index of each of these crystalline forms are different but similar in overall trend. Due to their different crystalline forms (referring back to figure 2.15), the bandgap of each polymorph of  $\text{TiO}_2$  will be different, which in turn means affects their individual photocatalytic activity. A mixture of these crystalline forms is commonly used to optimise samples of  $\text{TiO}_2$  for specific applications.

### 2.4.2 Nano-structuring

The surface of a photocatalytic particle is the location of its active sites; where the reaction occurs. Prior to nanotechnology, to maximise the number of active sites available for reaction to a particle, the overall particle was enlarged in bulk. Using nanotechnology however, it can be seen that by taking the particle down to a nanoscale, the surface area to volume ratio is increased, providing a greater surface area without physically increasing the bulk size of the particle<sup>3,65,1</sup>. A nanoparticle is described as a particle of size between 1 nm to 100 nm surrounded by an interfacial layer. Nanoparticles are used in a wide range of scientific fields, they are in effect the bridge between bulk materials and atomic scale structures<sup>65</sup>. These materials can be manufactured in either 0D (quantum dot), 1D (nanorod), 2D (nanosheets)



(a) A diagram representing the crystalline structures of the three polymorphs of TiO<sub>2</sub> a) anatase, b) rutile and c) brookite<sup>45</sup>.



(b) A graph to show the refractive index change of rutile, anatase and amorphous TiO<sub>2</sub> over the visible region<sup>15</sup>

Figure 2.15: Results from two separate publications showing the crystalline structure and refractive indices of anatase and rutile as well as amorphous TiO<sub>2</sub>. The difference in crystalline structure directly affects the refractive index amongst other optical properties for each crystalline structure.

or 3D (nanoparticle)<sup>65</sup>. It was discovered that reducing the size of a particle can influence its optical properties, and with a greater surface area to volume ratio, an increased number of active sites became available for accelerated chemical reactions<sup>65</sup>. The company Degussa produce a nano-structured  $\text{TiO}_2$  product that claims to have a high photocatalytic efficiency (as stated by Degussa)<sup>95</sup>. They state that this product consists of a combination of both rutile and anatase crystalline forms of  $\text{TiO}_2$ , however the ratio of one to the other is undefined. A recent publication into this product came to the conclusion that a mix of: 78% anatase, 14% rutile and a remaining 8% amorphous was the mixture<sup>96</sup>. This shows that both anatase and rutile combined produce a high photocatalytic efficiency. To achieve a high photocatalytic efficiency, the electron hole pairs produced must not recombine or must recombine on a long timescale, which Degussa have achieved<sup>95</sup>.

### 2.4.3 Limitations of $\text{TiO}_2$ bandgap

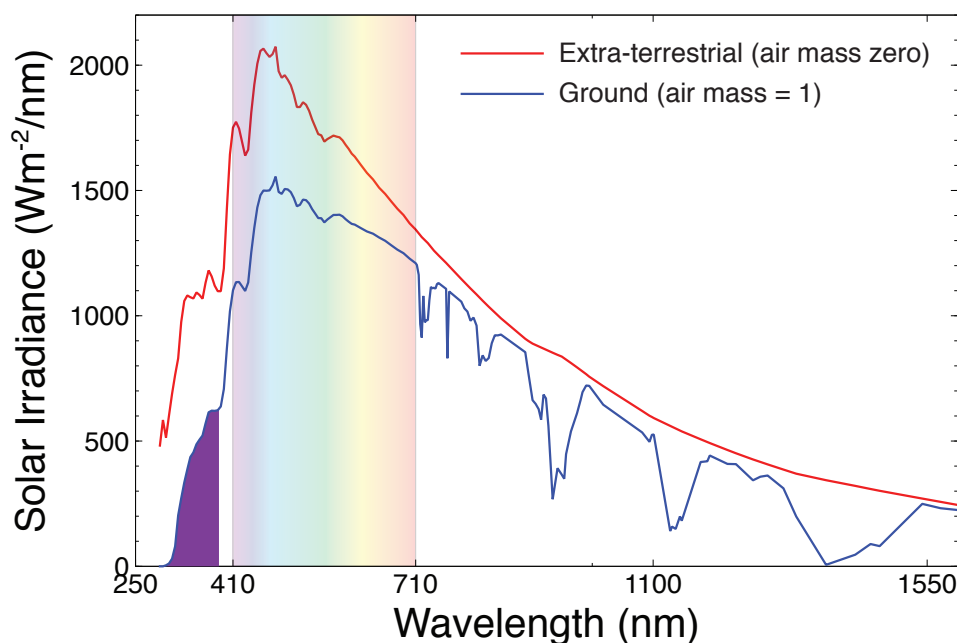


Figure 2.16: Solar irradiance spectrum plotted against emitted wavelength. The rainbow shading represents the visible spectrum, the dark purple area represents the ultra-violet portion of the emission.

P25 Degussa  $\text{TiO}_2$  has a bandgap between 3.2 eV to 3.4 eV, which means its activation energy

is in the ultra-violet region of the EM spectrum. Looking to figure 2.16 the irradiance of UV light in the solar spectrum is under half that seen in the visible spectrum, and it also comprises of a fraction of the full wavelength emission. This factor therefore limits the  $\text{TiO}_2$  application to UV irradiation, and minimises the photon flux available for reaction in real-world solar spectrum powered applications. In order to extend the wavelength range for  $\text{TiO}_2$ , its bandgap has to be manipulated towards the visible region. With reference back to section 2.3.3, the best way to achieve this outcome is to dope the material.

## 2.5 Simulating Pollutants

With the knowledge that  $\text{TiO}_2$  can be used in a water treatment reaction using the UV irradiation( in the solar spectrum, figure 2.16), the aim for this project was to measure the degradation reaction of organic chemical pollutants found in water sources using  $\text{TiO}_2$  as the photocatalyst. With reference to the opening chapter, the three main technologies in the field of water treatment all fail to remove dissolved pollutants in an inexpensive and effective manner. Two primary pollutants that have been proved highly toxic with direct causation of damage to the reproductive system, developmental problems, damage to the immune system and also as a carcinogenic, are benzene and dioxins<sup>136</sup>. These pollutants are consumed/ingested in developing countries through surface water sources. Local water sources such as lakes and rivers are exposed to agricultural/industrial waste which contain these pollutants.

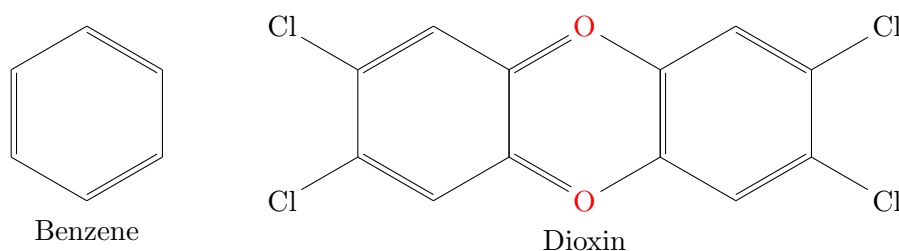


Figure 2.17: Chemical structures of benzene and 2,3,7,8-tetrachlorodibenzo-para-dioxin (2,3,7,8-TCDD) (dioxin).

Benzene and dioxins are both water soluble and are also transparent to visible light, which makes them challenging to observe optically<sup>136</sup>. In addition to these factors, they are both highly

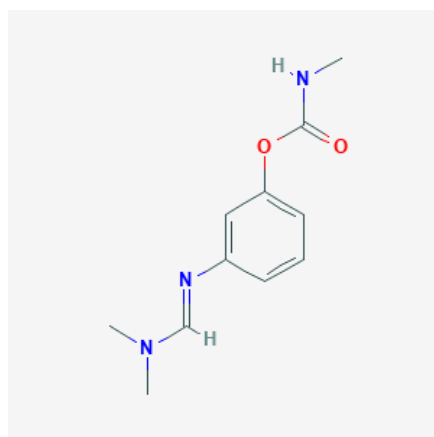


toxic and measuring them in a laboratory setting would prove dangerous. Benzene's structure is a simple aromatic ring (planar unsaturated ring of atoms reinforced by an interaction of the bonds forming the ring), whereas dioxin contains three stable ring structures linked by two oxygen molecules (see figure 2.17)<sup>136</sup>. Other common water pollutants that have been featured in recent publications on water treatment include:

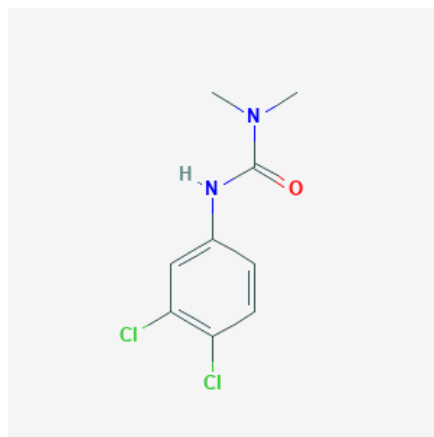
- **Formetante**, which is an insecticide that is used specifically on deciduous trees to remove fruit tree spider mites. It is fatal to humans if swallowed and highly toxic to aquatic life with long lasting effects<sup>81</sup>.
- **Diuron**, which is used as a herbicide to control broad leaved weeds, grass and mosses. It is negligibly water soluble and has high toxicity warnings for human consumption<sup>81</sup>.

Looking to figure 2.17, the common structure seen in both benzene and dioxin is the aromatic benzene ring. If you look at the structures of the other pesticides/insecticides mentioned above, they also contain this stable benzene ring (figure 2.18). To be able to mimic this structure, a proxy non-toxic pollutant was used for testing. A non-toxic chemical that shares similarities in chemical structure to the desired pollutants is methylene blue. Methylene blue and methyl orange are both non-toxic organic dyes that share the same aromatic ring structures seen in the benzene/dioxins<sup>7</sup>. In addition to their chemical structure, they are both water soluble and strongly coloured dyes and undergo an optical colour change reaction that can be observed during degradation<sup>44</sup>.

Methylene blue is a non-toxic, photoactive phenothiazine dye. In the latter years of the 19<sup>th</sup> century it was the first synthesized antimalarial drug<sup>19,111</sup>. After multiple experimental trials in 2010 it was combined with other medications such as amodiaquine and was shown to be effective in the treatment of falciparum malaria<sup>7</sup>. One of methylene blues applications after the 19<sup>th</sup> century was in the staining of biological cells for microscopy imaging<sup>99</sup>. Preceding this, methylene blues non-toxic soluble properties meant it could be employed in heterogeneous photocatalysis research, where currently a large volume of data on its dried/hydrate state has been recorded<sup>44,58,7</sup>. Powdered methylene blue appears dark green in colour, however when dissolved in water appears blue (becomes methylene blue hydrate). This phenomenon is due



- (a) The chemical structure of Formetate contains a central aromatic ring similar to benzene.<sup>94</sup>



- (b) The chemical structures of Diuron, just as formetate and benzene has a central aromatic ring in structure

Figure 2.18: The chemical structures of Formetate and Diuron which both contain a central aromatic ring, similar to dioxin and benzene<sup>102</sup>.

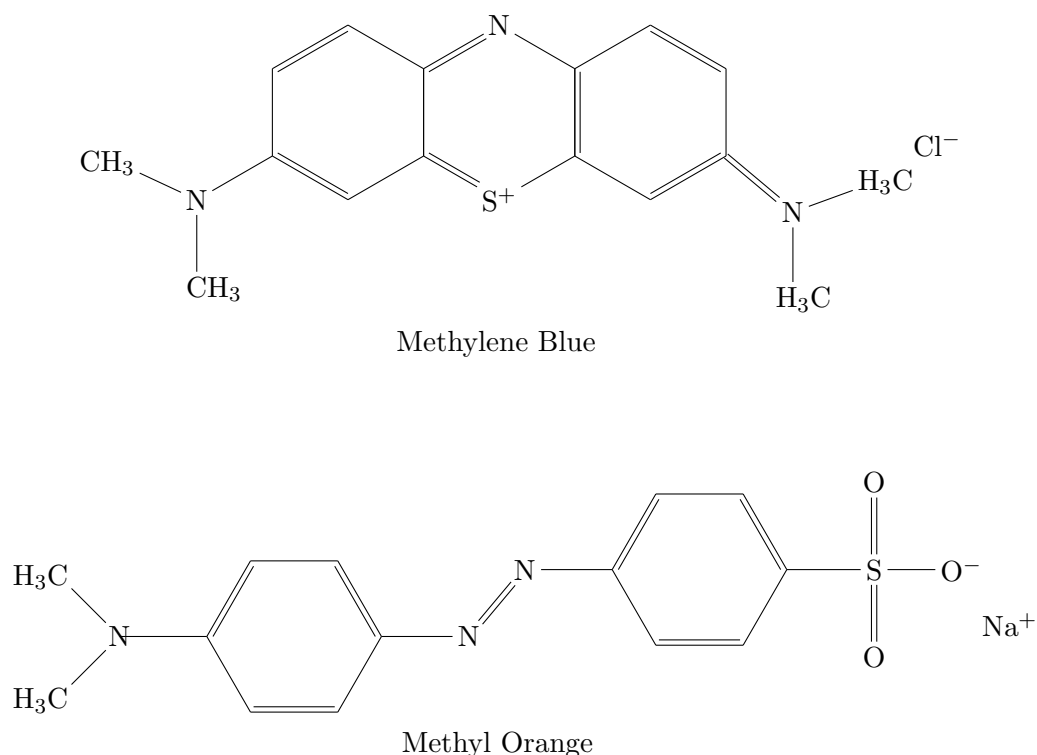


Figure 2.19: Chemical structures of methylene blue and methyl orange

to the fact that each methylene blue hydrate molecule has 3 water molecules to one methylene blue molecule<sup>58,7</sup>. The absorption spectrum for methylene blue hydrate shows a distinct peak in the visible at approximately 660 nm (see figure 2.20). This meant that the colour present throughout the reaction could be identified using a red laser diode with visible light near 660 nm (see section 2.6).

Despite extensive research into TiO<sub>2</sub> photocatalysis, the fundamental reaction pathways are still yet to be experimentally established/published<sup>31,78</sup>. A new technique for optically monitoring the photocatalytic reaction in real-time to identify the reaction pathways during reaction was used in this PhD project. The reaction measured was the degradation of methylene blue (a proxy pollutant) using TiO<sub>2</sub> as the photocatalyst. This degradation reaction was observed in a simple experimental setup and analysed accordingly.

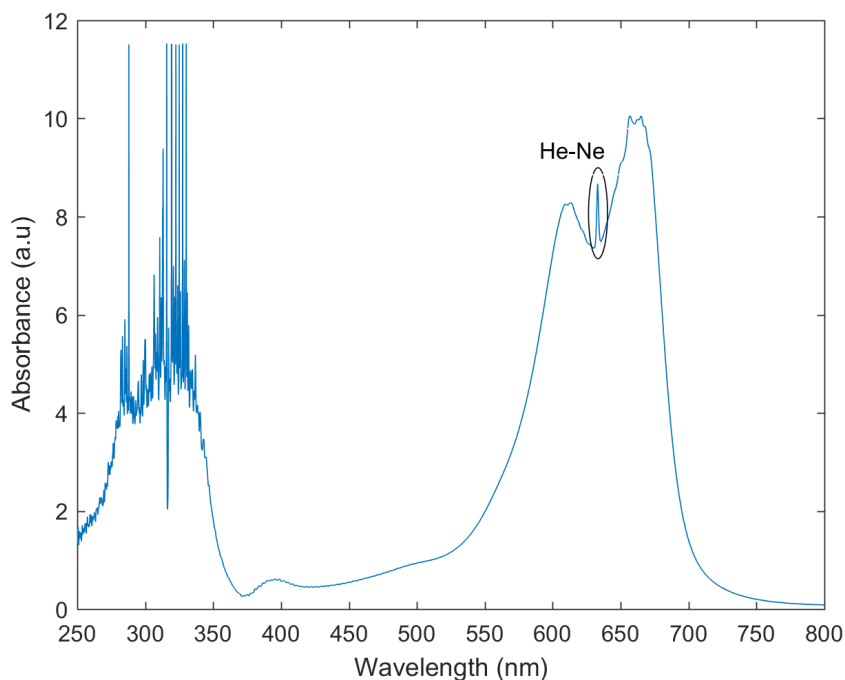


Figure 2.20: Absorption spectrum of methylene blue hydrate, measured using a 1 cm flowcell in a BRUKER Vertex spectrometer and visible light. The peak at 660 nm is clear, however the peaks at 330 nm and 280 nm are unclear due to the high concentration of the methylene blue causing noise to overcome the signal at the detector.

## 2.6 Experimental Determination of Reaction Lifetime

As mentioned previously, an optical measurement technique was required to identify the lifetime of a degradation reaction. Methylene blue is a strongly coloured dye, therefore qualitatively a colour change reaction could be observed. However, visually observing a colour change can't quantify the lifetime of the reaction, or identify any numerical experimental parameters (e.g. maximum input concentration). For a quantitative measurement, the measurement parameters must be precise for repeatability and integrity in the results, this meant that this initial experiment was run 10 times averaged for analysis. Once the initial parameter space of the experiment had stabilized ( a fixed input concentration, a value for the amount of time it took for the overall visible clearing of the dye), the degradation experiment could be measured quantitatively by determining a reaction lifetime.

The reaction lifetime can be classified as the time taken for a particular stage in the reaction

to be reached. For this project, the amount of time it took for  $\frac{1}{e}$  of the pollutant to decay was measured. In order to quantitatively measure this, the Beer-Lambert law was used which identifies the relationship between concentration and absorbance of a sample. Light can be transmitted through a material, propagating in the same direction as the incident beam (see figure 2.21). Photons can transfer energy to atoms within the material, and this is classed as absorbed light. Light that leaves a material with a different trajectory to that of its input beam is categorised as scattered/reflected light. Absorption and scattering/reflection are processes that occur at atomic levels, whereas transmission is a process that allows the input light to pass through the material with no atomic interaction<sup>146</sup>. To analyse a materials atomic composition, the absorbance is commonly measured and as mentioned previously, the relationship between absorbance and concentration is identified using the Beer-Lambert Law.

### 2.6.1 The Beer-Lambert Law

The Beer Lambert law relates the attenuation of light to properties of the material through which the light has travelled. This law was first discovered pre-1729 by Pierre Bouguer, but Johann Heinrich Lambert is often accredited for it<sup>72</sup>. Lambert stated that the absorbance of a material is directly proportional to its thickness (optical path length). Building from this, August Beer discovered that absorbance is proportional to the concentration of the attenuating species within the material<sup>13</sup>. The modern day law combines these two and has the form:<sup>97</sup>:

$$A = \epsilon C b, \quad (2.8)$$

where  $A$  is the absorbance,  $C$  is the concentration,  $\epsilon$  is the absorbance co-efficient of the material and  $b$  is the path length.

To understand where the relationship between absorbance and concentration originates, the Beer-Lambert law equation must be derived from first principles<sup>127</sup>. The model seen in figure 2.21 assumes an input beam of light is incident to a solution containing solutes that absorb a fraction of the input light. As the solution absorbs the light, the intensity of the light seen on the other side will decrease. The extent with which the intensity decreases is dependent upon

three factors<sup>127</sup>:

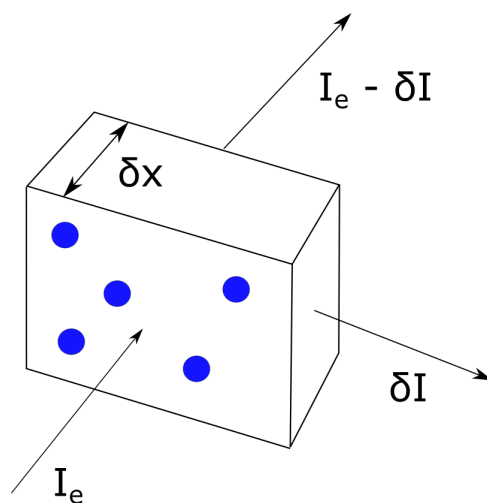


Figure 2.21: Diagram to represent the Beer-Lambert Law. Here, a simple model of a small block of a solution is drawn to identify the Beer-Lambert Law equation from first principles.  $I_e$  is the input intensity of light,  $\delta I$  is the absorbed light and  $\delta x$  is the thickness of the block<sup>127</sup>.

1. **Concentration ( $C$ )** - If there are more molecules of a sample in a solution of the same volume, the solution will absorb more light.
2. **Epsilon ( $\epsilon$ )** - The amount of light each molecule absorbs will directly affect the overall absorbance through the solution.
3. **Path length ( $b$ )** - If the concentration remains constant and the light path through the solution increases, then the solution's absorbance will also increase.

Figure 2.21 shows a model which assumes that a solution can be broken down into small uniform blocks of thickness  $\delta x$ . To calculate the number of moles present in a single unit,  $n$  throughout the block thickness  $\delta x$  use equation:

$$n \times s \times \delta x, \quad (2.9)$$

where  $s$  is the cross-sectional area of the block.

The fractional proportion of each molecule in solution that absorbs light can be calculated by introducing the molecular cross-sectional area(  $\sigma$  ), this value can be represented as  $\frac{\sigma}{s}$ .

relates to individual molecules however, so to apply this to all molecules within a fixed block, this becomes:

$$n \times \sigma \times \delta x. \quad (2.10)$$

In order to relate this fractional proportion to the light absorbed, the light intensity must be introduced into the above equations. The difference between the input light intensity and the output light intensity can be classed as the absorbance ( $\delta I$ ). The absorbance represents the proportion of input light that is absorbed by each molecule, which gives it a negative value. Thus, the proportion of light absorbed with respect to input light intensity is  $\frac{-\delta I}{I_e}$ .

$$\int_{I_e}^{I_b} \frac{\delta I}{I_x} = \sigma n \int_0^b \delta x, \quad (2.11)$$

$$\ln \left( \frac{I_e}{I_b} \right) = \sigma n b.$$

Equation 2.11 provides an expression for the absorbance, however the units can be further simplified to:

$$\ln \frac{I_e}{I_b} = \frac{C \times b \times \sigma \times 6.02 \times 10^{20}}{2.303}, \quad (2.12)$$

where  $\ln \left( \frac{I_e}{I_b} \right)$  is the absorbance through the solution,  $C$  is the concentration measured in Mol/L,  $b$  is the path length through the solution, and  $\frac{\sigma \times 6.02 \times 10^{20}}{2.303}$  is a constant specific to one solute present within the solution and is characterised by  $\varepsilon^{127}$ . This equation is the Beer Lambert Law and it identifies the relationship between concentration, absorbance and path length<sup>127</sup>.

### 2.6.1.1 Calculating a reaction lifetime

The first experiments recorded for this project monitored a degradation reaction of a test pollutant (methylene blue) over a 24 hour time period in the visible region, the results of which

can be seen in figure 2.24. The variable constants for this experiment were the path length  $b$  and extinction coefficient  $\varepsilon$ . Using the Beer-Lambert Law and the knowledge that absorbance is the inverse of transmission, the absorbance was plotted as a function of time and consequently a decay constant was calculated<sup>81</sup> see equation 2.13).

$$\frac{dA}{dt} = -\beta A. \quad (2.13)$$

Rearranging for absorbance, gives the solution:

$$A = e^{-\beta t}, \quad (2.14)$$

where  $\beta$  is the decay constant,

$$\beta = \frac{1}{\tau}, \quad (2.15)$$

and  $\tau$  is the reaction lifetime.

### 2.6.1.2 Monitoring reaction lifetime

One of the aims of this project was to produce a reaction lifetime for methylene blue degradation using  $\text{TiO}_2$  as the photocatalyst. The experimental setup followed the same basic structure of figure 2.22. The initial stages of the project monitored a colour change reaction both qualitatively and quantitatively using the experimental setup seen in figure 2.23.

The experimental apparatus of this project consisted of two circuits, one for measurement and the other for reaction. Pipes connecting a pyrex beaker, flowcell and micro pump facilitate the photocatalysis reaction. The catalyst used was  $\text{TiO}_2$  and the activation source was a UVA LED (365 nm / 3.39eV)<sup>130</sup>. The second circuit facilitated the measurement of the reaction, with a red laser diode and a photodiode either side of a flowcell. The voltage read at the photodiode was measured throughout the reaction and converted into absorbance for analysis. The reaction begins with the catalyst, which for this project was fixed to a substrate (fixed bed system). Previous publications have stated that a slurry system has been used to increase the



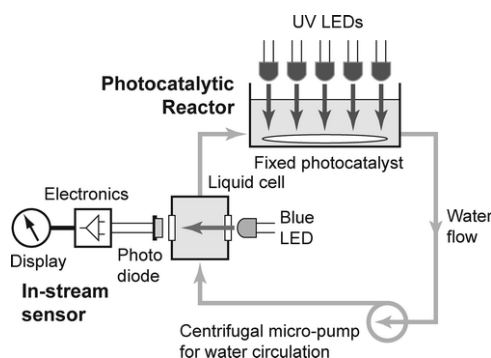
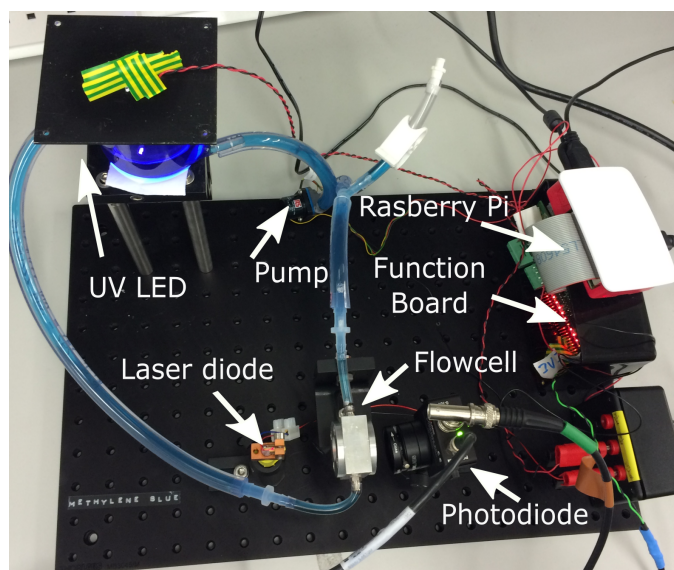


Figure 2.22: Schematic diagram of experimental setup used in Nickels, Patrick *et al.* To measure the reaction, a blue LED was shone through a flowcell, and the light detected at the photo diode was then recorded for subsequent analysis. The chemical reaction monitored is activated in the photocatalytic reactor, where a wafer spin coated with a photocatalyst ( $\text{TiO}_2$ ) degrades a proxy pollutant under the irradiance of a UV LED (365 nm). The solution containing the pollutant is circulated throughout the apparatus by means of a centrifugal micro-pump<sup>93</sup>.

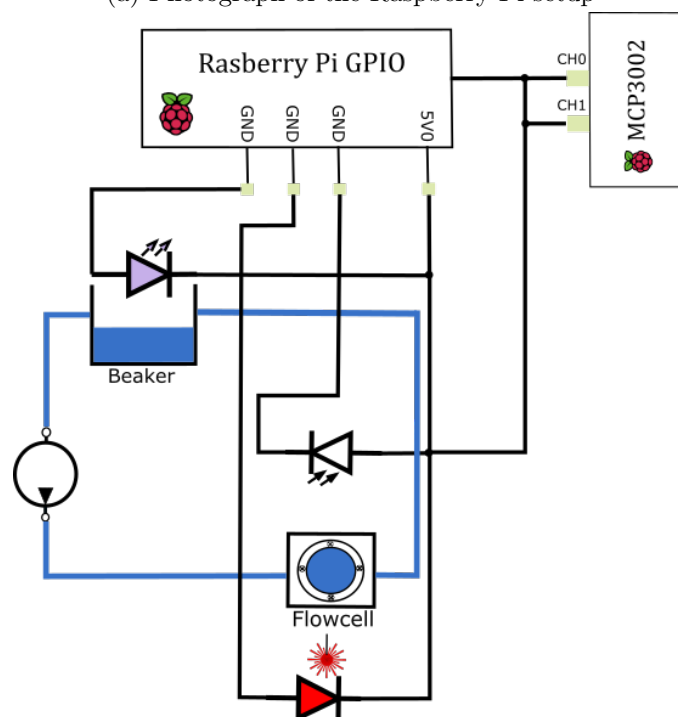
intimacy between the catalyst and solution. However, for a sustainable reaction this method presents problems as for each run (full degradation reaction) the whole system has to be flushed and rinsed of the catalyst. Whereas, should the catalyst be confined to a substrate (fixed bed system), the cleaning time between reactions is significantly reduced making the reaction more sustainable.

$\text{TiO}_2$  was spin-coated onto a silicon wafer and placed at the base of a pyrex beaker beneath a UV LED for activation. The spin-coating process used a Laurell Spin-3000. A silicon wafer was spun at 3000 rpm for 60 s, and a 3 ml coating consisting of a mixture of: 800 mg of Degusa P25  $\text{TiO}_2$  nanoparticles, 8 ml of isopropyl-alcohol (IPA) and 25  $\mu\text{l}$  of Triton X-100 was measured onto the wafer. IPA is used as a liquid base for the nanoparticles, and Triton X-100 is a surfactant that was used as a wetting agent, this meaning it changes the viscosity of the solution which helped to coat the wafer. The reason that silicon wafers were used was due to its material properties' (non-toxic, inexpensive and inert in aqueous solutions). After coating, the wafer was then placed onto a hot plate set at  $450^\circ\text{C}$ , to remove the IPA and Triton X-100 from the substrate, leaving only the  $\text{TiO}_2$  nanoparticles.

Following a user-written Python programme the voltage readings were collected and analysed using an analogue to digital convertor (ADC). An ADC chip converts a continuous signal to



(a) Photograph of the Raspberry Pi setup



(b) Drawing of the experimental setup. There are three circuits. The first (black) is the electronic circuit that records the voltage seen by a photodiode, via an ADC connected to the Raspberry PI. The other black circuit powers both the red LED and the blue UV LED. The circuit (blue) is an aqueous circuit connected by pipes; this circuit contains the aqueous sample and is where the photocatalytic reaction is facilitated. This reaction is methylene blue degradation as a result of UV activation of  $\text{TiO}_2$  nanoparticles, which are fixed to a substrate and placed at the base of the beaker.

Figure 2.23: The experimental setup using a Raspberry Pi and function board to power and record a methylene blue degradation reaction.

a discrete digital value, for example converting photons incident on a photodiode to a digital value representing the magnitude of the voltage/current. On the basis of this analysis, a graph of the degradation reaction was plotted, and a reaction lifetime was determined from the fit (see figure 2.24).

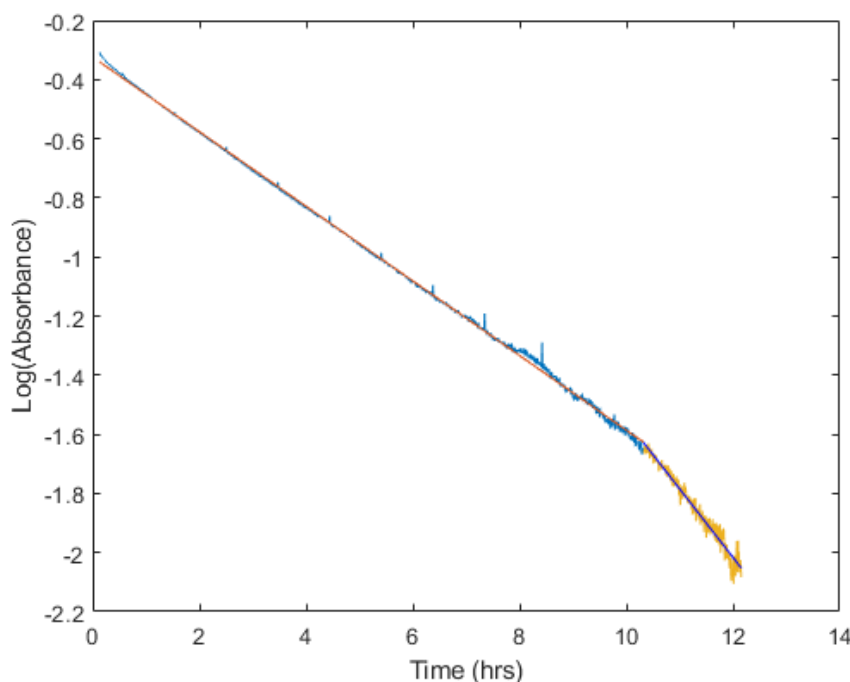


Figure 2.24: Absorbance plotted on a logarithmic scale which shows the reaction lifetime can be fitted with two different first order polynomials. The first fit gives a reaction lifetime of  $7.92 \pm 0.04$  hours, with the second fit giving a value of  $4.31 \pm 0.02$  hours.

The experimental parameters used to achieve the result in figure 2.24 were as follows, 100 mA for the UV LED, 16 mA for the red laser diode, 3.5 V for the micro-pump, a consistent laboratory environment of 23.4°C, 75 ml of de-ionised water (used instead of tap water, due to limescale deposits coating the wafer) and finally a 2 ml input of milli-molar methylene blue solution. Using these parameters, a degradation lifetime of  $7.92 \pm 0.04$  hours was measured over the first 10 hours, with reaction completion (absorbance  $\approx 0$ ) seen at 12 hours. This result was consistently repeatable, providing valuable information into organic dye degradation in the visible region. Figure 2.24 shows a clear bi-linear fit to the absorbance data over time (with small periodic peaks seen as a result of the red laser LED suffering from current fluctuations). The bi-linear

nature of the graph insinuates that the reaction remains at a constant pace until 10 hours in, and then speeds up. This could be a consequence of methylene blue bonding to the wafer within the first 75 % of the reaction and only being fully removed in the last 2(+) hours. This ‘build-up’ of methylene blue will be further discussed within the last chapter of this thesis. However, what can be said about this data is that the initial stages of the reaction (first few hours) should be a focus for the later experiments, where the reaction pathways were to be identified.

This result indicates reaction completion both quantitatively and qualitatively though a colour change, which provides valuable information about the reaction. Whilst this information is of value, the molecular components of the reaction were yet to be measured in real-time. Measuring the vibrational motion of each chemical bond over the course of the full reaction is one way that this is possible. To measure the vibrational bonds, a new measuring technique was used, infrared (IR) spectroscopy<sup>39</sup>. One form of IR spectroscopy is Fourier transform infrared spectroscopy (FTIR), which is reviewed in chapter 3. Methylene blue degradation is an aqueous reaction, and although FTIR spectroscopy is one of the key technologies used in bond kinetic identification, it encounters difficulties when measuring aqueous samples<sup>83,87</sup>. The high absorbance characteristic of water in the MIR region (mid infrared) limits the ability to measure it, providing difficulties in measuring reactions that are aqueous (see figure 4.6). Therefore, the experimental apparatus using the Raspberry Pi and 1 cm flowcell (figure 2.23) had to be re-designed for the purpose of aqueous spectroscopy<sup>39</sup>. The new experimental design used optical techniques such as millimetre capillary cells and attenuated total internal reflection (ATR) units. These technologies incorporate different optical techniques for passing IR light through the sample. The thin capillary cell physically minimises the path length to reduce the effect of absorbance through the sample (with reference to equation 2.8), whereas ATR techniques use the principle of total internal reflection to minimise the effective path length of the IR light through the sample. For a direct comparison, a 1 mm path length capillary cell and four ATR units (made from different materials) were designed, manufactured and tested for this project.

## 2.7 Summary

To begin this chapter, catalysis was discussed as they were used in this project to effectively lower the activation energy of a reaction. The benefit to using catalysts in a reaction is that they can effectively lower the activation energy in a reaction without consuming themselves, giving them the advantage of sustainability. There are two main types of catalysts, those that are in the same state and those that are found in a different state to reactants, these are called homogeneous and heterogeneous catalysts respectively. Catalysts require an activation source (most commonly heat), however photocatalysts can also be activated by light. Once activated, photocatalysts facilitate a reaction that produces free radicals. Similar to photocatalysts, semiconductors are also activated by an energy source. The band structure of semiconductors can be calculated from the Kronig-Penney model solution to the Schrödinger equation which shows how semiconductors differ from insulators and conductors. Semiconductors can be described as having two primary bands called the conduction and the valence band. The energy gap between these bands is known as the bandgap. The bandgap energy is the threshold required to excite an electron from the valence band to the conduction band. This bandgap can be manipulated via the process of doping to effectively change the required energy for excitation.

The reason for discussing both photocatalysts and semiconductors is that this project used a material that acts as both. This material is titanium dioxide ( $\text{TiO}_2$ ).  $\text{TiO}_2$  has been seen to facilitate a water splitting reaction which consequently gives it potential applications in water treatment. The only limitations seen with using pure  $\text{TiO}_2$  is that its bandgap is within the UV region of the solar spectrum. The solar irradiance in the UV region is a fraction of the irradiance seen over the visible region thus, to effectively change the bandgap of  $\text{TiO}_2$ , doping has to take place. This thesis' aim was to measure a water treatment reaction using proxy water pollutants. The desired pollutants were benzene and dioxin which are water soluble, colourless and highly toxic. Due to the toxicity of these pollutants they couldn't be used, so simulation pollutants were measured that shared similarities in chemical structure with the desired pollutants. The simulation pollutant used was methylene blue which is a non-toxic organic dye. With methylene blue being strongly coloured, a colour change degradation reaction could be observed when

using  $\text{TiO}_2$  in a photocatalytic reaction. This colour change reaction needed to be measured quantitatively to identify a reaction lifetime. Measuring the absorbance and using the Beer-Lambert law highlighted the relationship between absorbance and concentration and a reaction rate was calculated. Whilst measuring the colour change gives a reaction lifetime, this value doesn't provide any information as to the chemistry of the reaction. The aim of this thesis was to measure a water treatment reaction by analysing the reaction pathways in real time. UV/Vis measurements don't provide any information into the chemical bonds present throughout the reaction. For this, the infrared region of the electromagnetic spectrum must be used. However, this brings new challenges in water absorbance and consequently new experimental design.

## 3 Vibrational Spectroscopy

From chapter 2, a reaction rate among other experimental parameters were measured. Whilst this data provides quantitative information about the rate of a colour change reaction, it doesn't given any information into the reaction chemistry. So, to measure the chemistry of the reaction, the internal atomic bonds must be identified. A common method for this it to measure the vibrational frequency of the atomic bonds present throughout the reaction. To do this, a technique called vibrational spectroscopy is used.

### 3.1 Background to Vibrational Spectroscopy

#### 3.1.1 Vibrational modes

Atomic movement within a molecule can be either translational, rotational, vibrational or a combination. Translational motion describes the movement of molecules from one place to another in the same/different direction whilst remaining in the same dimensional axis. Rotational motion describes the molecules motion in and around the axis. Finally, vibrational motion describes the change in dipole moment of a stationary diatomic/polyatomic molecules fixed at a coordinate position as a result of an input frequency<sup>6</sup>. Infrared (IR) spectroscopy as a technology gives rise to recognition, approximation and structural determination of compounds<sup>50</sup>. The method in which it does this, is through identification of vibrational modes present in a molecular sample. Vibrational movement in molecules is measured by analysing the change in dipole moment in response to input frequency. Dipole moments occur when there is a separation of charge, this can be between ions in an ionic bond or between atoms in a covalent bond. Dipole moments come from a difference in electronegativity<sup>51</sup>. Due to this, monatomic molecules or

diatomic molecules of the same atom (e.g oxygen) don't display vibrational movement and therefore can't be measured using this technique.

The underlying principle of vibrational spectroscopy is that a molecule acts similarly to simple harmonic motion. This means, the vibrational frequency depends on the masses of the constituent atoms in the molecule and on the strength of the bonding. Heavier atoms vibrate slower than lighter atoms, and consequently require more energy to vibrate. A strong chemical bond can be modelled by a tight spring, this meaning the vibrational frequency will be higher<sup>114</sup>. A simple model of a diatomic molecule is two masses connected by a spring. When modelling masses on a spring, Hooke's law can be used (equation 3.1). This fundamental physics principle is dependent upon two variables, the materials spring constant and the reduced mass. In the case of diatomic molecules, the spring constant can be used to model the vibrational frequency of the bond and the reduced mass can be used as a combined mass value (of each individual atom bound in a molecule).

$$\tilde{\nu} = \frac{1}{2\pi c} \sqrt{\frac{K}{\mu}}, \quad (3.1)$$

Where  $c$  = speed of light ( $\text{m s}^{-1}$ ),  $K$  = force constant ( $\text{cm}^{-1}$ ) and  $\mu$  = reduced mass (kg). The reduced mass can be calculated using,

$$\mu = \frac{m_1 m_2}{m_1 + m_2}, \quad (3.2)$$

with  $m_1$  and  $m_2$  as the individual masses of the atoms within the molecule.

The product of shining infrared light at diatomic/polyatomic molecules is a recorded vibration that causes a change in atomic separation. Whilst diatomic molecules are an important model when looking at simple vibrational spectroscopy, the polyatomic molecule is more commonly found within complex samples (such as that used within this project). Using the simple model of a polyatomic molecule consisting of three atoms, there are basic vibrational movements that can occur, these are called the vibrational modes. These modes can be categorised into: stretching and bending. Stretching is when the inter atomic distance along the axis of the bond continuously changes. Bending is when the angle between two bonds changes, see figure 3.1 for



a full list.

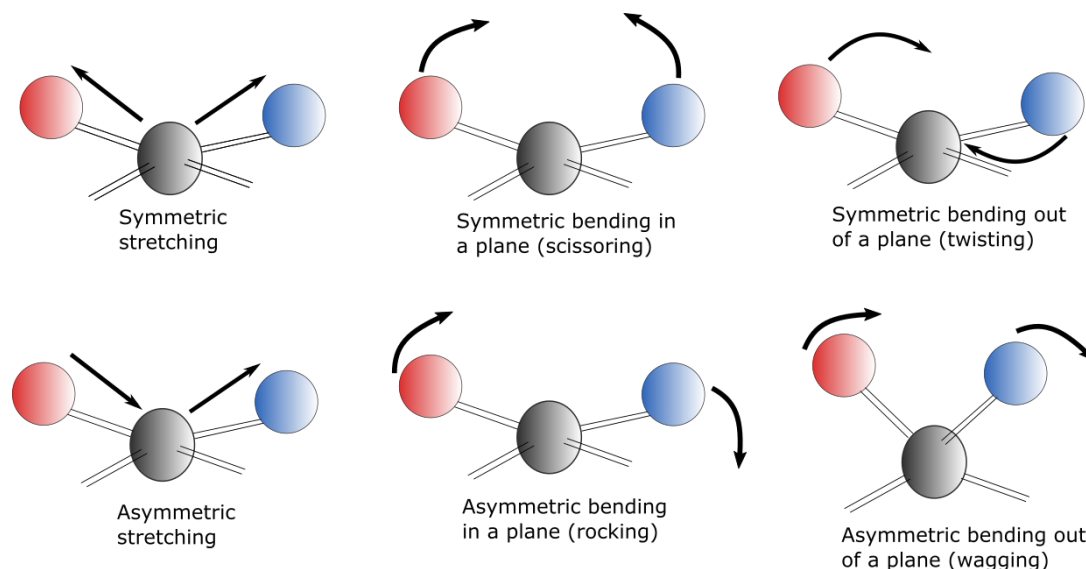


Figure 3.1: The vibrational modes of diatomic molecules present within the MIR region. Here, the common vibrational modes include stretching and bending both in plane and out of plane.

Diatomic/ polyatomic molecules can be categorised based on their structure, whether they are linear or non-linear. Each of these structures affects an atom's degree of freedom; this can be generalised in equations 3.3 and 3.4. A molecule consisting of 'N' number of atoms has a total of  $3N$  degrees of freedom, with respect to the three axes outlined in Cartesian coordinates. Linear molecules are aligned on a single axis (single straight line) and therefore cannot facilitate rotational movement around the bond axis. Looking at equation 3.3, this is reflected in the number of degrees of vibrational modes for linear molecules. Non-linear molecules however have a non-linear structure and therefore have a greater degree of freedom overall, but a smaller degree of vibrational modes<sup>50</sup>. Non-Linear molecules have 3 degrees of freedom for rotational movement, 3 for translational movement and the remainder as vibrational movement. Linear molecules however, have 3 for translational and only 2 for rotational as there is no rotational movement on the linear axis<sup>49</sup>.

Mathematically the vibrational normal modes for linear and non-linear molecules can be expressed as:

$$\text{Degree of freedom for vibrational modes of Linear Molecules : } (3N - 5) \quad (3.3)$$

$$\text{Degree of freedom for vibrational modes of Non-Linear Molecules : } (3N - 6) \quad (3.4)$$

To measure the vibration modes of molecular samples, infrared light is used.

### 3.1.2 Group Theory

Every normal mode has a specific type of symmetry associated with it therefore to understand the symmetry of a mode a point group of the molecule has to be discovered. With this in mind, it is unsurprising that each normal mode forms a basis set for an irreducible representation of the point group the molecule belongs to.

### 3.1.3 Infrared Radiation

Infrared (IR) radiation was first theorised and documented by astronomer Sir William Herschel in 1800, where he observed radiation with energy lower than red light from a temperature shift on a thermometer<sup>56</sup>. Since this discovery, IR radiation has been used in a variety of applications, from the pharmaceutical industry to thermal imaging, IR radiation has provided an insight into molecular imaging<sup>12</sup>. The most common technology that uses the IR spectrum to identify molecular structures can be seen in spectroscopy. An IR spectrometer contains IR light sources that irradiate a sample on one side, and detect the transmission through the sample on the other. The transmission signal from the sample can be translated into vibrational bond frequencies to analyse a sample's molecular composition.

The IR region of the full EM spectrum traverses  $12\,800\text{ cm}^{-1}$  to  $50\text{ cm}^{-1}$ , where  $\text{cm}^{-1}$  is the unit for wavenumber. Wavenumber is given by  $1/(\text{wavelength in cm})$  and is labelled as the spatial frequency ( $\nu$ ). In the IR region there are three wavelength groups: the near-infrared

(12 800  $\text{cm}^{-1}$  to 4000  $\text{cm}^{-1}$ ), the mid-infrared (4000  $\text{cm}^{-1}$  to 200  $\text{cm}^{-1}$ ) and the far-infrared (100  $\text{cm}^{-1}$  to 50  $\text{cm}^{-1}$ ). The IR region can also be split into two regions of chemical characterisation<sup>20</sup>. The first is known as the functional group which is from 4000  $\text{cm}^{-1}$  to 1000  $\text{cm}^{-1}$  and the second is from 1000  $\text{cm}^{-1}$  to 400  $\text{cm}^{-1}$  which is known as the fingerprint region<sup>50</sup>. The fingerprint region contains many different vibrational bands with overtones (overlapping frequencies), which can be complex to analyse. The functional group however is where the majority of stretching frequencies appear, and each functional group (i.e alcohol, amine) has a clear vibrational frequency profile.

Sample selection for IR spectroscopy requires the molecules within the sample to allow a change in dipole moment when excited with IR frequencies. Whilst the majority of diatomic/polyatomic molecules display clear vibrational frequency modes, there are several homonuclear diatomic molecules such as  $\text{Cl}_2$ ,  $\text{O}_2$  and  $\text{N}_2$  which cannot be tested using spectroscopy as they display no dipole change<sup>114</sup>. Molecules, based on their geometry and the mass of each atom within the molecule, will produce a signature vibrational frequency when excited with infrared light. To understand what each molecular frequency represents, they must first be measured and a common technique used for this application is infrared spectroscopy.

## 3.2 Infrared Spectroscopy Techniques

Infrared spectrometers are used to measure fingerprint frequencies of molecules in samples by passing infrared (IR) light through the sample, and detecting the resultant spectrum. The resultant spectrum identifies the frequencies that are present in the sample, those that have a weaker amplitude or are missing from the final spectrum have been absorbed by the sample. From this spectrum, an understanding of the molecular composition of a sample can be achieved. The way that the IR light is passed through the sample differs between spectrometers, the first model of a spectrometer is called a dispersive spectrometer.

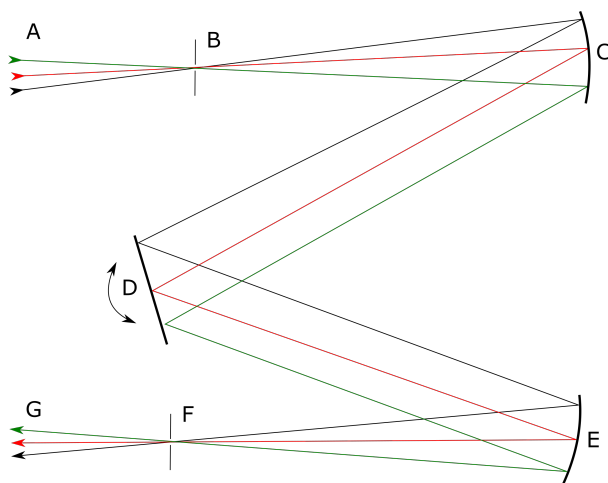


Figure 3.2: Diagram of the Czerny Turner monochromator design. A light source (A) is focused onto a single slit (B) and then collimated by a parabolic mirror (C). The collimated light is then diffracted by a moveable grating (D) and re-focused again by a second parabolic mirror (E) and exits via an exit slit (F).

### 3.2.1 Dispersion Spectroscopy

The first IR spectrometer was developed in the 1950's and is called a dispersive spectrometer. It incorporates an optical splitting system using a sodium chloride prism. Due to the nature of the prism, the measurement region is narrow, and the sample preparation required for measurement rendered the instrument too specialized for wide scale application<sup>110</sup>. The second generation of spectrometer replaced the sodium chloride prism with an optical grating and is called a monochromator spectrometer (see figure 3.2). The grating was used in place of the crystal due to the optical transparency of the prism which limited the spectroscopy technique. Using the grating meant discrete wavelengths of the IR spectrum were produced, enabling known frequencies to be observed separate from the full spectrum. This generation of spectrometer is unique and largely advantageous for samples of known bond frequencies. However, limitations in measurement speed, and samples with unknown chemical contents lead to a third generation of spectrometer<sup>36</sup>.

The current third generation model of spectrometer replaced the monochromator grating, with a moving Michelson interferometer, it also included a computerized algorithm using Fourier transform technology. This type of spectrometer is the most powerful and consequently is still in

operation today and is called a Fourier transform infrared spectrometer (FTIR). Before talking about FTIR spectroscopy and its advantages, the components of a dispersive spectroscopy system will be explained<sup>10</sup>. The core components of a dispersive IR spectrometer comprise of a radiation source, monochromator and detector. The radiation sources are made from inert solids that when heated emit black body radiation. From the emitted radiation the monochromator disperses/separates the full span of the IR region into narrow frequency ranges<sup>10</sup>. Dispersive spectrometers incorporate dual beams; one for sample measurements and the other for reference. The sample beam is passed through the sample compartment, whilst the reference beam is passed through a reference compartment for analytical comparison. From the sample/reference chambers the frequency signal is split through a monochromator into each respective component frequency. The slits can be narrowed/widened to either give a greater resolution or a greater photon flux at the detector. The detector then convert an analogue signal into an electrical signal; which can then be computationally processed to produce the final spectrum<sup>114</sup>.

### 3.2.2 FTIR Spectroscopy

FTIR spectrometers are the third generation infrared spectrometer; surpassing its predecessor dispersive IR spectrometers<sup>126</sup>. An FTIR spectrometer has similarities with its predecessor; it consists of an IR source, Michelson interferometer, sample compartment, detector, amplifier and analogue to digital convertor (ADC)<sup>110</sup>. The internal components of a spectrometer facilitate a light path that is passed through a sample to a detector for measurement. From the IR source to the detector the light is split into two and then recombined. The physical term for two waves of light meeting one another is interference<sup>123</sup>. Interference occurs when two waves meet to form a resultant wave. This wave can be of greater/lower or equal amplitude to that of the input waves dependent upon the nature of the interference, e.g constructive/destructive<sup>10</sup>. Constructive interference occurs when the peaks of two or more waves meet that share the same frequency. Destructive interference occurs if the peak of one wave meets the trough of another that share same frequency<sup>104</sup>. The resultant wave, as a product of interference, shows the difference between the individual wave amplitudes, see figure 3.3.

Interference is an important phenomenon in wave theory, and it is based on phase difference.

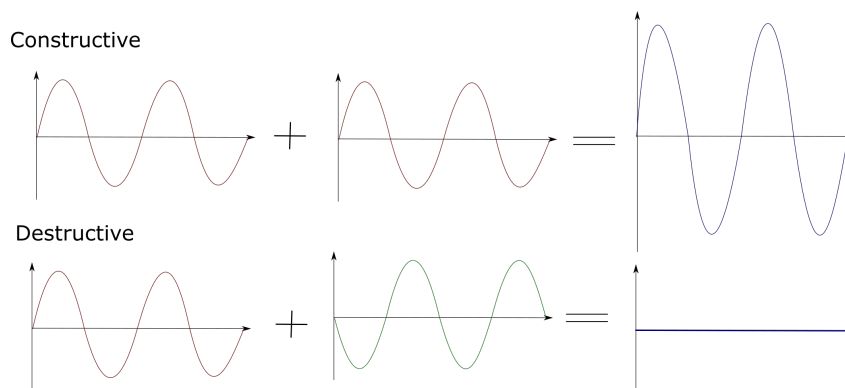


Figure 3.3: Diagram representing constructive and destructive wave interference.

Phase is defined as the position of a point in time on a waveform cycle. For one complete cycle of an oscillating sine wave there are  $360^\circ$  of phase. Phase is an expression of relative angular displacement between two related features, be that axis-crossings/peaks/troughs of two or more waves with the same frequency<sup>144</sup>. Constructive interference occurs when two or more waves display a phase difference equal to an even multiple of  $\pi$  ( $180^\circ$ ), whereas destructive interference occurs at odd multiples of  $\pi$ . These are extreme scenarios however, and the interference of two waves whose phase difference lies between the odd/even integer multiples of  $\pi$ , produces a resultant wave with a displacement value that lies between that of the minimum and maximum values<sup>48</sup>. Inside of an FTIR spectrometer, interference plays an important role as the resultant spectrum (interferogram) is a product of interference between two signals. The input IR light is passed through a Michelson interferometer which coordinates two separate optical paths. These two paths are called the reference and sample beam paths.

### 3.2.2.1 Michelson Interferometer

As mentioned previously, the technique of interferometry requires a sample and reference beam, it is within the Michelson interferometer that this mechanism occurs. Looking at figure 3.4, there are two mirrors, one is the stationary and fixed to a single position, whilst the other mirror is mobile and moves across a fixed scale. The speed of the mobile mirror is dependent upon the users input frequency, and the movement itself incurs minimal friction by designing it to be seated on air bearings. Once both the reference and sample beams have passed through

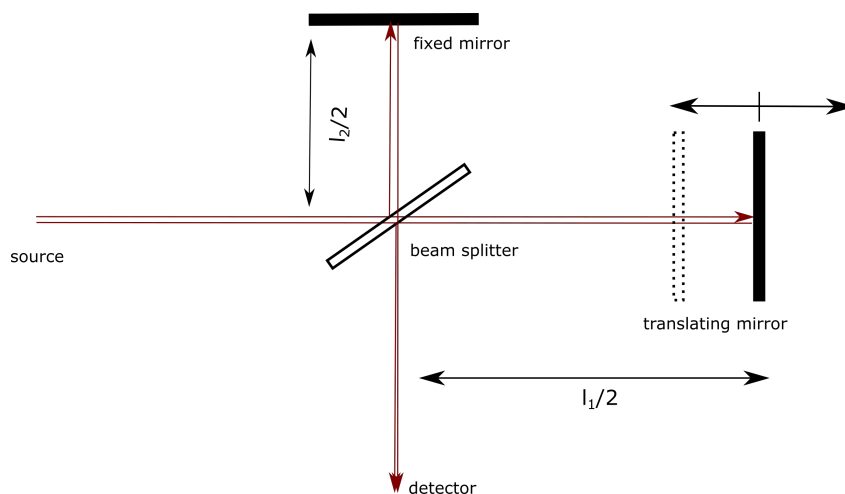


Figure 3.4: Schematics of the michelson interferometer found in an FTIR spectrometer<sup>114</sup> where 'l' represents the path length of the wave through each path (1,2).

the Michelson interferometer, they meet at the detector where the final result is measured as a function of the difference of path lengths<sup>114</sup>.

If both beams travel the same distance, the result is given as zero path difference (ZPD). This ZPD is a reference that acts as the central zeroed point. When the translating mirror is at its furthest extension with reference to the beam splitter, the path length is longer than that from the stationary mirror. The difference between the two path length distances is characterised as the symbol  $\Delta$  and is labelled as the mirror displacement. At the translating mirrors full extension, the light travelling to the translating mirror has a longer path length than that seen at the stationary mirror and the difference in path length is measured as  $\Delta$ . However, as the light reflects at the mirror, its optical path length is therefore expressed as  $2\Delta$ <sup>114</sup>. The optical path difference (OPD) between the mirrors can be characterised as:

$$\delta = 2\Delta. \quad (3.5)$$

If we relate the wavelength to the OPD and look at constructive interference, it can be seen that the OPD can be expressed as:

$$\delta = n\lambda \quad (3.6)$$

where  $n$  is an integer.

For destructive interference, where peaks and troughs meet, the OPD is expressed as:

$$\delta = \left(n + \frac{1}{2}\right)\lambda \quad (3.7)$$

By process of elimination, should the resultant wave be neither perfectly constructive nor destructive, then the final signal will be between maxima and minima. Due to the nature of the moving mirror, the intensity of the signal rises and falls to produce a cosine wave, this resultant wave can be plotted in what is known as an interferogram. This interferogram will present a single peak at ZPD, and low intensity oscillating signals either side<sup>12</sup>. For visual aids, figure 3.5 demonstrates the resultant interferogram of both broadband and monochromatic light sources<sup>123</sup>.

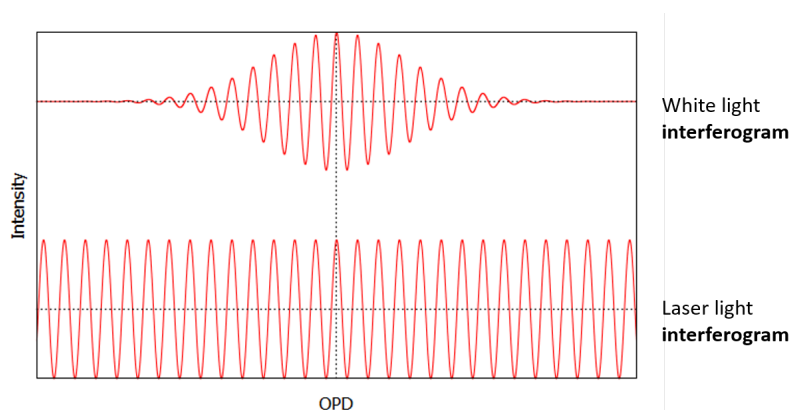


Figure 3.5: Interferograms of both broadband and monochromatic light<sup>123</sup>

Figure 3.5 shows the interferogram for white light and monochromatic laser light. As the laser light is monochromatic (a single wavelength), then the interferogram shows its regularity of oscillation and stability throughout all OPDs. The white light however, contains the full visible spectrum. In this spectrum there are different wavelengths and consequently different frequencies. When all of these waves are summed together, the resultant interferogram is what can be seen in figure 3.5. A further representation of this phenomenon can also be seen in figure 3.6.

Figure 3.6 shows a broadband light interferogram and its wave composition. It can be seen



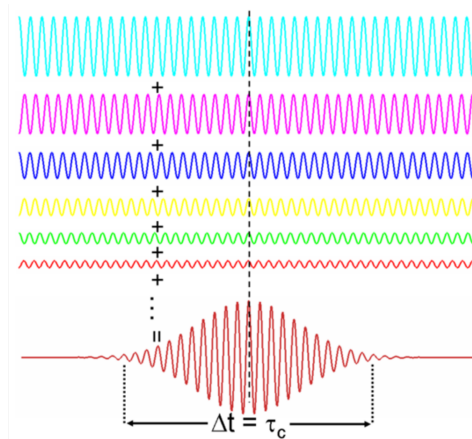


Figure 3.6: Decomposition of a broadband light source interferogram<sup>123</sup>

that from left to right, all of the component waves are in and out of phase with one another until they reach a central point (black dotted line). Here, they are all perfectly in phase with one another, this contributes to the largest peak seen in the broad band light interferogram and demonstrates what a broad band source interferogram looks like. These interferogram results are then further processed to identify what frequency components are present in the signal (as can be seen in figure 3.6), to do this an algorithm called Fourier transform is used.

### 3.2.2.2 Continuous and Discrete Fourier Transform

There are two fundamental sampling techniques that use the Fourier transform, these include continuous and discrete Fourier transform. The Fourier transform was named after French mathematician and physicist Jean Baptiste Joseph Fourier and it is used to convert an interferogram; which measures the optical path difference as a function of space, into a function of frequency, which gives a resultant spectra in wavenumbers. In order to follow the process of FT, the equations which define the algorithm must be understood for both continuous and discrete data. For a signal of uneven undefined length, continuous Fourier transform is used for analysis as it spans from  $-\infty$  to  $\infty$ . This can be seen in equation 3.8<sup>114,110</sup>.

$$X(v) = \int_{-\infty}^{\infty} x(t)e^{-j2\pi vt} dt \quad (3.8)$$

where  $v$  is the frequency term,  $t$  is the time and  $j$  is the imaginary unit.

Here, the first term  $x(t)$  is the function dependent upon time and the second term  $e^{-j2\pi vt}$  is the analysing function. If the detector has the capability to identify continuous frequencies (equation 3.8) it will translate a function in the time domain to a function in the frequency domain, consequently producing a frequency spectrum. However, should the detector be using an ADC, it will be limited to discrete fourier transform (DFT). DFT samples a discrete set of points from  $t = 0$  to  $t = N - 1$ , where  $N$  is the sample number (see equation 3.9)<sup>48</sup>.

$$X(k) = \sum_{t=0}^{N-1} x(t)e^{-j2\pi kn} \quad (3.9)$$

Aside from the set limits used for DFT, the fundamental difference seen between equations 3.8 and 3.9 is the substitution of the frequency over all time ( $vt$ ) continuously with the  $k^{th}$  frequency bin for all samples. The frequency  $v$  and the  $k^{th}$  frequency bin are related via:  $v = \frac{k}{N}$ , with  $N$  as the total number of samples. This equation can be further simplified using Eulers theory to give a result with one part real and the other imaginary (equation 3.10)<sup>48</sup>.

$$X_k = A_k + B_k j \quad (3.10)$$

The result can then be plotted onto an imaginary/real axis to give information on both the sinusoidal amplitude and the phase difference within specified frequency bins. Looking to equation 3.8, the exponential includes an imaginary term, whilst fast fourier transform (FFT) algorithms may use this equation, they may also choose to use the real equations, which are split into both cosine (see equation 3.11) and sine waves<sup>115</sup>.

$$F(v) = \frac{1}{\sqrt{2\pi}} \int_{-\infty}^{\infty} f(t) \cos(2\pi vt) dt \quad (3.11)$$

FTIR spectrometers have the benefit of this algorithm, unlike dispersive spectrometers. This is one of the advantages of using FTIR spectrometers over that of its predecessors for this project.

### 3.2.2.3 Advantages of FTIR

The components within an FTIR spectrometer give it unique advantages over its predecessor legacy dispersive models, these can be summarised in table 3.1.

Table 3.1: Advantages of FTIR over Dispersive spectroscopy

| Advantage | Description  |
|-----------|--|
| Fellgett  | In an FTIR spectrometer all of the wavelengths of light are detected at once, allowing faster acquisition times and a better signal to noise ratio <sup>90</sup> |
| Jacquinot | FTIR spectrometers don't require slits and can therefore achieve a much higher throughput than that of dispersive instruments <sup>90</sup>                      |
| Connes    | The spectral resolution of an FTIR spectrometer is determined by the maximum achievable value of optical path difference(OPD) <sup>90</sup>                      |

These advantages highlight the benefit of using an FTIR spectrometer for sample analysis (of samples with unknown chemical composition). Alongside these advantages, there are variables that require consideration when using FTIR spectroscopy as a measurement tool. One of these is the resolution (see the Connes advantage in table 3.1)<sup>42</sup>.

### 3.2.2.4 Resolution

The resolution of an FTIR instrument is one of the measurement parameters. It relates to the degree of precision with which measurement scans can be taken (the minimum peak interval that can be identified). If an input resolution of  $10 \text{ cm}^{-1}$  is chosen, the spectral resolution will be  $5 \text{ cm}^{-1}$ , this is due to the relationship between the spectral resolution and the OPD from the stationary/moving mirrors in the Michaelson interferometer (see equation 3.12)<sup>29</sup>.

$$\Delta\sigma = \frac{1}{2L} \quad (3.12)$$

where  $L$  is the OPD and  $\Delta\sigma$  is the spectral resolution.

Equation 3.12 states that the resolution of an FTIR instrument is dependent upon the working distance of the moving mirror. The Vertex 80V spectrometer from Bruker used in this project,

has a maximum spectral resolution of  $0.06\text{ cm}^{-1}$ , therefore an approximate OPD max of  $8\text{ cm}$ <sup>133</sup>. For a sample with spectral features that overlap (as seen in this project), a ‘higher’ resolution or smaller incremental wavenumber step must be set in order to distinguish one feature from the other<sup>110</sup>. When increasing the resolution of a measurement scan, the aperture size has to be taken into consideration. With a higher resolution, a greater number of unique band structures can be resolved, therefore the photon flux at the detector must be considered. The relationship between resolution and aperture size determines the intensity of photons at the detector. For example, a wide aperture setting maximizes the output from the IR source and the detector is flooded with signal. Each detector has a saturation point/threshold that if met will produce a resultant spectra of poor resolution. To counteract this, a balance between aperture size and resolution is required to achieve optimal experimental conditions<sup>114</sup>.

### 3.2.2.5 Detectors

In FTIR and dispersive spectroscopy the detector used needs to be responsive to the wavelength region of interest. Different materials are used for detectors for specific wavelength range sensitivity. These materials can be split into three categories: thermal, pyroelectric and photo-conducting. Thermo-couples consist of two junctions made from different metals, the potential difference between the junctions is measured and this value can be translated into a temperature. Pyroelectric detectors are typically made from single crystalline wafers of a material that has pyroelectric properties and are thermal detectors, therefore these detectors are commonly used for room temperature IR thermal measurements<sup>143,110</sup>.

The final type of detector used in spectrometers is photo-conducting, an example of this is mercury cadmium telluride (MCT) which is used as a cryogenic detector (low temperatures)<sup>48</sup>. As the name suggest photo conducting materials conduct a current when exposed to photons with sufficient energy (greater than the materials energy band gap). This however means that the material has to be kept at a low temperature as it is highly sensitive to photon energy. Consequently, MCT detectors are fitted with a small volume dewar for liquid nitrogen to maintain a low temperature. For comparison, the pyroelectric detectors work at room temperature and can be made from materials such as: deuterated triglycine sulfate, or for short (DGTS)<sup>114,8</sup>.

This project used an MCT detector for the measurement of an aqueous polar solvent in the MIR region.

### 3.3 Attenuated total internal reflection (ATR)

Looking back to chapter 2, a colour change reaction was measured and a reaction rate produced. The next step in measuring this reaction was to use FTIR spectroscopy to analyse the vibrational bonds present. However, using the same experimental setup seen in chapter 2 wouldn't work in the spectrometer. One of the reasons this setup wouldn't work in an FTIR spectrometer is that the sample compartment needs to be held at vacuum for the measurement and the current setup wasn't designed to hold a seal. More importantly however is the absorbance of IR light through an aqueous polar solvent (i.e  $\text{H}_2\text{O}$ ). To be able to measure the vibrational frequencies present in an aqueous solvent, the path length of the IR light through the solvent has to be reduced to minimise the large absorbance bands of IR seen in aqueous solutions. One way to achieve this is to use the principles of attenuated total internal reflection (ATR). ATR is an optical technique that, as a product of the Fresnel equations has been proven to produce an evanescent field which gives an effective reduced path length. The evanescent field has unique optical properties that make it a useful tool for detection. Specifically, an amplitude that exponentially decays from the material surface, giving it an effectively reduced path length through the solution and consequently mitigating the issues of IR absorbance seen through aqueous solutions. For the proof of this evanescent field, the Fresnel equations have been expanded in section 3.3.1.

#### 3.3.1 Fresnel Equations

The Fresnel equations describe the behaviour of light at a medium. They were first deduced by physicist Augustin-Jean Fresnel who was one of the first to identify light as a transverse wave. Following the Feynman lectures on physics<sup>37</sup>, the Fresnel equations have been derived.

With the assumption that the model (seen in figure 3.7) is in a homogeneous non-ferromagnetic medium, light incident upon an interface has three different paths of propagation: incident, reflected and transmitted. All three of these paths are plane waves and have respective electric

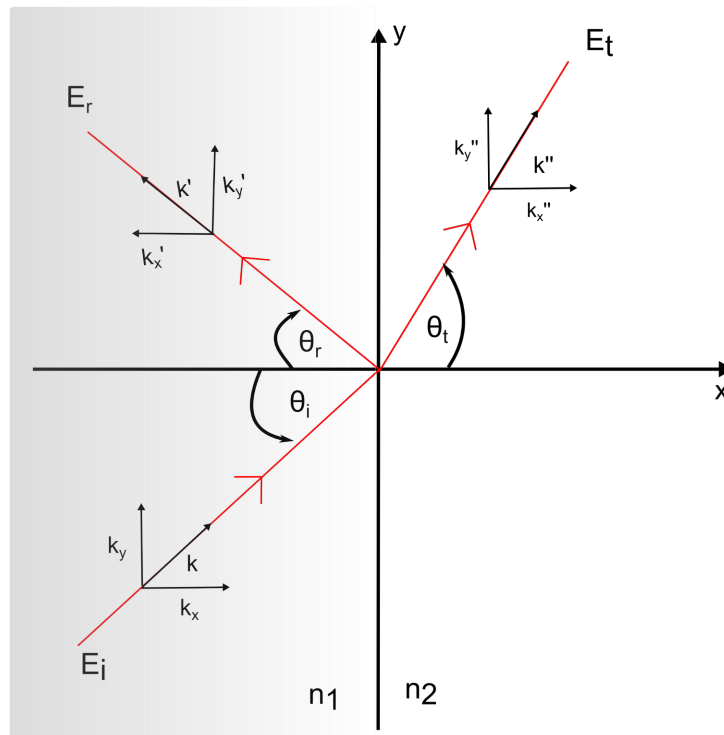


Figure 3.7: Propagation vectors for the incident, reflected and transmitted waves.

fields:

$$\mathbf{E}_i = \mathbf{E}_0 e^{i(\omega t - \mathbf{k} \cdot \mathbf{r})}. \quad (3.13)$$

Where  $\mathbf{E}_i$  is the amplitude at point  $\mathbf{r}$  (from the origin) at time  $t$ ,  $\mathbf{E}_0$  is the amplitude magnitude,  $\omega$  is the frequency and  $\mathbf{k}$  is the wavevector. Since  $\mathbf{k}$  is perpendicular to the  $z$ -axis,  $\mathbf{k} \cdot \mathbf{r} = k_x x + k_y y$ . The reflected wave can therefore be expressed as:

$$\mathbf{E}_r = \mathbf{E}'_0 e^{i(\omega' t - \mathbf{k}' \cdot \mathbf{r})}, \quad (3.14)$$

And transmitted as:

$$\mathbf{E}_t = \mathbf{E}''_0 e^{i(\omega'' t - \mathbf{k}'' \cdot \mathbf{r})}. \quad (3.15)$$

Using Maxwell's equations it can be seen that the  $y$ -component of the electric field  $\mathbf{E}$  is the same on both sides of the boundary (between air and medium)<sup>37</sup>. This gives an equation of:

$$E_{y1} = E_{y2}. \quad (3.16)$$

This displays a relationship between the three waves, and if the boundary conditions satisfy Maxwells' equations a further relationship can be stated:

$$\mathbf{E}_1 = \mathbf{E}_i + \mathbf{E}_r, \quad \mathbf{E}_2 = \mathbf{E}_t, \quad (3.17)$$

and

$$E_i + E_r = E_t. \quad (3.18)$$

Assuming that the  $\mathbf{E}$ -vector of an incoming wave is perpendicular to its propagating vector  $\mathbf{k}$ , the resultant values will depend on the direction (polarization) of the  $\mathbf{E}$ -vector. Therefore, to simplify the derivation only one case of polarization will be observed, p-polarized (parallel). For equation 3.18 to be true; two oscillating terms are equal to a third, all oscillations have to have the same frequency. This leads to the assumption that  $\omega = \omega' = \omega''$ . From this assumption, the wave vector can be treated in a similar manner, the magnitude of the wave vector  $\mathbf{k}$  is given by  $k^2 = \frac{n^2 \omega^2}{c^2}$ , where  $n$  is the refractive index of the medium,  $c$  is the speed of light and  $\omega$  is the frequency<sup>37</sup>.

Looking to equations 3.13, 3.14 and 3.15 and applying the boundary condition of  $x = 0$  the equation gives:

$$k_y'' = k_y' = k_y \quad (3.19)$$

further relationship to consider, seen in figure 3.7 are:

$$\frac{k''^2}{n_2^2} = \frac{k'^2}{n_1^2} = \frac{k^2}{n_1^2}, \quad (3.20)$$

$$\sin \theta_t = \frac{k_y''}{k''} \quad \sin \theta_i = \frac{k_y}{k}. \quad (3.21)$$

By substituting equation 3.19 into equation 3.21 snell's law can be derived:

$$n_1 \sin \theta_i = n_2 \sin \theta_t \quad (3.22)$$

Following Feynman's derivation<sup>37</sup>, the equation for the ratio of reflected wave to incident wave can be calculated:

$$\frac{E'_0}{E_0} = \frac{n_1 \cos \theta_i - n_2 \cos \theta_t}{n_1 \cos \theta_i + n_2 \cos \theta_t} \quad (3.23)$$

For waves at normal incidence, i.e  $\theta_i = 0$  and  $\theta_t = 0$ , equation 3.23 reduces to:

$$\frac{I_r}{I_i} = \frac{|E'_0|^2}{|E_0|^2} = \left( \frac{n_1 - n_2}{n_1 + n_2} \right)^2 \quad (3.24)$$

### 3.3.2 Evanescent field

Following on from the Fresnel equations, the case for total internal reflection was considered. To understand the conditions through which total internal reflection can occur, the critical angle must be considered. The critical angle is a threshold value (of  $\theta_i$ ) which causes the angle of the reflected wave  $\theta_t$  to become  $90^\circ$ <sup>37</sup> to that of the incident . To calculate this value, the formula is as follows:

$$\sin(\theta_C) = \frac{n_2}{n_1}, \quad (3.25)$$

Where  $n_1$  is the refractive index of the crystal and  $n_2$  is the refractive index of the sample.

It can be seen that at sub-critical angles ( $\theta_i < \theta_C$ ) the three plane waves referenced in equations 3.13, 3.14 and 3.15 exist. However, if the angle is super-critical ( $\theta_i > \theta_C$ ), the transmitted wave becomes an evanescent wave. This phenomenon can be explained by the solution to equations 3.19 and 3.20<sup>37</sup> . Substituting these equations together gives:

$$k_x'^2 = \frac{k^2}{n_1^2} - k_y^2 \quad (3.26)$$



where  $k_y = k \sin \theta_i$  and  $k = \frac{\omega n}{c}$

$$k_x''^2 = \frac{\omega^2}{c^2} (1 - n^2 \sin^2 \theta_i) \quad (3.27)$$

If  $n \sin(\theta_i)$  is greater than 1, then  $k_x''^2$  is a negative value, and consequently  $k_x''$  is a pure imaginary, e.g.  $\pm i k_I$ .

Thus the transmitted wave will take the form:

$$E_t = E_0 e^{\pm k_I x} e^{i(\omega t - k_y y)} \quad (3.28)$$

If we consider what this means,  $\pm k_I x$  is a scalar quantity, e.g. an amplitude coefficient that can have both positive and negative values<sup>37</sup>. Firstly, let's consider the positive case  $+k_I x$ , this would relate to an exponentially increasing field. For an exponential increase in energy, there has to be a source, or this term assumes that energy is created through propagation of the material which is not physically possible. This means that physically the only solution is that of  $-k_I$ , which indicates that the evanescent field decays exponentially with distance from the media interface<sup>37</sup>. Thus, the evanescent field can be used as an optical sensor over a specified distance (relating to its penetration depth). To calculate that distance, firstly normalize the electric field amplitude to give :

$$k_I = |k'| \sqrt{1 - \left(\frac{n}{n'}\right)^2 \sin^2 \theta_i} \quad (3.29)$$

Using the equation for the wave vector:

$$|k'| = \frac{2\pi n'}{\lambda_0} \quad (3.30)$$

The decay constant is  $k_I$  and the characterized decay length is the reciprocal of the decay constant:

$$d = \frac{1}{k_I} \quad (3.31)$$

The evanescent field's existence can be therefore proved from the Fresnel equations. As mentioned earlier, the evanescent wave has a specified decaying amplitude which is a function of wavelength, refractive index and incident angle. In addition to this, there are other variables to consider when using this technique. These include: material properties, depth of penetration, multi-reflection vs single reflection and intimacy of the sample and crystal.

### 3.3.3 Choice of ATR material for IR measurements

With the knowledge that ATR can reduce the effective path length of IR light through an aqueous sample, the next question was which material would be best to facilitate ATR in the IR. One of the greatest challenges with this technique is finding a suitable material that is transparent in the IR, so to not affect the results from the solvent at the detector. With this specification there are a select number of solid crystalline materials that are transparent in the IR, these can be seen in table 3.2. Of the materials that are available, each provide unique difficulties. For example, in addition to the tabled materials, there are other materials such as potassium bromide (KBr) however this material is water soluble and therefore not appropriate for measurement. Zinc selenide (ZnSe) is toxic and diamond (C) is expensive. The materials seen in table 3.2 display favourable optical properties in addition to their respective refractive indices. Calcium Fluoride is not only transparent in the near infrared region, but it also extends to the visible so can be used for multi-spectral purposes. Germanium, diamond, silicon and zinc sulphide are all transparent in the IR, inert in water and non-toxic. The one exception to this being Zinc Selenide, which when presented as a bulk solid is non-toxic. However, if it were to be polished/cut the waste is toxic and specific health and safety procedures are required for waste disposal.

This project began by testing some of the materials seen in table 3.2 for chemical stability in water and transmission seen through the materials. The first material tested was that of calcium fluoride ( $\text{CaF}_2$ ). Although it proved chemically stable in water, it was limited to the near infrared (NIR) spectral region and consequently couldn't provide valid information in the MIR which was required. After  $\text{CaF}_2$ , germanium (Ge), silicon (Si) and zinc sulphide ( $\text{ZnS}$ ) were tested; this will be discussed in further detail in chapters 4 and 5.

Returning to the theory of optical total internal reflection (TIR) between two materials, there are two conditions that a system must satisfy in order for the light to undergo TIR. The first condition is that the refractive index of the first material/media must be greater than that of the second, otherwise the light will not totally internally reflect (see equation 3.29). The second condition states that the incident angle of the input light must be equal to, or exceed that of the critical angle. Materials that are frequently used in ATR can be seen in table 3.2<sup>114</sup>.

Table 3.2: Material Properties for ATR application

| <b>Material</b>  | <b>Refractive index (at 6 <math>\mu\text{m}</math>)</b> | <b>Transmission Range (<math>\text{cm}^{-1}</math>)</b> |
|------------------|---|---|
| Calcium Fluoride | 1.3782  | 1000 - 76,900   |
| Germanium        | 4.0094  | 435 - 5,555   |
| Diamond          | 2.3779  | 1000 - 44,444   |
| Silicon          | 3.4202  | 666 - 8,333   |
| Zinc Selenide    | 2.4251  | 476 - 16,666  |
| Zinc Sulfide     | 2.238   | 769 - 10,000  |

### 3.3.4 Depth of penetration

As mentioned previously, the evanescent field has an exponentially decaying amplitude through a solution. The depth with which the evanescent wave propagates can be calculated using equation 3.32<sup>114</sup>.

$$d_p = \frac{\lambda}{2\pi(n_1^2 \sin^2 \theta - n_2^2)^{0.5}}, \quad (3.32)$$

where  $\theta$  is the angle at the media surface and  $\lambda$  is the incident wavelength.

Equation 3.32 shows that for short wavelengths, e.g visible light, there will be a much smaller penetration depth and consequently a weaker transmission as the evanescent waves effective penetration depth is dependent upon wavelength, the angle of incidence and the refractive indices of the respective media<sup>114</sup>. A graphical representation of this equation for the materials zinc sulphide, silicon and germanium can be seen in figure 3.8.

The specifications of penetration depth for each material used, requires a ‘correction’ factor for analysis<sup>114</sup>. This means that for any spectral data taken using ATR crystals, the effective

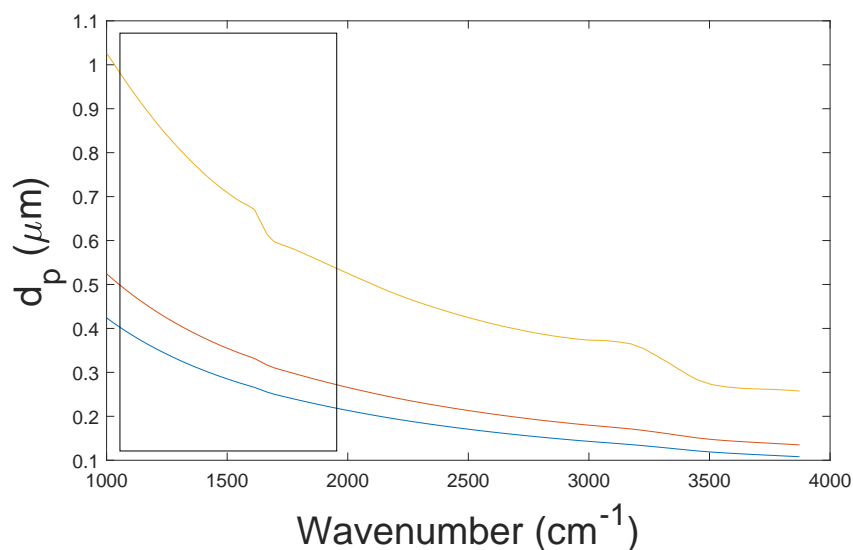


Figure 3.8: Plot of zinc sulphide (yellow), silicon (red), germanium (blue) and their respective effective penetration depths plotted against wavenumber. The black box represents the region of spectral interest in the MIR. This plot shows that ZnS has the greatest effective penetration depth of the three materials, with Si and Ge following a similar trend. The reason that ZnS has a greater penetration depth than both Si and Ge is due to its lower refractive index.

penetration depth at each wavelength has to be accounted for and the resultant spectrum has to be normalised with this correcting factor. Due to this, a user-written programme was written in Matlab to account for this correction factor.

### 3.3.5 Multi-reflection vs single reflection

In addition to the penetration depth, the effective penetration depth is important to consider and can be calculated from equation 3.33<sup>114</sup>.

$$EPL = Nd_p, \quad (3.33)$$

where  $N$  is the number of bounces and  $d_p$  is penetration depth.

This equation states that the effective penetration depth is dependent upon the number of internal reflections (the sum of each instance of TIR). This highlights the importance of a multi-

reflection design, as with an increase in number of reflections there should be a greater signal to noise as the effective path length will have increased<sup>114</sup>. This principle was tested, with a direct comparison between a single and multi-reflection ATR cell, the results can be found in chapter 4. As discussed previously, the penetration depth of the evanescent wave gives it a unique advantage as an optical sensor with tunable detection depth. The distance that the evanescent wave can propagate through a material, depends on the surface intimacy between the sample and the material. For example, if a pocket of air/gas is present between the ATR material and the sample, then the evanescent wave would propagate through the air, seeing it as an additional medium and consequently limiting the effective penetration depth through the top medium (the sample). This project examines a liquid sample which is passed over an ATR material (see table 3.2). Due to the nature of an aqueous sample, the surface intimacy wasn't a concern and the evanescent field was free to penetrate into the aqueous medium. However, should a third medium be introduced (bubbles in the sample), the intimacy between media would need to be further assessed<sup>114</sup>.

### 3.4 Summary

From the previous chapter it was concluded that measuring the colour change of a degradation reaction was of limited value. From this, vibrational spectroscopy was seen to be a better way to understand the chemistry of the reaction. When looking at vibrational spectroscopy, infrared light is used. However, when using infrared light with an aqueous sample, there are a number of challenges that aren't present in visible spectroscopy. The different models of spectrometer were then discussed concluding, that due to the unique advantages that fourier transform infrared (FTIR) spectroscopy has over dispersive spectroscopy, FTIR spectroscopy would be used for this project. Although FTIR has advantages at longer wavelengths, at shorter wavelengths FTIR becomes limited due to the number of points needed for the interferogram. Looking directly at the IR region means that longer wavelengths were required, so FTIR was the more suitable choice for this project. Measuring liquids in IR spectroscopy is difficult, specifically in polar aqueous samples. The absorbance of IR light through aqueous-based solutions is large,

and consequently the path length of the IR light through the sample needed to be reduced. To effectively reduce the path length through the solution, a 1 mm path length flowcell and attenuated total internal reflection cells (ATR) were designed and tested, the results of which can be found in the next chapter.

## 4 Initial optical results and design

In the previous chapter, a reaction rate was measured by recording a visible absorbance over time. The reaction rate was the main result however this setup was designed to explore different parameters of the experiment, i.e the input concentration of methylene blue and the time frame for the reaction. The conclusion from these results was that a colour change reaction provided limited information and IR spectroscopy was required to identify the chemical bonds present throughout the reaction. Before the IR region was tested, the same visible absorbance reaction was measured in the visible region using a Bruker Vertex 80V spectrometer. This reaction was measured using the same parameters as the visible absorbance reaction, with the only difference being the input wavelength.

### 4.1 Visible spectroscopy

Visible sources from the spectrometer produce wavelengths over the full visible region (400 - 700 nm), compared to the red laser diode used previously (near 600 nm). The 1 cm flowcell was placed into the sample compartment of the spectrometer and the reaction was measured in the visible region. Results from this measurement were directly compared to that seen in publication and can be seen in figure 4.2. Figure 4.1 shows a plot of absorbance against wavelength from a publication by Boehme *et al*<sup>17</sup>. This figure shows two visible spectral features at approximately 660 nm and shoulder at 615 nm. The features in the published spectrum show a correlation to the measured data with the same two spectral features displayed. Both the features present in published and measured figures show that the methylene blue molecule displays visible spectral features that disappear over the course of the reaction (as seen in the visible absorbance data).

The nature of this change is unclear from these results as only two features are measured, both of which are outside of the IR region of interest. However, this result does confirm the need to measure the reaction in the IR region to identify the chemical bonds changing over the full reaction.

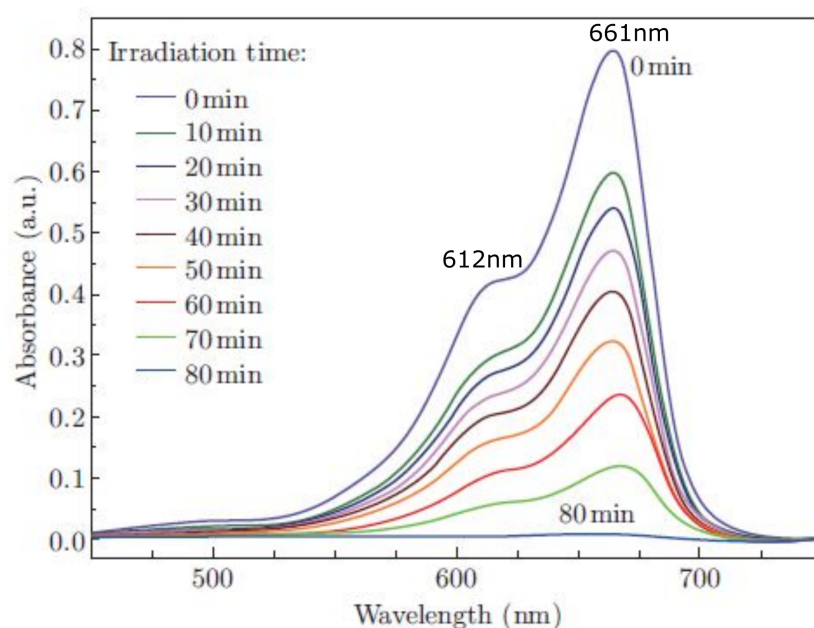


Figure 4.1: Published visible spectra of methylene blue photo catalytic degradation using mixed phase  $\text{TiO}_2$  nano-tubes and irradiated using UV LEDs. A concentration of  $3.12 \times 10^{-5}$  mol/L with reference to 1 g/L of photo catalyst was used. In the visible range of 500 - 750 nm there are two features overlapping creating a shoulder feature. Both peaks degrade over a similar time period<sup>17</sup>.

Although figure 4.2 and figure 4.1 display similar spectral features, the measured spectrum (figure 4.2) appears to show a higher absorbance in the feature at 635 nm than seen in the published graph. This is a consequence of the detectors dynamic range and a high concentration of the input methylene blue causing absorbance that is just greater than the threshold of detection. As the light seen through the flowcell is absorbed at these two frequencies, the electrical noise of the detector is greater than the signal detected at the start of the reaction. A quantitative way to understand the absorbance of the visible light through the methylene blue is to one again look at absorbance. Absorbance can be calculated as the natural log of the ratio of transmitted light (see equation 4.1).



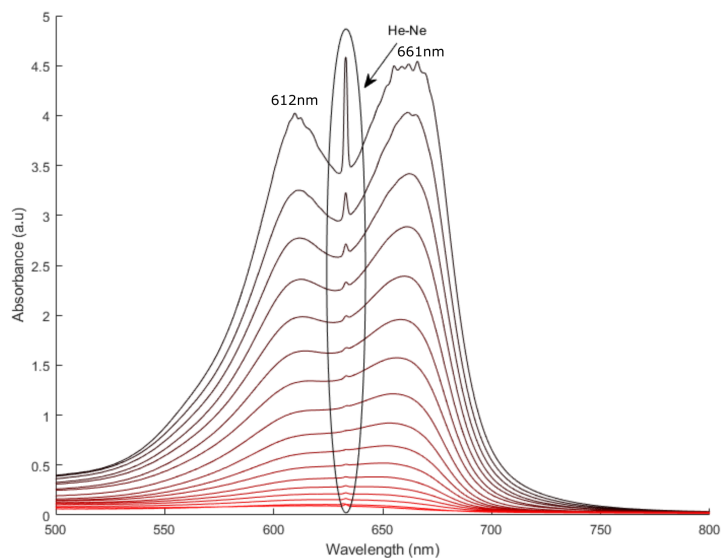
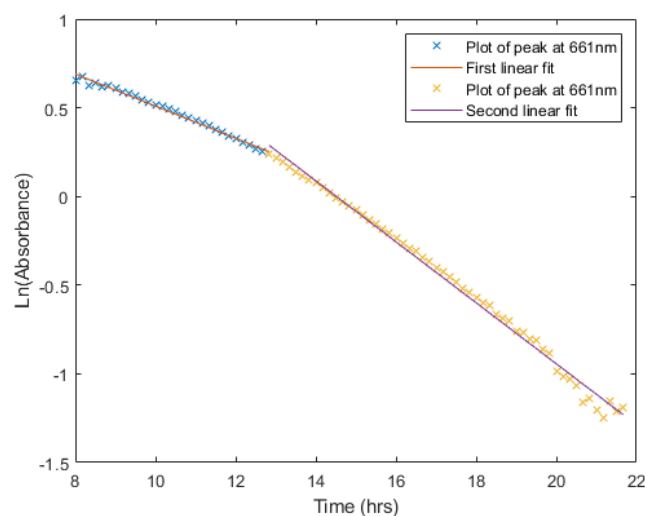


Figure 4.2: Measured methylene blue degradation over a 22 hour period using a millimolar concentration with reference to 0.2 g/L of  $\text{TiO}_2$ . The colour key goes from black at  $t=0$  (after the solution reaches a mixing equilibrium and the UV LED is switched on) to bright red at  $t=\text{end}$ .

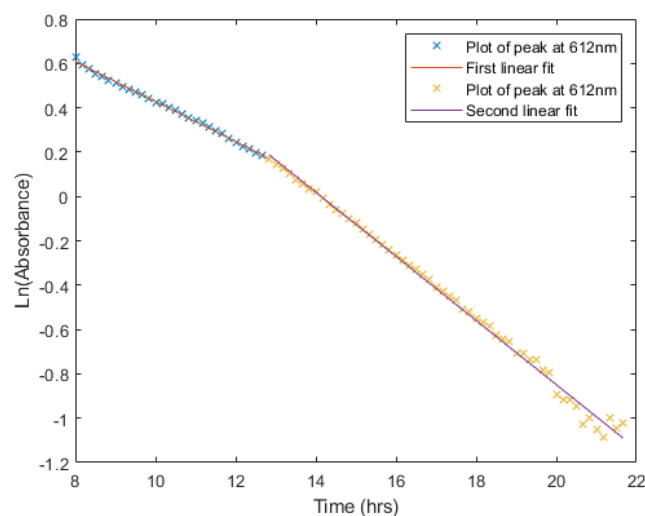
$$A = -\log \frac{1}{T} \quad (4.1)$$

Due to equation 4.1, for an absorbance of 1 a.u. (arbitrary units) 90% of the light is absorbed and for an absorbance of 2 a.u. 99% of the light is absorbed, thus for an absorbance of 4.5 - 5 a.u. there will be 99.99% of the light absorbed. This result explains the weak signal read at the detector for these two frequencies and the presence of electrical noise in the beginning spectra. Aside from the early spectra the peak amplitude for these spectral features was clear and consequently plotted against time to calculate a reaction rate, these result can be seen in figure 4.3.

The calculated reaction rates for the features at 661 and 612 nm were  $4.7 \pm 0.1$  hours and  $5.06 \pm 0.1$  hours respectively. The timescale of these figures starts as 8, as for the first 8 hours water backgrounds were measured using the same macro programme. For the peak seen at 661 nm, this should directly correspond to the visible absorbance data, however to facilitate the flowcell into the sample compartment of the spectrometer, extra piping was included which



(a) Plot of peak amplitude of the visible feature seen at 661 nm against time. The fitting function used for the first linear fit was  $y = -0.17x + 2.49$ , with the second linear fit giving function  $y = -0.09x + 1.41$ .



(b) Plot of peak amplitude of the visible feature seen at 612 nm on a logarithmic scale. The fitting function for the first linear fit was  $y = -0.145x + 2.04$ , with the second linear fit giving function  $y = -0.09x + 1.33$ .

Figure 4.3: Plots of the spectral feature peak amplitude at 661 nm and 612 nm against time. The fits for 661 nm gave an initial decay time of  $5.88 \pm 0.1$  hours, and secondary decay time (after the first 4 hours of the experiment) of  $11.1 \pm 0.1$  hours. The fits for 612 nm gave an initial decay time of  $6.9 \pm 0.1$  hours and a secondary decay time (after the first 4 hours of the experiment) of  $11.1 \pm 0.1$  hours.

could account for the change in reaction rate. Both peaks decay at the same rate, and that confirms that for the new experimental setup (the addition of longer pipes) a reaction rate of approximately 5 hours is expected. To progress this research, the project moved towards analysing the reaction using IR wavelengths, by designing a reduced path length flowcell.

## 4.2 1 mm pathlength flowcell results

In order to optimise the transmission through the sample a new optical unit was designed. Based on the 1 cm flowcell used for the visible absorbance data a 1 mm flowcell was designed and tested to determine whether an increase in transmission through the solution can be detected. The result was taken using a Bruker Vertex 80V FTIR spectrometer held under a vacuum pressure of 8hPa (to remove the IR bands found in the atmosphere from the spectrum). The experimental setup of the spectrometer can be seen in figure 4.5a.

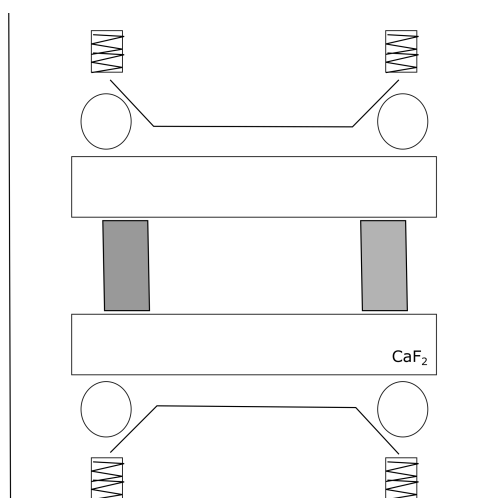
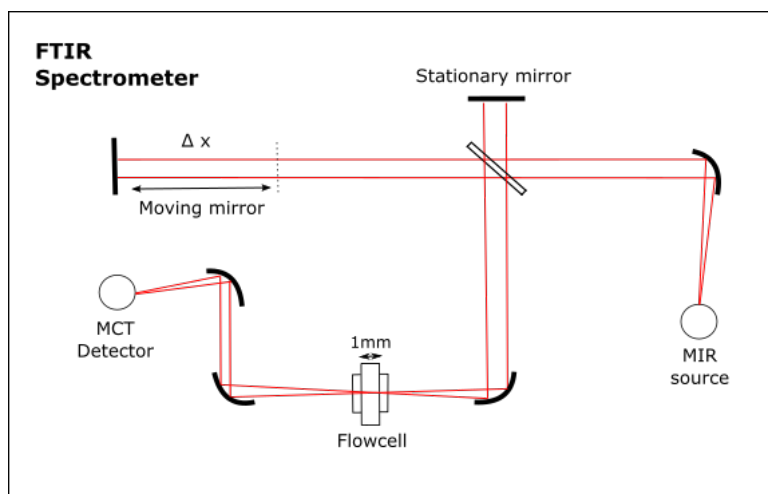


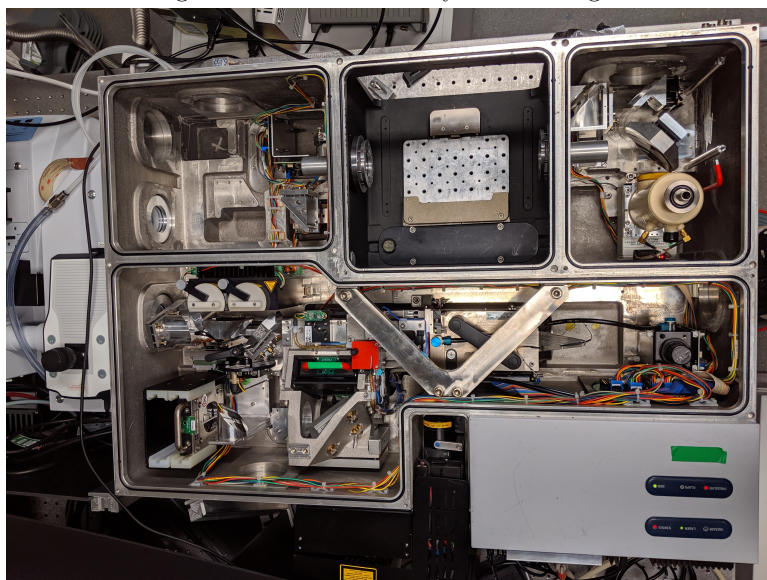
Figure 4.4: Not to scale diagram of the 1 mm path length flowcell. From the inside out, the grey blocks represent 1 mm spacers separating two  $\text{CaF}_2$  windows that are sealed by four O-rings. There are four screw threads that press the O-rings into a sealing position. The unit was made from aluminium and allowed the path length through the solvent to be reduced from the 1 cm flowcell.

The results from this experiment haven't been displayed in this thesis as the spectrum only contained noise. This then lead to the conclusion that a 1 mm flowcell provided a path length that was below the limit of what could be spectrally resolvable. Thus, the method of physically

reducing the path length of IR light through the solution by minimising the flowcell path length wasn't feasible for the resolution required in this experiment. As a result of this, the theory of attenuated total internal reflection (ATR) was considered and a primary ATR unit was designed and tested using  $\text{CaF}_2$  as a test material.



- (a) Diagram of the experimental setup using a 1 mm path-length flowcell inside a Vertex 80V FTIR spectrometer. A light source is passed through a beam splitter which directs the light to both a stationary and moving mirror.



- (b) Image of the inside of the FTIR spectrometer. The sample compartment can be seen as the top centre box. Either side of this box are the detector and the parabolic mirror seen in the schematic diagram respectively. The moving mirror and stationary mirror can be seen in the large open compartment on the bottom of this image.

Figure 4.5: Schematic diagram and photograph of the BRUKER Vertex 80V FTIR spectrometer.

### 4.3 Water absorptivity

As mentioned in the previous chapter, one of difficulties with measuring aqueous solutions in the IR region is the water absorption. To quantify this, a plot of water absorption co-efficient again wavelength can be seen in figure 4.6. The region of spectral interest for this project lies between 6 and 12  $\mu\text{m}$ , this can be otherwise known as the fingerprint region. Looking at figure 4.6, the absorptivity per metre ( $\text{m}^{-1}$ ) of water in this region is an average of  $10^5$ , whereas the absorptivity in the visible region is on average  $10^{-1}$ . This clearly displays the difficulty with measuring aqueous solutions in the IR region. In order to measure an aqueous solution in the IR, the path length of the light through the sample has to be considered, leading back to the Beer-Lambert law. The Beer-Lambert law shows that the absorption is proportional to the path length if the other parameters of the equation (molar absorption co-efficient and the concentration of the water) remain constant. This was explored experimentally by changing the flowcell path length.

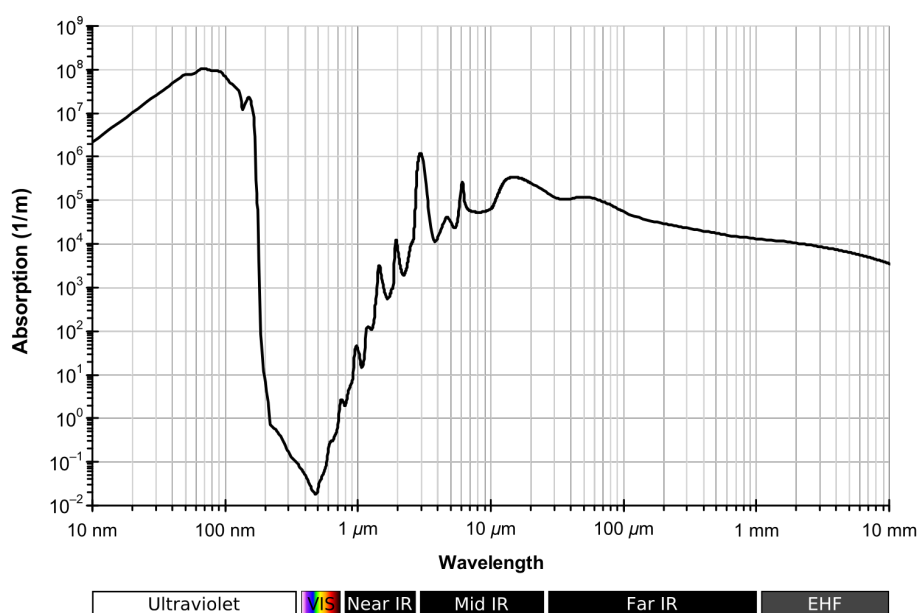


Figure 4.6: A graph to show the absorption of water measured over the IR spectrum. The MIR region of interest is between 6-12  $\mu\text{m}$ , and as can be seen from the graph, this region shows high absorption for water<sup>16</sup>.

From the previous experimental setup (figure 2.23), the flowcell used had a 1 cm path length.

Using the Beer-Lambert Law, the output signal for a 1 cm path length cell at a single wavelength of approximately 8  $\mu\text{m}$  gives an absorbance of  $10^3$ . Scaling down to a 1 mm path length, the same calculation gives a result of  $10^2$ . Continuing to scale down to a 1  $\mu\text{m}$  path-length, at a wavelength of 8  $\mu\text{m}$  the absorbance through the sample would be  $10^{-1}$ . These figures show that for an aqueous solution to be measured in the IR region, a thin capillary cell with a path length of 1 mm is at the limit of detection and to be able to maximise the transmission seen through the sample, a 1  $\mu\text{m}$  path length flowcell should be used. However, the manufacture of a 1  $\mu\text{m}$  path length flowcell proved difficult. So, a 1 mm path length flowcell was designed and tested with water (see figure 4.4). The results from this flowcell haven't been included as the weak signal to noise ratio resulted in a spectrum with no spectral features and dominated by noise. Based on the Beer-Lambert law calculations, this would explain why 1 mm path length flowcell produced a weak transmission through the solution. A further consideration in this experiment is the ratio of methylene blue to water molecules. For example, with a millimolar concentration of methylene blue further dissolved into 150 ml of de-ionized water, there are  $3.613 \times 10^{19}$  molecules of MB and  $5.0127 \times 10^{24}$  molecules of deionized water. Without the assumption that methylene blue molecules bond with a water molecule to become methylene blue hydrate, these figures identify that there are a greater number of water molecules to those of methylene blue. The ratio of methylene blue molecules to water molecules is approximately 0.0007 %. This value is extremely low, highlighting the difficulty in this measurement and the need for an optical technique with good resolution and sensitivity to detect the degradation reaction.

## 4.4 Attenuated Total Internal Reflection (ATR)

Attenuated Total Internal Reflection is an optical measuring technique that was first discussed in N.J.Haricks book entitled: Internal Reflection Spectroscopy<sup>54</sup>. ATR uses the principles of total internal reflection combined with the Fresnel equations to minimise the effective pathlength through a sample. For example, as seen in section 3.3.1 of chapter 3, the Fresnel equations are used to identify what happens when light interacts with media/material. The Fresnel equations

state that if light is incident upon a material with an angle greater than that of the critical angle, the light will be completely/totally reflected at the material surface. Intuitively, all of the energy from the input wave should also be reflected, however the Fresnel equations state that there always has to be a transmitted wave (due to the boundary conditions). Following the derivation of this transmitted wave, it shows that the transmitted wave is called the evanescent field. The amplitude of the evanescent field is smaller than that of a micron-scale flowcell, however this technique can be optimised and doesn't provide the same manufacturing difficulties, thus it was used.

#### 4.4.1 ATR calculations

For total internal reflection (TIR) through an optical material, the incident angle that light meets the surface at must exceed that of the critical angle (see section 3.3.1). The critical angle is expressed in equation 4.2,

$$\theta_C = \arcsin \frac{n_2}{n_1}. \quad (4.2)$$

When modelling light interactions with materials, ray tracing and trigonometry are the tools that were used. The model used to calculate each polishing angle was based on optical windows of each material that were 25×4 mm in diameter and thickness respectively (see figure 4.7). Once these models had been confirmed and error checked, the polishing units (designed with a polishing angle specific to each material) were manufactured and a lapping machine was used to hand polish each window to the calculated ATR angle.



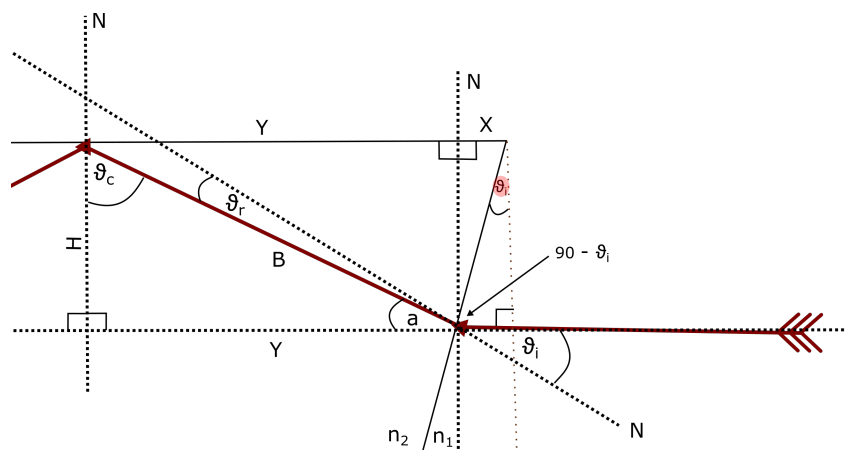


Figure 4.7: Schematic diagram to show the trigonometric calculations for the desired polishing angle to achieve total internal reflection for windows of specific optical materials. Where  $N$  represents the normal,  $n_1$  and  $n_2$  represent the respective refractive indices,  $\theta_i$  and  $\theta_r$  represent the incident and reflected angles and  $\theta_c$  represents the critical angle. The angle highlighted is the desired polishing angle, which equates to the incident angle  $\theta_i$ . The dotted red line is the initial shape of the optical window before polishing, this can be seen in figure 4.8.

The trigonometric model seen in figure 4.7 was applied to each optical material used within this project. The model makes an assumption about how much material will be removed through polishing to give a value of  $Y$ . This value can then be confirmed from the calculated value of  $\theta_i$  in post-calculation checks. For each material there were different values for  $\theta_i$ , as the value of refractive index of each material differs. From this model, an initial window was polished to facilitate a single internal reflection using calcium fluoride ( $\text{CaF}_2$ ), see figure 4.8.

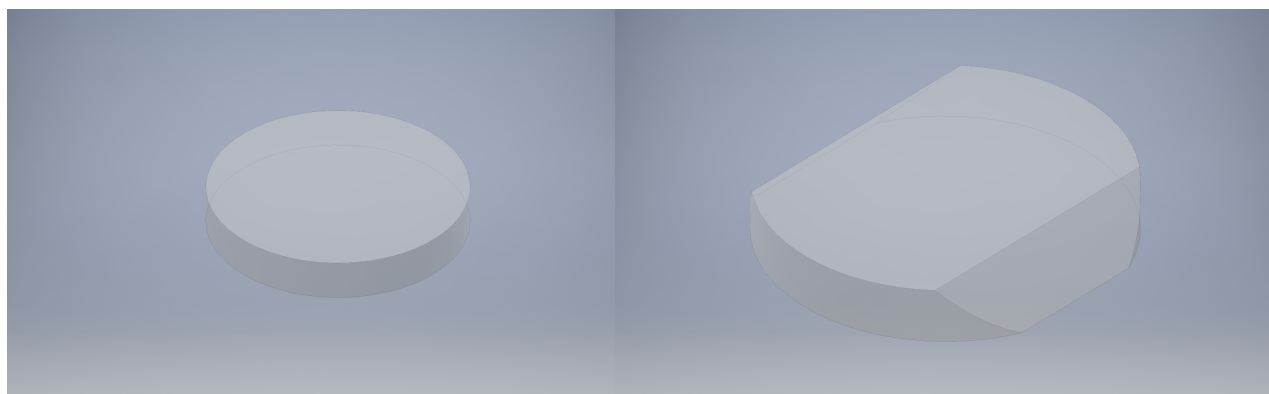


Figure 4.8: Two 3D models of a calcium fluoride  $\text{CaF}_2$  window before and after polishing respectively.

#### 4.4.2 Single reflection ATR

Once the mathematical models had produced values for polishing angles, the design of the ATR units were created using modelling software (Autodesk Inventor). But before the ATR units could be designed, the specifications for them were decided upon. The design for the ATR units had two key specifications; they must hold a seal under vacuum and they must optimise the surface area in contact with the sample. The first specification was required due to the nature of the experiment, as IR spectroscopy is a sensitive optical technique, environmental factors aside from the sample being measured must be contained. To remove environmental features from the final spectrum (water vapour and gas lines), the spectrometer is kept under a vacuum of 8hPa during measurements. In addition, two KBr windows were used to isolate the sample compartment from the interferometer compartment. KBr is a hygroscopic material, so any water leaks from the ATR units would damage the windows and ultimately the experiment. To ensure that the ATR units could hold a seal, once manufactured they were fitted with appropriate seals and pressure-tested outside of the spectrometer to check for water leaks. The second condition relates to the signal seen through the ATR crystals (polished windows). The evanescent field has an exponentially decaying amplitude and therefore a tunable detection region. Although increased sensitivity is an advantage in this project, the maximum penetration depth of the evanescent field for this project was a maximum of 10  $\mu\text{m}$ , thus making the signal to noise ratio of this optical technique only fractionally greater than that of 1 mm pathlength flowcell. However, unlike the thin flowcell technique, ATR can be optimised to increase the signal to noise transmission through the ATR crystal by incorporating multiple total internal reflections. To begin with, a simple single reflection unit was designed which used  $\text{CaF}_2$  as the material. The design for the  $\text{CaF}_2$  polishing unit can be seen in figure 4.9.  $\text{CaF}_2$  was chosen as the first material to test due to its favourable optical properties in the visible and infrared region (see table 4.1).

Table 4.1: Optical properties of  $\text{CaF}_2$ 

| Transmission range ( $\mu\text{m}$ ) | Refractive Index (at 5 $\mu\text{m}$ ) | Solubility (g/ 100g of water) |
|--------------------------------------|--|-------------------------------|
| 0.13 to 10                           | 1.399 08                               | 0.0017                        |

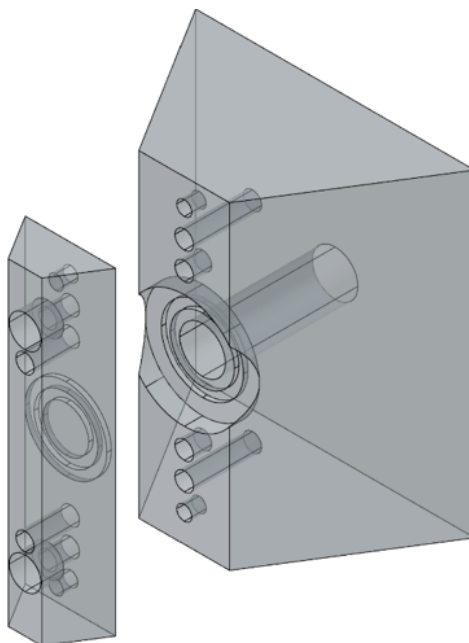


Figure 4.9: A 3D model of the first  $\text{CaF}_2$  single reflection ATR unit. A central groove was designed to hold the  $\text{CaF}_2$  polished window with O-rings in contact with both crystal surfaces. It was designed to ensure that both faces of the window could hold vacuum. The central bore was designed to hold a volume of the solution, this was in direct contact with the crystal face. It was also isolated with a plug design that held it at vacuum minimising water leaks.

#### 4.4.2.1 $\text{CaF}_2$ single reflection ATR

The  $\text{CaF}_2$  ATR polishing unit was designed for multi-purpose use; it was initially used to polish a window to a specified angle and then further used to house the ATR polished window and a sample volume for static visible/IR measurements. The first experiment using the  $\text{CaF}_2$  ATR unit was a simple observation of a He-Ne laser through the crystal. As the  $\text{CaF}_2$  material is transparent in the visible region, the He-Ne could be seen totally internally reflecting through the crystal and coming through the other side. By optically observing the red He-Ne light undergoing ATR through the  $\text{CaF}_2$  ATR crystal, a further experiment measuring deionised

(DI) water (placed in the volume behind the crystal face seen in figure 4.9) was undertaken. The results can be seen in figure 4.10. The figure shows a sharp peak in penetration depth at approximately  $1620\text{ cm}^{-1}$ , another more prominent peak at approximately  $2100\text{ cm}^{-1}$  and a final peak at  $2280\text{ cm}^{-1}$ . To correlate this data to the refractive index (figure 5.3) of  $\text{CaF}_2$  at these wavenumbers, it can be seen that the refractive index of water is very close to meeting that of  $\text{CaF}_2$  just before these wavenumber peaks. This suggests that at these points TIR has not occurred. Thus, the corrected spectrum displays different features to that of the raw spectrum. This result, in addition to  $\text{CaF}_2$ 's limited transparency in the IR region concluded that this material wasn't suitable for IR measurements. The correction factor used in figure 4.10 is the materials penetration depth.

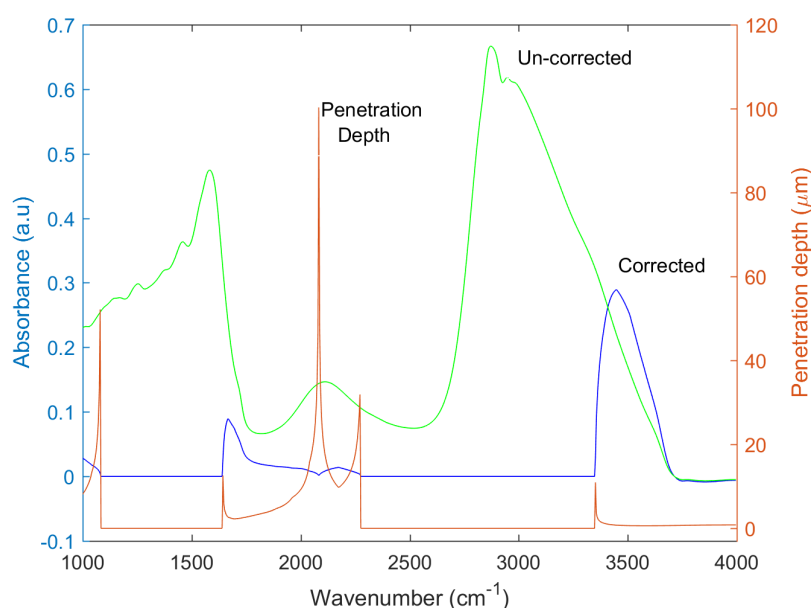


Figure 4.10: Deionised water absorbance spectrum using  $\text{CaF}_2$  ATR crystal, overlaid with  $\text{CaF}_2$  penetration depth and uncorrected water spectra (Corrected = Uncorrected/Penetration Depth). This graph shows that for a majority of the IR region,  $\text{CaF}_2$  has an effective penetration depth of 0, this is due to its refractive index being too close to that of water.

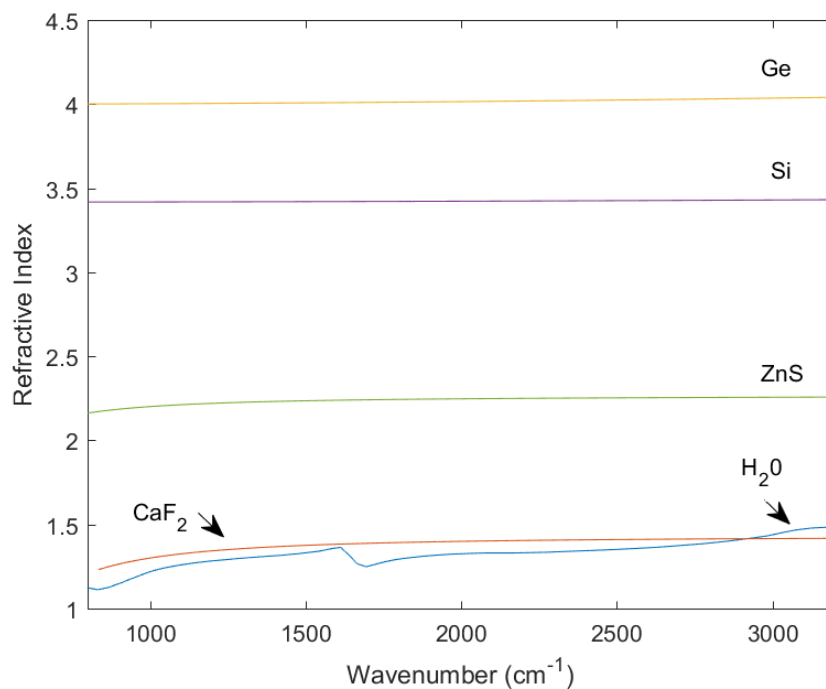


Figure 4.11: Refractive index over the MIR region for  $\text{CaF}_2$ , Ge, ZnS,  $\text{H}_2\text{O}$  and Si.

The result from figure 5.3 show that for TIR to occur in an IR transparent material, its refractive index must be at least 1.5 times greater than that of water. From this, alternative IR transparent optical materials were tested. With the pathlength through the sample significantly reduced using ATR as a technique, each proposed material was then further analysed. Due to the limitations of using  $\text{CaF}_2$  for IR measurements, the next material tested was Germanium (Ge). The refractive index of Ge is almost 3 times greater than that of  $\text{CaF}_2$ , which meant the calculated polishing angle of the window was far shallower. Figure 4.12 shows both the  $\text{CaF}_2$  and Ge polishing units next to one another; the main difference in design between these units is polishing angle which is unique to each materials based on their refractive index (see figure 3.32 in chapter 3).

From the  $\text{CaF}_2$  design, the Ge ATR unit was modelled, manufactured and tested. The result from the single reflection Ge ATR unit highlighted that the signal seen through the ATR crystal needed to be increased. The first technique used for increasing the signal was to increase the gain on the signal channel for the spectrometer. Whilst this boosted the signal, it also enhanced

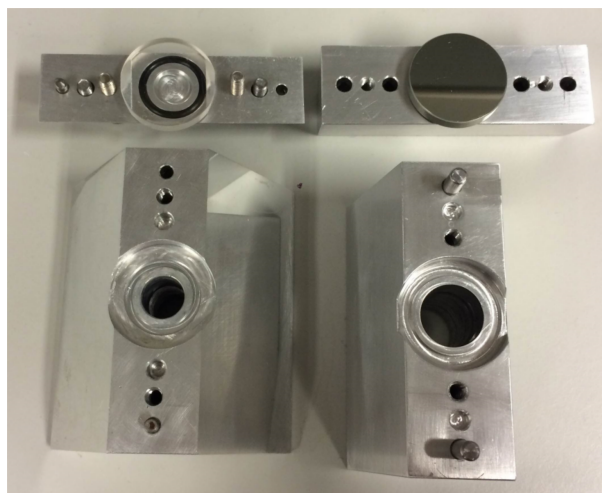


Figure 4.12:  $\text{CaF}_2$  (L) and Ge (R) single reflection units. The  $\text{CaF}_2$  unit displays a wider design and therefore a shallower polishing angle compared to that of the Ge unit whose higher refractive index correlates to a shallower design and broader polishing angle.

the noise and was therefore not an appropriate method for optimization. The next technique was to introduce a  $3.6\text{ }\mu\text{m}$  long pass filter in front of the ATR unit to remove unwanted spectral information and optimize the region of interest. This method increased the signal, but not enough to resolve spectral features. Consequently, the calculations for ATR measurements were revisited, and the effective path length through the ATR units were calculated. The effective path length (as described in chapter 2) states that the number of points of reflection through the crystal linearly increases the effective depth of penetration of the evanescent wave. From this, multi-reflection ATR units were modelled, manufactured and tested.

## 4.5 Multi-reflection ATR sensitivity

Based on the theory of effective path length (EPL) (equation 3.33), multi-reflection crystals (up to 3 reflections) allow an increase in the signal seen at a detector. Figure 4.13a represents a simple ray diagram for a crystal undergoing 1,2 and 3 internal reflections.

Figure 4.13 is not to scale, as for the same material ATR crystal, each increase in the number of internal reflections would result in a change of polishing angle. With reference to figure 4.7, the geometry of the single reflection unit identifies a single reflection at one face. The design

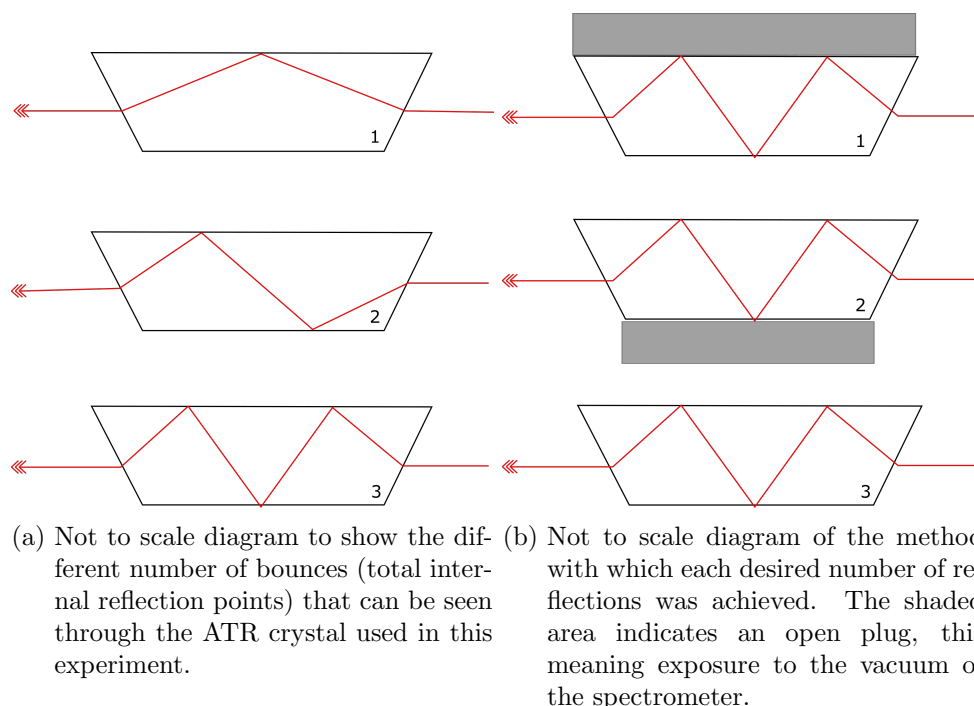
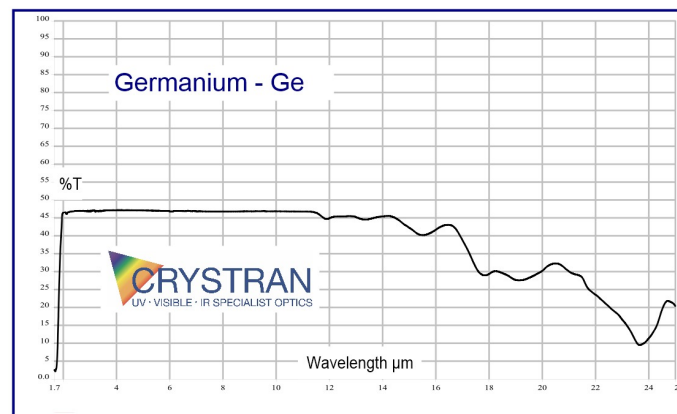
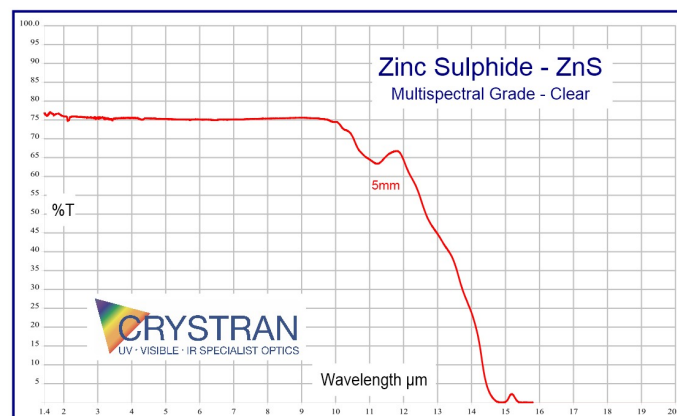


Figure 4.13: Diagram to represent the desired internal reflections (L) and the method with which each reflection was achieved (R).

of the multiple reflection units; in this case multiple reflections combined with appropriate plumbing, were modelled just as the single reflection units were, with the same assumption of distance  $Y$  (which again, was verified with further calculations). The benefit of having multiple reflections is that one face can be isolated from the other to create an effective 1, 2 or 3 reflection unit. The theory of effective path length (EPL) states that the signal seen through the ATR crystal will linearly increase with number of internal reflections, this was then experimentally tested using both Ge and ZnS multi-reflection units (material spectrum for each can be seen in figure 4.14). The reasoning behind testing ZnS was due to a chemical stability issue what arose from using Ge (described in more detail in chapter 5.4). The ZnS multi-reflection crystal was tested in the same experimental setup that can be seen in figure 4.5a with the flowcell replaced with the ATR unit.



(a) Germanium material transmission spectrum over the IR region as published by Crystran<sup>32</sup>.



(b) Zinc sulphide material transmission spectrum over the Vis/IR region as published by Crystran<sup>32</sup>.

Figure 4.14: Material transmission spectra of both germanium and zinc sulphide as published by Crystran<sup>32</sup>.



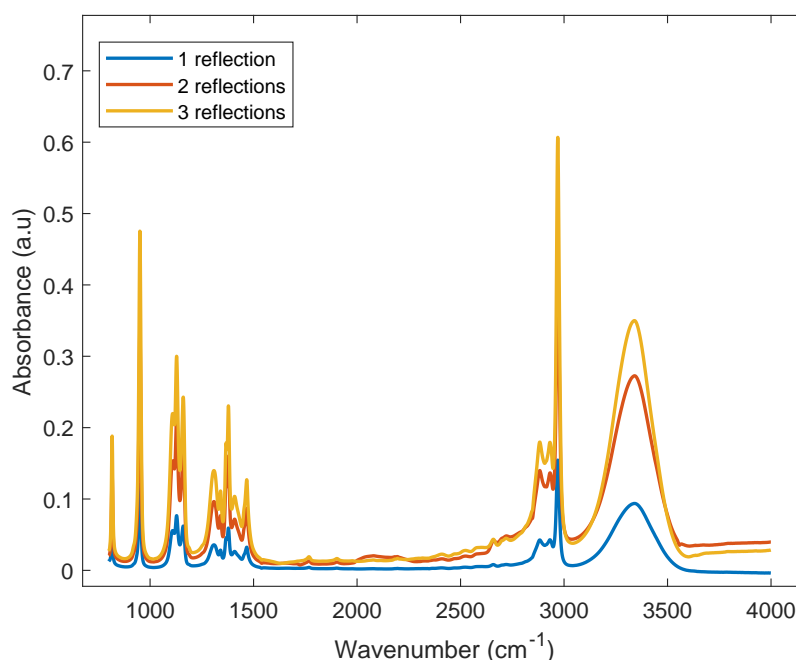
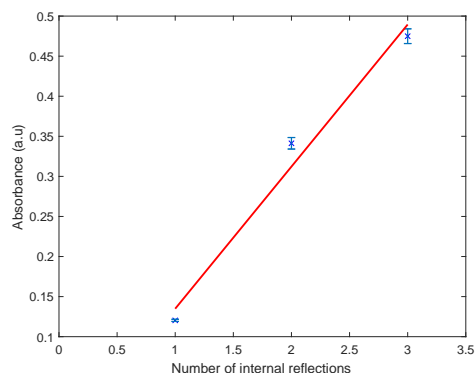


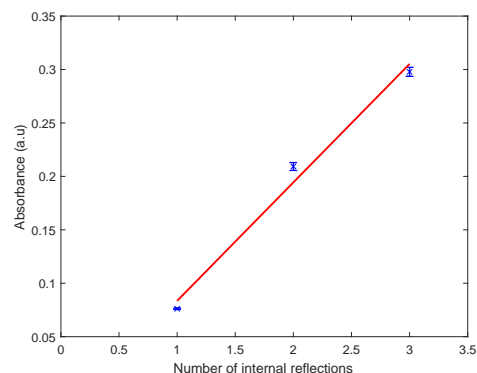
Figure 4.15: Graph to show the averaged change in signal from single to multiple internal reflections inside a ZnS ATR crystal. The control sample used was IPA.

The natural progression from Ge was ZnS due to its material spectrum, which illustrated no spectral features over the region of interest (fingerprint region). Finding a material that is transparent in the IR region, non-toxic and water insoluble proved difficult but zinc sulphide was the final material tested (amongst others) in an ATR unit. For the experimental results seen in figure 4.15, the zinc sulphide crystal was used. To minimise the variable changes between measurements (1 to 2 to 3 reflections) a control sample was used; isopropyl alcohol (IPA). IPA was used as it has a clearly defined IR spectra that has been well documented for comparison for each reflection measurement. The results for the IPA infra-red spectrum for 1, 2 and 3 reflections can be seen in figure 4.15. Figure 4.16 shows the peak amplitude absorbance values at the three most prominent spectral features in the IPA spectrum. The results from 1, 2 and 3 reflections (seen in figure 4.15) displayed the same spectral features, with the three most prominent peaks consistently at  $951\text{ cm}^{-1}$ ,  $1129\text{ cm}^{-1}$  and  $3327\text{ cm}^{-1}$ . Looking at figure 4.15 it is clear that there is an increase in signal with more reflections through the ATR crystal.

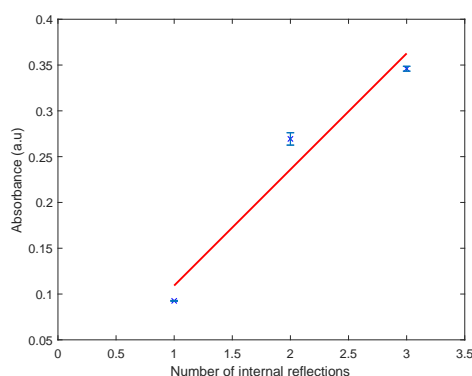
However, to understand the relationship between data sets, the peak amplitudes at the three most prominent features were plotted and analysed.



(a) Peak height at 951 cm<sup>-1</sup>



(b) Peak height at 1129 cm<sup>-1</sup>



(c) Peak height at 3327 cm<sup>-1</sup>

Figure 4.16: Single to multi-reflection data which displaying a linear trend on all peak amplitudes. Thus, demonstrating the theory of effective path length.

The first spectral feature seen at 951 cm<sup>-1</sup> shows a linear trend. Following this peak is the feature at 1129 cm<sup>-1</sup>, whose line of best fit follows the same overall linear trend. The final graph shows the feature at 3327 cm<sup>-1</sup> which is part of a broad feature seen between 2800 and 3000 cm<sup>-1</sup>. The fit of the peak seen at 3327 cm<sup>-1</sup> is outside of the error bars but still displays an overall linear trend. The error bars seen plotted are the standard deviation of the number of spectra measured. These results were measured a varying number of times for each reflection which means that the standard deviation of the 2 and 3 reflection data is larger than that of the 1 reflection. This is because the 1 reflection data has a larger sample size than that of either 2 or

3. Should this measurement be repeated an equal number of measurements would be taken for each reflection. However, these three figures confirm the theoretical linear relationship between number of internal reflections and effective path length of the evanescent wave. The reason that these figures display a poor linear fit to the data points is due to a baseline shift. When changing the effective number of internal reflections (see figure 4.13) the full apparatus was cleaned, however possible residue IPA or cleaning solutions could have remained on the face of the ATR crystal which could have an affect on the baseline for this experiment. This point is confirmed by analysing figure 4.15 where the baseline movement between 1,2 and 3 reflections is clear, leading to the possibility of a systematic error. Another possible cause of this effect could be due to a temperature change over the experiment, causing an overall baseline shift which would affect the peak amplitudes measured. Overall however, the results confirm theoretical predictions that an increased number of internal reflections consequently increases the effective path length of the evanescent wave through the sample, which in turn increases the signal seen through the ATR unit.

## 4.6 Summary

In chapter 3 a degradation reaction using  $\text{TiO}_2$  as the photocatalyst and methylene blue as a simulation pollutant was measured in a visible absorbance experiment. This experiment resulted in a reaction rate and the natural progression from this was to identify the reaction chemistry by using FTIR spectroscopy. The first measurement taken in this chapter was to confirm the reaction rate calculated by the visible absorbance experiment. To do this, a visible spectroscopy experiment was recorded and the spectral features seen in the visible were analysed for comparison with the visible absorbance data. The results from this experiment confirmed that the reaction had an average reaction rate of 5 hours which was similar to previous results, but cannot be directly compared as the experimental setup changed to accommodate longer pipe fittings. Progressing from this data to infrared measurements meant that the Beer-Lambert law had to be re-considered. The Beer-Lambert law shows that the absorbance through a sample is proportional to the path length, if the other parameters of the equation remain constant. In

the previous experiment a 1 cm flowcell had been used, this path length was substituted into the Beer-Lambert law and the result showed that the absorbance value through water was below the limit of detection. Down scaling to a 1 mm path length however, gave a result that would be on the limit of detection. So, a 1 mm path length flowcell was designed and tested. The results from this flowcell showed that the absorbance through this path length were too close to the threshold for detection and concluded that a narrower path length would be desirable, but the manufacturing difficulties meant this wasn't possible. As a result of this, alternative optical technique was considered that used the principles of attenuated total internal reflection (ATR).

The first ATR model was designed using basic trigonometry to identify a polishing angle for windows of different optical materials, with the first material as  $\text{CaF}_2$ . One of the reasons for  $\text{CaF}_2$  was due to its transparency in the visible region. The benefit of transparency in the visible is that a laser could be directly shone through the crystal and the internal reflections could be optically observed. From optical confirmation that the calculations and model were correct, the  $\text{CaF}_2$  ATR crystal was measured in the IR region. The results of this experiment concluded that  $\text{CaF}_2$  was a poor material for this project, as its transparency was limited in the IR region, and its low refractive index created difficulty when using samples of similar refractive index. Moving on from  $\text{CaF}_2$ , three more materials were modelled and tested, germanium (Ge), silicon (Si) and zinc sulphide ( $\text{ZnS}$ ). These materials displayed a clear transparency over the full IR region and had high refractive indices (4, 3.4 and 2.2 respectively). In addition to the single reflection models that had previously been designed and tested, multiple reflection models were made. The theory of effective path length and its linear relationship with the number of internal reflections was experimentally tested and proven. The next stage in this project was to identify which materials were transparent in the IR and could be used for the final chemical degradation measurement. Each material was selected for its optical properties and its chemical stability. To confirm the design for each multi-reflection ATR unit, each ATR crystal was used to measure simple solvents for their identifiable spectral fingerprints. The results for the materials germanium (Ge), silicon (Si) and zinc sulphide ( $\text{ZnS}$ ) can be found in the next chapter.

## 5 Vibrational modes using ATR materials

This chapter focuses on three materials used as ATR crystals, these include germanium (Ge), silicon (Si) and zinc sulphide (ZnS). Each material was measured in the IR to identify its unique material spectral features. Following this experiment, the materials were used to identify simple solvents spectrally and in doing so ,create a spectral catalogue which was used in the analysis of the degradation reaction data (seen in the final results chapter). The materials were tested for their optical properties in addition to their chemical stability, to discover which material would be used for the real-time degradation measurement. Before measuring the crystal features, a review on vibrational modes has been included in order to understand the spectral results obtained throughout this chapter.

### 5.1 Vibrational Modes Background

This topic has been briefly covered in the Background Theory chapter, however a review on the topic of vibrational modes has also been included here to give the results stated context. The MIR region of the IR spectrum is where the molecules within a sample experience vibrational motion. The MIR region can be split into two main groups; the functional group and the fingerprint region. The fingerprint region spans  $400 - 1050 \text{ cm}^{-1}$  and the functional group extends from  $1000 \text{ cm}^{-1}$  to  $4000 \text{ cm}^{-1}$ . The fingerprint region; as labelled, identifies unique vibrational frequencies of bending vibrations for each molecular bond (fingerprints)<sup>27,9,116</sup>. The functional group typically presents fewer spectral features as the modes that are common to this region are typically stretching vibrations and overtones of the frequencies seen in the fingerprint region<sup>118</sup>.

As mentioned in section 3.1, there are three movements that an excited molecule experiences: vibrational, rotational and translational however this project focused on the vibrational modes within molecules. When analysing vibrational movement of a molecule, the terminology of normal modes is used. Normal modes are used to describe the different vibrational motions in molecules. Each mode has a different type of motion and an associated symmetry<sup>23</sup>. Group theory is a useful tool to determine what symmetries the normal modes contain and can therefore predict if these modes will be IR/ Raman active. Character tables are used in group theory to determine the symmetry of all possible motions, which are then assigned to rotation, translation and vibration. The procedure for this begins with assigning x,y,z coordinates to each atom, then determining how each axis transforms for every class of symmetry operation in the group, sum the characters in each case and then refer to the character table to deduce what each molecule's vibrational modes could be. Group theory can be used to predict vibrational modes and then further identify which of those modes will be IR/Raman active. For a diatomic molecule to be IR active, it has to have a non-zero value of change in dipole moment (with respect to a change in bond distance), and have a vibrational frequency resonance within the IR region<sup>23</sup>.

Group theory is good for theoretical calculations of vibrational modes, however another way to model vibrational motion in molecules is to simply treat a diatomic molecule as two masses connected by a spring. When modelling masses on a spring, Hooke's law can be used (equation 5.2), this fundamental physics principle is dependent upon two variables, the material's spring constant and the reduced mass. In the case of diatomic molecules, the spring constant can be used to model the vibrational frequency of the bond and the reduced mass is used, which can be expressed as in terms of the individual atomic masses  $m_1, m_2$ ,

$$\frac{1}{\mu} = \frac{1}{m_1} + \frac{1}{m_2}. \quad (5.1)$$

The reason the reduced mass is used here is to maintain the centre of mass for a molecule (which will be unaffected by the vibration of the molecule). The reduced mass of a molecule will be affected if an atom in a molecule is changed to an isotope, in which case the mass number of that atom will change and therefore so will the reduced mass. This in turn affects

the vibrational modes of the molecule as it is used to calculate the vibrational frequency of the molecular bonds. The vibrational frequency of the bond can be modelled using,

$$\tilde{\nu} = \frac{1}{2\pi c} \sqrt{\frac{K}{\mu}}, \quad (5.2)$$

where  $c$  = speed of light ( $\text{m s}^{-1}$ ),  $K$  = force constant ( $\text{cm}^{-1}$ ) and  $\mu$  = reduced mass (kg).

The vibrational frequency of a diatomic molecular bond can be modelled using equation 5.2 if the bond length is known. This calculation is one way to identify the vibrational frequency for each bond within a molecule, however when analysing polyatomic complex molecules, this quantitative method becomes problematic. Based on the model of two atoms attached by a spring, molecular bond frequencies can be calculated giving each atom a molecular fingerprint. These frequencies are commonly found in a section of the infrared region called the fingerprint region. An alternative way to identify bond frequencies is experimentally. To experimentally determine molecular bond frequencies, infrared light is passed through the material and the molecular bonds present will absorb their respective resonant frequencies. With a combination of the experimental spectrum and quantitative predictions (using equation 5.2), simple molecular bonds can be identified from their fingerprint in the MIR region. To test this theory, solvents with simple chemical compositions were measured to identify their frequency response using FTIR spectroscopy.

## 5.2 Experimental Setup

Following the results seen in previous chapters, this experiment used a static system for measurement. The ATR polishing unit designs were applied to all materials and the ATR crystals were placed in the sample compartment which can be seen in figure 5.1. The measuring instrument used was a Bruker Vertex 80V spectrometer, and the ATR crystals were aligned in the spectrometer using holder designs that haven't been included in this thesis.

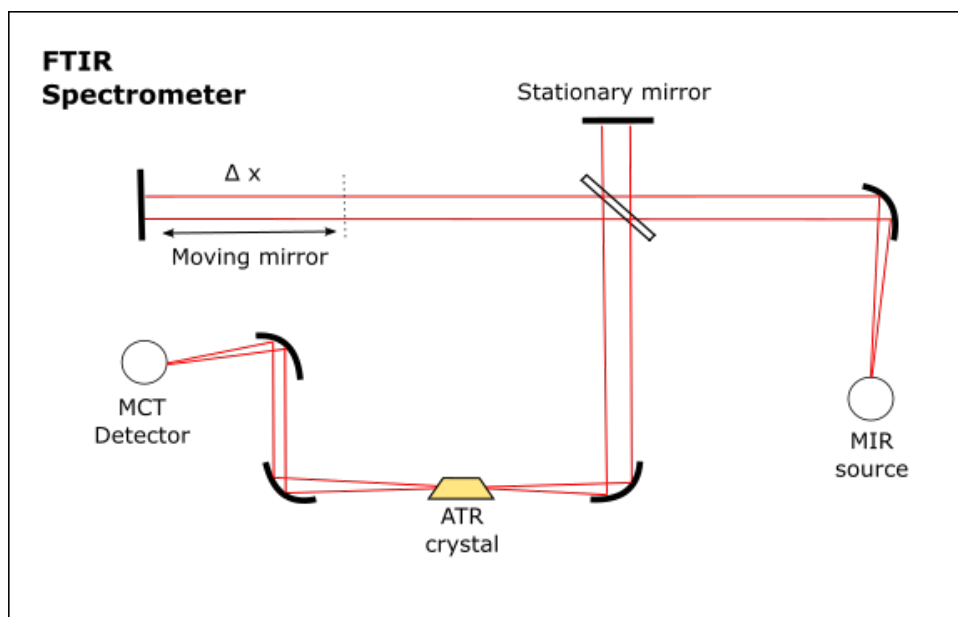


Figure 5.1: Full FTIR setup with ATR flowcell in the sample compartment. The ATR crystal is held in place using the designs seen in the previous chapter.

### 5.3 MIR Optical Properties of ATR Materials

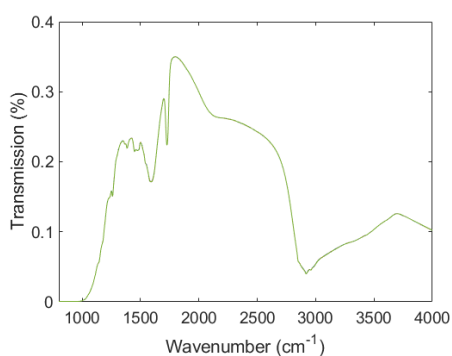
This section shows the spectrum measured using each ATR material and common solvents. The first solvent used was water which show a simple O–H stretch in its spectrum. After water, the next solvents tested increased in chemical complexity and incorporated aromatic features (similar to those seen in methylene blue). The results were catalogued to show the progressive spectral complexity with increasing molecular size. The specific solvents that were chosen share similar chemical structures with that of the organic dye methylene blue to simulate what the first spectra in the degradation reaction should look like. Before the solvents were tested however, the materials used as ATR crystals were measured for their individual material spectrum, highlighting any conflicting features in the target area of interest and revealing the transparency of the material in the IR.

#### 5.3.1 ATR Materials

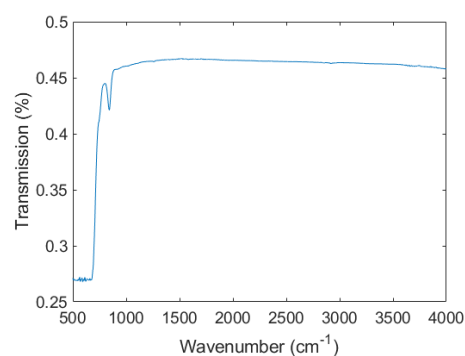
The ATR crystals used in this experiment were made from polished optical windows of specific IR materials. Each material was polished to a unique angle, calculated to facilitate total internal



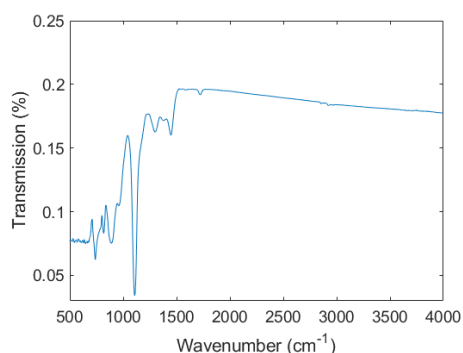
reflection of the input light through the crystal (an extensive look at these equations can be seen in chapter 4). The first experiment using the ATR crystals was to analyse the ATR materials themselves.  $\text{CaF}_2$  as a material for ATR proved limited in the mid infrared (MIR) region due to its restricted transparency. Figure 5.2a confirms that  $\text{CaF}_2$  has limitations as an IR material as it displays spectral features in the region of interest. This meaning, large drops in transmission can be seen in the MIR region which limits the amount of spectral information that can be resolved, in addition to this the spectral features of the material show a strong transmission and would be difficult to remove in analysis. Consequently, alternative materials for the ATR crystal were tested that were transparent in the full IR region. The materials chosen to test were: germanium (Ge), silicon (Si) and zinc sulphide ( $\text{ZnS}$ ) as they were insoluble in water and non-toxic. Toxicity is an important factor for these ATR crystals as they were hand polished using a lapping machine, therefore the materials chosen must be non-toxic.



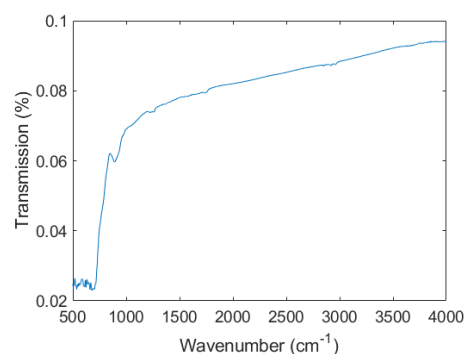
(a)  $\text{CaF}_2$  material spectrum in the IR region.



(b) Ge material spectrum in the IR region.



(c) Si material spectrum in the IR region.



(d)  $\text{ZnS}$  material spectrum in the IR region.

Figure 5.2: Infra-red material spectra of a)  $\text{CaF}_2$ , b) Ge, c) Si and d)  $\text{ZnS}$

In addition to transparency across the IR region, another key material property that makes it suitable for ATR measurements is its refractive index. For instance, the material  $\text{CaF}_2$  has a refractive index close to that of water over the MIR region and consequently only displays TIR at small wavelength ranges. Based upon these results, an ideal material for ATR applications must have a refractive index significantly larger than that of water (see figure 5.3).

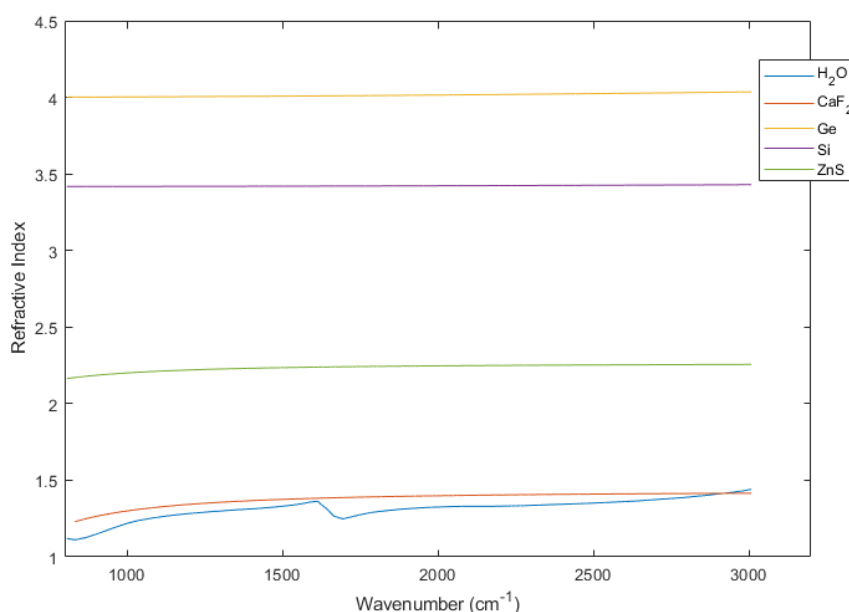


Figure 5.3: Refractive index range over the MIR region for  $\text{CaF}_2$ , Ge, ZnS,  $\text{H}_2\text{O}$  and Si.

After  $\text{CaF}_2$  was deemed unfit for the purpose of this project, the next material tested was Ge (a common material used in the ATR field of research). With reference to figure 5.2, the transmission through Ge shows transparency across the full MIR region, with no obvious spectral features. The transmission seen through the material is greater than that of  $\text{CaF}_2$ , and it has a refractive index (at  $1000\text{ cm}^{-1}$ ) of  $\approx 4.0$ ; which is 3 fold greater than that of  $\text{CaF}_2$ <sup>76</sup>. Germanium is one of the most common ATR materials due to its reliability and favourable optical properties<sup>30,35,61</sup>.

The next material tested was Si due to its water insolubility and optical similarities to Ge. It has a high refractive index, and its IR transmission shows no spectral features for half of the MIR region (see figure 5.2). However, the other half of the MIR region shows material spectral

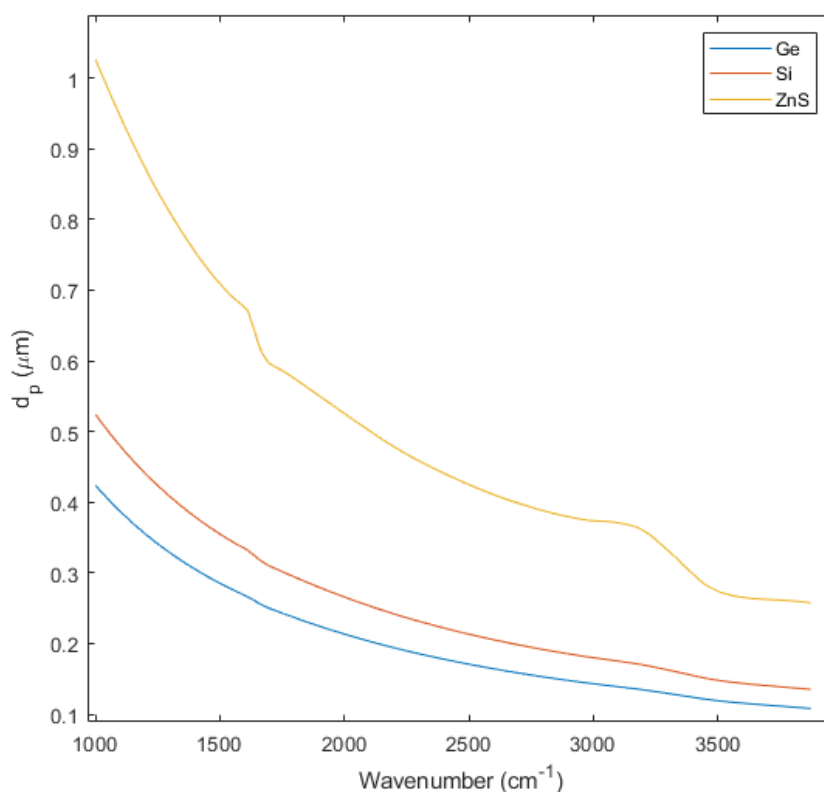


Figure 5.4: Effective penetration depth for Ge, ZnS and Si. The refractive index of each of these materials is directly related to the effective penetration depth, in addition to the polishing angles previously calculated for each material.

features that prove difficult to remove in analysis. Si as a material is inert in the presence of multiple solvents and non-toxic to polish. For these reasons it was used for the bond catalogue seen in section 5.3.2, however due to its spectral limitations (material features), it wasn't chosen to monitor the degradation reaction seen in chapter 6. Finally, ZnS was tested. the result can be seen in figure 5.2, this spectrum shows the weakest transmission signal of all the materials. Nonetheless, it shows no material spectral features throughout the MIR region. ZnS has a refractive index almost double that of water, is water insoluble and non-toxic. Its transparency throughout the full MIR region makes it is a viable material for ATR. Consequently, ZnS was used in both this bond catalogue chapter and in the optical detection of methylene blue degradation.

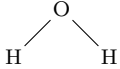
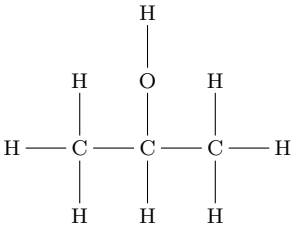
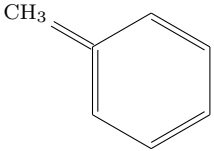
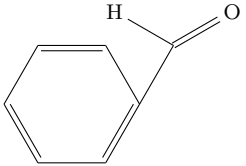
Once the material spectra for each ATR crystal had been recorded and analysed, the next

test used the ATR units to measure control samples. The samples chosen were well published/documented simple solvents that displayed characteristic bonds similar to that of methylene blue; labelled as control samples as they were measured in the stationary ATR units (see setup in chapter 5.2). These solvents were measured and a '*bond catalogue*' was generated. The purpose of creating this bond catalogue was to aid in analysis when the full methylene blue degradation reaction was monitored. With an idea as to where each vibrational mode could occur graphically, the full degradation run data could be better managed.

### 5.3.2 Bond Catalogue

Looking back to chapter 2, the chemical structure of methylene blue can be directly compared to that of benzene/dioxins. Because of this, the solvents tested in this chapter consisted of bonds similar to that found in both methylene blue. To understand what these solvents look like spectrally, their respective transmission spectra from published sources can be seen in figures 5.5 - 5.8. This section shows the progressive spectral information seen from a simple water molecule ( $\text{H}_2\text{O}$ ) to molecules with aromatic rings such as benzaldehyde. From these results, each material was analysed to see which was the best to use in the final optical detection experiment. Tests for each material include measuring the spectrum from simple solvents and chemical stability in water.

Table 5.1: Bond Catalogue

| Sample            | Chemical bonds present   | Vibrational Frequency range ( $\text{cm}^{-1}$ )           | Chemical structure   |
|-------------------|--|--|--|
| Water             | O–H stretch<br>O–H bend  | 3000–4000<br>1550–1650                                     |   |
| Isopropyl Alcohol | O–H stretch<br>C–H stretch<br>C–C–O stretch<br>C–O stretch<br>CH <sub>3</sub> –C–CH <sub>3</sub> stretch | 3000–4000<br>2800–3000<br>1100–1130<br>800–1000<br>940–960 |   |
| Toluene           | C–H stretch<br>C=C stretch   | 2800–3000<br>1500–1600                                     |   |
| Benzaldehyde      | C=O stretch<br>C–H stretch<br>C=C stretch  | 1600–1700<br>2900–3000<br>1500–1600                        |  |

## 5.3.2.1 Published spectra

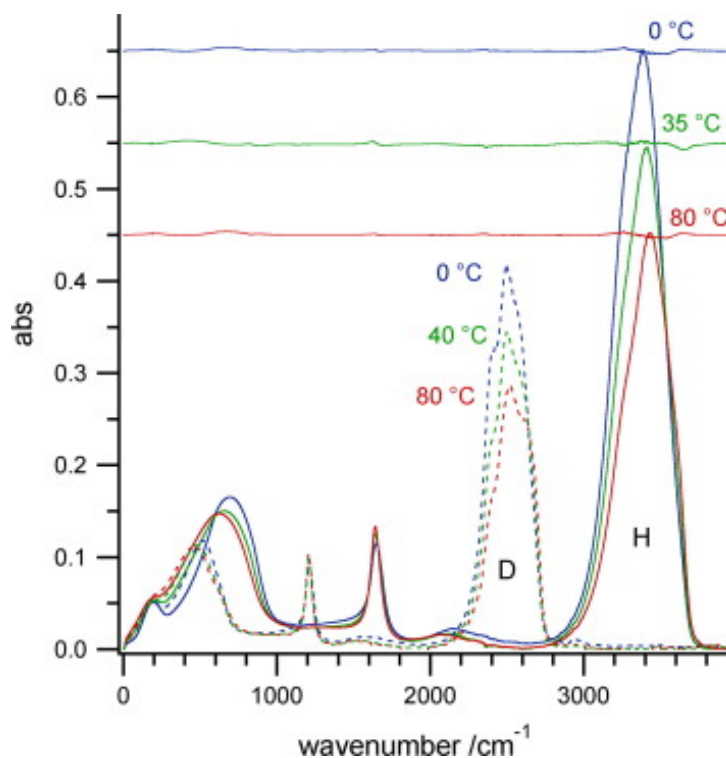


Figure 5.5: Published spectrum using  $1\mu\text{m}$  thick sample of 'normal' liquid water (filled line) and heavy water (dotted line) at three different temperatures<sup>83</sup>

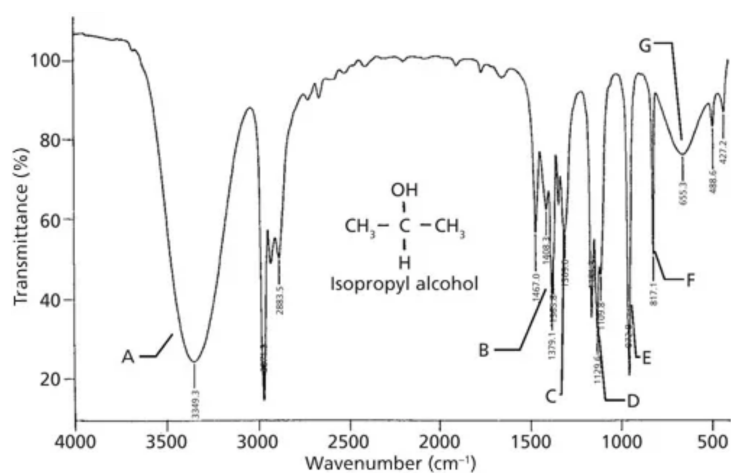


Figure 5.6: Published transmission spectrum of a thin capillary film containing isopropyl-alcohol (IPA). A- (O-H) stretch, B- Split ( $\text{CH}_3$ ) umbrella mode, C- (O-H) in-plane bend, D- ( $\text{C}-\text{C}-\text{O}$ ) assymmetric stretch, E- ( $\text{CH}_3-\text{C}-\text{CH}_3$ ), F- ( $\text{C}-\text{C}-\text{O}$ ) symmetric stretch and G- (O-H) out of plane bend<sup>113</sup>

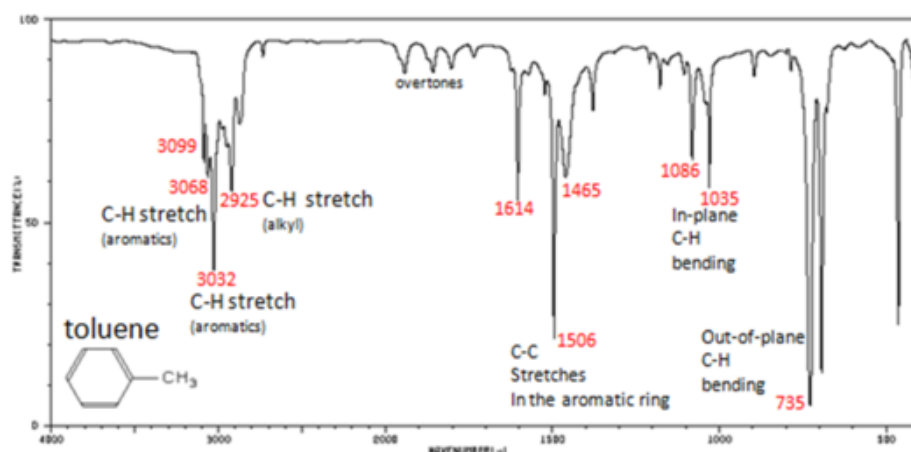


Figure 5.7: Published transmission spectrum of toluene with bond assignment<sup>24</sup>

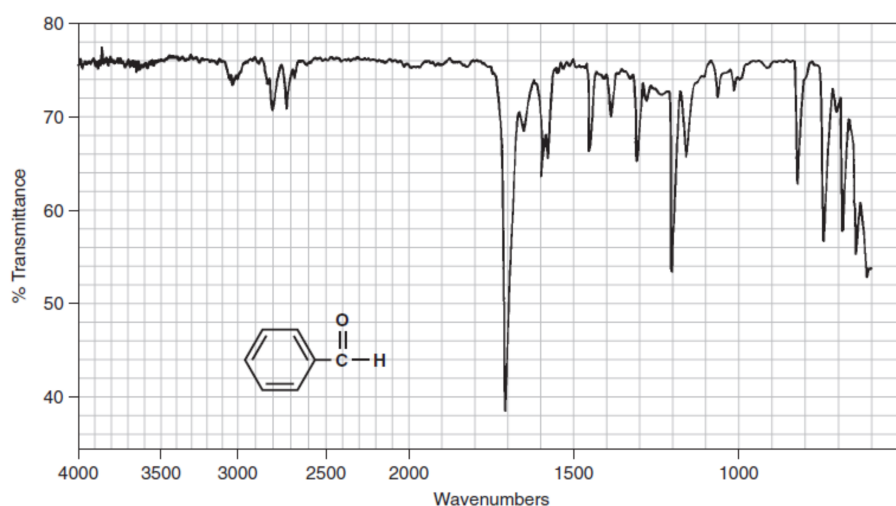


Figure 5.8: Published transmission spectrum of benzaldehyde measured between two KBr plates<sup>73</sup>

### 5.3.2.2 Germanium (Ge)

The first solvent to be measured was water, using a multi-reflection Ge ATR crystal. The result can be found in figure 5.9. Figure 5.9 displays both the corrected and uncorrected (raw data) water spectra using the multi-reflection Ge ATR crystal. In order to correct an ATR spectrum, the effective penetration depth of the evanescent wave is calculated. The effective penetration depth of the evanescent wave is dependent on the refractive index of the material and the polishing angle which had been previously calculated. Correcting the ATR spectrum is

important to be able to directly compare it to the transmission spectrum obtained in figure 5.5. The first feature to note is a broad O–H stretch centred at approximately  $3400\text{ cm}^{-1}$ . This is a broad band which implies that it is a combination of frequencies, this feature agrees with both table 5.1 and figure 5.5 in both location and width. The other prominent peak is seen at  $1600\text{ cm}^{-1}$  which represents the bending of the O–H bond, this also agrees with both table 5.1 and figure 5.5. Figure 5.9 confirms that the calculations of the polishing angle for Ge were correct and that the ATR crystal was accurate and reliable for future measurements. The correction factor for Ge can be seen clearly in figure 5.9. The raw absorbance spectrum of  $\text{H}_2\text{O}$  shows two features that have a ratio of approximately 3:1. After correcting the data the ratio of the peaks has increased to approximately 5:1. Looking back to figure 5.4 the effective penetration depth in Ge shows that features at short wavelengths should become more prominent after correction, which is what can be seen in figure 5.9. This correction factor was consequently used for all of the spectral results seen in this chapter.

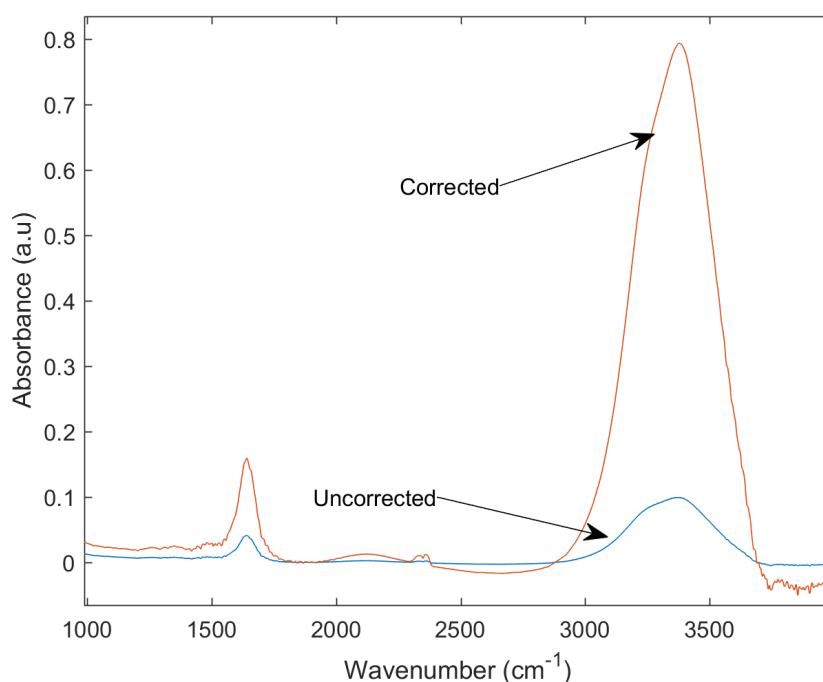


Figure 5.9: Deionised water spectrum using Ge multi-reflection ATR crystal, both ‘corrected’ and ‘raw data’. The correction factor for this graph was the effective penetration depth. The expected result from this correction was to see features at shorter wavelengths becoming more prominent and that is what can be seen.



The next control sample tested was isopropyl-alcohol (an aliphatic hydrocarbon compound) and the result can be seen in figure 5.10. The broad spectral peak seen in figure 5.10 is in the same location as the O–H stretch seen in the H<sub>2</sub>O spectrum (from 3000 cm<sup>-1</sup> to 4000 cm<sup>-1</sup>). Another large feature is seen at 2900 cm<sup>-1</sup>. This feature is sharp and narrow in nature which implies there are no overtones/combinations in this region. Referring to table 5.1 it identifies this bond as a C–H stretch, this feature can also be seen in figure 5.6. One of the strongest features present in figure 5.6 is seen at approximately 952 cm<sup>-1</sup>, this feature represents a CH<sub>3</sub>–C–CH<sub>3</sub> stretch. And, just as the previous features, it is present in figure 5.10 and table 5.1. More importantly, the shape of this feature is sharp and narrow (the same as the C–H stretch) which will make this feature identifiable in a more complex spectrum. This result acts as a confirmation that the Ge ATR crystal works and has a high level of sensitivity.

The subsequent control sample tested was toluene, and the results using the Ge multi-reflection crystal can be seen in figure 5.11. Toluene is an aromatic hydrocarbon, this meaning it has C=C bonds (see benzene structure in chapter 3). The same prominent features that can be seen in IPA are also present in toluene, for example the C–H stretch seen between 2800 and 3000 cm<sup>-1</sup>. However, this region encompasses both the C–H alkyl stretch (non-aromatic) and the C–H aromatic stretch. Identifying these aromatic features was important for the eventual analysis of the degradation reaction (see final chapter). Another large peak can be found at 1496 cm<sup>-1</sup>, which from figure 5.7 can be assigned to a C–C stretch in the aromatic ring. The bond vibrations in aromatic structures identify the stability of the structure, and consequently are of particular interest to this project. The primary difference between toluene and IPA is the introduction of the double bond, specifically the C=C aromatic chemical bond. The C=C aromatic stretch can be seen in figure 5.11 at approximately 1603 cm<sup>-1</sup> which agrees with figure 5.7. This feature is crucial to the final aims of this project as this will be one of the major bonds to monitor over the course of the full dye degradation reaction.

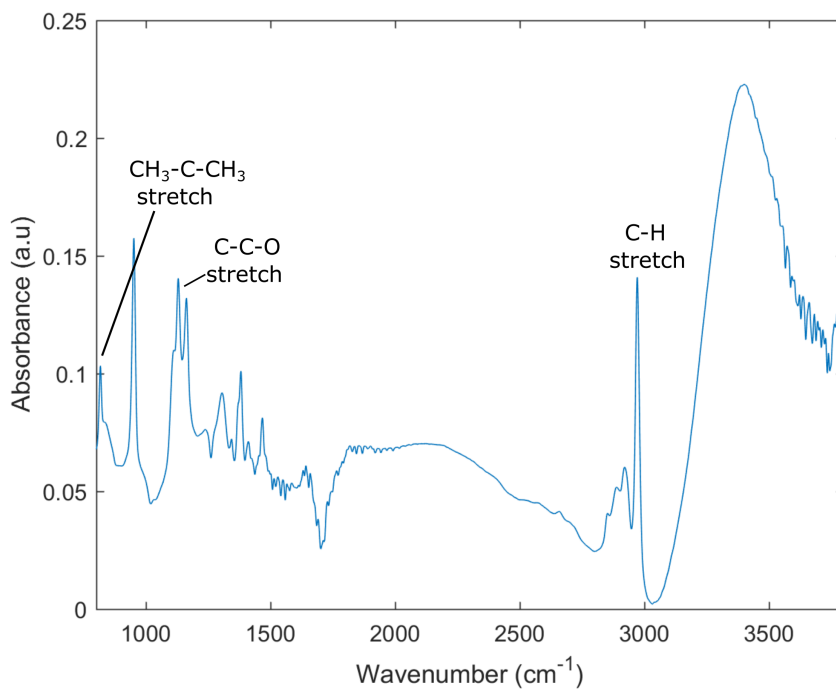


Figure 5.10: Isopropyl alcohol spectrum using the Ge multi-reflection ATR crystal. The difference in chemical structure between IPA and water introduces a C-H stretch which can be seen between 2800- 3000  $\text{cm}^{-1}$ , a CH<sub>3</sub> - C-CH<sub>3</sub> stretch at 940-960  $\text{cm}^{-1}$  and a C-C-O stretch at 1100-1130  $\text{cm}^{-1}$ .

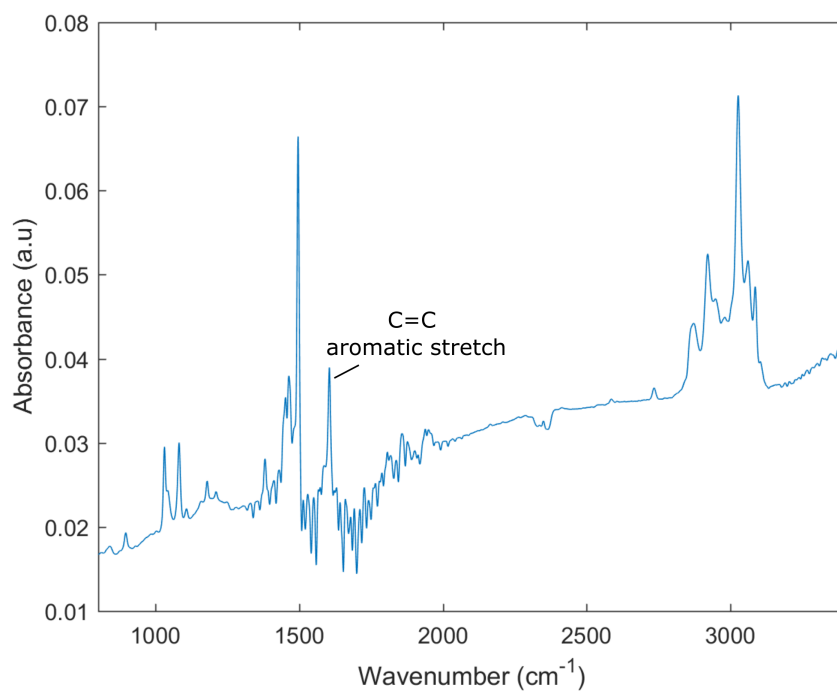


Figure 5.11: Toluene spectrum using a multi-reflection Ge ATR crystal. The difference between toluene and IPA is the introduction of an aromatic ring and the aromatic features seen between 1500 and 1600  $\text{cm}^{-1}$  which correspond to a C=C aromatic stretch.

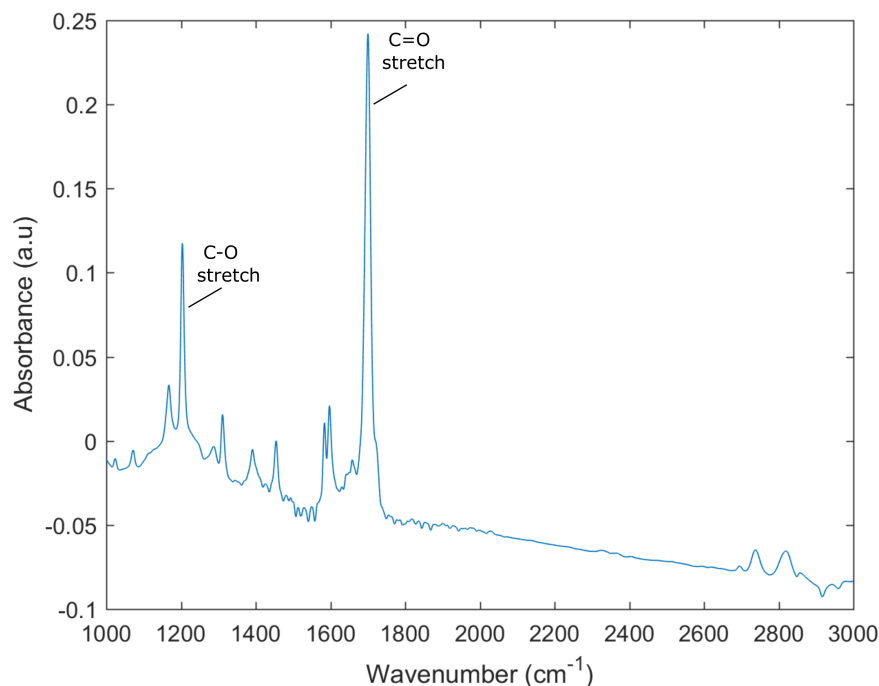


Figure 5.12: Benzaldehyde spectrum using a multi-reflection Ge ATR crystal. The difference between toluene and benzaldehyde is the external C=O stretch seen between 1680 and 1700  $\text{cm}^{-1}$ .

Moving to the final control sample measured, benzaldehyde. Benzaldehyde was chosen as a progression from toluene due to its external double bond from the aromatic ring. The resultant spectrum (see figure 5.12) confirmed the location of the C=C stretch seen in toluene. Looking at figure 5.12 the prominent features can be seen at approximately 1700, 1600 and 1200  $\text{cm}^{-1}$ . The feature at 1700  $\text{cm}^{-1}$  can be assigned to the functional group C=C aromatic stretch in addition to the feature at 1600  $\text{cm}^{-1}$ . This is in agreement with figure 5.8 and table 5.1. A conclusion from this result is that for similar chemical structures the same vibrational functional groups can be found within a window of wavenumber values. The last spectral feature is seen at 1200  $\text{cm}^{-1}$  which can be assigned to a C–O stretch; this also agrees with table 5.1 and figure 5.8, further validating the Ge ATR design. From these results, Ge was seen to be an ideal material for ATR measurements.

### 5.3.2.3 Silicon (Si)

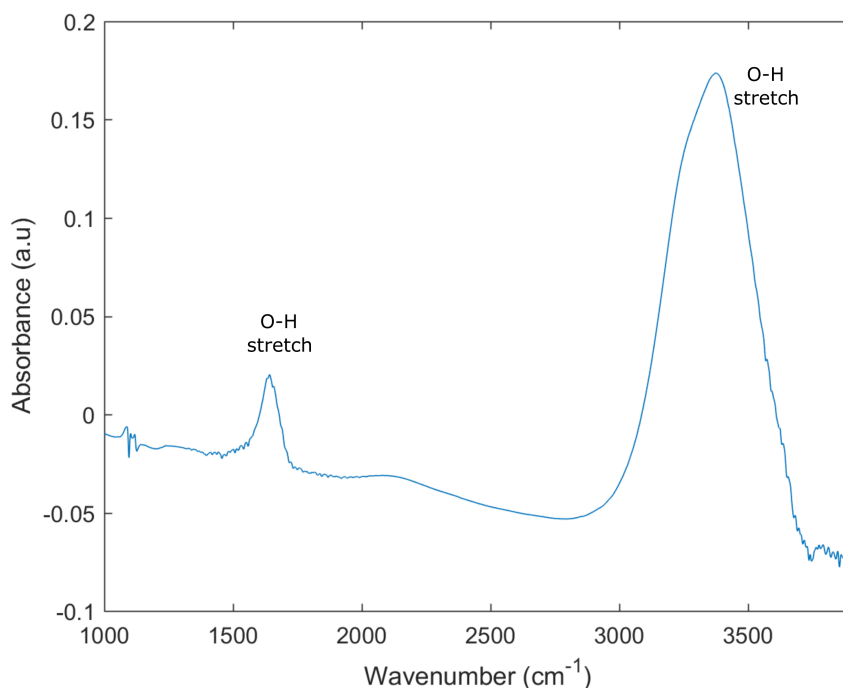


Figure 5.13: Deionised water spectrum using a multi-reflection Si ATR crystal. The same broad water features that were seen using Ge are also present at  $1600\text{ cm}^{-1}$  and between  $3000$  and  $4000\text{ cm}^{-1}$ .

In addition to germanium, both silicon and zinc sulphide were tested for all four control samples. The result for water using a multi-reflection silicon ATR crystal can be found in figure 5.13. The resultant spectrum from the silicon ATR crystal displayed similarities with that of the germanium. Figure 5.9 and figure 5.13 show the same two prominent features from  $3000\text{ cm}^{-1}$  to  $4000\text{ cm}^{-1}$  and from  $1500\text{ cm}^{-1}$  to  $1600\text{ cm}^{-1}$ . The only difference between the  $\text{H}_2\text{O}$  spectrum using the Ge and Si crystal is the transmission seen through the crystal. For example, the O–H stretch seen from  $3000\text{ cm}^{-1}$  to  $4000\text{ cm}^{-1}$  reached a peak absorbance of 0.348 using the Ge, whereas with Si shows a peak absorbance value of 0.17. This result can be explained by looking at the transmission spectrum through each material in the IR (see figure 5.2). Si and Ge have similar refractive indices (3.5 and 4.0 respectively) over the full IR region. However, their material spectra under IR light show that Ge has less spectral features in the MIR region of

interest compared to Si and consequently is more suitable to ATR measurements in the IR.

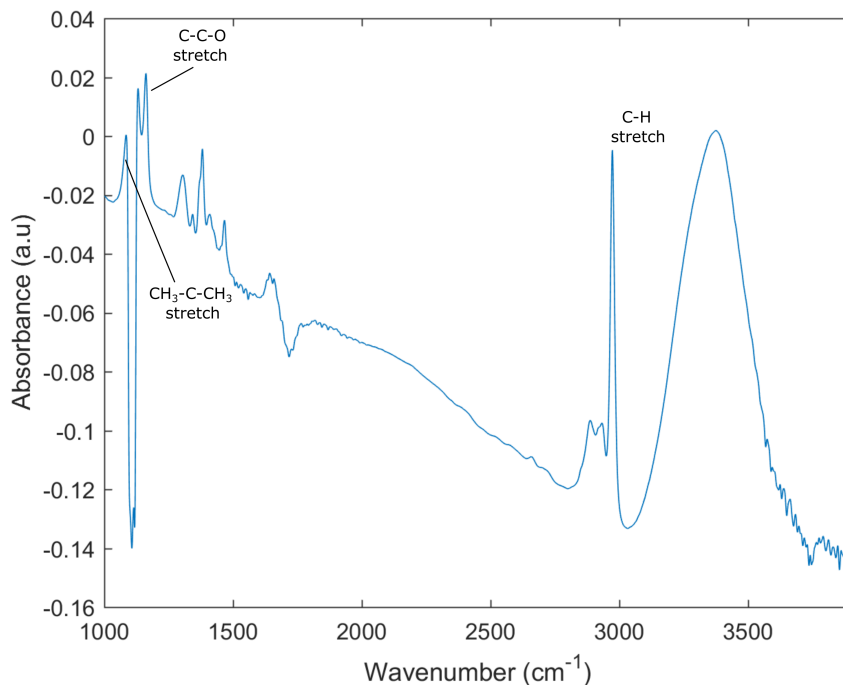


Figure 5.14: Isopropyl alcohol spectrum using a multi-reflection Si ATR crystal. The same spectral features seen with the Ge crystal can also be seen here. There is a C-H stretch between 2800- 3000  $\text{cm}^{-1}$ , a CH<sub>3</sub> - C-CH<sub>3</sub> stretch at 940-960  $\text{cm}^{-1}$  and a C-C-O stretch at 1100-1130  $\text{cm}^{-1}$ . The main difference being the transmission signal between the materials and the baseline of the spectrum.

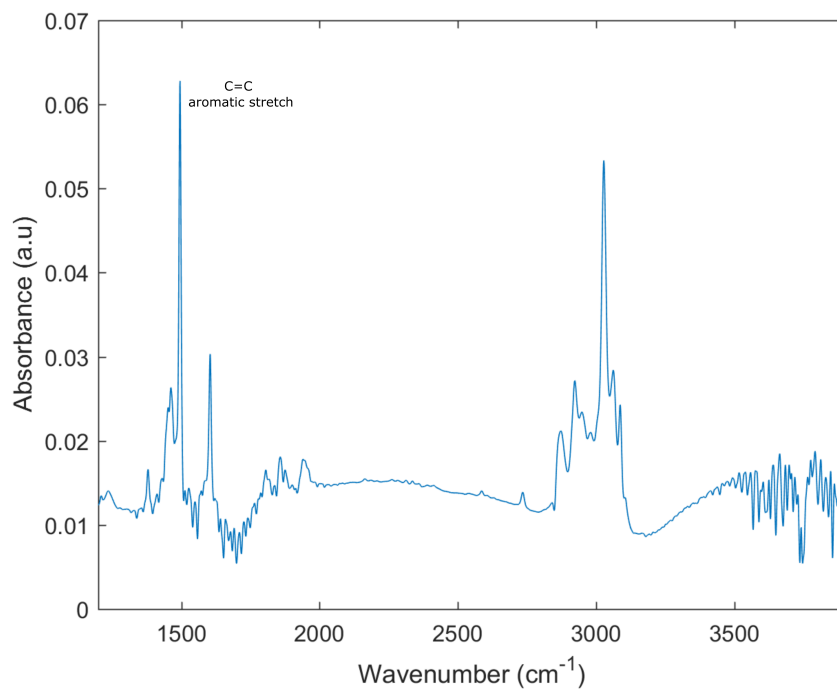


Figure 5.15: Toluene spectrum using a multi-reflection Si ATR crystal. The same features that were seen using the Ge crystal can also be seen with the Si; the introduction of an aromatic ring and the aromatic features can be seen between 1500 and 1600 cm<sup>-1</sup> which correspond to a C=C aromatic stretch.

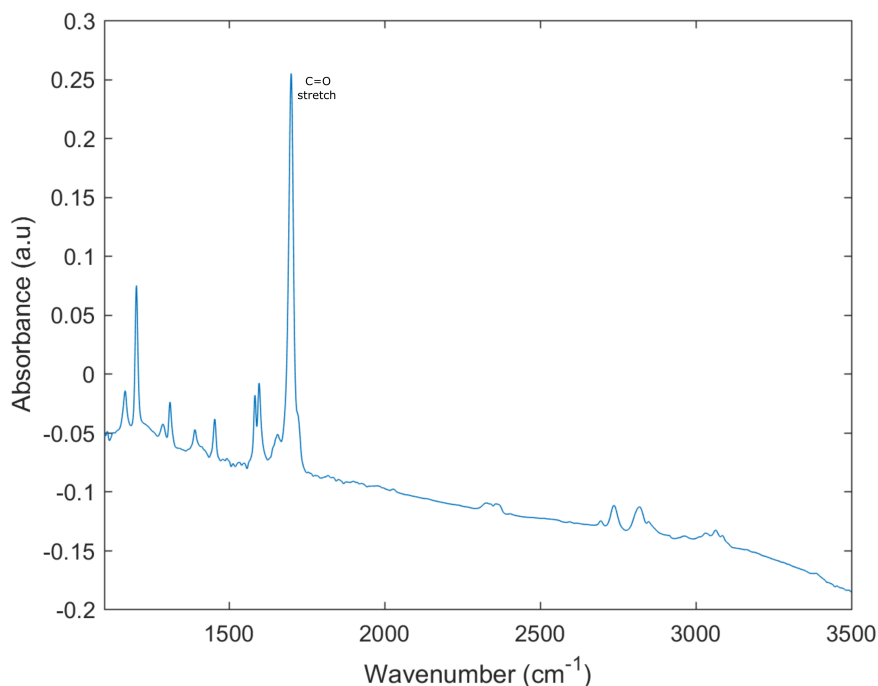


Figure 5.16: Benzaldehyde spectrum using a multi-reflection Si ATR crystal. This spectrum shows the same spectral features that could be seen using the Ge crystal; the addition of an external C=O stretch seen between 1680 and 1700  $\text{cm}^{-1}$

IPA was then measured using the Si multi-reflection crystal and the result can be found in figure 5.14. Here, a linear trend can be seen as a baseline for the spectrum, this could be a product of the correction factor or a result of background division (looking back to figure 5.2 the silicon graph from 1500  $\text{cm}^{-1}$  to 4000  $\text{cm}^{-1}$  displays a downward linear trend). The transmission material graphs were important to be able to understand which features/trends were from the sample itself or a response of the material used. In this case, the background material spectrum doesn't affect the features present but has however changed the baseline. The following solvent tested was toluene (see figure 5.15). Just as the water and IPA spectra, this result along with the graph of benzaldehyde (figure 5.16) shows the same functional groups present with half the peak amplitude of that seen when using Ge. The importance of understanding ATR spectra and the possible issues that can occur was essential for the final chapter where the full reaction was measured.

The benefit of generating this bond catalogue was due to the similarities in the structures



measured to that in methylene blue/methyl orange. In addition to identifying bond signatures, the potential materials used as internal reflection elements were tested to confirm whether the mathematical calculations (calculated polishing angles) of the crystals themselves were correct. The results of this bond catalogue confirmed that both Ge and Si were reliable ATR materials and the initial ATR material tested ( $\text{CaF}_2$ ) was found to be unsuitable for ATR measurements. Preceding the control sample results, each material was then tested to identify its chemical stability in water; as the dye degradation reaction takes place in an aqueous medium. In order to test this, each materials chemical stability was monitored over a 12/24 hour time period.

## 5.4 Chemical Stability of ATR Materials in Water

The final aim of this project was to monitor a dye degradation through the identification of reaction pathways in real-time. Therefore, the material used as an ATR measurement crystal must be stable when exposed to an aqueous solution. To measure each materials chemical stability, water was passed across both faces of the crystal and the spectral activity over a time period was recorded. If the material was unstable in the presence of water, a chemical reaction at the crystal surface would result in a change in spectral baseline over time. The experimental setup was the same as seen in section 5.2, and the FTIR spectrometer was left to measure over a 12 hour time period for Ge.

### 5.4.0.1 Germanium Chemical Stability In Water

Germanium has been frequently used in ATR optical measurements as a result of its material spectrum in the IR region, chemical stability and high refractive index<sup>5</sup>. In addition to this, Ge has a low toxicity, and has be seen to remain inert in the presence of multiple chemical solutions<sup>30</sup>. Currently in the field of ATR detection Ge is commonly used as a biosensor<sup>30,134</sup>. Publications using Ge as an ATR biosensor coat the Ge with elements such as: biological materials<sup>35</sup>, iron<sup>82</sup> or other protective materials. The need for a protective layer is a direct consequence of the solubility of  $\text{GeO}_2$  in water.  $\text{GeO}_2$  has a solubility of  $4.47 \text{ g L}^{-1}$  in water<sup>33,4</sup>. Ge naturally has a protective oxide layer when exposed to to atmospheric conditions. This

oxide layer has a high solubility in water and consequently, a chemical stability in water test was undertaken using Ge.

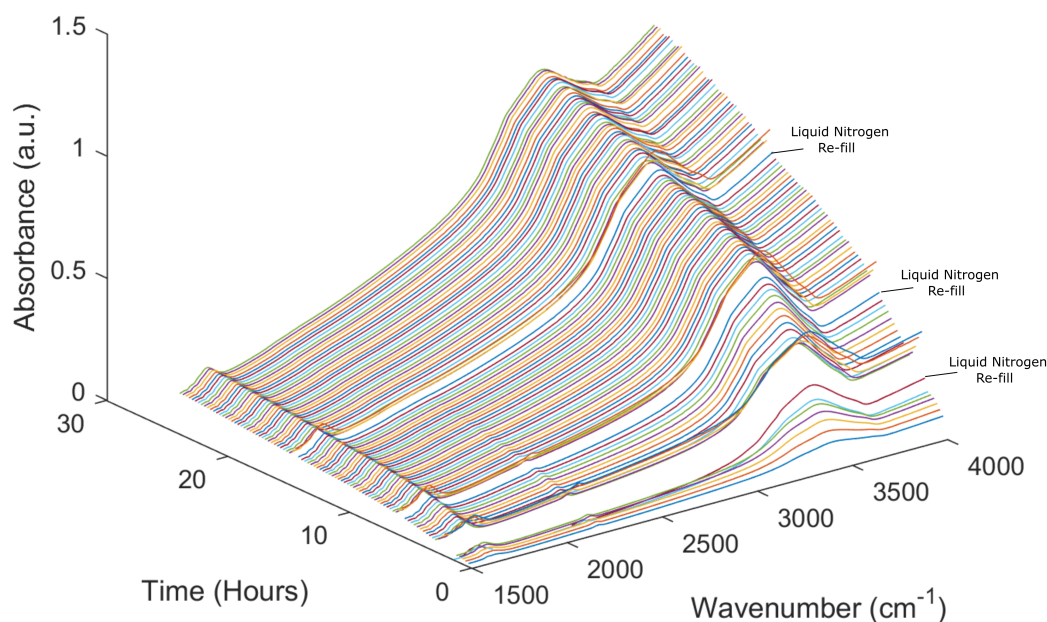


Figure 5.17: Absorbance spectrum of a multi-reflection Ge crystal measuring its chemical stability in water over a 24 hour time period. The baseline of the spectrum rapidly changes over the 24 hour time period, indicating that the crystal surface was reacting with the water and changing the background spectrum.

The results from the Ge ATR chemical stability in water experiment can be seen in figure 5.17. Although the spectra don't change over time, the indicator that the crystal surface was etching due to  $\text{GeO}_2$  solubility in water was the baseline movement. If the material displayed chemical stability in water, a flat baseline with minimal variation would be the resultant spectrum. However, the baseline of the spectrum gradually increased over time indicating a change at the crystal surface. The specific issue that can be seen as a result of this experiment is the long exposure of  $\text{H}_2\text{O}$  on the Ge surface. Over long exposures, potentially a greater amount of  $\text{GeO}_2$  could be dissolved into solution, thus adding  $\text{GeO}_2$  to the chemical reaction. In addition to the graphical evidence of Ge ATR instability, the crystal appeared etched after the experiment (see

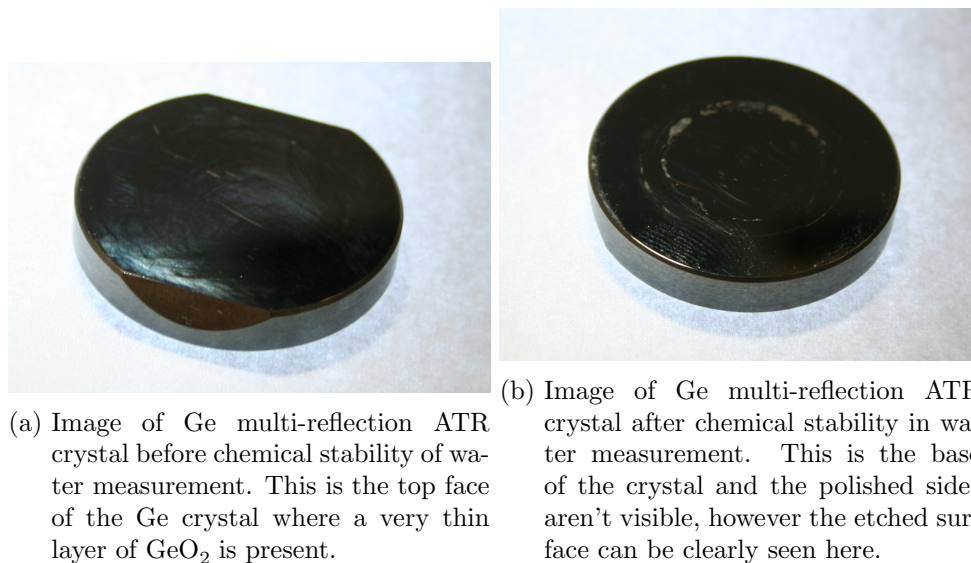


Figure 5.18: Images of the multi-reflection Ge ATR crystal before and after the chemical stability in water measurement.

figure 5.18). The crystal was imaged before and after reaction (see figure 5.18), these images show a thin layer removed from the material surface, in the centre of the ATR crystal. The gradual removal of thin layers of  $\text{GeO}_2$  was thought to be changing the baseline of the chemical stability measurements. This was evident from the water stability graph displayed in figure 5.17. Although Ge displays favourable optical properties for ATR, its chemical instability in water removes it as a possibility for long life-time reaction measurements.

In addition to the crystal surface measurement, the temperature of the reaction was measured to identify if a temperature change in the experiment could also be contributing to a baseline drift. For this, the chemical stability test was repeated and the temperature was simultaneously measured over the full stability run. The result showed a minor temperature fluctuation of  $2^\circ\text{C}$ . This was deemed too smaller change to be affecting the baseline of the spectrum and consequently was no longer thought of as a possible cause of baseline drift.

#### 5.4.0.2 Silicon Chemical Stability In Water

After analysing the results from Ge ATR chemical stability, it was clear that alternative materials with similar optical properties needed to be tested. The subsequent material tested was

that of Si. The same experimental setup was used to restrict variable changes between material measurements. The results of the Si chemical stability test can be seen in figure 5.19, and similar to the Ge data this has been displayed in a 3D line plot (normalised to a background of water).

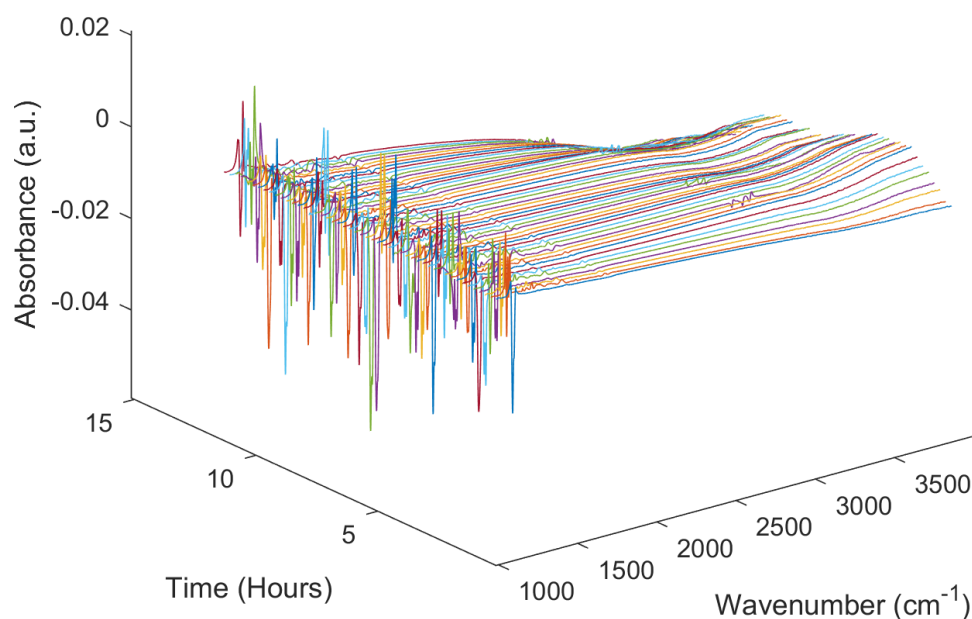


Figure 5.19: Absorbance spectra of a multi-reflection ATR Si crystal measuring its material response to water over a 12 hour time period. Each spectrum had been normalised to the first water background to clearly identify baseline drift.

Compared to  $\text{GeO}_2$ , silica/silicon dioxide ( $\text{SiO}_2$ )<sup>74</sup> has a water solubility of  $0.12 \text{ g l}^{-1}$ . This value suggests that the solubility of  $\text{SiO}_2$  should reach an equilibrium point in water and remain stable thereafter. The low water solubility of  $\text{SiO}_2$  estimates that an equilibrium point state will be evident within the first quartile of the experiment (with reference to the Ge stability experiment). Figure 5.19 shows that this predication is inaccurate, with the baseline changing continually throughout the duration of the experiment. In the MIR region of interest ( $1000 - 2500 \text{ cm}^{-1}$ ) the baseline remains consistent, indicating that Si is chemically stable and fit for

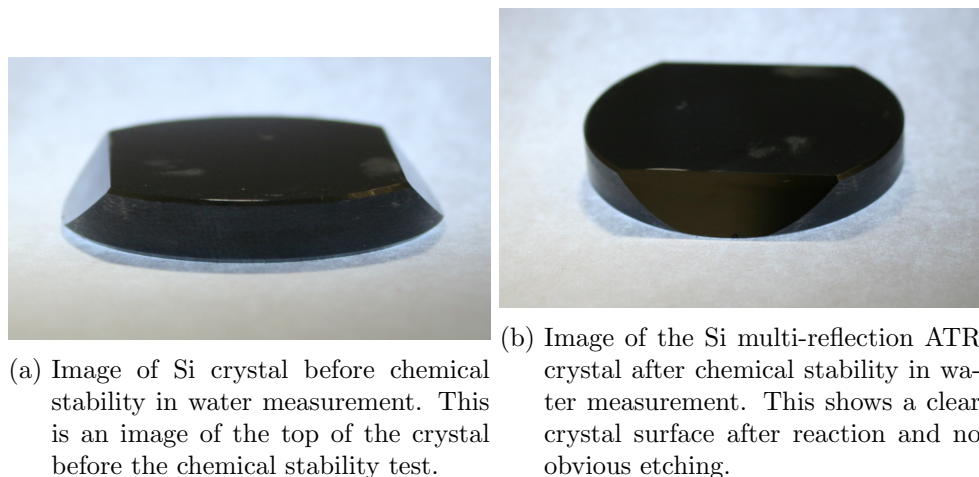


Figure 5.20: Images of the Si ATR crystal before chemical stability in water measurements

purpose as a material for the final experiment. Whilst it displays chemical stability in the region of interest, its material spectrum shows limitations over half of the IR region of interest (see figure 5.2), therefore another ATR material was tested, Zinc Sulphide.

#### 5.4.0.3 Zinc Sulphide Chemical Stability In Water

The chemical stability in water spectrum of ZnS can be seen in figure 5.2. As mentioned previously in section 5.3.1 over the IR spectrum ( $1100\text{ cm}^{-1}$  to  $4000\text{ cm}^{-1}$ ) ZnS doesn't display any material features, and its refractive index stands in-between that of  $\text{CaF}_2$  and Si. A further advantage of using ZnS is its effective penetration depth, which is almost twice that of Si. The final test of material chemical stability in water proved it to be a useful material for ATR measurements (see figure 5.21). Making a direct comparison between the Ge and ZnS (figures 5.17 and 5.21), the baseline for ZnS is flat, with the only variation accounted for by noise or as a product of normalisation. Both Ge and ZnS were measured under the same control parameters. Figure 5.21 shows that the baseline for ZnS remained consistent over time and for this reason, ZnS was chosen as the ATR material for the dye degradation reaction. Following this result, the ZnS ATR crystal was further tested for its chemical stability in the methylene blue solution used for reaction.

The final test was monitoring chemical stability throughout the reaction itself ( $\text{H}_2\text{O}$  with the

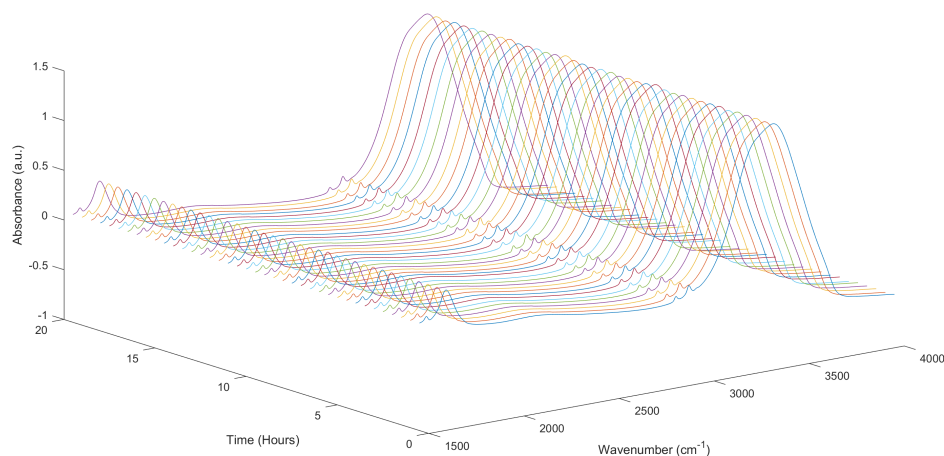


Figure 5.21: Absorbance spectra using a multi-reflection ZnS crystal measuring its material response to water over a 12 hour time period. This data has been normalised to an air background and shows that ZnS has good chemical stability in water.

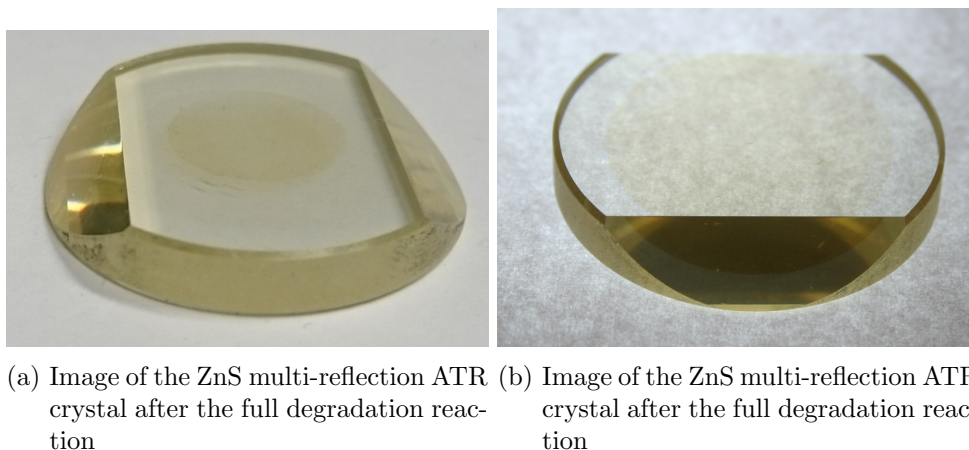


Figure 5.22: Images of the ZnS multi-reflection ATR crystals after the full methylene blue degradation reaction. The optical staining effect identifies a possible reaction happening at the crystal surface.

test pollutant methylene blue). Figure 5.22 shows the ZnS multi-reflection crystal after the full methylene blue degradation reaction had optically cleared. The deposited ring seen was initially thought to be staining, as the ZnS crystal remained constant in the chemical stability in water test. However, after attempting to remove the stain by cleaning the surface with IPA and acetone, the yellow pattern remained. To effectively remove the stain, the crystal face was polished to remove a thin layer (1-10  $\mu\text{m}$ ). This led to the conclusion that the crystal itself degrades over time during the reaction. The damage to the crystal surface was less compared to Ge, as the ZnS showed a uniform discolouring effect, whereas the Ge showed an eroding effect that changed the morphology of the crystal surface. The spectral results seen in chapter 6 indicate that this process occurs at a slower rate for ZnS than Ge, and consequently wasn't a major limiting factor for the full degradation run.

## 5.5 Summary

The first test measurements in this chapter were of each material to identify their unique material spectrum signatures in the MIR region of interest. These measurements were important to identify specific material features in the spectral region of interest (for methylene blue). As can be seen in this chapter, the only material that displayed significant material features was  $\text{CaF}_2$ , however this material had already been deemed unfit for MIR ATR measurements. Once the material features for each material had been analysed, well known solvents were tested to firstly identify if each crystal design was correct, and secondly to identify how much signal was detected using each crystal. The solvents were chosen specifically as they shared common chemical structures with that of methylene blue which gave an idea as to where each spectral feature may be in the full reaction experiment. Once the design model for each material had been proven to work by using the ATR crystals to measure solvents with clear spectral features, the chemical stability in water of each material was tested. The first material tested was Ge which is a common material used for ATR units. The results from this experiment showed that a surface level of  $\text{GeO}_2$  that had formed on the crystal surface was water soluble, consequently degrading the crystal surface when exposed to water on a long timescale. An etched pattern

consistent with the direction of the flow of the water was seen on the crystal surface. The result of this showed the baseline of spectra measured drifting over time. This effect meant that despite the optical benefits of using Ge as an ATR crystal, it couldn't be used in the final reaction of this project and an alternative material had to be found. ZnS displays a spectrally clear IR spectrum and chemical stability in water. It is equally non-toxic and has a high effective path length as a consequence of its refractive index. This material was further tested for its chemical stability in a methylene blue degradation reaction, and the result showed a chemical reaction at the crystal surface. The reaction results in a uniform stain like pattern on the crystal surface and happens over a long time-scale. However, ZnS was the material compromise used in the final optical detection measurement seen in the next chapter.



## 6 Real-time MIR Spectroscopy of Methylene Blue Photocatalytic Reactions

This chapter reports on real-time experiments, where the progress of a  $\text{TiO}_2$  photocatalytic-mediated degradation reaction of methylene blue in water is measured. In addition to this experiment, the visible colour change was measured simultaneously to correlate the two techniques. The initial section of this chapter reviews the current knowledge into photocatalytic chemistry and the recent publications of methylene blue degradation using  $\text{TiO}_2$ . From this, a refined model of the experimental setup is shown along with a description of the limitations of that setup. Following this is the first result of the chapter: steady-state methylene blue in the IR. The potential challenges of in-situ measurements are then outlined followed by the methods with which some of these were mitigated. The next section of this chapter explains the algorithm used for fitting the data, followed by the results, discussion and conclusions from the experiment.

### 6.1 Current Knowledge of $\text{TiO}_2$ Photocatalytic Chemistry

Before the experimental results are presented and discussed, it is important to know the current research in this field to be able to identify the similarities and differences in my results compared to that of previous publication. In 1972, titanium dioxide ( $\text{TiO}_2$ ) was used in a water splitting reaction, this promoted its application in other water ‘cleaning’ reactions, namely a dye degradation<sup>40</sup>. The specific dyes used in these experiments all shared similarities in their chemical structure to that of common agricultural waste pollutants (i.e benzene, dioxin). The most common organic dye used as a test pollutant is methylene blue<sup>58,43</sup>. Methylene blue has a

similar stable aromatic ring structure to that of benzene/dioxins, and the reaction pathways of its degradation has been theorised by different sources<sup>58,55,98</sup>. To monitor this reaction (methylene blue degradation) using visible light spectroscopy is simple due to the low absorbance of visible light through aqueous solutions (see section 4.3). However, when measuring an aqueous sample (water-soluble dyes) in the infrared (IR) region the water absorbance is much higher, causing a potential problem in measurement sensitivity. As a result of this, there is currently a lack of published data displaying the degradation reaction using  $\text{TiO}_2$  in real-time. For the purpose of this project, methylene blue degradation was measured in real-time using published data on the methylene blue hydrate spectrum as a tool for bond analysis<sup>98</sup>. Although there are publications discussing the reaction pathways for methylene blue, there is still no clear outcome. The two key papers focused on in this chapter were used for comparison to the reaction results measured. The first publication of interest is entitled ‘Manifestation of intermolecular interactions in FTIR spectra of Methylene Blue molecules’<sup>98</sup>, as the title suggests its aim was to both calculate and measure intermolecular interactions between methylene blue molecules. The results from this publication show the possible intermolecular grouping that methylene blue could have when in its hydrate form (figure 6.1).

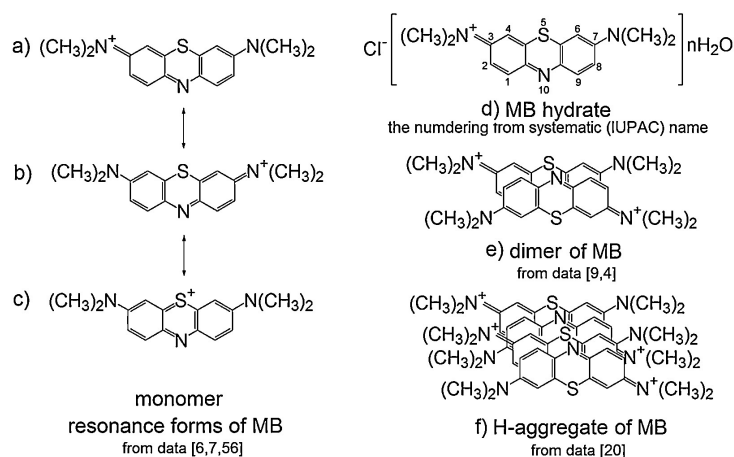


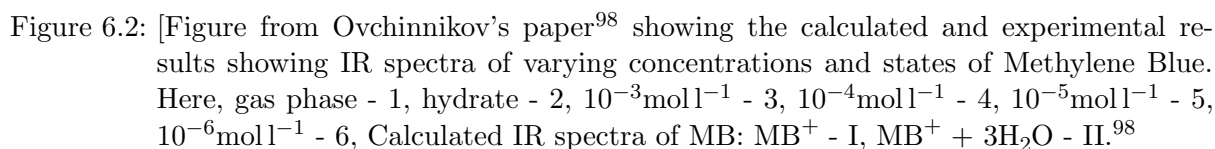
Figure 6.1: Structural representation of possible methylene blue groupings in solution. Should the methylene blue molecules aggregate together, the first stage of the reaction may see them separate<sup>58</sup>.

The dimerisation/aggregation of methylene blue molecules affects the frequency position of each spectral feature in the resultant spectrum. This is due to each formation of methylene

blue aggregate/dimer displaying a different spectral shift (see figure 6.2). In post-analysis of the results from the MB degradation reaction, this figure helped to determine whether the initial stages of the reaction are simply dimers/aggregates forming, and if so how they then degrade based on their initial formation. In this same publication, an experimental result shows different concentrations of methylene blue dried onto materials and their resultant spectra. As mentioned previously, measuring an aqueous reaction in the IR presents difficulties, therefore the results seen in figure 6.2 have been obtained through dried hydrate samples at different concentrations. The materials used to dry these samples onto were both potassium bromide (KBr) and potassium chloride (KCl) windows, whose optical transparency in the IR makes them advantageous for IR measurements, though they are too soluble for aqueous ATR.

Looking to figure 6.2, it is important to consider spectral drift throughout the reaction. For example, in figure 6.2 the C=C heterocyclic vibrational stretch seen in MB hydrate at  $1594\text{ cm}^{-1}$  in graph number 2 shifts to a doublet feature between  $1620$  and  $1640\text{ cm}^{-1}$  for graph number 4 (micro-molar concentration of MB). This shift indicates that the resultant spectrum seen for this project will lie somewhere between these two features. Figure 6.2 shows that methylene blue has a wealth of spectral features to observe, nonetheless this project focused on modelling the behaviour of the bonds seen between  $1000$  and  $2000\text{ cm}^{-1}$  as this is the region of interest.

With reference to figure 6.2, the measured spectrum was compared with the graph labelled number 3. This spectrum was used for comparison with the results measured in this project as the starting concentration of methylene blue was the same ( $10^{-3}\text{ mol l}^{-1}$ ). Spectrum 3 in figure 6.2 displays the initial methylene blue spectrum, the first feature seen in the region of interest (from  $1000$  to  $2000\text{ cm}^{-1}$ ) is a doublet between  $1620$  and  $1650\text{ cm}^{-1}$ . The doublet shows a strong signal at  $1620\text{ cm}^{-1}$ , which has been assigned to both C=N and C=C heterocyclic stretching from Ovchinnikovs paper<sup>98</sup>. These peaks correlate to the central structure of the aromatic ring seen within methylene blue. Therefore, monitoring these features throughout the duration of the reaction will indicate if the stable central structure remains stable or degrades over time. Should any of the aromatic heterocyclic bonds be broken throughout the reaction, the structural integrity of the methylene blue molecule will be compromised, ultimately leading to full molecular breakdown and a conclusion can be made that the methylene blue has been ‘cleaned’



The next region of interest is located at  $1444\text{ cm}^{-1}$ , where there is a weak peak. This peak has been assigned to C=S<sup>+</sup> heterocyclic stretching, this peak is a fraction of the amplitude of that seen at  $1620\text{ cm}^{-1}$ , however it provides valuable information about the central aromatic structure and its bond kinetics over the course of the reaction. Further proof of this vibrational

mode can be found at  $1355\text{ cm}^{-1}$ , where a weak peak is also assigned to  $\text{C}=\text{S}^+$  stretching, and a larger peak adjacent to it (doublet) at  $1340\text{ cm}^{-1}$  is assigned to a  $\text{C}-\text{N}$  (in  $\text{N}-\text{CH}_3$ ) stretching, this is the other exterior bond on the methylene blue molecule. Following these features, the next vibrational mode present can be seen at  $1185\text{ cm}^{-1}$ . This frequency has been assigned to a  $\text{C}-\text{H}$  heterocyclic out of plane stretch, the relating in-plane stretch showing the same bond can be seen at  $1258\text{ cm}^{-1}$ . These features show the structurally weaker bonds within the aromatic structures and consequently were monitored in this project. The final feature seen in figure 6.2 of interest is seen at  $1143\text{ cm}^{-1}$ . This feature is assigned to  $\text{C}-\text{N}$  heterocyclic bending in plane. Whilst this feature doesn't represent the double bonded structure seen in the aromatic rings, it provides an indicator as to whether part of the aromatic ring breaks throughout the reaction.

In addition to understanding the spectra of methylene blue in various forms and conditions, it is important to consider the breakdown process and products, including intermediates. Based on measurements of molecular mass throughout methylene blue degradation the intermediate products have been theorised in a secondary paper written by Houas *et al*<sup>58</sup>. Figure 6.3 is from Houas' publication and it proposes that the first bonds to break in a methylene blue degradation reaction are the  $\text{N}=\text{C}-\text{H}$  and  $\text{C}=\text{S}^+$ . In parallel to these bonds breaking there are equally bonds being created which can be seen as  $\text{N}-\text{H}_2$ ,  $\text{S}=\text{O}$  and  $\text{S}-\text{C}$ <sup>58</sup>. These theoretical degradation pathways are justified through the molecular weight of the molecule at each stage; for the purposes of this project the first stage was considered to be the colour change, thus these bond creations/breakdowns were focused on in the resultant spectrum. Based on theory<sup>59</sup> and figure 6.2, the  $\text{C}=\text{S}^+$  bond can be found at  $\approx 1355\text{ cm}^{-1}$ , and the  $\text{C}-\text{N}$  heterocyclic bond can be found at  $\approx 1557\text{ cm}^{-1}$ . In conjunction with these bonds breaking, there is also bond creation occurring. Due to this, the two bonds that were also monitored in this project were at  $1264\text{ cm}^{-1}$  and  $1391\text{ cm}^{-1}$  which can be assigned to  $\text{C}-\text{H}$  bending out of plane and  $\text{C}-\text{H}$  stretch in plane respectively<sup>98</sup>. Once an understanding of the methylene blue spectrum and possible reaction pathways had been identified, the reaction itself was monitored using a similar experimental setup to that seen previously.

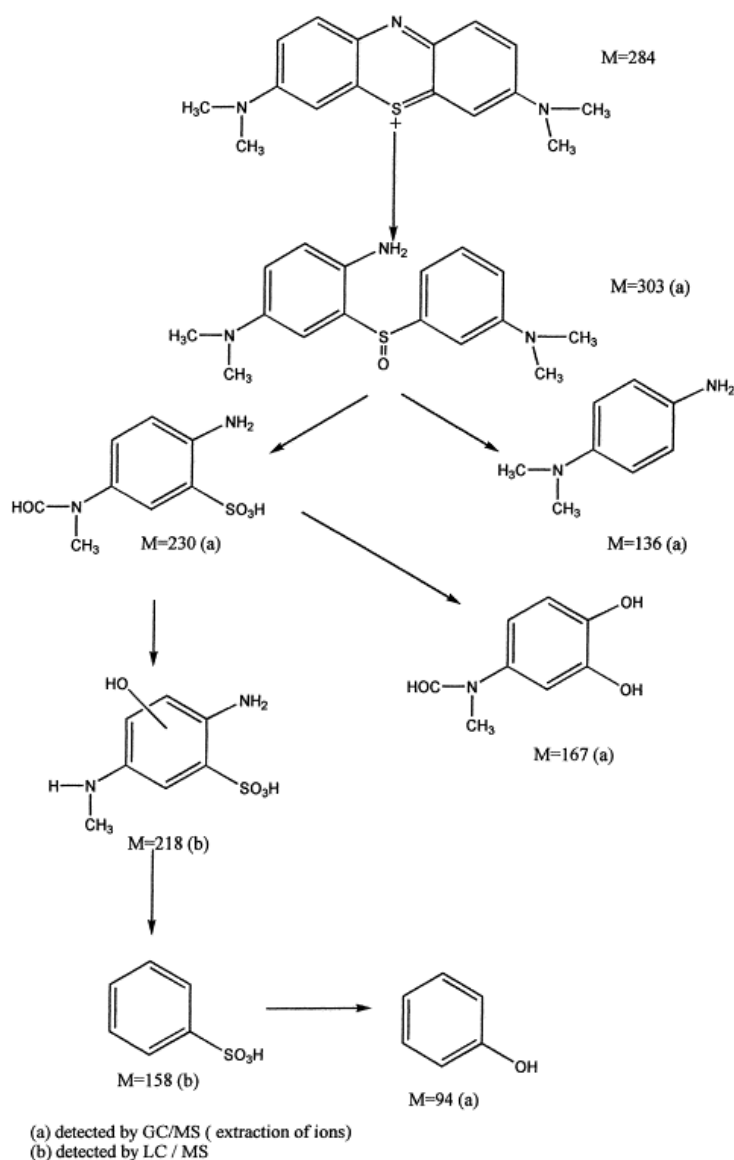


Figure 6.3: Figure from the Houas paper<sup>58</sup> which shows the proposed theoretical break down of methylene blue degradation. The first stage of the reaction involves the C=S<sup>+</sup> bond breaking to a C-S, C-H and S=O will be formed. It then suggests that the nitrogen bond at the top of the central aromatic ring breaks C=N breaks to form C-H and C-NH<sub>2</sub>. Although there are multiple stages before arriving at a single aromatic ring, the first two stages will be focused on for the purposes of this project.

## 6.2 Refining the Experimental Setup

Measuring an aqueous solution using IR spectroscopy is possible using ATR. However, there are still experimental challenges that had to be overcome. The aim of this experiment was

to simultaneously measure both MIR spectroscopy using an ATR flowcell and monitor the visible absorbance using the 1 cm flowcell. This proved difficult as only a small amount of the MIR optical path was transmitted through the ATR crystal. A further consideration for this experiment was the presence of atmospheric gases such as  $\text{H}_2\text{O}$  and  $\text{CO}_2$ , so the constraints on the quality of the vacuum were higher. To achieve a consistent vacuum a scroll pump was used to purge the atmospheric gases from the spectrometer, consequently removing their distinct fingerprints from the resultant spectra. In addition to this, there was the issue of protecting the internal optical components in the FTIR from accidental water leaks. The MIR components (such as the beam splitter) are hygroscopic, and in the worst cases deliquescent, so protecting them was essential. This is however particularly challenging due to the piping and sealing of optical units in the spectrometer which was held under vacuum, compared to atmospheric pressure. The sample compartment was isolated from the rest of the spectrometer to protect the optics, which proved difficult. However, in the early stages of this experiment there were leaks and this isolation precaution protected the internal components of the spectrometer. To isolate the sample compartment, two potassium bromide (KBr) windows were used. These windows added difficulty to the experiment as KBr is also hygroscopic, and with initial leaks and ambient-humidity, began to become clouded. The clouding of these windows was on a significantly longer timescale than each measurement which meant it wasn't a spectrally limiting factor.

### 6.3 Steady-state Spectroscopic Measurements

To be able to track reaction pathways, a base spectrum of methylene blue hydrate was needed for comparison (see figure 6.5). So, the first result measured using the experimental setup seen in section 6.2 was the methylene blue hydrate spectrum. The process of measuring this included injecting the starting concentration of methylene blue (millimolar) into the system without either the UV LED or  $\text{TiO}_2$  present. One of the primary reasons to analyse the methylene blue spectrum before looking at the full reaction, is for calibration and to identify the location of vibrational features. The stronger peaks seen in the published spectrum of figure 6.2 are at 1600, 1355 (doublet) and  $1370\text{ cm}^{-1}$  and the measured result of methylene blue hydrate match

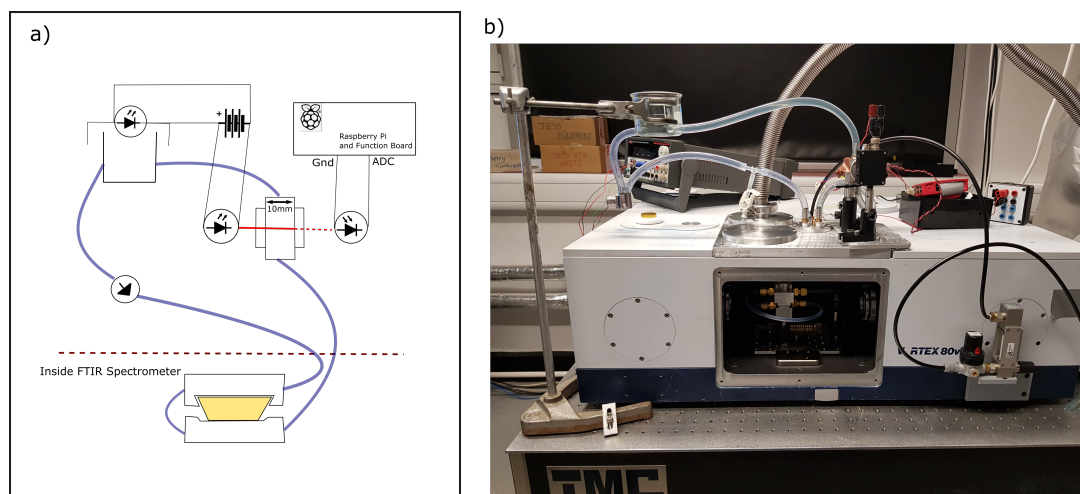


Figure 6.4: a) Schematic diagram of the experimental setup b) An image of the experimental set-up using VERTEX80V spectrometer from BRUKER. The diagram shows the ATR cell inside the spectrometer kept at vacuum and the pipe connectors that allow the water and methylene blue to flow throughout the full circuit. The photocatalytic reaction happens in the beaker with a UV LED illuminating a wafer that has been spin-coated with  $\text{TiO}_2$  nanoparticles. The absorbance is measured with the flowcell (the same as the visible data collected in chapter 2). Finally, the water and methylene blue mixture is passed over both faces of the ATR crystal where the infrared measurements take place and a resultant spectrum is produced.

these same frequency peaks. This proved one of two things, firstly that the ZnS ATR unit worked, and secondly that the published IR spectrum of dried methylene blue was an accurate representation of methylene blue hydrate.

## 6.4 Challenges of In-situ Real-time Measurements

With ATR, it was now possible to measure aqueous solutions using IR spectroscopy. However, the results from each experiment using ATR showed significant challenges in doing ATR measurements over long timescales. This is due to a background division where the signal is on top of a large water absorption, and is consequently very small. As a result of this, the experiment is extremely sensitive to any other changes relative to this background. In an effort to minimise this, parameters of the experiment that could change the baseline were tested.



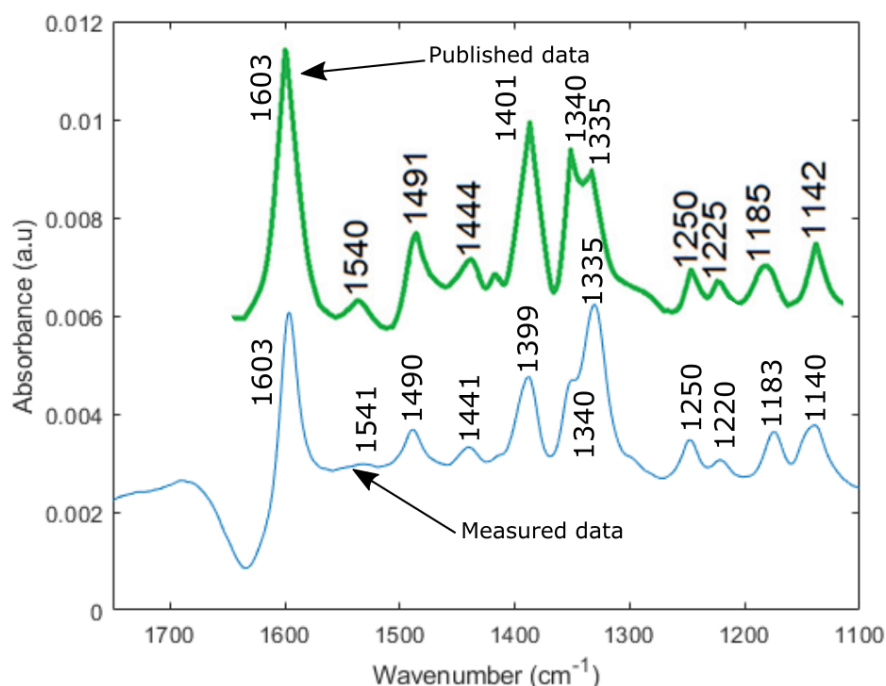


Figure 6.5: Graph showing the direct comparison between a measured spectrum of a millimolar solution of methylene blue and the published results of the same concentration. These two spectra have been overlaid for direct comparison, the measured spectrum was plotted and the respective published graph from figure 6.2<sup>98</sup> was calibrated to the initial peak for comparison. From this plot it is clear that both spectra have the same features but with different intensities at some frequencies (i.e the shoulder feature seen at 1355  $\text{cm}^{-1}$ ).

#### 6.4.1 Mixing Issues

The initial visible absorbance circuit consisted of a smaller number of elements in comparison to that seen in this experiment. The visible flow cell was specifically designed to encourage mixing by offsetting the entrance and exit pipes to facilitate internal rotation. Likewise, the reaction vessel was also designed in this way (as modelled in the Nickels, Patrick *et al* paper<sup>93</sup>). However, with severe constraints on vacuum, the pipes in this experiment were much longer and the ATR flowcell was more complex in design (double-sided ATR bounce geometry). Unlike the visible absorbance experiment where the mixing of the methylene blue with water was generally achieved in an hour, this new setup has inherent difficulties. In addition to the initial spectrum of methylene blue, a secondary measurement to monitor the methylene blue mixing within the

ZnS ATR crystal was recorded. The results of this measurement can be seen in figure 6.7, and a simplified figure with the first and last spectra recorded can be seen in figure 6.6.

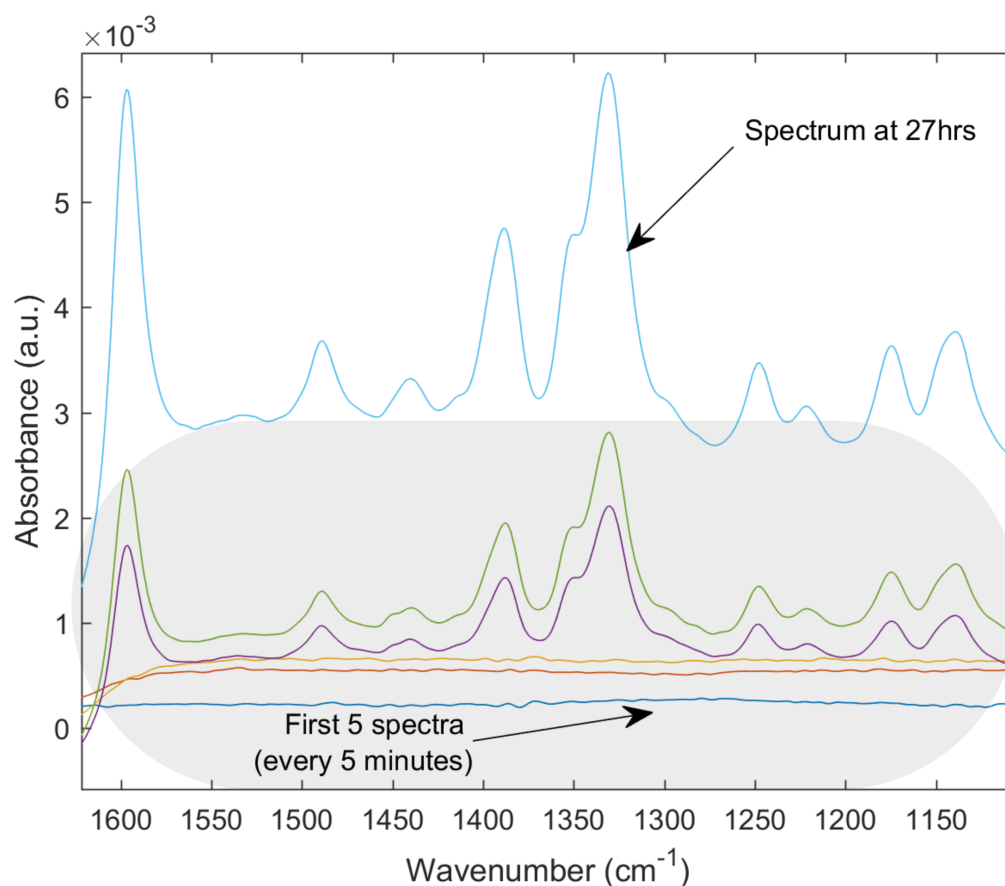


Figure 6.6: Graph showing the initial water background (bottom three spectra) and the 'mixing' process when 10 ml of millimolar methylene blue is added to 150 ml of deionised water. The spectrum at the top shows the stable 'mixed' result of methylene blue (normalised to a water background) and the lower 5 spectra show the initial 'mixing' stages of the experiment (No catalyst or UV).

Figure 6.7 highlights the possibility of methylene blue aggregation in the initial stages of the experiment, a possible product of poor mixing. The concentration of the methylene blue in the system was millimolar, and therefore could have been introduced to the system in molecule aggregations such as dimers/trimers. An initial 'mixing stability' measurement was run over a time period of 6 hours which illustrated that within a timescale of an hour, the methylene blue spectral features could be resolved. Figure 6.6 shows a significant baseline drift over the course

of the 6 hours, this can be seen in greater detail in figure 6.7. This could be a consequence of the ATR flowcell design; the theory that there is a small pocket of liquid held at an ATR facet which remain stationary over the entirety of the experiment. In order to mitigate these problems, the flowcell was mounted vertically to remove any air bubbles and the methylene blue was added to the system at least 6 hours before the full reaction began.

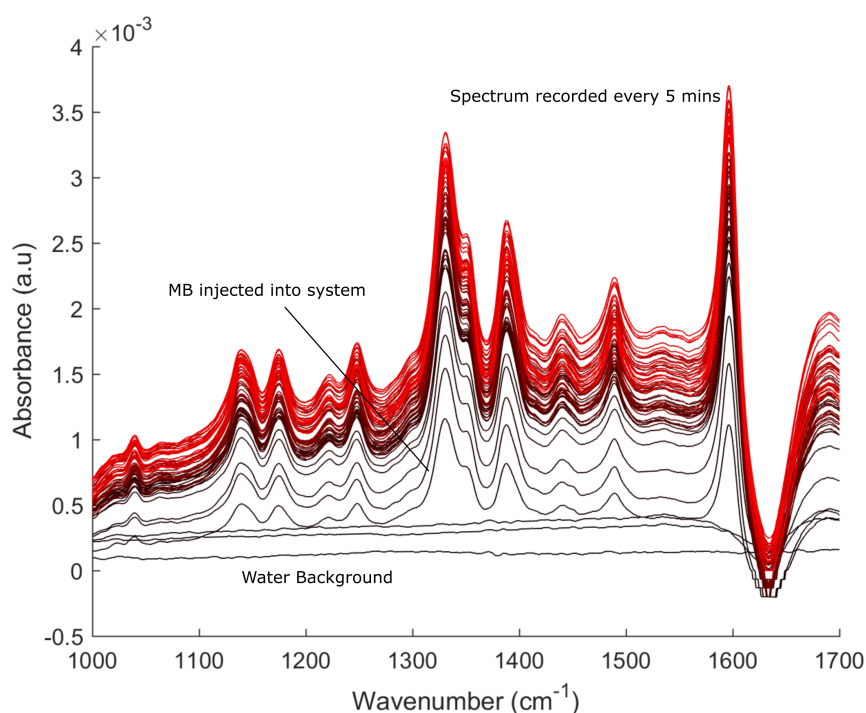
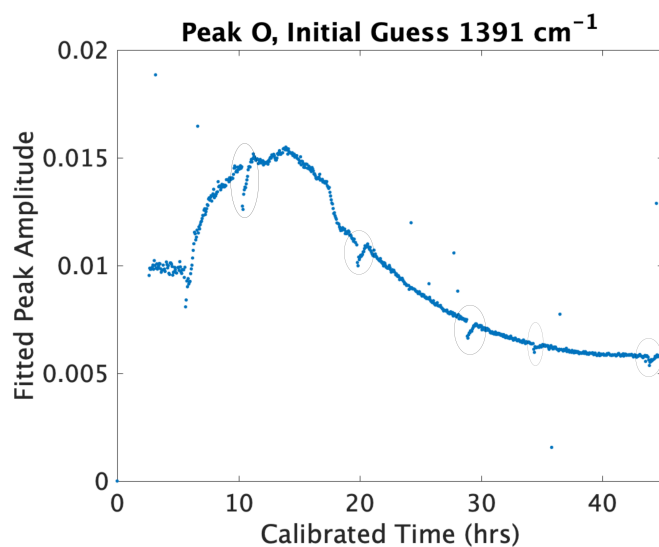


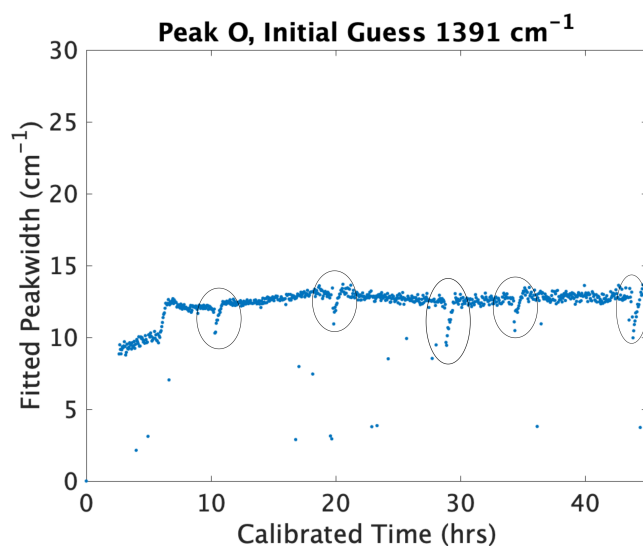
Figure 6.7: Graph showing the chemical stability of ZnS using a millimolar solution of methylene blue. The colour key seen here is black is  $t=0$ , red is  $t=6$  hours, with a spectrum taken every 5 minutes.

#### 6.4.2 Detector hold time

Looking to figure 6.7 there is a noticeable baseline drift on the data. This drift could either be a consequence of the ZnS crystal surface reaction a product of poor design, or due to the detector cooling cycles. The mercury cadmium telluride (MCT) detector must be kept at 77 K throughout the measurement. To achieve this, a dewar that is in direct contact with the detector is filled with liquid nitrogen. The dewar is kept under vacuum and has a maximum hold-time of 12 hours when the dewar jacket is optimally pumped. The question that arose from this figure



(a) Peak amplitude plot for a vibrational frequency of  $1391\text{ cm}^{-1}$ . This plot identifies the MCT cooling cycles as signified on the graph.



(b) Peak width plot for a vibrational frequency of  $1391\text{ cm}^{-1}$ . This plot identifies regular MCT cooling cycles as signified on the graph.

Figure 6.8: Figures to show the peak amplitude and peak width for a vibrational frequency of  $1391\text{ cm}^{-1}$ . The graphs themselves will be discussed later, however the periodic MCT filling points seen throughout the full degradation run show that it has no effect on the baseline.

was whether the filling process directly affected the baseline drift seen in figure 6.7. To be able to better understand the answer to this, figure 6.8 is considered. This data will be discussed in

greater detail in the following section, however for the purpose of this section the MCT filling points seen on the plots will be discussed. The MCT filling points can be seen periodically in the data. More importantly, before and after the top up points the baseline appears to return to an equilibrium point and the data trend remains consistent with no discontinuities. This can be seen in all of the peak analysis in the next section, and consequently rules out possibility that the MCT filling cycle caused the baseline drift.

## 6.5 Rationale for Using a Peak Fitting Algorithm

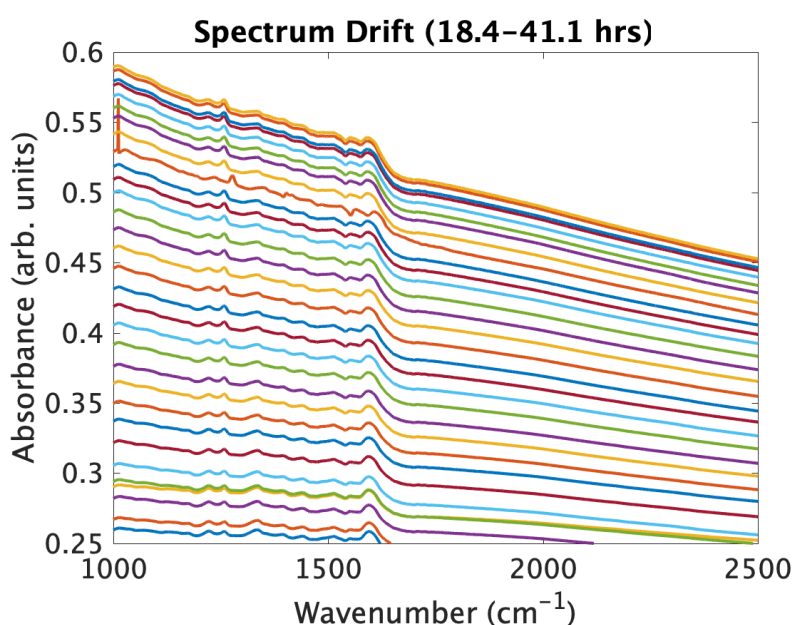


Figure 6.9: Infrared ATR absorbance spectrum plotted in time steps of approximately 47 minutes over the time range 18.4-41.1 hours. The earliest spectrum is at the bottom of the graph. There are two trends which are clear from this data: the baseline drifts to higher values of absorbance with increasing time, and the slope of the baseline gets steeper with increasing time.

The overall aim of these experiments was to understand the chemistry of the photocatalytic degradation of methylene blue at a molecular level. According to the Beer-Lambert law, the absorbance is proportional to the concentration, which we can interpret as the number of absorbers in the material. Since each molecular bond leaves its own characteristic fingerprint in the spectrum, we should be able to gain information about how the number of one type of

bond changes over the course of the photocatalytic reaction. Ultimately the aim is to use this information to decipher the steps in the degradation reaction. In analysing the time-resolved spectral data for the reaction, there are two major challenges to be overcome. An understanding of these challenges can be seen with reference to figure 6.9.

The expected spectra obtained from this experiment were a result of measuring the absolute absorbance of a line and tracking this over time. This experiment displayed more difficulties, as the methylene blue spectrum sits on top of a large water background which needed to be subtracted. There are two trends that are immediately obvious considering figure 6.9. The baseline underneath the methylene blue spectral features appeared to change: it appeared to drift to higher values of absorbance with time, and the slope appeared to grow steeper over time. It is not clear why this would be the case, but it is well-known that the ATR technique is highly sensitive to changes at the interface between the crystal and the liquid. The experiments showed that the ZnS crystal becomes stained over the duration of the experiment. The cause of this staining is still unclear, however a source of this phenomenon could be due to slow surface reactions between the methylene blue and the ZnS surface. The theory behind this possible staining effect can be seen explained in section 6.6.3.

In order to subtract the baseline, an assumption that the changing baseline was an experimental artefact and that neither the drift or change of the baseline have a detrimental effect on the absolute absorbance of the methylene blue spectral features relative to the baseline. This assumption is justified through the close inspection of the collection of MIR peaks, which revealed that there were always three stationary points between the methylene blue peaks where the absorption drops to the baseline value. These three stationary points can always be fitted to a straight line (as shown in figure 6.10). The interpretation of this statement is that these three points are zeros of absorbance for the methylene blue relative to the base line absorption of water.

Each peak in the spectrum is then fitted gaussian line-shape according to the equation. A gaussian fit was chosen for the lineshape as it is commonly used to describe lines which have been inhomogeneously broadened. This would be appropriate for spectral lines that have been

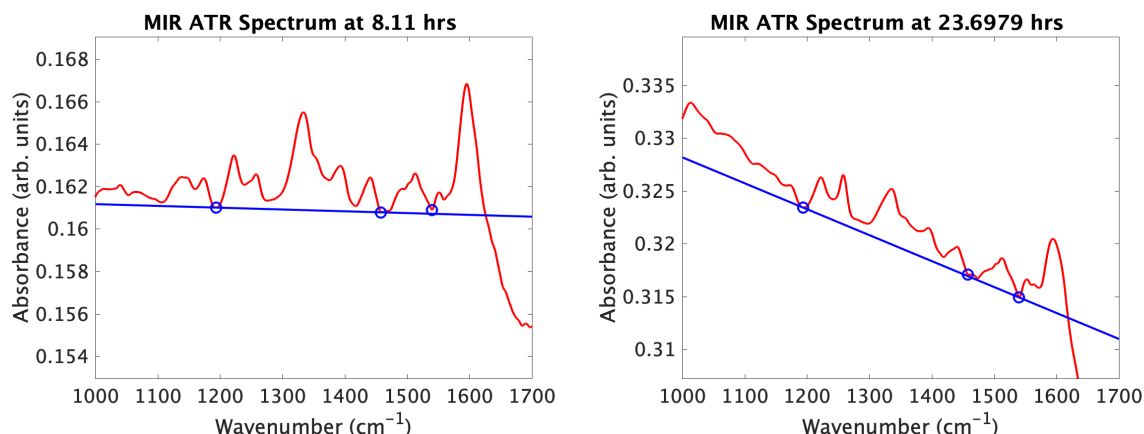


Figure 6.10: ATR spectra recorded at two different times showing how the baseline changes. The three stationary points (marked by blue circles) always fit on the line.

broadened because they are in liquid. The overall fitting function was then,

$$\text{Abs}(k) = (m \cdot k + c) \left[ A_1 \exp \left[ -\frac{1}{2} \left( \frac{k-k_1}{\sigma_1} \right)^2 \right] + A_2 \exp \left[ -\frac{1}{2} \left( \frac{k-k_2}{\sigma_2} \right)^2 \right] \dots + 1 \right], \quad (6.1)$$

where the first peak has amplitude  $A_1$ , centre wave number  $k_1$ , and width  $\sigma_1$ , and so on for each additional peak in the fit. It is easy to see that this expression reduces to the equation of a line when all the peak amplitudes are zero, i.e.

$$\lim_{A_n \rightarrow 0} [\text{Abs}(k)] = m \cdot k + c. \quad (6.2)$$

The initial guesses for the fit were manually coded, by inspecting the full spectrum and a non-linear regression function in Matlab called '**nlinfit**' was used. The initial guesses were sent to the '**nlinfit**' function in the form of a column vector ' $\text{fit}_{start}$ ' composed of triples  $\{A_n, \sigma_n, k_n\}$ , along with the data for each spectrum, i.e.

$$\text{fit}_{end} = \mathbf{nlinfit}(\text{data}(k), \text{fit}_{start}, \text{Abs}(k)) \quad (6.3)$$

and the fitted peak values were returned as a second column vector composed again of the fitted triples  $\{A_n, \sigma_n, k_n\}$ . The optimisation of the fitting function took a considerable amount of time with the first attempt at fitting to known peak locations (from figure 6.2). Initially,

these known peak vibrational frequencies were input as the initial guesses for the fits which proved to be partially successful. However, the most successful strategy was to fit the data piecewise to remove any anomalous fits to the outside of the spectral data. Three pieces were sufficient to achieve a stable fit, as shown in figure 6.11. This figure illustrates the difficulty in fitting this data using gaussians and highlights that there were additional peaks present not seen in ovchinnikovs paper<sup>98</sup> which further confused the fitting algorithm.

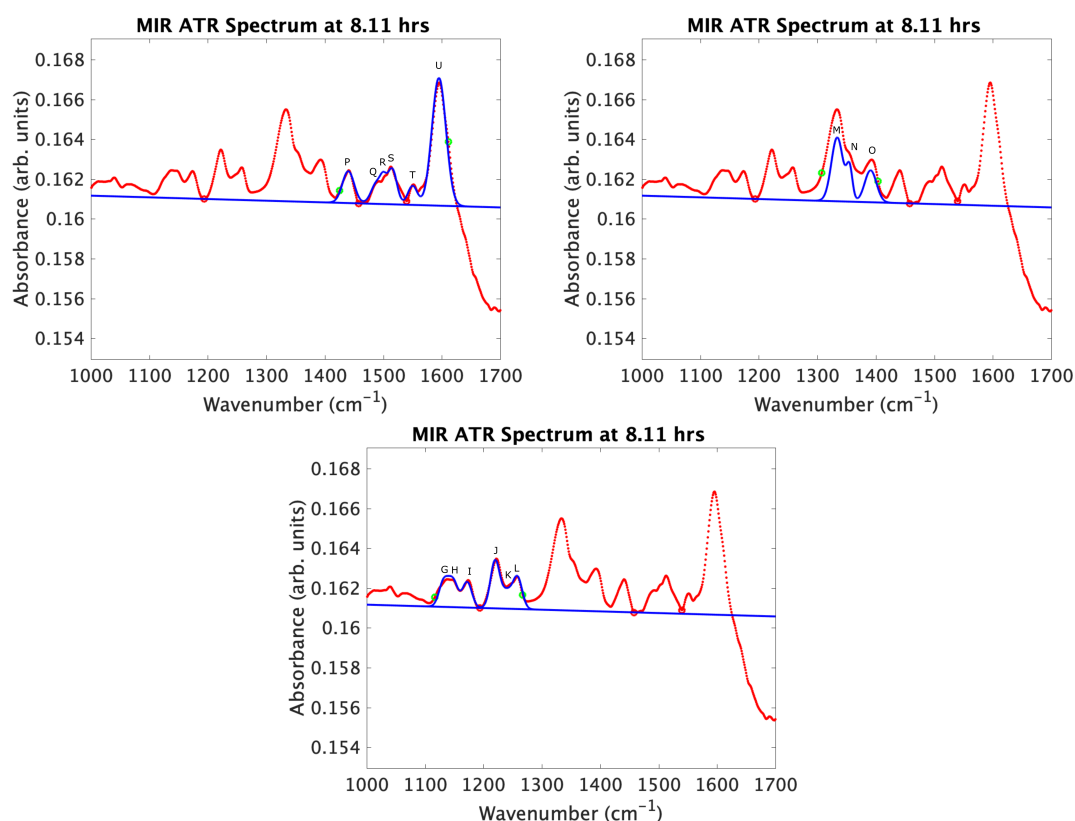


Figure 6.11: Initial attempts at the piecewise fitting windows showing the three groups of peaks labelled from right to left (low to high wavenumber), U-P, O-M, L-G.

To overcome the difficulty in fitting, additional peaks were added where visibly peaks could be seen in the spectrum, and the resultant fit can be seen in figure 6.11. In some instances (e.g. peak Q) there was a peak added to the function that later was removed as it was seen to be weak in intensity and therefore wasn't used in the final analysis (see figure 6.11). In order to visualise the component gaussians used in the final fitting algorithm seen in figure 6.12, the deconvolved graphs of just the gaussian fits were included in this thesis. As can be seen in



figure 6.12, the fitting algorithm produced a smooth fit to the spectral data. To further test the algorithm's function, each spectrum throughout the whole reaction was fitted and visual confirmation at each stage identified the algorithm produced a good fit to the data.

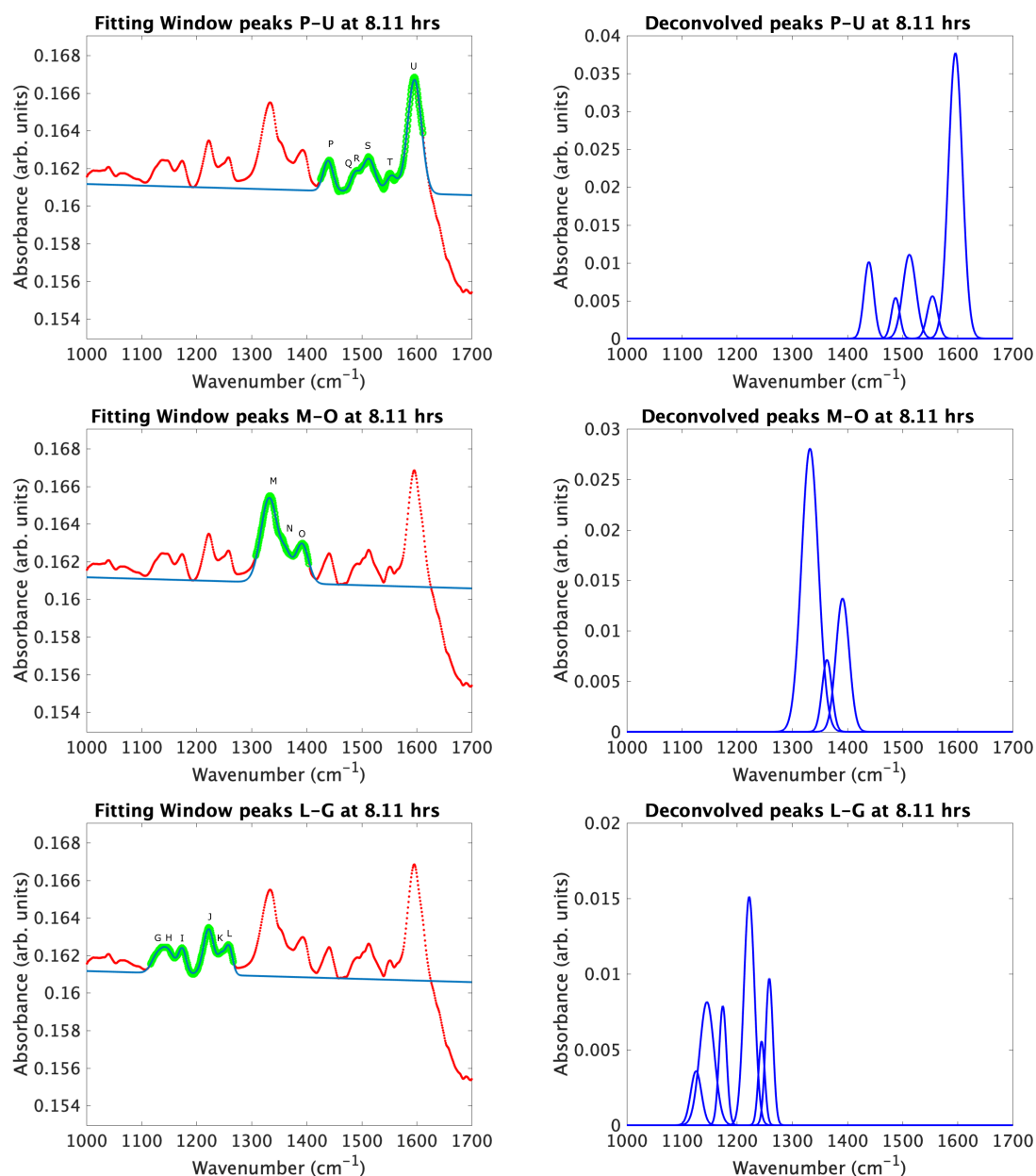


Figure 6.12: In the left column: Fitted data showing the three groups of peaks labelled from right to left (low to high wavenumber), G-L, M-O, P-U. In the right column: The corresponding de-convolved peaks with the baseline removed.

## 6.6 Results and Discussion

### 6.6.1 Visible absorbance result

The visible absorbance data was collected simultaneously with the IR measurements, the results can be seen in figure 6.13. These results are similar to those seen from the Raspberry Pi setup with a similar overall decay time (time for  $\frac{1}{e}$  to be removed from solution). The initial experimental setup seen in figure 6.4 was used for the first test measurements of this reaction, however due to the poor dynamic range of the Raspberry Pi it was replaced by a Keithley multimeter. The reaction time calculated from this Keithley multimeter setup data was  $8.85 \pm 0.04$  hrs (using the same methods as seen in chapter 2). This agrees with the first visible spectroscopy data seen in figure 4.2 in chapter 4 which mimicked the same experimental setup. This reaction time could then be used as a baseline for comparison against each bond's degradation monitored in the full degradation reaction.

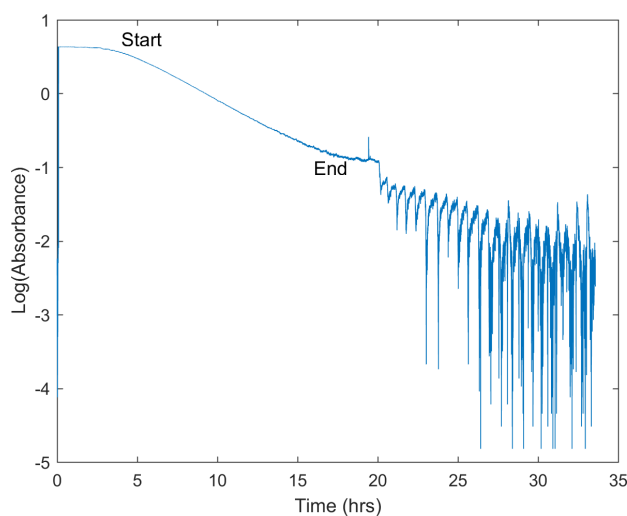


Figure 6.13: Visible absorbance data on a logarithmic scale over the full degradation reaction. The initial 6 hours were the mixing period of the methylene blue with deionised water. The start and end text indicates the points at which the data was linearly fitted.

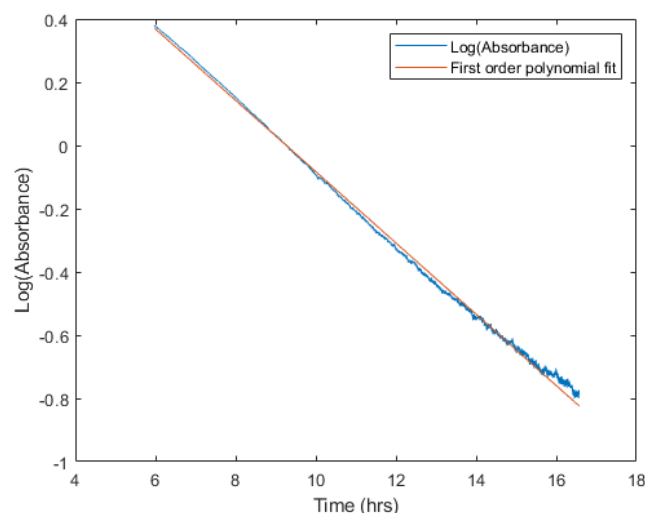


Figure 6.14: Fitted data from the visible absorbance plot seen in figure 6.13. The linear fit gave a gradient of -0.113 which translates to a reaction time of  $8.85 \pm 0.04$  hrs.

### 6.6.2 Peak fitting result

Using the peak fitting algorithm each resolvable peak was analysed by plotting peak amplitude, peak width and central peak frequency against time, the results can be seen in figures 6.15...6.20. These results contain a large amount of spectral information, and so to begin with figures 6.15 and 6.16 will be discussed. These graphs represent the peaks amplitudes of the features seen throughout the spectrum, the letter identifier of each peak was assigned from a central bond of interest at  $1334\text{ cm}^{-1}$  that was labelled M, with the adjacent bonds labelled accordingly. The over-ruling trend of the peak amplitudes seen over time show a common initial increase, followed by a time of equilibrium and ending with an exponential decay. The first conclusion to be taken from these results is that the ATR equipment used for optical detection of a reaction worked, and the data produced provides a better understanding of the reaction pathways throughout methylene blue degradation (using a ZnS ATR crystal).

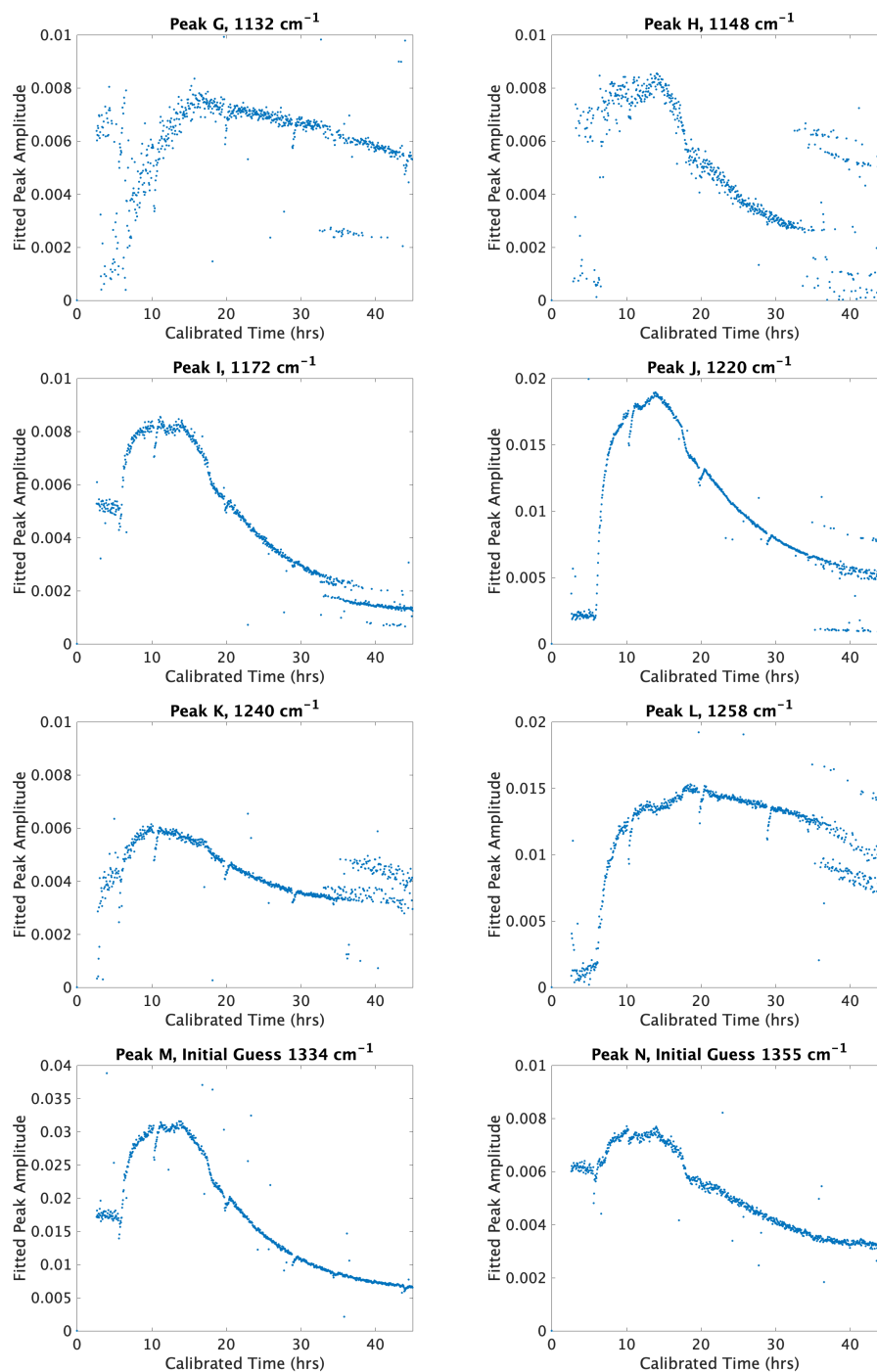


Figure 6.15: Fitting peak amplitude for peaks G-N.

In addition to the peak amplitude graphs, the peak centres were analysed to ensure that the initial guesses used for fitting were correct. As can be seen in figures 6.17 and 6.18, the majority of peak positions remained constant around a central value, with other peaks shifting

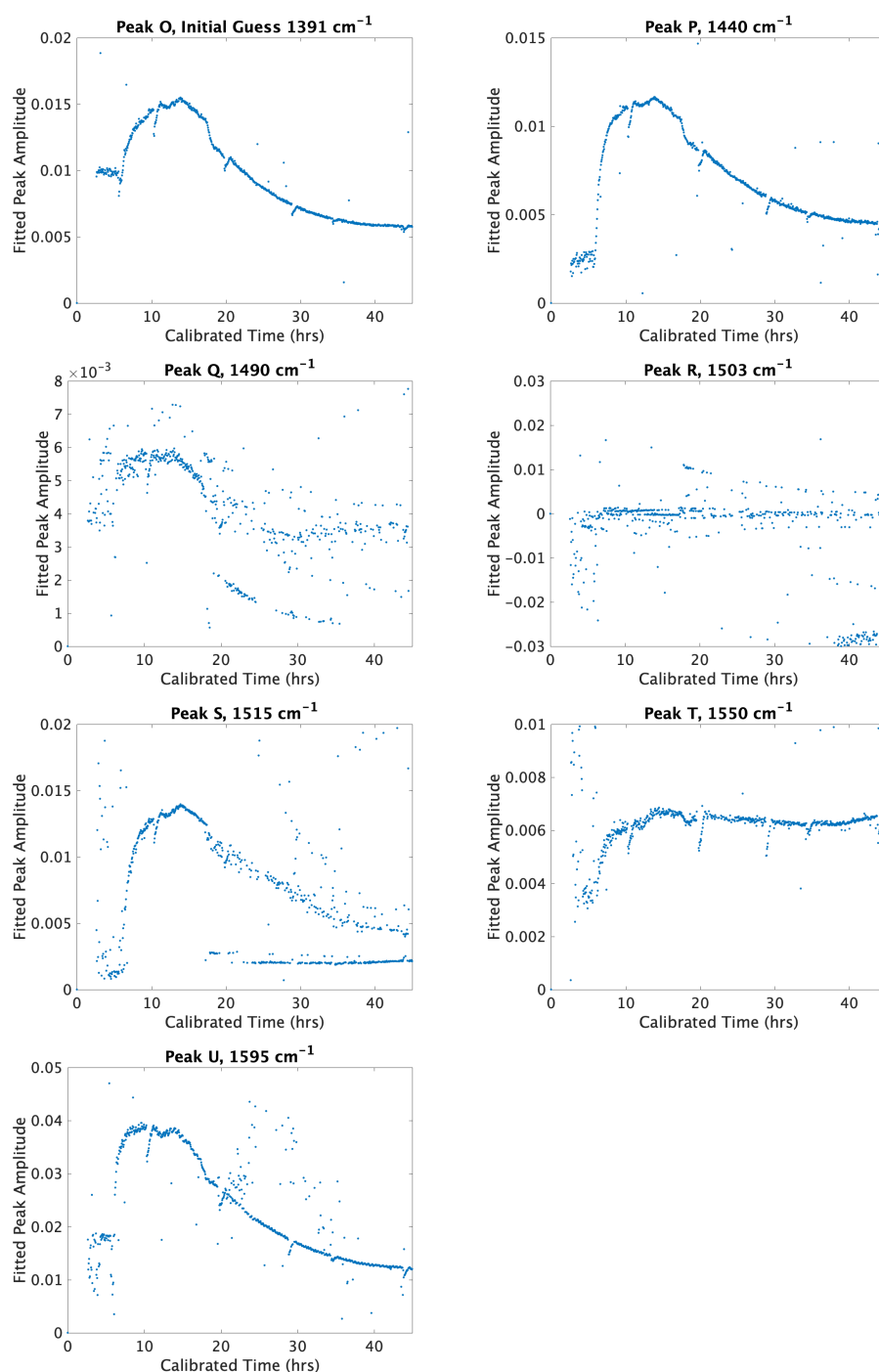


Figure 6.16: Fitting peak amplitude for peaks O-U.

throughout the reaction. Peaks R, Q and S show an unclear trend as peak R was fitting a zero amplitude peak (anomaly of the algorithm). What can be concluded from these figures is that the initial guesses for peak locations (found from figure 6.2) were correct. Finally, the peak

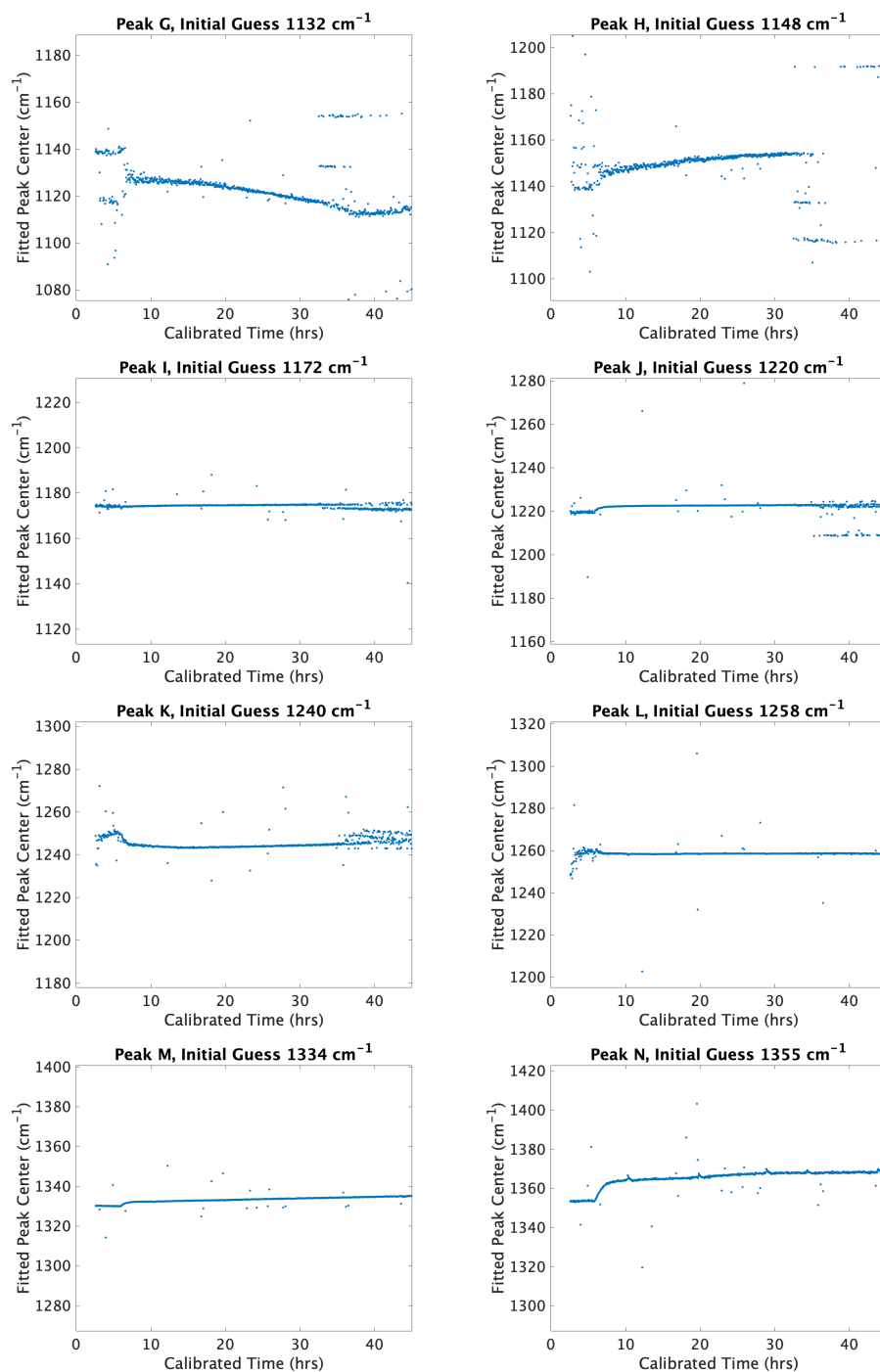


Figure 6.17: Fitting peak centres for peaks G-N.

width of each peak were plotted to identify whether the initial guesses for the algorithm were correct. The results of this can be seen in figures 6.19 and 6.20. Peak G is the only peak that displays changes in both peak width and peak centre, this is due to its position in the fitting

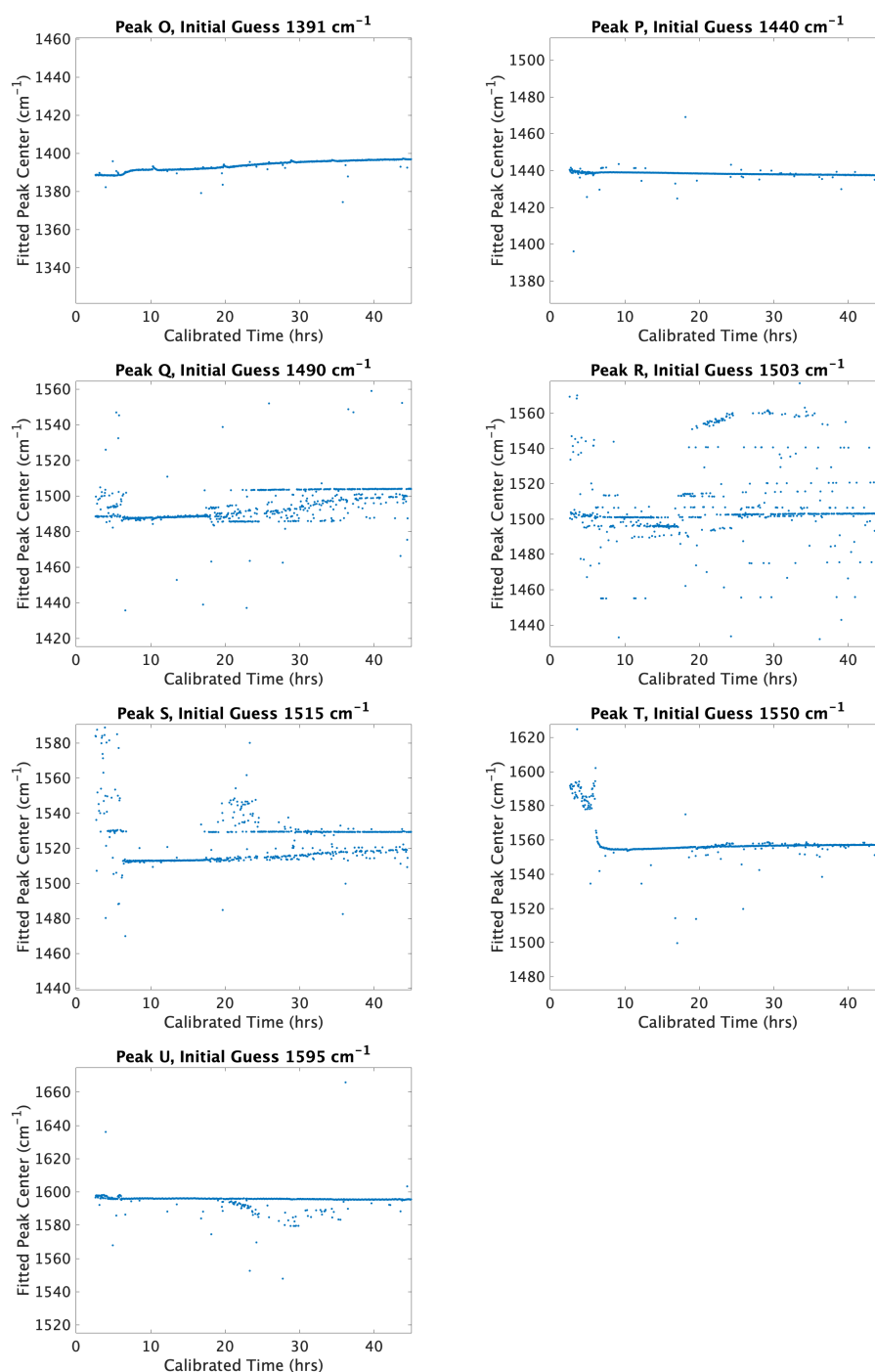


Figure 6.18: Fitting peak centres for peaks O-U.

algorithm. Both peak G and peak U are on the edge of the fitting window, the data either side of this window dramatically changes throughout the reaction therefore these fits were difficult to perfect. A consequence of this is a poor fit to peak G. Aside from this, all other peaks remain

consistent over the full reaction which is another indication that the initial guesses for peak width were correct.

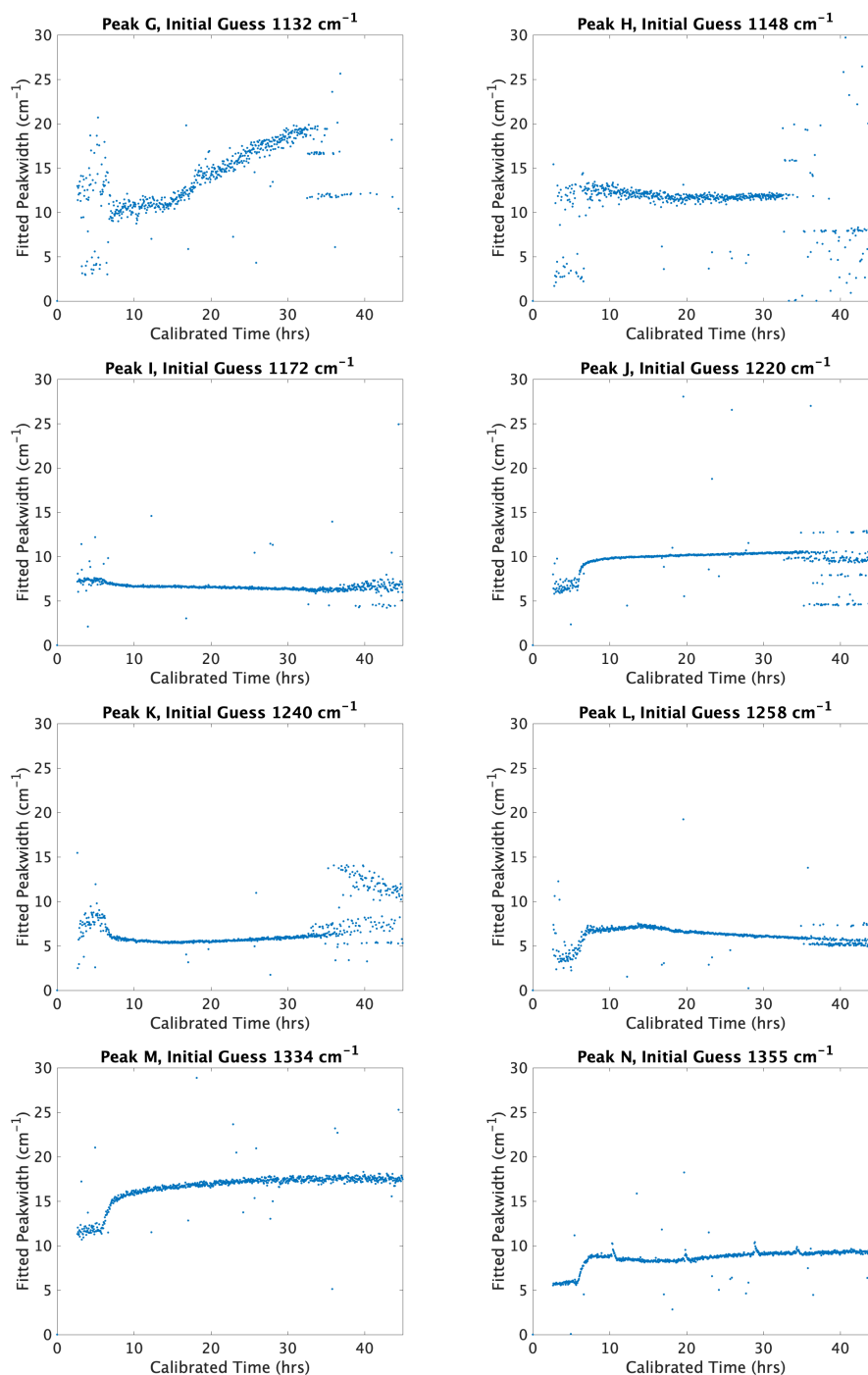


Figure 6.19: Fitting peak widths for peaks G-N.



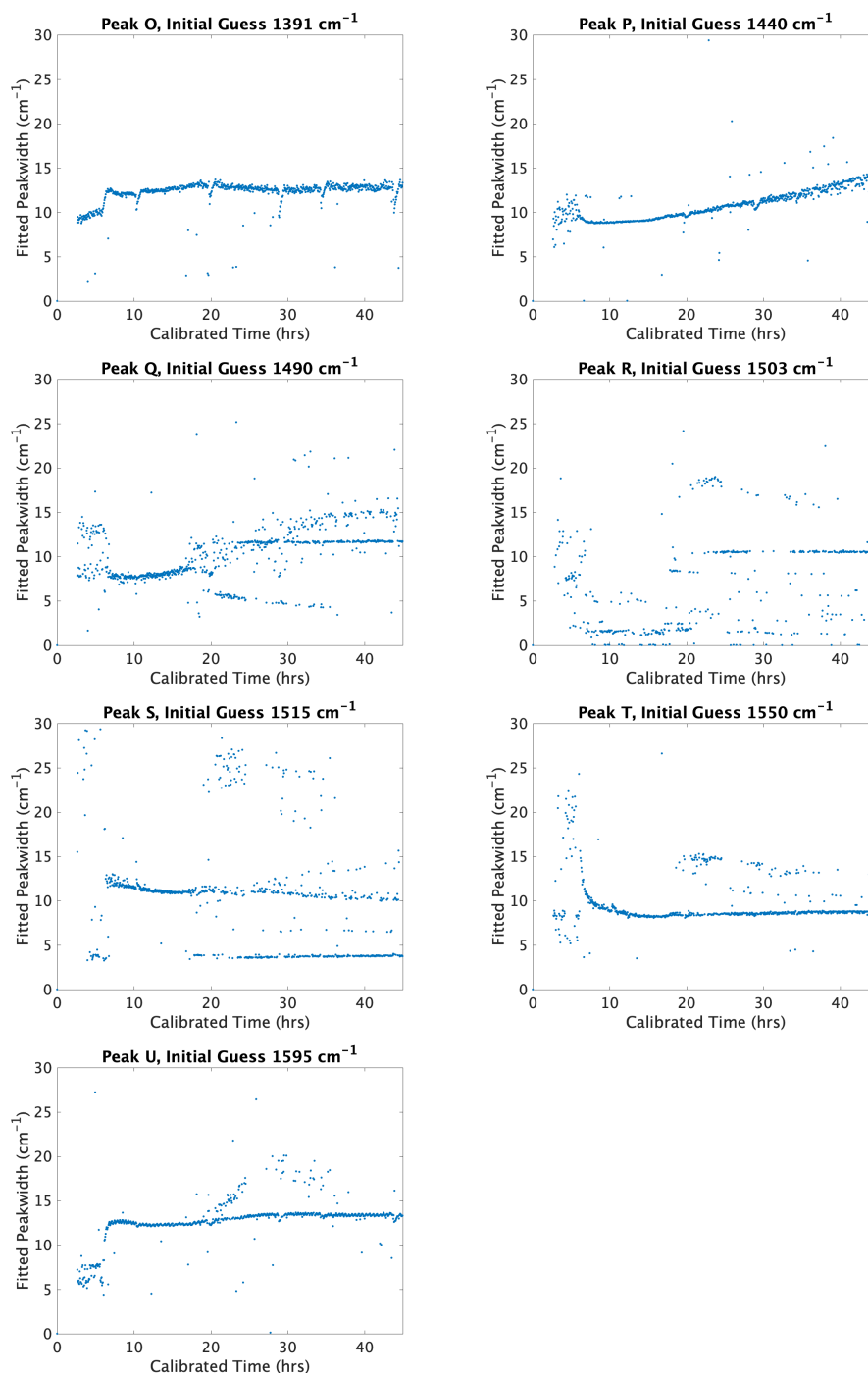


Figure 6.20: Fitting peak widths for peaks O-U.

With reference to the first 15 hours ( the beginning 6 hours of the experiment monitored the mixing process of the methylene blue molecules, followed by the UV LED and  $\text{TiO}_2$  being introduced to the system at  $T=6$  hours), there is an initial state of equilibrium followed by a

clear exponential increase seen across all peak heights. The mixing process discussed in section 6.4.1 could be seen in some of these molecular lines, for example peaks G,H,K,Q and T all display an increase in peak amplitudes over the initial 6 hour mixing period. However, peaks I,J,L,M,N,O,P,S and U all display a very small difference in peak amplitudes over the same time frame. This could suggest that the mixing within the ATR cell could be on the same timescale as that seen in the visible flowcell making it a non-issue with regards to this experiment. The cause of the initial increases in peak amplitude after the allotted mixing time were yet to be understood, however an initial theory was posed. This uniform trend seen in all peak height figures was theorized to be a direct affect of association /dissociation of the methylene blue molecules (dimers/trimers) on the ZnS surface. To be able discuss this association/ dissociation process, the MIR absorbance data was further analysed.

### 6.6.3 Understanding the MIR absorbance data

Figure 6.21 shows the integrated MIR absorbance data over the range of interest (1100-1600  $\text{cm}^{-1}$ ). The integrated absorption curve has four distinct phases. At  $T = 0$  the methylene blue was added to the water and the pump was turned on. There was an initial fast rise in the absorbance in the first few minutes as the methylene blue dye began to move through the system. This stabilised quickly, so that between  $T = 0 \rightarrow 6$  hrs the MIR absorbance stays reasonably constant as the dye mixes and reaches a stable concentration. Note that there is no evidence of any reaction during this stage. At  $T = 6$  hrs the UV lamp was turned on, and the  $\text{TiO}_2$  photocatalyst mediated reaction begins. This was evidenced by a measurable decrease in the visible absorbance, also shown in figure 6.21. The MIR absorbance showed rapid increase in absorbance during this phase. This is interesting because according to the visible data, the methylene blue is continuously being broken down, and yet the integrated MIR absorbance is increasing. Even though the methylene blue molecule is being cleaved, the total number of chemical bonds from the pristine methylene blue molecule should be more-or-less the same as the number of bonds in the daughter products. So, this relatively large increase in absorbance is a puzzle. By about  $T = 10$  hrs the rate of change of absorbance appears to slow down and stabilise to a maximum value. It remains reasonably stable for the next 4 hrs, and then starts

to decrease (after  $T = 14$  hrs), returning to approximately the initial absorbance level when the dye was fully mixed at  $T = 6$  hrs, just before the UV lamp was turned on.

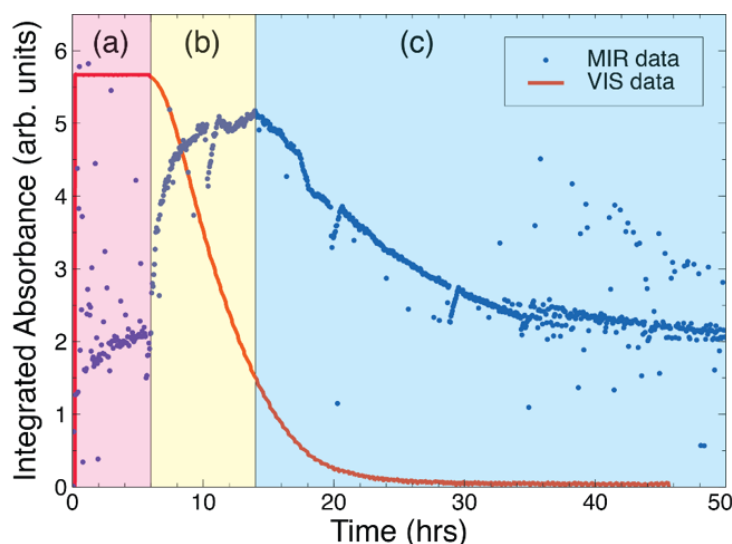


Figure 6.21: Blue circles: Time evolution of background subtracted integrated absorbance in the range  $1100\text{--}1600\text{ cm}^{-1}$  over the course of the methylene blue reaction. Red line: Time evolution of the visible absorbance measured simultaneously in the flow cell. The three different phases of the curve refer to (a) The methylene blue solution mixing thoroughly with the pump running for approximately 6 hours after the dye was initially added at  $T = 0$ . (b) Rapid increase in integrated MIR absorbance immediately on UV lamp turn on (which also coincides with the onset of the visible change in absorbance). (c) After 14 hours the absorbance begins to decrease with time.

### 6.6.3.1 Surface Plasmon Sensors and the Langmuir Model

The time evolution of the MIR absorbance shows remarkable similarity to another type of reaction curve well-known in bio-sensing. Surface plasmons are collective electron oscillations that can occur on the surface of a metal. They do not normally couple to electromagnetic radiation because of the momentum mismatch between the plasmons and the normal normally accessible  $k$ -vectors of light. However, Heinz Raether discovered that very specific geometries could be exploited to couple electromagnetic radiation to the surfaces plasmons<sup>107</sup>. In a groundbreaking paper published the following year together with Erich Kretschmann<sup>69</sup>, they published the now famous Kretschmann-Raether geometry which exploits total internal reflection to excite

surface plasmons in a thin metallic layer evaporated onto a glass substrate. Like the ATR geometry used in this experiment, surface plasmons resonance is also very sensitive to small changes in the optical properties near the surface of the metal, and thus it may be used as a sensor to monitor chemical processes at metal interfaces<sup>105,46,57</sup>. The adhesion of molecules to a surface was first described by Irving Langmuir in 1916, for which he was later awarded the Nobel Prize in Chemistry (1932). Consider a concentration of molecules available for adsorption on a surface with a concentration of adsorbing sites<sup>89</sup>. The reversible equation defining this adsorption reaction is,



where  $[AB]$  describes the concentration of the adsorbed complex on the surface. The rate at which this reversible adsorption reaction proceeds is given by,

$$\frac{d[AB]}{dt} = [A][B]k_{on} - [AB]k_{off} . \quad (6.5)$$

It is assumed that the signal  $R$  measured is proportional to the concentration  $[AB]$ , and that the maximum signal  $R_{max}$  (when all of the adsorbing sites are occupied) is proportional to  $[B]$ . This allows the rate equation to be rewritten,

$$\frac{dR}{dt} = k_{on}[A]R_{max} - (k_{on}[A] + k_{off})R . \quad (6.6)$$

Integration of this equation gives,

$$R = \frac{k_{on}[A]R_{max}}{k_{on}[A] + k_{off}} \left( 1 - e^{-(k_{on}[A] + k_{off})t} \right) . \quad (6.7)$$

If the conditions are changed so that the concentration  $[A]$  falls to zero, then  $AB$  will begin to dissociate to restore the equilibrium and consequently  $R$  will fall according to the equation,

$$\frac{dR}{dt} = -k_{off}R , \quad (6.8)$$

with solution,

$$R = R_{max}e^{-k_{off}t} . \quad (6.9)$$

This ideal signal response  $R$  to a step function change in the concentration of  $[A]$  is plotted in figure 6.22 for different values of concentration  $[A]$ .

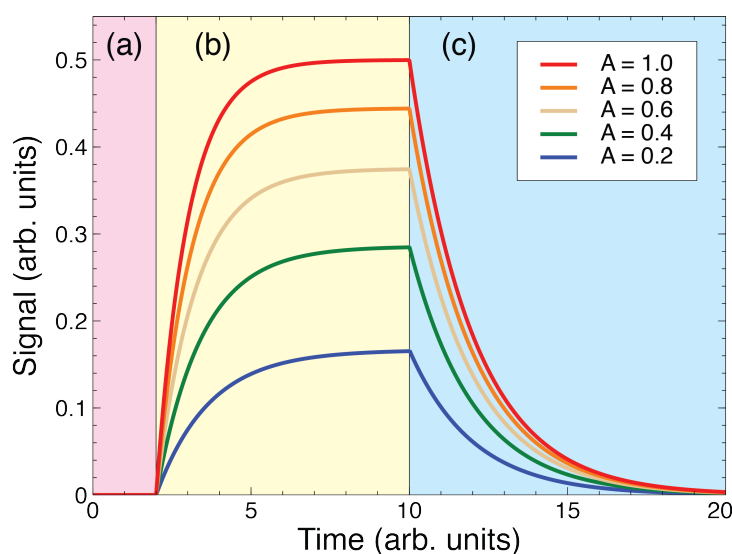


Figure 6.22: Signal response  $R$  to step function changes in the concentration of adsorbed molecules on a surface. The concentration  $[A]$  is turned on at  $t = 2$ , and the association phase begins. The value of  $R_{max} = 1$ , and  $k_{on} = k_{off} = 0.5$ . (a) Concentration of  $[A] = 0$ . (b) The concentration  $[A]$  is turned on. (c) Dissociation phase where the concentration  $[A]$  is turned off

The values of  $k_{on}$  and  $k_{off}$  can be inferred from the shape of the signal response in the association and dissociation phases respectively.

### 6.6.3.2 Hypothesised Explanation for MIR Behaviour

The shape of figure 6.21 might be explained by the a similar adsorption process on the surface of the ZnS ATR crystal. The MIR absorbance does not appear to change significantly during the mixing phase indicating that the methylene blue solution is stable. However as soon as the UV light is switched on, the absorbance increases rapidly, which might indicate that one of the products of the photo-decomposition of methylene blue is attaching to the surface of the

ZnS. There are possible modifications to the model just described to account for an exponential decrease in the concentration of the hypothesised adsorbent in solution as might be predicted from the visible absorbance data.

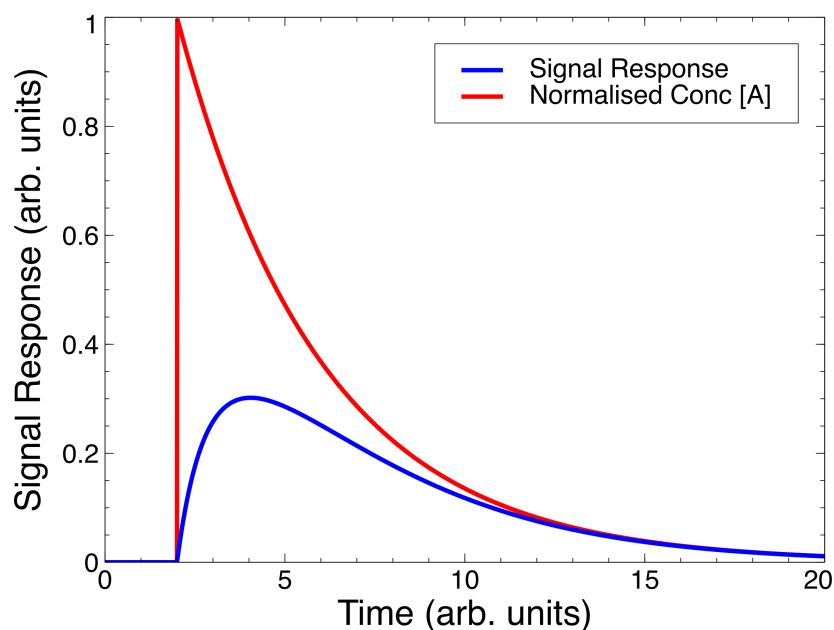


Figure 6.23: Signal response  $R$  to changes in the concentration of adsorbed molecules on a surface under the same detector parameters used in figure 6.22. The concentration  $[A]$  is turned on at  $t = 2$ , and decreases exponentially with a rate constant  $k = 0.25$ . This plot highlights that the rate of decay of the sensor signal is a convolution of the  $k_{off}$  rate and the exponential decay of the concentration  $[A]$ .

Figure 6.23 shows the signal response expected when the concentration of  $[A]$  decays exponentially as might be predicted making reference to the visible absorbance data. The curve in this figure is similar in shape to the data in figure 6.21. However this figure also raises an important point. The decay of the signal response is a convolution of the  $k_{off}$  rate and the exponential decay of the concentration  $[A]$ . This means that in order to extract the true photocatalytic reaction rates from the MIR absorbance data some a-priori knowledge of the surface adsorption would be needed to deconvolve the two rates. The dissociation rate would also need to be significantly faster than the reaction rate.

### 6.6.4 Calculating a decay time for each bond

An initial analysis of the dissociation and degradation reaction of each vibrational bond was done by plotted each peak height (from 15 hours) on a logarithmic scale to calculate a decay time, the results of which have been collated in table 6.1. The results from table 6.1 have been directly compared with the visible absorbance data to identify a dissociation time, which, in turn could also be seen as a degradation time for each bond.

| Wavenumber (cm <sup>-1</sup> ) | Peak label | Decay time (hrs) | Assignment <sup>98</sup> |
|--------------------------------|------------|------------------|--------------------------|
| 1595                           | U          | 11.6 ± 0.05      | (C=C)het , (C=N)het      |
| 1550                           | T          | n/a              | (C-N)het                 |
| 1440                           | P          | 11.95 ± 0.1      | unassigned               |
| 1391                           | O          | 10.5 ± 0.5       | (CH)as                   |
| 1355                           | N          | 12.0 ± 0.1       | (C=S <sup>+</sup> )het   |
| 1334                           | M          | 9.5 ± 0.01       | C-N in N-CH <sub>3</sub> |
| 1258                           | L          | 29.7 ± 0.01      | CH                       |
| 1240                           | K          | 19.1 ± 0.1       | (C-C)het                 |
| 1220                           | J          | 9.66 ± 0.01      | (C-C)het                 |
| 1172                           | I          | 10.29 ± 0.5      | (CH)het                  |
| 1148                           | H          | 9.39 ± 0.1       | (C-N)het                 |
| 1132                           | G          | n/a              | (C-N)het                 |

Table 6.1: Table of potential bond assignments from the Ovchinnikov *et al* paper<sup>98</sup>. Here ‘het’ stands for heterocyclic stretch and ‘as’ represents asymmetric stretch.

The trend of the majority of these peaks is a decay over a long time scale with peaks R,Q and S displaying a poor trend as they represent peaks with weak signal. The poor fitting of a weak amplitude peaks directly affects the peaks adjacent to them, therefore these peaks were not analysed in detail. In addition to an overall decaying trend in the data, there is also an initial increase after the TiO<sub>2</sub>/UV had been added to the reaction which could be a direct effect of the mixing process or instead a real effect as a result of the TiO<sub>2</sub>/UV activation. From the Houas *et al* publication<sup>58</sup>, the proposed initial stage of the breakdown of a methylene blue molecule shows that the first bonds to break are the N=C-H and C=S<sup>+</sup>. As a consequence of this the N-H<sub>2</sub>, S=O and S-C are then created. Reviewing Ovchinnikovs paper<sup>98</sup>, the vibrational frequency assigned to a C=S<sup>+</sup> stretch is at 1355 cm<sup>-1</sup> and a C-N heterocyclic stretch can be seen at 1335 cm<sup>-1</sup>. For a more extensive list of bond assignment please see table 6.1.

Focusing on the theoretical degradation process, peaks N, L, T, G and H were analysed. Peak N shows an initial increase (along with the other peaks) then remains steady until approximately 15 hrs where it begins to quickly decay, and at 18 hrs it then gradually decays and finally stabilises. The other peaks fitted in this figure don't fit the same trend and show different start times for decay. Looking at table 6.1 decay times have been measured for each of these peaks. The results in figure 6.1 give a first estimation of the reaction pathways based on the decay times of each bond. From table 6.1 the times show that in the dissociation phase of the reaction (when the methylene blue begins to degrade) the first peak to break is the C–N heterocyclic peak (peak H). After this, the external C–N in N–CH<sub>3</sub> bond begins to breakdown (peak M), followed by the C–C heterocyclic stretch (peaks J/K). If Houas' theoretical breakdown is to be followed, as the C=N bond decreases the C–H bond should increase, this bond is assigned to peak L. However, as can be seen in figure 6.15 this isn't the case in the long timescale, but up until 20 hrs it does show an increase in trend. These results contain a wealth of chemical information into the degradation reaction, however without modelling each stage of the reaction structure on a molecular level, conclusions as to the reaction pathways cannot be concluded. What can be concluded is that this optical measuring technique has worked and it can be used to identify chemical reactions in aqueous solutions using IR spectroscopy.

## 6.7 Summary

This chapter tested a ZnS ATR crystal with a modified experimental setup to measure a steady-state spectrum of methylene blue which agrees with that seen in recent publications. Initial tests highlighted the potential difficulties with the full degradation measurement. The first of these was the potential mixing of the methylene blue which could have been affecting the baseline of the spectra. With reference to the ATR cell design, originally the thought that a small pockets of liquid had been held inside the cell, causing the mixing process to take longer than that seen in the visible absorbance setup was postulated. However, after analysing each peak amplitude from the final spectra, the majority of peaks displays a constant amplitude in the first 6 hrs of the experiment (when only methylene blue was present). In addition to this,



the detector filling cycles were thought to affect the baseline drift of the spectra, but the peak amplitude graphs also confirmed that this wasn't a possibility, as before and after filling the baseline returned to its previous position. This then removed the possibility of the detector filling cycle contributing to the overall baseline shift observed. Therefore, a further theory was investigated which identified that single methylene blue molecules could have been adsorbed onto the ZnS surface, reached an equilibrium state and then finally dissociated from the surface and degraded. This theory is based on an equation called the Langmuir adsorption isotherm, and after comparing this principle to my data, there were strong similarities present. The conclusion from this investigation is that this theory could account for both a baseline shift over time and the uniform increase in all of the vibrational bond peak height signals throughout the first quartile of the experiment. Further quantitative analysis is required to confirm this theory and has consequently been identified as a future work for the project.

The experiment was run with both a visible absorbance setup and an ATR unit to measure MIR spectroscopy results simultaneously. The results from the visible absorbance flowcell showed a similar reaction time to that seen previously with the same added experimental equipment. The peaks seen throughout the reaction were plotted using a peak fitting algorithm and the results showed an overall decaying trend over a long time period. These results show a wealth of spectral information that require further analysis, this is included in the proposed future work for this project. From this thesis, an optical measurement of a degradation reaction using IR spectroscopy was successfully observed. Nonetheless, the experiment needs to be improved to optimise the time of reaction. Two specific ways that this experiment could be improved on is: by re-designing the ATR cell to allow a smaller volume of solution in the system and to increase the amount of photocatalyst present for reaction. These improvements will be expanded on in the final conclusions chapter. The main result from this experiment is that an aqueous reaction was and can be optically measured using ATR units and IR spectroscopy which has fulfilled the final aim of this thesis.

## 7 Conclusions and Future work

### 7.1 Summary and Perspective on Main Research Outcomes

Infrared spectroscopy is a powerful technique for measuring the vibrational frequencies of molecular bonds and hence it is commonly used as an identification tool in chemistry. For this reason, the region of the electromagnetic spectrum from around 8-12  $\mu\text{m}$ , is often called the fingerprint region. However, taking infrared measurements in an aqueous sample presented difficulties. Whilst the atmosphere is effectively transparent at visible wavelengths, many atmospheric trace gases such as water vapour and carbon dioxide have strong absorption bands in the IR which can overcome other spectral information. Consequently, many infrared measurements need to be taken under vacuum, to remove the influence of these gases on the measurement, this complicates the design of any experimental apparatus for this purpose. An additional difficulty is the absorption of IR light in aqueous liquids, making any form of transmission spectroscopy difficult. Liquid cells can of course be designed to have very short path lengths, but if the cell is to allow a continuous flow of liquid then this would produce a severe constriction in any flow system. It was for this reason that the principles of ATR were investigated, to effectively reduce the effective path length of IR light through an aqueous sample. However, when constructing an ATR crystal, the crystal material properties need to meet certain criteria (specific to this experiment), i.e the crystal material needs to be simultaneously transparent to infrared light and chemically stable in aqueous solutions, which provides further difficulty. Many of the conventional infrared materials fail under these conditions, including but not limited to a material commonly used for ATR crystals, Germanium (Ge). While Ge is chemically stable in the presence of liquids for short periods, experimental results indicate that it is not chemically

stable for continuously monitoring reactions in an aqueous environment. Silicon (Si) is chemically stable in an aqueous environment but its infrared transparency is disrupted by several strong absorption bands. These problems are discussed in chapter 5. Following this work, it was concluded that the best compromise material was Zinc Sulphide (ZnS). ZnS is non-toxic (unlike its sister infrared material ZnSe) and so it was able to be cut and polished. Unlike Ge, the long time-scale chemical stability experiments performed in water gave promising results, and it displayed no problematic spectral features in the electromagnetic window of greatest interest for chemical bond sensing.

As previously mentioned, the effective path length through aqueous media needed to be short enough to allow the infrared light (MIR) to traverse the medium without being fully absorbed. ATR is a convenient way of effectively reducing the path length seen through the aqueous medium to the length scale of evanescent waves (microns). However, early experiments showed that the sensitivity was then too low to detect the infrared spectral features of methylene blue in the millimolar concentrations necessary to detect reaction pathways. To solve this problem the ATR prisms and flowcell were redesigning to accommodate multiple bounces, thereby increasing the effective path length to a point where the sensitivity was sufficient to resolve the spectral features of the methylene blue molecule (these design rules are discussed in chapter 4).

Once the ZnS ATR cell had been optimised for optical detection, the main goal of this research was achieved; monitoring the infrared spectral signature of methylene blue in real-time during a photo catalytic degradation experiment (this is the work which is described in chapter 6). With a refined experimental setup, both the visible absorbance data and the reaction chemistry could be measured simultaneously. However, one final challenge with regards to the spectral data collected became clear. For reasons which have been postulated, the water baseline on which the methylene blue infrared absorption peaks sit, drifts very slowly over time. This is undoubtedly a consequence of the very long experimental timescales, which are typically 2-3 days. In order to remove this effect from the final data set, a peak fitting algorithm that de-convolved the peaks from the drifting baseline was developed. From this, the various peaks in the spectrum could be monitored and their changes could be recorded accurately over time. More work is needed to decipher what these trends mean, and collaborations with chemists who can model

these reactions will be necessary before these results can be fully understood. For example, the build up of apparent staining on the ZnS crystal face which was thought to be a product of association/dissociation of intermediate products of the methylene blue degradation. This effect can be seen consistently across all peaks measured, which upon repetition produced the same data trends. To elaborate on the results obtained in this final chapter (chapter 6), the concept of surface plasmon sensors and the langmuir model was introduced. The Langmuir model of association and dissociation was used as a hypothesised explanation for the behaviour of the peaks seen throughout the degradation reaction. However, this still remains to be quantified and proved in future work.

At the end of this PhD the main result (seen in chapter 6) indicated that mid-infrared ATR spectroscopy is a means to follow the molecular bonding during photocatalytic reactions in situ, and this thesis has shown it to work in real-time. Throughout this PhD the equipment was tuned and optimised to be able to produce the results seen in chapter 6, however there is considerable scope to further develop this technique in the future.

## 7.2 Future Work

The experiments have proven the viability of this spectroscopy technique for reaction monitoring in situ. The work should be seen as a proof-in-principle rather than a finished job, and there are many avenues for improvement. Some easy wins are discussed below.

### 7.2.1 Speeding up the Reaction

A limiting factor in these experiments was length of time it took to complete the chemical reaction. Typically, this was 2-3 days. There were a number of problems associated with this. Firstly, the MCT detector needs to be continuously topped up with liquid nitrogen every 12 hrs, and this disturbs the experiment. Secondly, there is significant drift of the water baseline over the time needed to perform the experiment. A simple hypothesis that might account for this effect could be related to a very slow surface reaction on the ZnS ATR crystal. One way of mitigating these problems would be to increase the speed of the reaction, and this could be

achieved by significantly reducing the volume of methylene blue solution circulating relative to the available surface area of  $\text{TiO}_2$ . This could be easily achieved by significantly reducing the length of pipework around the loop. A factor of two decrease in volume would be straightforward, although it would take a redesign of the current setup. Another way of improving the methylene blue volume to  $\text{TiO}_2$  surface ratio would be to look at ways of increasing the available surface area of  $\text{TiO}_2$ . At the moment, we only use one coated side of a 2 inch silicon wafer. Perhaps both sides of a UV transparent wafer like quartz could be coated with  $\text{TiO}_2$  to increase the activation surface for reaction, in addition to this, there may also be benefits in geometrically stacking wafers. These techniques are to be considered in the future development of this project.

### 7.2.2 Increasing the Sensitivity

The results from the ATR crystals showed that 3 reflections were sufficiently sensitive to monitor the methylene blue infrared absorption peaks. Other geometries could be explored to increase the number of bounces and consequently the sensitivity. This might additionally mean that less concentrated solutions could be used as the starting point, which would also contribute to speeding up the reaction.

### 7.2.3 Experimental Variables

The final experiment monitored the reaction that occurred when  $\text{TiO}_2$  was illuminated with light that fell within its bandgap. The future of this experiment could see the bandgap of the photo catalyst changing towards the visible region (due to the abundance of visible light in the solar spectrum). A further experiment that could be done, would be to measure the photon flux from the UV LED used, and to understand the potential benefits of changing the UV wavelength/intensity on the reaction.

### 7.2.4 Chemical Stability of ATR Crystal

The choice of ZnS for the ATR crystals used in these studies was a compromise. An understanding as to why the ZnS becomes stained during the reaction is still unknown, but theory suggests

that there may be a slow surface reaction taking place throughout the reaction. To mitigate this difficulty, the sister infrared material of ZnS, ZnSe could be tested if coated with a chemically stable material to remove the potential toxicity risk. In addition to ZnSe there is another stable material that wasn't used in this project due to restricted resources, that of Diamond. Diamond is transparent within the desired window of infrared frequencies, but is expensive and would present the challenge that it could not be cut or polished in-house due to its material properties (it is too hard). However, with progressing diamond growth technologies, diamond ATR crystals could be making their way to market, however this then limits the flexibility of in-house production (limited to the number of reflections that can be bought). One additional possibility would be to look towards coating another infrared material with diamond to make it chemically stable in aqueous environments. Throughout this PhD project, the Ge ATR crystal was used to attempt a diamond growth onto one of the facets, however these preliminary tests failed and due to the project's time restrictions, this idea was discarded. So, this method could be re-visited in the future of this PhD project.

### 7.2.5 Improving the Peak Fitting Algorithm

The peak fitting algorithm that was generated for this PhD project requires optimisation. Currently, the initial guesses for the peak centres/peak height and peak widths are chosen manually aside from the `nlinfit` function, and these initial guesses are used in a loop which cycles through all the spectra. The next step in developing this peak fitting algorithm would be to implement generating first guesses based on each spectrum inside the loop automatically from each dataset. This would undoubtedly lead to greater stability and possibly mean that the piecewise fitting of the spectrum could be dispensed with. This PhD project achieved its goal; to be able to detect a chemical reaction using novel optical measurement apparatus (ATR crystals). With the final results chapter as a baseline for the future of this work, and the future experiments/optimisations that have been outlined above, this research could give valuable information to the field of water treatment. The results from this PhD project could lead to a simple, inexpensive and sustainable water treatment technology that could ultimately contribute to the fight against the world water crisis.

### 7.2.6 Surface Analysis Techniques

Due to the material coating difficulty seen within the last few months of this PhD project, this phenomenon could be further analysed through the use of a dectack machine to profile the effect of the ‘staining’ on the ZnS crystal. Further experimental techniques that could be used to identify the surface if the ZnS post-reaction are XPS (X-ray photoelectron spectroscopy), surface characterisation using AFAS (advanced faults analysis software), AFM (atomic force microscopy) or other such material surface techniques. In addition to measuring the staining post-reaction, the Langmuir model could be used to simulate the association/dissociation of the methylene blue molecule to the ZnS surface. With an accurate simulation of the association/dissociation process, and real-time experimental results, the two can be compared to further this PhD research into ZnS surface chemistry in a photocatalytic organic dye degradation reaction.

# Bibliography

- [1] Syed Nabeel Ahmed and Waseem Haider. “Heterogeneous photocatalysis and its potential applications in water and wastewater treatment: a review”. In: *Nanotechnology* 29.34 (Aug. 2018), p. 342001. ISSN: 0957-4484. DOI: [10.1088/1361-6528/aac6ea](https://doi.org/10.1088/1361-6528/aac6ea).
- [2] Uduak G Akpan and Bassim H Hameed. “Parameters affecting the photocatalytic degradation of dyes using TiO<sub>2</sub>-based photocatalysts: a review”. In: *Journal of hazardous materials* 170.2-3 (2009), pp. 520–529.
- [3] Fritz Allhoff, Patrick Lin, and Daniel Moore. *What is nanotechnology and why does it matter?: from science to ethics*. John Wiley & Sons, 2009.
- [4] AS Almuslem et al. “Water soluble nano-scale transient material germanium oxide for zero toxic waste based environmentally benign nano-manufacturing”. In: *Applied Physics Letters* 110.7 (2017), p. 074103.
- [5] D. E. Aspnes and A. A. Studna. “Dielectric functions and optical parameters of Si, Ge, GaP, GaAs, GaSb, InP, InAs, and InSb from 1.5 to 6.0 eV”. In: *Physical Review B* 27.2 (Jan. 1983), pp. 985–1009. ISSN: 0163-1829. DOI: [10.1103/PhysRevB.27.985](https://doi.org/10.1103/PhysRevB.27.985).
- [6] P. W. (Peter William) Atkins and Julio. De Paula. *Elements of physical chemistry*. 5th. Oxford: Oxford University Press, 2009, p. 578. ISBN: 9780199226726.
- [7] Scott S. Auerbach et al. “Toxicity and carcinogenicity studies of methylene blue trihydrate in F344N rats and B6C3F1 mice”. In: *Food and Chemical Toxicology* 48.1 (Jan. 2010), pp. 169–177. ISSN: 0278-6915. DOI: [10.1016/J.FCT.2009.09.034](https://doi.org/10.1016/J.FCT.2009.09.034).
- [8] I. M. Baker. “MCT Photoconductive Infrared Detectors”. In: *Mercury Cadmium Telluride*. Chichester, UK: John Wiley & Sons, Ltd, Sept. 2010, pp. 429–446. DOI: [10.1002/9780470669464.ch18](https://doi.org/10.1002/9780470669464.ch18).
- [9] Patrick J Baker et al. “Structural consequences of sequence patterns in the fingerprint region of the nucleotide binding fold: implications for nucleotide specificity”. In: *Journal of molecular biology* 228.2 (1992), pp. 662–671.
- [10] David W. (David Warren) Ball and Society of Photo-optical Instrumentation Engineers. *Field guide to spectroscopy*. SPIE, 2006, p. 110. ISBN: 9780819463524.
- [11] Adir Bar-Lev. *SEMICONDUCTORS AND ELECTRONIC DEVICES 2nd EDITION*. Ed. by 2nd. Prentice-Hall International, Inc., 1984, pp. 60–68. ISBN: 0-13-806265-X.



- [12] R Barnes, Urner Liddel, and V Williams. “Infrared Spectroscopy. Industrial Applications”. In: *Industrial & Engineering Chemistry Analytical Edition* 15.11 (Nov. 1943), pp. 659–709. ISSN: 0096-4484. DOI: [10.1021/i560123a001](https://doi.org/10.1021/i560123a001).
- [13] Beer. “Bestimmung der Absorption des rothen Lichts in farbigen Flüssigkeiten”. In: *Annalen der Physik und Chemie* 162.5 (Jan. 1852), pp. 78–88. ISSN: 00033804. DOI: [10.1002/andp.18521620505](https://doi.org/10.1002/andp.18521620505).
- [14] Tadhg P Begley. “Photoenzymes: a novel class of biological catalysts”. In: *Accounts of chemical research* 27.12 (1994), pp. 394–401.
- [15] A Bendavid and Philip Martin. “Review of thin film materials deposition by the filtered cathodic vacuum arc process at CSIRO”. In: *Journal of the Australian Ceramic Society* 50 (2014), p. 86.
- [16] John E. Bertie and Zhida Lan. “Infrared Intensities of Liquids XX: The Intensity of the OH Stretching Band of Liquid Water Revisited, and the Best Current Values of the Optical Constants of H<sub>2</sub>O(l) at 25°C between 15,000 and 1 cm<sup>-1</sup>”. In: *Applied Spectroscopy* 50.8 (Aug. 1996), pp. 1047–1057. ISSN: 0003-7028. DOI: [10.1366/0003702963905385](https://doi.org/10.1366/0003702963905385).
- [17] Mario Boehme and Wolfgang Ensinger. “Mixed Phase Anatase/rutile Titanium Dioxide Nanotubes for Enhanced Photocatalytic Degradation of Methylene-blue”. In: *Nano-Micro Letters* 3.4 (Dec. 2011), pp. 236–241. ISSN: 2311-6706. DOI: [10.1007/BF03353678](https://doi.org/10.1007/BF03353678).
- [18] Geoffrey Colin Bond. “Heterogeneous catalysis”. In: (1987).
- [19] Mamadou Bountogo et al. “Efficacy of methylene blue monotherapy in semi-immune adults with uncomplicated falciparum malaria: a controlled trial in Burkina Faso”. In: *Tropical Medicine & International Health* 15.6 (June 2010), pp. 713–717. ISSN: 13602276. DOI: [10.1111/j.1365-3156.2010.02526.x](https://doi.org/10.1111/j.1365-3156.2010.02526.x).
- [20] Thirimachos Bourlai. *Face recognition across the imaging spectrum*, p. 383. ISBN: 3319285017.
- [21] Elizabeth C. Butler and Allen P. Davis. “Photocatalytic oxidation in aqueous titanium dioxide suspensions: the influence of dissolved transition metals”. In: *Journal of Photochemistry and Photobiology A: Chemistry* 70.3 (1993), pp. 273–283. ISSN: 1010-6030. DOI: [https://doi.org/10.1016/1010-6030\(93\)85053-B](https://doi.org/10.1016/1010-6030(93)85053-B).
- [22] John Calkins, James D Buckles, and John R Moeller. *The role of solar ultraviolet radiation in ‘natural’ water purification*. 1976.
- [23] Robert L Carter. *Molecular symmetry and group theory*. Wiley New York, 1998.
- [24] Pamela M Chu et al. “The NIST quantitative infrared database”. In: *Journal of research of the National Institute of Standards and Technology* 104.1 (1999), p. 59.

- 
- [25] *Clean Water Crisis Facts and Information*. URL: <https://www.nationalgeographic.com/environment/freshwater/freshwater-crisis/> (visited on 08/21/2018).
- [26] Richard Connor. *The United Nations world water development report 2015: water for a sustainable world*. Vol. 1. UNESCO publishing, 2015.
- [27] Marek Danilczuk et al. “Understanding the fingerprint region in the infra-red spectra of perfluorinated ionomer membranes and corresponding model compounds: Experiments and theoretical calculations”. In: *Journal of Power Sources* 196.20 (2011), pp. 8216–8224.
- [28] Kathleen A Davis. “Titanium dioxide”. In: *Journal of Chemical Education* 59.2 (1982), p. 158.
- [29] Locke Dean Spencer. *Introduction to FTS.pdf*. Tech. rep. 2003.
- [30] Sabrina Devouge et al. “Surface functionalization of germanium ATR devices for use in FTIR-biosensors”. In: *Journal of Colloid and Interface Science* 332.2 (Apr. 2009), pp. 408–415. ISSN: 0021-9797. DOI: [10.1016/J.JCIS.2008.12.045](https://doi.org/10.1016/J.JCIS.2008.12.045).
- [31] Veronica Diesen. *Heterogeneous TiO<sub>2</sub> Photocatalysis-Fundamental Chemical Aspects and Effects of Solid Phase Alterations*. Tech. rep.
- [32] Harry D Downing and Dudley Williams. *Optical Constants of Water in the Infrared*. Tech. rep. 12. 2082. DOI: [10.1029/JC080i012p01656](https://doi.org/10.1029/JC080i012p01656).
- [33] James W. E. Drewitt et al. “Structure of GeO<sub>2</sub> glass at pressures up to 8.6 GPa”. In: *Physical Review B* 81.1 (Jan. 2010), p. 014202. ISSN: 1098-0121. DOI: [10.1103/PhysRevB.81.014202](https://doi.org/10.1103/PhysRevB.81.014202).
- [34] Paul Erhart et al. “Band structure of indium oxide: Indirect versus direct band gap”. In: *Physical review B* 75.15 (2007), p. 153205.
- [35] Pedro LV Fale and KL Andrew Chan. “Preventing damage of germanium optical material in attenuated total reflection-Fourier transform infrared (ATR-FTIR) studies of living cells”. In: *Vibrational Spectroscopy* 91 (2017), pp. 59–67.
- [36] M. Farooq Wahab. “An easily constructed monochromator”. In: *Resonance* 14.10 (Oct. 2009), pp. 996–1002. ISSN: 0971-8044. DOI: [10.1007/s12045-009-0096-3](https://doi.org/10.1007/s12045-009-0096-3).
- [37] Richard P Feynman, Robert B Leighton, and Matthew Sands. *The Feynman Lectures on Physics*. II. Basic Books, 1964, pp. 33–1, 34. ISBN: 978-0-465-02494-0.
- [38] R. (Roberto) Fornari. *Single crystals of electronic materials : growth and properties*. ISBN: 008102097X.
- [39] Steven N Frank and Allen J Bard. *Infrared Spectroscopy in Surface Chemistry*. Tech. rep. 5. 1966, p. 1648.
-

- [40] AKIRA FUJISHIMA and KENICHI HONDA. “Electrochemical Photolysis of Water at a Semiconductor Electrode”. In: *Nature* 238.5358 (July 1972), pp. 37–38. ISSN: 0028-0836. DOI: [10.1038/238037a0](https://doi.org/10.1038/238037a0).
- [41] Akira Fujishima, Tata N Rao, and Donald A Tryk. “Titanium dioxide photocatalysis”. In: *Journal of photochemistry and photobiology C: Photochemistry reviews* 1.1 (2000), pp. 1–21.
- [42] “Fundamentals of FT-IR 2.1 Principle of Spectral Measurements”. In: (2017). DOI: [10.1007/978-4-431-56493-5\\_2](https://doi.org/10.1007/978-4-431-56493-5_2).
- [43] MA Al-Ghouti et al. “The removal of dyes from textile wastewater: a study of the physical characteristics and adsorption mechanisms of diatomaceous earth”. In: *Journal of environmental management* 69.3 (2003), pp. 229–238.
- [44] P Ken Gillman. “CNS toxicity involving methylene blue: the exemplar for understanding and predicting drug interactions that precipitate serotonin toxicity”. In: *Journal of Psychopharmacology* 25.3 (Mar. 2011), pp. 429–436. ISSN: 0269-8811. DOI: [10.1177/0269881109359098](https://doi.org/10.1177/0269881109359098).
- [45] Nicolas Godbert, Teresa Mastropietro, and Teresa Poerio. “Mesoporous TiO<sub>2</sub> Thin Films: State of the Art”. In: June 2018. ISBN: 978-1-78923-327-8. DOI: [10.5772/intechopen.74244](https://doi.org/10.5772/intechopen.74244).
- [46] JG Gordon II and S Ernst. “Surface plasmons as a probe of the electrochemical interface”. In: *Surface Science* 101.1-3 (1980), pp. 499–506.
- [47] A. E. Goresy et al. “An Ultradense Polymorph of Rutile with Seven-Coordinated Titanium from the Ries Crater”. In: *Science* 293.5534 (Aug. 2001), pp. 1467–1470. ISSN: 00368075. DOI: [10.1126/science.1062342](https://doi.org/10.1126/science.1062342).
- [48] P R Griffiths. “Fourier transform infrared spectrometry.” In: *Science (New York, N.Y.)* 222.4621 (Oct. 1983), pp. 297–302. ISSN: 0036-8075.
- [49] Peter R. Griffiths. *Chemical infrared Fourier transform spectroscopy*. Wiley, 1975, p. 340. ISBN: 0471327867.
- [50] Peter R. Griffiths and James A. De Haseth. *Fourier transform infrared spectrometry*. Wiley-Interscience, 2007, p. 529. ISBN: 9780471194040.
- [51] EA Guggenheim. “The computation of electric dipole moments”. In: *Transactions of the Faraday Society* 47 (1951), pp. 573–576.
- [52] Robert C Gumerman, Russell L Culp, and Sigurd P Hansen. “Estimating Water Treatment Costs. Volume 2. Cost Curves Applicable to 1 to 200 MGD Treatment Plants”. In: (1979).

- [53] V.P. Gupta and V.P. Gupta. “Interaction of Radiation and Matter and Electronic Spectra”. In: *Principles and Applications of Quantum Chemistry* (Jan. 2016), pp. 291–337. DOI: [10.1016/B978-0-12-803478-1.00009-1](https://doi.org/10.1016/B978-0-12-803478-1.00009-1).
- [54] N. J. Harrick. *Internal reflection spectroscopy*. Harrick Scientific Corp, 1967, p. 327. ISBN: 0933946139.
- [55] Jean-Marie Herrmann. “Heterogeneous photocatalysis: fundamentals and applications to the removal of various types of aqueous pollutants”. In: *Catalysis Today* 53.1 (Oct. 1999), pp. 115–129. ISSN: 0920-5861. DOI: [10.1016/S0920-5861\(99\)00107-8](https://doi.org/10.1016/S0920-5861(99)00107-8).
- [56] William Herschel and J. L. E. (John Louis Emil) Dreyer. *The scientific papers of Sir William Herschel : including early papers hitherto unpublished. Volume 1*, p. 597. ISBN: 1108064620.
- [57] Jí Homola, Sinclair S Yee, and Gunter Gauglitz. “Surface plasmon resonance sensors”. In: *Sensors and Actuators B: Chemical* 54.1-2 (1999), pp. 3–15.
- [58] Ammar Houas et al. “Photocatalytic degradation pathway of methylene blue in water”. In: *Applied Catalysis B: Environmental* 31.2 (May 2001), pp. 145–157. ISSN: 0926-3373. DOI: [10.1016/S0926-3373\(00\)00276-9](https://doi.org/10.1016/S0926-3373(00)00276-9).
- [59] I.A.DEGEN. *Tables of Characteristic group frequencies for the interpretation of infrared and raman spectra*. ACOLYTE PUBLICATIONS, 1997, pp. 48, 67–70. ISBN: 0 9531205 0 3.
- [60] Alex Ibbadon et al. “Heterogeneous Photocatalysis: Recent Advances and Applications”. In: *Catalysts* 3.1 (Mar. 2013), pp. 189–218. ISSN: 2073-4344. DOI: [10.3390/catal3010189](https://doi.org/10.3390/catal3010189).
- [61] Dimitri Ivanov et al. “Evaluation of the ordering of membranes in multilayer stacks built on an ATR-FTIR germanium crystal with atomic force microscopy: the case of the H<sup>+</sup>, K<sup>+</sup>-ATPase-containing gastric tubulovesicle membranes”. In: *Biophysical journal* 87.2 (2004), pp. 1307–1315.
- [62] Tarek S. Jamil et al. “Homogeneous photocatalytic processes for degradation of some endocrine disturbing chemicals under UV irradiation”. In: *Journal of Water Process Engineering* 18 (Aug. 2017), pp. 159–168. ISSN: 2214-7144. DOI: [10.1016/J.JWPE.2017.04.005](https://doi.org/10.1016/J.JWPE.2017.04.005).
- [63] William P Jencks. *Catalysis in chemistry and enzymology*. Courier Corporation, 1987.
- [64] Robert W Johnson and RH French. “Light-scattering efficiency of white pigments: an analysis of model core-shell pigments vs. optimized rutile TiO<sub>2</sub>”. In: *TAPPI Journal* 80 (1997).

- [65] Ibrahim Khan, Khalid Saeed, and Idrees Khan. “Nanoparticles: Properties, applications and toxicities”. In: *Arabian Journal of Chemistry* (May 2017). ISSN: 1878-5352. DOI: [10.1016/J.ARABJC.2017.05.011](https://doi.org/10.1016/J.ARABJC.2017.05.011).
- [66] Soonhyun Kim, Hyunwoong Park, and Wonyong Choi. “Comparative Study of Homogeneous and Heterogeneous Photocatalytic Redox Reactions:-  $\text{PW}_{12}\text{O}_{40}$  vs  $\text{TiO}_2$ ”. In: (2004). DOI: [10.1021/JP049789G](https://doi.org/10.1021/JP049789G).
- [67] Helmut Knözinger and Karl Kochloeff. “Heterogeneous Catalysis and Solid Catalysts”. In: *Ullmann’s Encyclopedia of Industrial Chemistry*. Weinheim, Germany: Wiley-VCH Verlag GmbH & Co. KGaA, Jan. 2003. DOI: [10.1002/14356007.a05\\_313](https://doi.org/10.1002/14356007.a05_313).
- [68] Wo Kohn and No Rostoker. “Solution of the Schrodinger equation in periodic lattices with an application to metallic lithium”. In: *Physical Review* 94.5 (1954), p. 1111.
- [69] Erwin Kretschmann and Heinz Raether. “Radiative decay of non radiative surface plasmons excited by light”. In: *Zeitschrift fr Naturforschung A* 23.12 (1968), pp. 2135–2136.
- [70] Keith J. (Keith James) Laidler, John H. Meiser, and Bryan C. Sanctuary. *Physical chemistry*. Houghton Mifflin, 2003, p. 1060. ISBN: 0618123415.
- [71] S Lakshmi, R Renganathan, and S Fujita. “Study on  $\text{TiO}_2$ -mediated photocatalytic degradation of methylene blue”. In: *Journal of Photochemistry and Photobiology A: Chemistry* 88.2-3 (1995), pp. 163–167.
- [72] Johann Heinrich Lambert and David L. DiLaura. *Photometry, or, On the measure and gradations of light, colors, and shade : translation from the Latin of Photometria, sive, De mensura et gradibus luminis, colorum et umbrae*. [New York?]: Illuminating Engineering Society of North America, 2001. ISBN: 9780879951795.
- [73] Heike Lampert, Werner Mikenda, and Alfred Karpfen. “Molecular geometries and vibrational spectra of phenol, benzaldehyde, and salicylaldehyde: experimental versus quantum chemical data”. In: *The Journal of Physical Chemistry A* 101.12 (1997), pp. 2254–2263.
- [74] LENNTECH. *Silicon (Si) and water*.
- [75] Michael E Levinstein, Sergey L Rumyantsev, and Michael S Shur. *Properties of Advanced Semiconductor Materials: GaN, AlN, InN, BN, SiC, SiGe*. John Wiley & Sons, 2001.
- [76] H. H. Li. “Refractive index of silicon and germanium and its wavelength and temperature derivatives”. In: *Journal of Physical and Chemical Reference Data* 9.3 (July 1980), pp. 561–658. ISSN: 0047-2689. DOI: [10.1063/1.555624](https://doi.org/10.1063/1.555624).
- [77] LIFESAVER. *Water Filters — LifeSaver Portable Water Filters — Essential For Survival*. URL: <https://iconlifesaver.com/> (visited on 08/28/2018).

- [78] Amy L. Linsebigler, Guangquan. Lu, and John T. Yates. “Photocatalysis on TiO<sub>2</sub> Surfaces: Principles, Mechanisms, and Selected Results”. In: *Chemical Reviews* 95.3 (May 1995), pp. 735–758. ISSN: 0009-2665. DOI: [10.1021/cr00035a013](https://doi.org/10.1021/cr00035a013).
- [79] GA Luna-Acosta et al. “One dimensional Kronig-Penney model with positional disorder: Theory versus experiment”. In: *Physical Review B* 80.11 (2009), p. 115112.
- [80] Th. Maggos et al. “Photocatalytic degradation of NO<sub>x</sub> gases using TiO<sub>2</sub>-containing paint: A real scale study”. In: *Journal of Hazardous Materials* 146.3 (July 2007), pp. 668–673. ISSN: 0304-3894. DOI: [10.1016/J.JHAZMAT.2007.04.079](https://doi.org/10.1016/J.JHAZMAT.2007.04.079).
- [81] S Malato et al. “Photocatalytic treatment of water-soluble pesticides by photo-Fenton and TiO<sub>2</sub> using solar energy”. In: *Catalysis Today* 76.2-4 (Nov. 2002), pp. 209–220. ISSN: 0920-5861. DOI: [10.1016/S0920-5861\(02\)00220-1](https://doi.org/10.1016/S0920-5861(02)00220-1).
- [82] Filippo Mangolini, Antonella Rossi, and Nicholas D Spencer. “In situ attenuated total reflection (ATR/FT-IR) tribometry: a powerful tool for investigating tribochemistry at the lubricant–substrate interface”. In: *Tribology Letters* 45.1 (2012), pp. 207–218.
- [83] Yves Mar’echal. “The molecular structure of liquid water delivered by absorption spectroscopy in the whole IR region completed with thermodynamics data”. In: *Journal of Molecular Structure* 1004.1-3 (Oct. 2011), pp. 146–155. ISSN: 0022-2860. DOI: [10.1016/J.MOLSTRUC.2011.07.054](https://doi.org/10.1016/J.MOLSTRUC.2011.07.054).
- [84] BRIAN J McCarthy and ROBERT B Church. “The specificity of molecular hybridization reactions”. In: *Annual review of biochemistry* 39.1 (1970), pp. 131–150.
- [85] D. Melgoza, A. Hern’andez-Ram’irez, and J. M. Peralta-Hern’andez. “Comparative efficiencies of the decolourisation of Methylene Blue using Fenton’s and photo-Fenton’s reactions”. In: *Photochemical & Photobiological Sciences* 8.5 (2009), p. 596. ISSN: 1474-905X. DOI: [10.1039/b817287k](https://doi.org/10.1039/b817287k).
- [86] Andrew Mills, Richard H. Davies, and David Worsley. “Water purification by semiconductor photocatalysis”. In: *Chemical Society Reviews* 22.6 (Jan. 1993), p. 417. ISSN: 0306-0012. DOI: [10.1039/cs9932200417](https://doi.org/10.1039/cs9932200417).
- [87] Francis M. Mirabella. “Principles, Theory and Practice of Internal Reflection Spectroscopy”. In: *Handbook of Vibrational Spectroscopy*. Ed. by Peter R. Griffiths. Chichester, UK: John Wiley & Sons, Ltd, Aug. 2006. DOI: [10.1002/0470027320.s2301](https://doi.org/10.1002/0470027320.s2301).
- [88] Matteo Monai et al. “Brookite: Nothing New under the Sun?” In: *Catalysts* 7.10 (Oct. 2017), p. 304. ISSN: 2073-4344. DOI: [10.3390/catal7100304](https://doi.org/10.3390/catal7100304).
- [89] Thomas A Morton, David G Myszka, and Irwin M Chaiken. “Interpreting complex binding kinetics from optical biosensors: a comparison of analysis by linearization, the integrated rate equation, and numerical integration”. In: *Analytical biochemistry* 227.1 (1995), pp. 176–185.



- [90] Laurence A. Nafie and Max Diem. “Theory of High Frequency Differential Interferometry: Application to the Measurement of Infrared Circular and Linear Dichroism via Fourier Transform Spectroscopy”. In: *Applied Spectroscopy*, Vol. 33, Issue 2, pp. 130-135 33.2 (Mar. 1979), pp. 130–135.
- [91] Kazuya Nakata and Akira Fujishima. “TiO<sub>2</sub> photocatalysis: Design and applications”. In: *Journal of Photochemistry and Photobiology C: Photochemistry Reviews* 13.3 (Sept. 2012), pp. 169–189. ISSN: 1389-5567. DOI: [10.1016/J.JPHOTOCHEMREV.2012.06.001](https://doi.org/10.1016/J.JPHOTOCHEMREV.2012.06.001).
- [92] Meng Ni et al. “A review and recent developments in photocatalytic water-splitting using TiO<sub>2</sub> for hydrogen production”. In: *Renewable and Sustainable Energy Reviews* 11.3 (2007), pp. 401–425.
- [93] Patrick Nickels et al. “Laboratory scale water circuit including a photocatalytic reactor and a portable in-stream sensor to monitor pollutant degradation”. In: *Industrial & Engineering Chemistry Research* 51.8 (2012), pp. 3301–3308.
- [94] R A Niemann. “Determination of formetanate hydrochloride in selected fruits by coupled-column cation exchange liquid chromatography.” In: *Journal of AOAC International* 76.6 (), pp. 1362–8. ISSN: 1060-3271.
- [95] Teruhisa Ohno et al. “Morphology of a TiO<sub>2</sub> Photocatalyst (Degussa, P-25) Consisting of Anatase and Rutile Crystalline Phases”. In: *Journal of Catalysis* 203.1 (Oct. 2001), pp. 82–86. ISSN: 00219517. DOI: [10.1006/jcat.2001.3316](https://doi.org/10.1006/jcat.2001.3316).
- [96] B. Ohtani et al. “What is Degussa (Evonik) P25? Crystalline composition analysis, reconstruction from isolated pure particles and photocatalytic activity test”. In: *Journal of Photochemistry and Photobiology A: Chemistry* 216.2-3 (Dec. 2010), pp. 179–182. ISSN: 1010-6030. DOI: [10.1016/J.JPHOTOCHEM.2010.07.024](https://doi.org/10.1016/J.JPHOTOCHEM.2010.07.024).
- [97] Keith B. Oldham and J. Mark Parnis. “Shining light on Beer’s law”. In: *ChemTexts* 3.2 (June 2017), p. 5. ISSN: 2199-3793. DOI: [10.1007/s40828-017-0042-z](https://doi.org/10.1007/s40828-017-0042-z).
- [98] Oleg V. Ovchinnikov et al. “Manifestation of intermolecular interactions in FTIR spectra of methylene blue molecules”. In: *Vibrational Spectroscopy* 86 (Sept. 2016), pp. 181–189. ISSN: 0924-2031. DOI: [10.1016/J.VIBSPEC.2016.06.016](https://doi.org/10.1016/J.VIBSPEC.2016.06.016).
- [99] Jesung Park et al. “Dye-enhanced multimodal confocal microscopy for noninvasive detection of skin cancers in mouse models”. In: *Journal of biomedical optics* 15.2 (2010), p. 026023.
- [100] José Peral, Javier Muñoz, and Xavier Domènech. “Photosensitized CN- oxidation over TiO<sub>2</sub>”. In: *Journal of Photochemistry and Photobiology A: Chemistry* 55.2 (1990), pp. 251–257.
- [101] Robert J Petersen. *Composite reverse osmosis and nanofiltration membranes*. 1993.

- 
- [102] G. Pfeifer and R. Boistelle. “Experimental and theoretical morphologies of diuron, N’-(3,4-dichlorophenyl)-N,N-dimethylurea”. In: *Acta Crystallographica Section B Structural Science* 52.4 (Aug. 1996), pp. 662–667. ISSN: 01087681. DOI: [10.1107/S010876819600047X](https://doi.org/10.1107/S010876819600047X).
- [103] Verena Pfeifer et al. “Energy Band Alignment between Anatase and Rutile TiO<sub>2</sub>”. In: *J. Phys. Chem. Lett* 4 (2013), p. 4187. DOI: [10.1021/jz402165b](https://doi.org/10.1021/jz402165b).
- [104] R. L. Pfleegor and L. Mandel. “Interference of Independent Photon Beams”. In: *Physical Review* 159.5 (July 1967), pp. 1084–1088. ISSN: 0031-899X. DOI: [10.1103/PhysRev.159.1084](https://doi.org/10.1103/PhysRev.159.1084).
- [105] I Pockrand et al. “Surface plasmon spectroscopy of organic monolayer assemblies”. In: *Surface Science* 74.1 (1978), pp. 237–244.
- [106] John Anthony Pople. “The molecular orbital theory of chemical valency. V. The structure of water and similar molecules”. In: *Proceedings of the Royal Society of London. Series A. Mathematical and Physical Sciences* 202.1070 (1950), pp. 323–336.
- [107] H Raether. “Surface plasma oscillations as a tool for surface examinations”. In: *Surface Science* 8.1-2 (1967), pp. 233–246.
- [108] Research Nester. *Commercial UV Water Purifier Market Size : Global Industry Demand, Growth, share & Forecast 2024*. URL: <https://www.researchnester.com/reports/commercial-uv-water-purifier-market/510> (visited on 08/29/2018).
- [109] Muhammad El-Saba. “Energy Band Theory & Classification of Solids”. In: Dec. 2015, p. 128. ISBN: 2010/16036.
- [110] Vidi. Saptari and Society of Photo-optical Instrumentation Engineers. *Fourier transform spectroscopy instrumentation engineering*. SPIE, 2004, p. 118. ISBN: 9780819451644.
- [111] Beth Shaz et al. *Transfusion medicine and hemostasis : clinical and laboratory aspects*, p. 1015. ISBN: 9780123971647.
- [112] Nobuaki Shimizu et al. “Sonocatalytic degradation of methylene blue with TiO<sub>2</sub> pellets in water”. In: *Ultrasonics sonochemistry* 14.2 (2007), pp. 184–190.
- [113] Brian C. Smith. “Alcohols—The Rest of the Story”. In: ().
- [114] Brian C. Smith. *Fundamentals of Fourier transform infrared spectroscopy*. CRC Press, 2011, p. 193. ISBN: 9781420069297.
- [115] Julio A. N. T. Soares. “Introduction to Optical Characterization of Materials”. In: *Practical Materials Characterization*. New York, NY: Springer New York, 2014, pp. 43–92. DOI: [10.1007/978-1-4614-9281-8\\_2](https://doi.org/10.1007/978-1-4614-9281-8_2).
- [116] George. Socrates. *Infrared and raman characteristic group frequencies : tables and charts*. John Wiley & Sons, 2007, p. 347. ISBN: 9780470093078.
-



- [117] Srinivasa Sourirajan et al. *Reverse osmosis*. London, UK: Logos Press Ltd., 1970.
- [118] Barbara Stuart. “Infrared spectroscopy”. In: *Kirk-Othmer Encyclopedia of Chemical Technology* (2000), pp. 1–18.
- [119] Kiyoshi Takahashi, A. (Akihiko) Yoshikawa, and Adarsh Sandhu. *Wide bandgap semiconductors : fundamental properties and modern photonic and electronic devices*. Springer, 2007, p. 460. ISBN: 9783540472353.
- [120] Kiyoshi Takahashi, Akihiko Yoshikawa, and Adarsh Sandhu. “Wide bandgap semiconductors”. In: *Springer-Verlag Berlin Heidelberg*. (2007), p. 239.
- [121] Masato Takeuchi et al. “Mechanism of Photoinduced Superhydrophilicity on the TiO<sub>2</sub> Photocatalyst Surface”. In: (2005). DOI: [10.1021/JP058075I](https://doi.org/10.1021/JP058075I).
- [122] Hui Ling Tan, Fatwa F. Abdi, and Yun Hau Ng. “Heterogeneous photocatalysts: an overview of classic and modern approaches for optical, electronic, and charge dynamics evaluation”. In: *Chemical Society Reviews* 48.5 (Mar. 2019), pp. 1255–1271. ISSN: 1460-4744. DOI: [10.1039/C8CS00882E](https://doi.org/10.1039/C8CS00882E).
- [123] *Theory 2: White Light Interference and Coherence — Optical Profilometer Training*.
- [124] Thomas Scientific. *Mesh Filter at Thomas Scientific*. URL: <https://www.thomassci.com/scientific-supplies/Mesh-Filter> (visited on 06/12/2018).
- [125] Thomas Vinciguerra. *Barry Commoner - An Environmentalist From the '70s Still Has Hope - The New York Times*.
- [126] Nicholas C. Thomas. “The early history of spectroscopy”. In: *Journal of Chemical Education* 68.8 (Aug. 1991), p. 631. ISSN: 0021-9584. DOI: [10.1021/ed068p631](https://doi.org/10.1021/ed068p631).
- [127] Chisato Tsuji. *IB Higher Level Maths Exploration Derivation of the Beer-Lambert Law*. Tech. rep.
- [128] Chiara Uboldi et al. “Role of the crystalline form of titanium dioxide nanoparticles: Rutile, and not anatase, induces toxic effects in Balb/3T3 mouse fibroblasts”. In: *Toxicology in Vitro* 31 (Mar. 2016), pp. 137–145. ISSN: 0887-2333. DOI: [10.1016/J.TIV.2015.11.005](https://doi.org/10.1016/J.TIV.2015.11.005).
- [129] Tsutomu Umebayashi et al. “Visible light-induced degradation of methylene blue on S-doped TiO<sub>2</sub>”. In: *Chemistry Letters* 32.4 (2003), pp. 330–331.
- [130] *UV LEDs — RS Components, data sheet on their website*.
- [131] “UV purification of air and water in dental operatories”. In: (Nov. 1998).
- [132] M. Vallet-Regi et al. “A New Property of MCM-41:- Drug Delivery System”. In: (2000). DOI: [10.1021/CM0011559](https://doi.org/10.1021/CM0011559).
- [133] *VERTEX 80/80v - Overview - VERTEX 80/80v FT-IR spectrometers — Bruker*.

- [134] M Voue et al. “Biochemical interaction analysis on ATR devices: A wet chemistry approach for surface functionalization”. In: *Langmuir* 23.2 (2007), pp. 949–955.
- [135] Water Aid. *WaterAid — The wonderful things you did - annual report 2016-17*. Tech. rep.
- [136] WHO. *Dioxins and their effects on human health*. 2016.
- [137] WHO. *World Health Organisation- Maternal and Child Health : KENYA*. Tech. rep.
- [138] “WHO — Water and sanitation”. In: *WHO* (2017).
- [139] Jimmie L Williams. “Monolith structures, materials, properties and uses”. In: *Catalysis Today* 69.1-4 (2001), pp. 3–9.
- [140] Gideon P Winward et al. “Chlorine disinfection of grey water for reuse: effect of organics and particles”. In: *Water research* 42.1-2 (2008), pp. 483–491.
- [141] Th. Wolkenstein. “The Electronic Theory of Photocatalytic Reactions on Semiconductors”. In: *Advances in Catalysis* 23 (Jan. 1973), pp. 157–208. ISSN: 0360-0564. DOI: [10.1016/S0360-0564\(08\)60301-6](https://doi.org/10.1016/S0360-0564(08)60301-6).
- [142] Eli Yablonovitch. “Photonic band-gap structures”. In: *JOSA B* 10.2 (1993), pp. 283–295.
- [143] Kansho Yamamoto et al. “Pyroelectric aluminum nitride micro electromechanical systems infrared sensor with wavelength-selective infrared absorber”. In: *Applied Physics Letters* 104.11 (2014), p. 111111.
- [144] ”Time to Z” and Frequency from A. *Phase*. National Institute of Standards and Technology (NIST).
- [145] Zhaoguo Zhang et al. “Fabrication of titanium dioxide with durable superhydrophilicity by anodization”. In: *RSC Advances* 5.118 (Nov. 2015), pp. 97702–97709. ISSN: 2046-2069. DOI: [10.1039/C5RA17847A](https://doi.org/10.1039/C5RA17847A).
- [146] Paul W. Zitzewitz and Mark. Davids. *Glencoe physics : principles and problems*. Glencoe/McGraw-Hill, 1999, p. 800. ISBN: 0028254732.